

Gutachter:

1. PD Dr. Harald Hoppe
2. Dr. Jeffrey Kettle

Friedrich-Schiller-Universität Jena
Glasgow University

Tag der Verteidigung: 20.10.2022

Table of Contents

Documentation of Authorship	
1 Introduction	1
P1 Agrivoltaics – the Perfect Fit for the Future of Organic Photovoltaics	12
P2 Transmission Windows of Charge Transport Layers and Electrodes in Highly Transparent Organic Solar Cells for Agrivoltaic Application.....	17
P3 Robustness of polymer solar cell stability against semiconductor properties and its susceptibility towards layer stack variations	18
P4 Performance and Stability of Organic Solar Cells bearing Nitrogen Containing Electron Extraction Layers	27
P5 An effective method of reconnoitering current-voltage (IV) characteristics of organic solar cells	34
7 Summary	43
8 Zusammenfassung.....	46
Abbreviations	49
Symbols.....	50
References	51
Publication List	58
Acknowledgements	61
Declaration of Authorship / Selbstständigkeitserklärung.....	62
Publications P1 to P5.....	63

Documentation of Authorship

Erklärung zu den Eigenanteilen der Promovendin/des Promovenden sowie der weiteren Doktorandinnen/Doktoranden als Co-Autorinnen/-Autoren an den Publikationen und Zweitpublikationsrechten bei einer kumulativen Dissertation

Für alle in dieser kumulativen Dissertation verwendeten Manuskripte liegen die notwendigen Genehmigungen der Verlage („Reprint permissions“) für die Zweitpublikation vor.

Die Co-Autorinnen/-Autoren der in dieser kumulativen Dissertation verwendeten Manuskripte sind sowohl über die Nutzung, als auch über die oben angegebenen Eigenanteile der weiteren Doktorandinnen/Doktoranden als Co-Autorinnen/-Autoren an den Publikationen und Zweitpublikationsrechten bei einer kumulativen Dissertation informiert und stimmen dem zu.

Die Anteile der Promovendin/des Promovenden sowie der weiteren Doktorandinnen/Doktoranden als Co-Autorinnen/Co-Autoren an den Publikationen und Zweitpublikationsrechten bei einer kumulativen Dissertation sind in der Anlage aufgeführt.

Name der Promovendin/ des Promovenden	Datum	Ort	Unterschrift
--	-------	-----	--------------

Ich bin mit der Abfassung der Dissertation als publikationsbasierte Dissertation, d.h. kumulativ, einverstanden und bestätige die vorstehenden Angaben.

Name Betreuerin/ Betreuer	Datum	Ort	Unterschrift
------------------------------	-------	-----	--------------

Name Betreuerin/ Betreuer	Datum	Ort	Unterschrift
------------------------------	-------	-----	--------------

Introduction

1 Introduction

Within the next decades humankind has to face one of the most serious and biggest challenges. The complete energy system has to be changed from its current, fossil fuel-dominant state into a renewable and eco-friendly alternative. The necessity of this modification arises from the looming threat of a massive global climate change, which will likely be followed by huge impacts on civilization up to collapse. This scenario is not without precedents in human history, as the disintegration of ancient civilizations in the near east^[1] or the collapse of Mayan society^[2] was to a major extent fostered by local changes in climate patterns. A change in climatic patterns as current model calculations predict might result, due to our highly integrated global economy, in a complete collapse of the world economy accompanied by wars, famines and massive worldwide immiseration. The chaos induced through the global SARS-CoV-2 pandemic already gave a first indication of what even a minor disruption of the global supply chain means for most peoples' everyday live. As the goal is to preserve civilization as we know it, on the one hand we certainly have to move away from fossil fuels, but on the other hand still have to provide civilization with sufficient energy in the meantime.

One of the largest prospected sources for energy will be solar energy, especially in the form of photovoltaics (PV)^[3]. Photovoltaics has shown a massive reduction in cost for the last 20 years (Figure 1), as well as a massive expansion of deployment^[4]. Of course, these two measures are interconnected via the economies of scale. However, this deployment needs to be further accelerated especially with the next 10 years if the 1.5 Degree Celsius target should be seriously kept^[5]. So far, the industrial standard for PV are solar modules made from wafer-based mono-crystalline silicon solar cells. Though silicon itself is cheap and earth-abundant, the production of solar cells from this material is time and energy consuming. Furthermore, Si-PV is heavily relying on silver as material for electric contacts and as a consequence Si-PV manufacturing is consuming a large portion of the world's yearly silver production^[6]. Thus, potential supply chain issues are additionally threatening the PV production. Concerning applications, the bulky and stiff nature of silicon solar modules limits their area of application and slows down their installation. Given these drawbacks, modern research is seeking for attractive alternatives to Si-PV.

A potential alternative to silicon-based PV is printed PV. Currently there are two major technologies in development, on the one hand organic-inorganic hybrid perovskites and organic PV on the other hand. Printed PV comes with the added advantage of an inherently low energy footprint^[7] in manufacturing as well as a high processing speed^[8], and therefore an inexpensive production as well as faster and cheaper extension^[9] of production capabilities compared to Si-based technology. If printing is done on flexible^[10] substrates in a roll-to-roll manner for example, one will first get even higher manufacturing speeds, and second greater ease of installation and faster deployment times^[11]. Both of these technologies –hybrid perovskites and organic PV– come with their individual advantages and drawbacks. Concerning Perovskite PV, high-performance compositions achieve performances in the lab on a par with crystalline silicon. However, due to their reliance on lead they might impose some not yet fully evaluated environmental and health risks. Organic PV (OPV) on the other hand do not reach the same performance as Perovskite PV yet, but does not have negative impact in terms of environment and health^[12]. Due to these advantages this work focuses on OPV.

Introduction

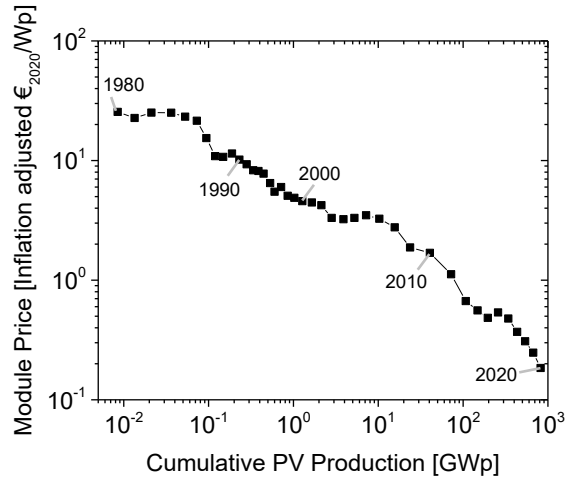


Figure 1: Development of the price per photovoltaic module throughout the last four decades. The Price has been reduced by more than two orders of magnitude^[4].

OPV is based on organic semiconductors^[13], materials which are characterized by a high degree of conjugation, i.e. molecules or polymers with alternations between single and double/triple bonds^[14]. As a consequence, an organic semiconductor with a sufficiently large conjugation length will show light absorption in the visible range of the electromagnetic spectrum. Moreover, through a clever combination of adequate chemical moieties, which are either electron withdrawing or electron pushing, a push-pull effect can be created and its absorption can even be shifted more towards the near-infrared range^[10, 15]. This effect is especially important for PV applications, because as most of the photon density of the solar spectrum is highest in the red and NIR range of it. A peculiarity of organic semiconductors is the fact that they only show a specific window of absorption window, i.e. organic semiconductors absorb only in a narrow range above their bandgap. In contrast, to inorganic semiconductors, which strongly absorb all photons which are higher in energy than their particular bandgap. Organic semiconductors do so only in a relatively narrow range above their bandgap. Thus, this constrained absorption makes them especially useful candidates for manufacturing semi-transparent photovoltaic devices^[10, 16], in contrast to their inorganic counterparts. Furthermore, organic semiconductors exhibit a low dielectric function and hence show a high exciton binding energy between 0.3 and 1 eV^[17].

The large exciton binding energy is responsible for the excitonic nature of device operation. In order to generate photocurrent an electron donor material and acceptor material have to be blended, at whose interface excitons can be split. One prerequisite for the morphology of the donor-acceptor blend and semiconductor heterojunction arises from the rather short lifetime of excitons. After an exciton has been generated within the donor phase through absorption of a photon, it has to diffuse towards the donor-acceptor interface in order to generate an electron-hole pair^[13b, 18]. Due to the short exciton life time, the exciton diffusion length is in the order of a few tens of nm^[19]. Thus, the ideal active layer structure as schematically depicted in Figure 2 has to provide particular peculiarities. The first one is a finely intermixed morphology on a scale of approximately 20 nm in order to increase the donor-acceptor interface and enable charge generation^[17e, 18, 20]. The second one is to a certain degree pure phases of donor and acceptor, which have to be all interconnected; i.e. all donor phases have to be interconnected to all other donor phases and the same for the

Introduction

acceptor phases, to allow for an efficient transport of charge carriers towards the electrodes^[21]. And the third peculiarity is that the donor has to preferentially accumulate towards the hole extracting contact, while the acceptor has to accumulate towards the electron extracting contact, i.e. a vertical layer stratification^[22]. In the case of bulk-heterojunction cells which is the research standard, such kind of morphology is solely developed on the basis of self-ordering processes. Donor and acceptor are usually dissolved in a common solvent and get coated onto a substrate usually via spin coating to create a uniform film^[23].

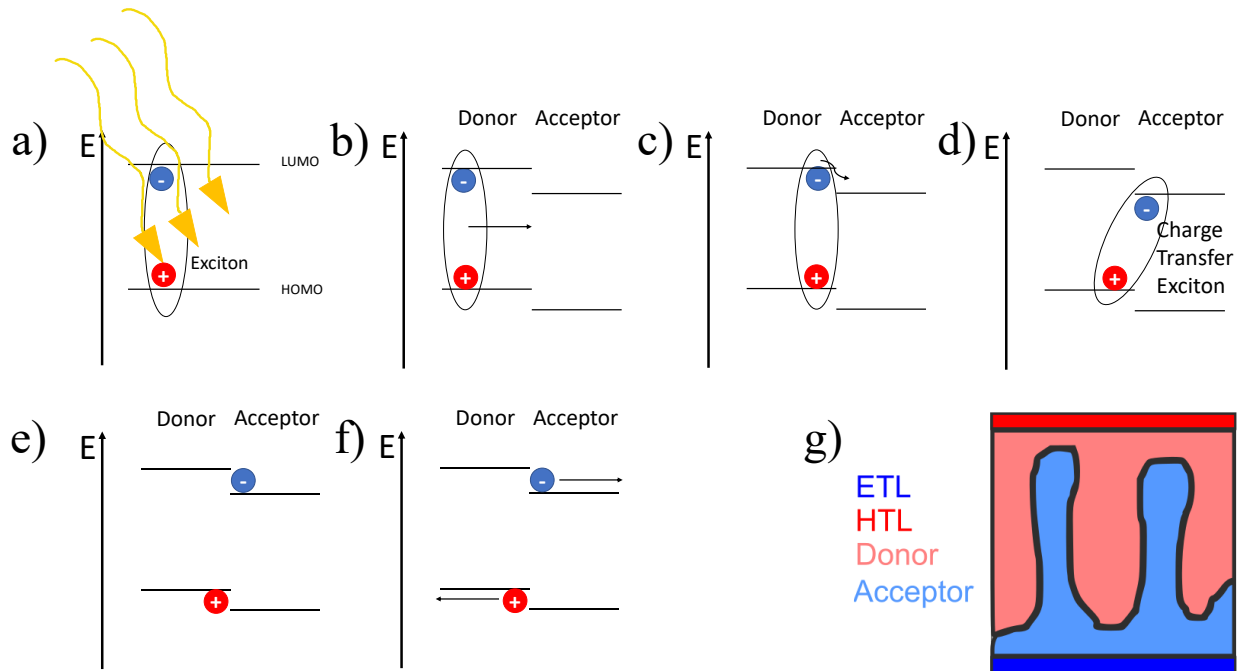
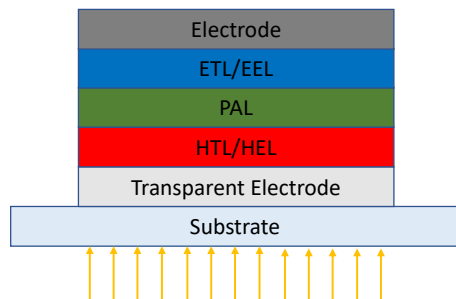


Figure 2: Charge carrier generation process in an organic solar cell, a) light absorption, b) exciton diffusion, c) charge transfer exciton formation, d) charge transfer exciton, e) charge separated state, f) charge transport. g) Bulk-heterojunction morphology of an organic solar cell, including adjacent hole transport layer (HTL) and electron transport layer (ETL).

Conventional

- PIN-Diode



Inverted

- NIP-Diode

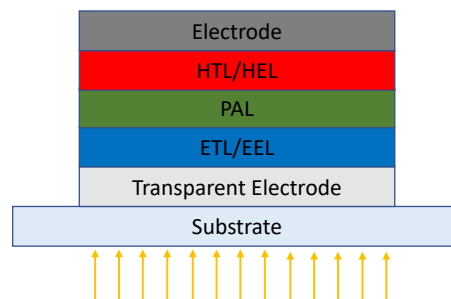


Figure 3: The two different architecture types used for organic solar cells; the usual difference is towards which contact side the respective charge carriers are extracted towards. EEL: Electron extraction layer; ETL: Electron Transport Layer; HEL: Hole extraction layer; HTL: Hole Transport Layer; PAL: Photoactive layer.

Introduction

In an OPV device there are usually different other layers adjacent to the active layer; those are a hole transport or hole extraction layer (HTL/HEL) as well as an electron transport or extraction layer (ETL/EEL) (Figure 3). They are required for multiple reasons, as they provide a good ohmic contact to the electrode materials and allow for efficient charge carrier collection and extraction^[24]. They also act as a barrier for charge carriers of the opposite kind and thus prevent recombination. The last component of organic solar cells are the electrodes, required to collect the charge carriers and connect the device to any load^[25]. For solar cells in general, the hole or electron extraction and the electrode layer adjacent to the transparent substrate need to be highly transparent in the absorption range of the photoactive layer (PAL) in order to allow a sufficient amount of light to reach the active layer. In the particular case of semi-transparent solar cells, the other charge transport layer (CTL) and substrate have to be highly transparent as well^[16b].

In principle there are two different architectures for OPV devices^[26], which are shown in Figure 3. On the one hand, there is the conventional architecture where the transparent electrode represents the cathode and low work function metals are usually used as anode material^[26]. On the other hand, there is the inverted architecture, where the transparent electrode represents the anode and high work function metals like silver are used as cathode material^[26-27]. The inverted architecture was especially introduced to increase the stability of OPV devices, as low work function metals are very prone to oxidation^[27-28].

In Figure 4 the development of officially registered record efficiencies for OPV devices over the last 20 years is shown^[29]. Though first research on organic solar cells already started back in the 1970s, devices back then only reached very low power conversion efficiencies (PCEs) below 1%^[30]. The early development of OPVs was mostly driven by improvement in design of the active layer. In Figure 5 different active layer morphologies are shown. At the very beginning of OPV research single layer devices were manufactured, which inherently showed a low efficiency^[30a]. Due to the high exciton binding energy of organic semiconductors, only very few charge carriers were formed which could have been extracted. After this was understood, the planar bi-layer structure was developed^[13a], where a flat layer of acceptor material was deposited on top of a layer of donor material or vice versa. Though devices of such a kind exhibited a more efficient charge carrier generation at the interface between donor and acceptor and provided an improved efficiency, they were suffering from drawbacks. Due to the low exciton diffusion length, either planar bi-layers had to be very thin resulting in a reduced absorption of the incident light and hence exciton generation, or for thicker donor or acceptor layers excitons decayed before reaching the donor-acceptor interface resulting in a reduced generation of free charge carriers.

Introduction

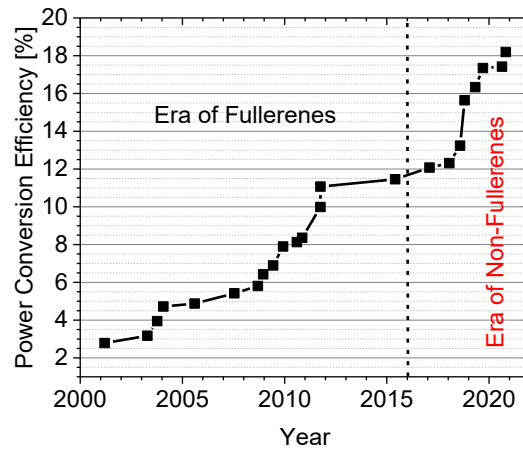


Figure 4: Record efficiency development over time for OPV devices according to the National Renewable Energies Laboratory (NREL) efficiency chart.

The next morphological development were bulk-heterojunctions, where donor and acceptor materials are mixed in a precursor solution and a film of a finely mixed morphology between donor and acceptor phase upon deposition^[31]. This morphology provided further improvement in performance, as now active layers can be thick enough to absorb most of the incident light, while the donor-acceptor interface is drastically increased and the required length for exciton diffusion is reduced. In addition, reliable transport pathways for charge carriers towards the contacts could be established^[19b, 31b, 32]. This kind of active layer morphology represents for the most part the OPV research today. As a final point, also ordered heterojunction approaches should be mentioned, where order is established by other means than de-mixing due to thermodynamic driving forces. Instead donor and/or acceptor are individually structured to form an interlocking (interdigitated) morphology^[33].

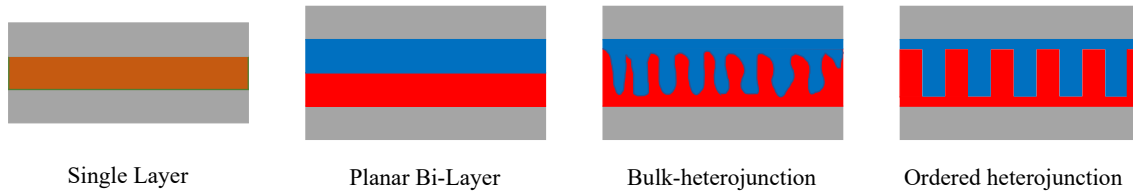


Figure 5: Development of the active layer morphology over the history of OPV research.

Besides the development in active layer morphology, there was also development in active layer materials. One big step was the discovery of fullerene as efficient electron acceptors^[13b]. The importance of this discovery is visible through the still-valid distinction between two main eras, the era of fullerenes and the era of non-fullerenes (Figure 4). Up to 2016 the best performing OPV devices contained some sort of fullerene as the main electron accepting component. Fullerenes are a group of spherically shaped carbon allotropes (Figure 6) which were discovered in the late 1980s^[34] and first used for organic solar cells in the early to mid-1990s^[13b]. Due to their shape, they aggregate and de-mix from the donor forming pure phases and allowing for efficient charge carrier transport^[32]. Though fullerenes enabled a massive improvement in OPV performance, they also suffer from several drawbacks. The production of fullerenes is rather energy intensive, their energy

Introduction

levels cannot be easily modified and only in a limited range^[35]. Furthermore, they tend to over aggregate resulting in a too coarse morphology and therefore loss in donor-acceptor interface and photocurrent^[35]. Moreover, fullerenes merely absorb in the solar spectrum which is why they barely contribute to the photocurrent of the device^[35].

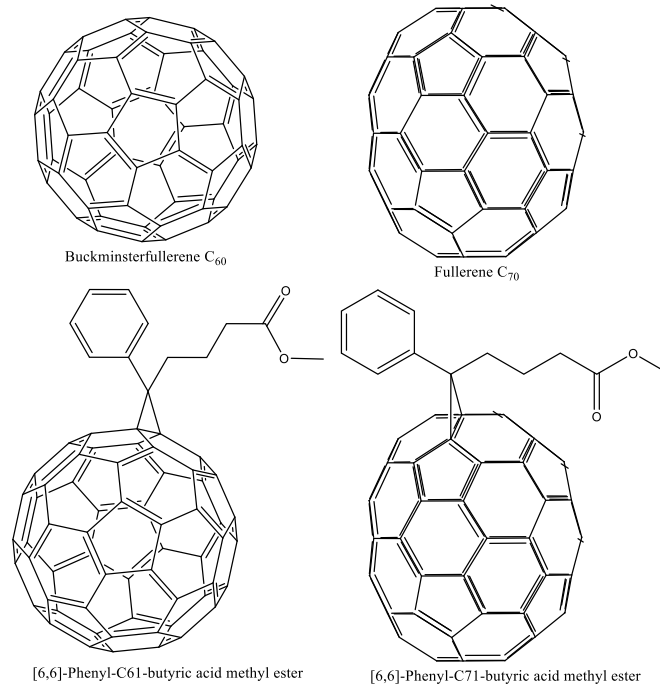


Figure 6: Different commonly used fullerene-based acceptors in organic solar cells.

Most of the development in performance during the fullerene era was achieved through designing donors which absorbed light in the red and NIR region of the solar spectrum where most photons are available, Figure 7 shows some commonly used polymer donors used in OPV research. One of the first driver of progress was *poly-3-hexylthiophene* (P3HT)^[36]. This homopolymer is easy to synthesize and nowadays one of the cheapest organic semiconducting polymers and available at scale. Due to the fact that P3HT forms semi-crystalline structures, it is still a widely used model compound. The Next big steps came with co-polymers like *poly[[9-(1-octylnonyl)-9H-carbazole-2,7-diyl]-2,5-thiophenediyl-2,1,3-benzothiadiazole-4,7-diyl-2,5-thiophenediyl]* (PCDTBT)^[37] and *poly-[[4,8-bis[(2-ethylhexyl)oxy]benzo[1,2-b:4,5-b']dithiophene-2,6-diyl][3-fluoro-2-[(2-ethylhexyl)carbonyl]thieno[3,4-b]thiophenediyl]]* (PTB7)^[38], PCDTBT had a very deep HOMO level which allowed for increased voltages in combination with fullerene acceptors^[39]. PTB7 and related polymers, instead, showed a red shifted absorption spectrum allowing for increased photocurrents^[38, 40]. Another important step in the development of semiconducting polymers were polymers like *poly-[(2,6-(4,8-bis(5-(2-ethylhexyl)thiophen-2-yl)-benzo[1,2-b:4,5-b']dithiophene))-alt-(5,5-(1',3'-di-2-thienyl-5',7'-bis(2-ethylhexyl)benzo[1',2'-c:4',5'-c']dithiophene-4,8-dione)]* (PBDB-T) and *Poly-[(5,6-difluoro-2,1,3-benzothiadiazol-4,7-diyl)-alt-(3,3''-di(2-octyldodecyl)-2,2';5',2'';5'',2'''-quaterthiophen-5,5'''-diyl)]* (PffBT4T), which showed a strong temperature dependent aggregation already in solution. This behavior paves the way to a pre-patterning effect for the BHJ morphology during film formation^[41].

Introduction

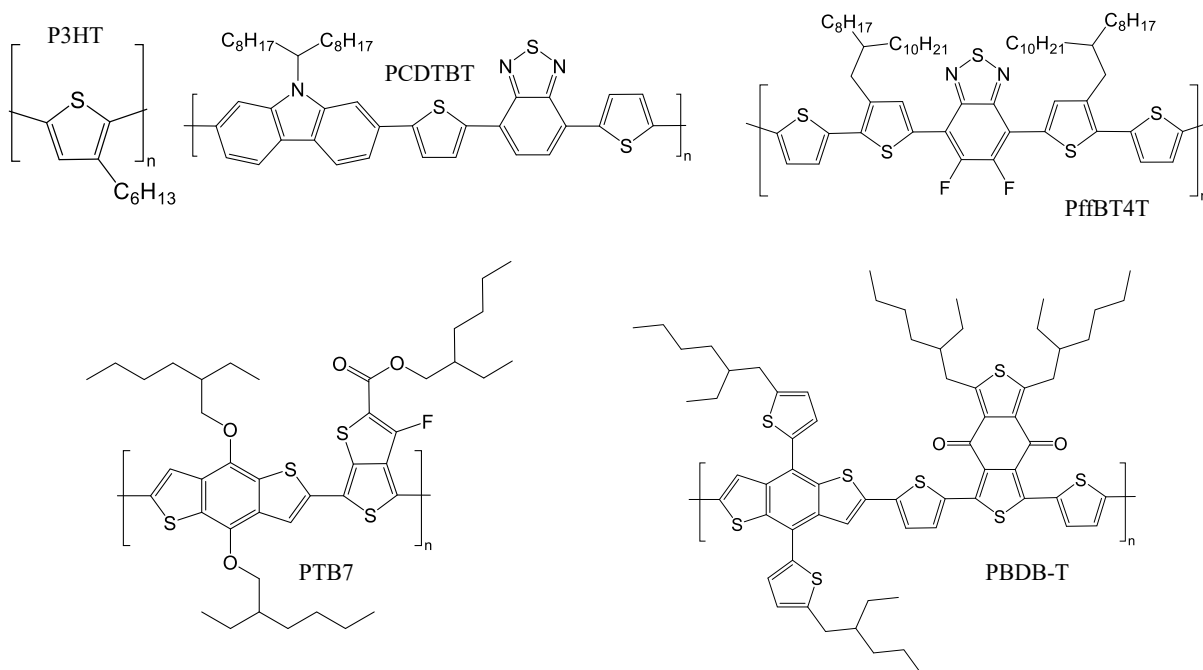


Figure 7: Donor polymers usually used in organic solar cells.

Although research on alternatives to fullerenes as acceptor material in OPV was ongoing already years before 2016, only in 2016 the first solar cell devices which performed on a par or even better than the best fullerene devices was published^[42]. This progress was enabled by two important characteristics of non-fullerene acceptors (NFAs). First, NFAs allow for proper control of their stacking due to their mostly planar structure and second their small bandgap in combination with mid bandgap donors allows to increase short circuit current densities^[43]. Further enhancement of device efficiency past 2016 was mainly driven by a reduction in voltage loss^[44] and an increase in fill factor^[45]. The synthetical flexibility of NFAs also allowed for a wider variation in HOMO and LUMO energy levels and the NFAs bandgaps^[35]. Concerning the planar structure of most NFAs, controlling their stacking behavior is very important, as strong π - π stacking might result in excessive crystallization and phase separation^[43a].

In Figure 8 several commonly used NFAs are shown. The first OPV device that showed an efficiency being on a par with the best performing fullerene-based solar cells was made from 3,9-bis(2-methylene-(3-(1,1-dicyanomethylene)-indanone))-5,5,11,11-tetrakis(4-hexylphenyl)-dithieno[2,3-d':2',3'-d']-s-indaceno[1,2-b:5,6-b']dithiophene (ITIC) as NFA in combination with PBDB-T as donor^[42a]. ITIC is especially structured with an electron donating core and electron withdrawing end units. In the following years ITIC was modified in multiple ways, such as methylation^[42b] or halogenation^[46] of the electron withdrawing capping groups at both ends of the molecule as shown on the example of 3,9-bis(2-methylene-((3-(1,1-dicyanomethylene)-6,7-difluoro)-indanone))-5,5,11,11-tetrakis(4-hexylphenyl)-dithieno[2,3-d':2',3'-d']-s-indaceno[1,2-b:5,6-b']dithiophene (IT-4F)^[46a]. The fluorination resulted in a modification of HOMO, LUMO and bandgap and improved the device performance up to 13%^[47]. Roughly at the same time

Introduction

(5*Z*,5'*Z*)-5,5'-((7,7'-(4,4,9,9-tetraoctyl-4,9-dihydro-*s*-indaceno [1,2-*b*:5,6-*b'*]dithiophene-2,7-diyl) bis(benzo[*c*][1,2,5]thiadiazole-7,4-diyl))bis(methanylylidene))bis(3-ethyl-2-thioxothiazolidin-4-one) (IDTBR) was combined with P3HT and showed a high efficiency above 6% and excellent stability over 3000 h^[48]. This was especially interesting as P3HT is a cheap and easy to synthesize polymer.

Another important NFA family developed from 2015 on were the so called Y-themed NFAs^[49], with 2,2' - ((2*Z*,2'*Z*) - ((12,13-bis (2-ethylhexyl) -3,9-diundecyl-12,13-dihydro - [1,2,5] thiadiazolo [3,4-*e*] thieno [2'',3'':4',5'] thieno [2',3':4,5] pyrrolo [3,2-*g*] thieno [2',3':4,5] thieno [3,2-*b*] indole-2,10-diyl) bis (methanylylidene)) bis (5,6-difluoro-3-oxo-2,3-dihydro-1*H*-indene-2,1-diylidene))dimalononitrile (Y6) as an exemplary member. For Y-themed molecules the A-D-A structure of ITIC was extended creating an acceptor-donor-acceptor-donor-acceptor (A-D-A-D-A) structure. This structure resulted in even smaller bandgaps of around 1.4 eV, in comparison to 1.6 eV for ITIC. Recently, The Y-Family of acceptors is also responsible for most the latest records of up to 19% PCE for OPV devices^[50].

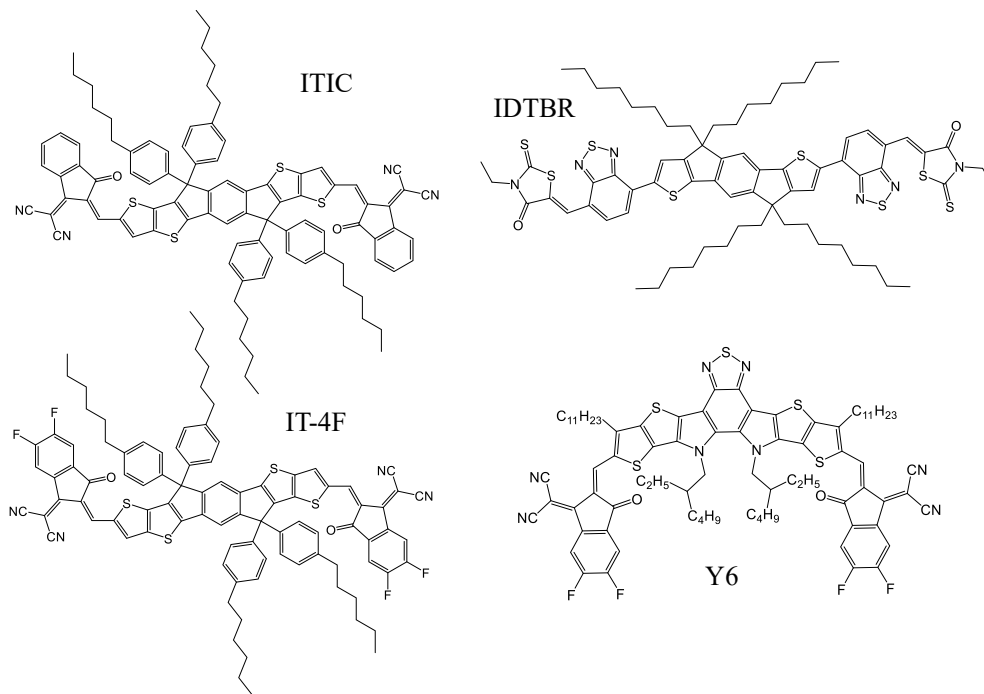


Figure 8: Commonly used NFAs in organic solar cell research since 2016.

Except for efficiency in the last years OPV devices made a lot of strides in terms of stability, which is another important factor for being viable as a commercial technology. Whereas early devices showed stabilities of just a few hours, recently extrapolated lifetimes of up to 30000 h were achieved under illumination assuming 1000 sun hours per year^[51], this represents a lifetime of 30 years, which is compatible with the current industry expectation for Si-based PV modules. Some of the important findings obtained in the last decades leading to this increase in lifetime shall be summarized here. One important factor for stability are aromatic structures within the backbones of the organic semiconductors. early semiconducting polymers such as *polyphenylenevinylene* contained aliphatic double bonds, which were easily oxidized and therefor the performance

Introduction

decayed quickly due to a loss in conjugation^[52]. In addition, it was found that a high degree of crystallinity can improve stability for two main reasons^[53]. First, the increased density of crystallized materials reduces the ingress rate of extrinsic factors like water and oxygen. Second intermediate steps in degradation necessitate an increased backbone flexibility and a reduced backbone planarity^[54]. As it was found that degradation proceeds via first a tilting of moieties out of the molecular plane, as this disrupts the planarity, it would also weaken π - π -stacking, which is a prerequisite for crystallization. That means very crystalline materials show resistance against a loss of backbone planarity. From the role of the degree of crystallinity the impact of the side chains attached to the polymer or molecule follows. Side chains provide solubility and can prevent excessive stacking. However, if side chains induce too much disorder, the degree of crystallinity will be drastically reduced resulting in poor stability. Recently it was shown that thermal stability in polymer:NFA blends is not conveyed via a stable morphology, but actually by a kinetic hindrance for de-mixing, i.e. diffusion coefficients of NFAs in the polymer matrix is so low, that the blend will not de-mix within the useful lifetime of the device^[21a].

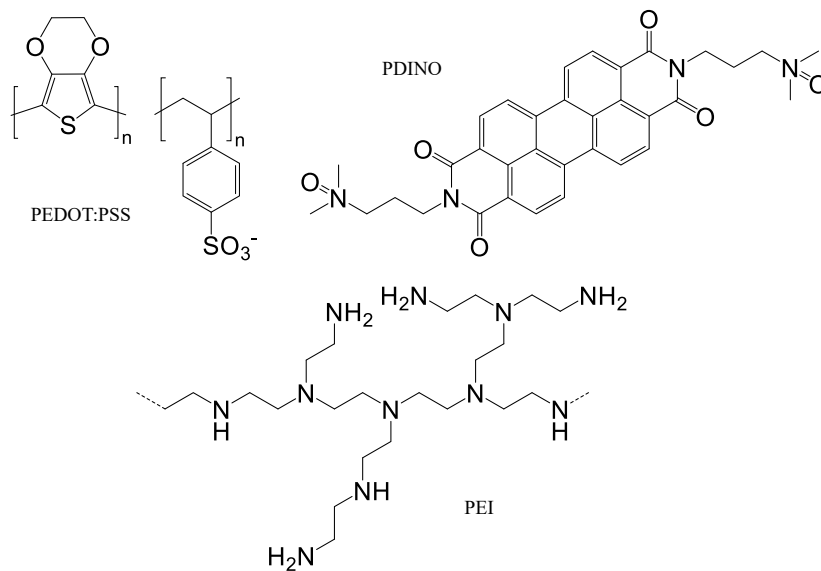


Figure 9: Organic charge extraction/transport materials commonly used in organic solar cells.

Another important topic in regards to performance as well as stability is the choice of the charge transport layers in OPV devices. As already stated they have to be transparent, provide a low ohmic contact with the respective electrode, and efficiently collect and/or transport charge carriers. There are three main types of charge transport layers, highly doped organic semiconductors, organic insulators, and metal oxides^[24d, 55]. Some examples of commonly used organic semiconductors are *poly(3,4-ethylenedioxythiophene) polystyrene sulfonate* (PEDOT:PSS, Figure 9) and *2,9-Bis[3-(dimethylamino)propyl]anthra[2,1,9-def:6,5,10-d'e'f']diisoquinoline-1,3,8,10(2H,9H)-tetrone* (PDINO)^[24c, 56], an example of a widely used organic insulator is *polyethylenimine* (PEI)^[57], and some commonly used metal oxides are *zinc oxide*, *titanium dioxide*, *molybdenum oxide* and *tungsten oxide*. Also, hybrids of the aforementioned material classes are reported^[55].

The impact of the charge extraction layers on the device performance is due to multiple factors. These layers are capable to form an ohmic contact between active layer and electrodes, which is

Introduction

usually evoked by an inherent electric dipole moment^[57]. As a result, the work function of the electrode is shifted to be more compatible with the respective HOMO of the donor or LUMO of the acceptor and facilitates a more efficient hole or electron extraction without an energy barrier. Furthermore, organic charge extraction layers can also passivate the electrode interface by forming coordinative bonds with the surface of either metal or metal oxide electrodes^[58], both of the aforementioned effects are shown in Figure 10. In addition, the charge transport layers can also have a strong impact on the active layer stratification^[22b], i.e. it is preferable that the bulk-heterojunction (BHJ) blend is enriched in donor near the hole extracting layer, whereas the acceptor is concentrated at the electron extracting layer. Mixing PEDOT:PSS with tungsten oxide nanoparticles and creating hybrid HTL, resulted in the surface free energy of the HTL being modified to be closer to the surface free energy of the donor of the blend, resulting in a preferential layer stratification and an increase in fill factor^[45b].

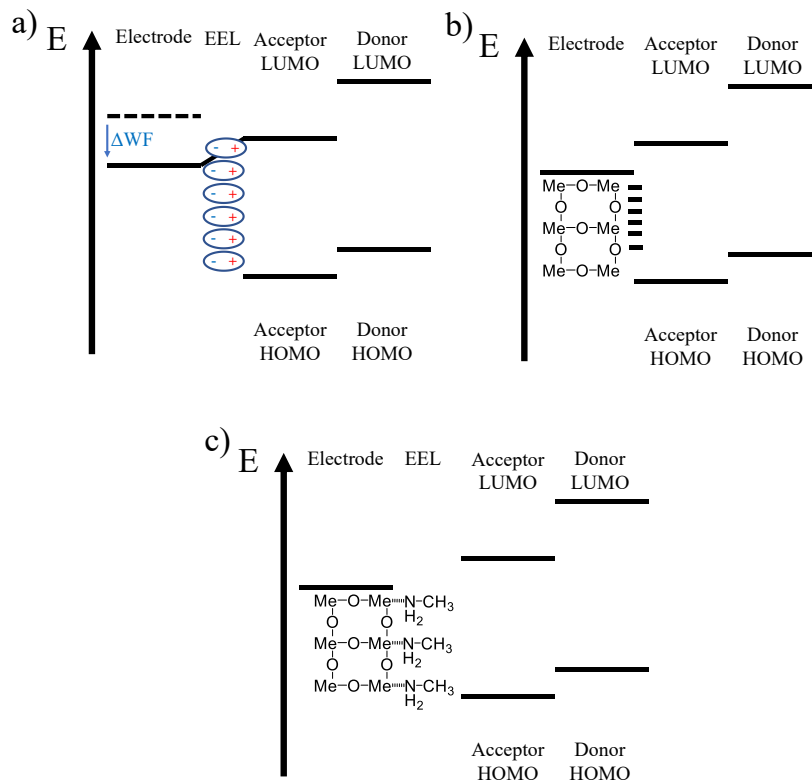


Figure 10: The impact of charge extraction layers on the interface between active layer and electrode, a) dipole of electron extracting layer is oriented in a fashion that the work function of the electrode gets lowered and an otherwise existing energy barrier gets removed; b) without an EEL there are states in the gap at the interface due to dangling bonds from the electrode, which are recombination centers; c) passivation of such dangling bonds by formation of coordinative bonds between EEL and electrode..

Concerning stability, the charge transport layers also play an important role. For example, PEDOT:PSS is hygroscopic and takes up water from ambient atmosphere which has multiple detrimental effects. On the one hand water reduces the PEDOT:PSS film conductivity through film swelling and therefore lowering the probability of hopping of charge carriers from one PEDOT chain to another PEDOT chain^[28a, 52, 59]. Due to the acidic nature of PEDOT:PSS moisture ingress can also accelerate etching of metal oxides, such as indium tin oxide which is commonly used as transparent electrode^[60]. In addition, Literature also reported on the usage of moisture sensitive

Introduction

materials such as *lithium fluoride* or *calcium* as electron extracting layers. However, ingress of environmental moisture was quickly degrading those materials resulting in blocking layers and catastrophic failure of devices^[28a, 61]. In conventional layer stacks ETLs require metals with a low work function like aluminum, which are in general very moisture and oxidation sensitive^[27].

As mentioned above the inverted layer stack was developed in order to improve the stability of organic solar cells. In the case of an inverted stack high work function metals being less prone to oxidation can be used as back electrode (cathode in this case), whereas the transparent electrode is the anode^[27-28]. In the inverted layer stack metal oxides like *titanium oxide* and *zinc oxide* are used^[27, 55]. Though these metal oxides are not water^[62] and oxygen sensitive, they cause certain other problems. In several studies it was shown that these metal oxides needed light exposure of the solar cells in order to attain their full performance^[63]. Moreover, this so-called light soaking effect was not permanent, i.e. the performance gain disappeared in the dark and a new light soaking period was required^[64]. For a device intended to work under changing illumination conditions, this is a rather detrimental effect. Even more severe is the degradation evident in devices made with TiO_x and ZnO ETLs^[65]. When exposed to UV irradiation oxygen atoms adsorbed at the surface can be desorbed and form trap states at the interface between ETL and active layer. This effect especially reduces the fill factor throughout ageing.

Besides the aforementioned effects, which were already discovered before the broad introduction of NFAs, the usage of NFAs led to new degradation pathways stemming from interactions between charge transport and active layer. Such interactions have been found if either strongly basic or strongly acidic charge transport layers, such as PEI or PEDOT: PSS, were employed^[66]. If the vinylidene groups of most NFA acceptors (Figure 8) can be attacked by these charge transport materials, the conjugation of the NFA will be disrupted resulting in a loss of absorption capabilities and introduction of trap states.

The recently set lifetime records for OPV were also critically influenced by the design of the CTLs^[51a, 67]. For these record setting devices modified metal oxide charge transport layers were used. These publications reported about the degradation of the active layer due to the metal oxide at their direct contact. In order to prevent this type of degradation, additional organic layers were introduced between the metal oxide transport layer and the active layer and the lifetimes of devices improved significantly. The authors introduced buffer layers in inverted solar cells to both, the anode as well as the cathode and consequently the initial burn-in of the device was removed nearly entirely. A similar effect was observed for another study that reported a lifetime of above 30000 h, where a fullerene derivative was used as cathode buffer layer in an inverted OPV devices and the burn-in vanished.

So far, the most basic workings and challenges for OPV have now been presented. In the following chapters **P1** and **P2** it will be discussed on which sector OPV should focus in order to profit from economies of scale and to be able to enter the market after two decades of intensive development. **P1** is focusing on the advantages of OPV if applied to agriculture. This chapter discusses the synergies of applying OPV to polytunnels to increase the yield for crop production and attain a higher degree of water and soil conservation, especially in arid conditions. A calculation of the potentially achievable performance based on detailed balance is given and the potential for agrivoltaics is evaluated. This chapter closes with the comparison of published active layer

P1 Agrivoltaics – the Perfect Fit for the Future of Organic Photovoltaics

materials and the photosynthetically active absorption of plants, and how well they already complement each other. **P2** is briefly discussing the potential of commonly used charge transport layers for OPV applications, with special focus on the application in the field of agrivoltaics. Usually the CTLs' UV/Vis transmission is reported in a too narrow range for seriously assessing the materials' compatibility for agrivoltaic applications.

The next two chapters **P3** and **P4** are discussing the impact of charge transport layers on the stability and performance of OPV devices. **P3** is about a large interlaboratory round robin study, where five labs across Europe constructed OPV devices and distributed them between three other labs for stability testing. The results of this study showed the importance of the layer stack design for the overall stability of OPV devices, but also the importance of a good encapsulation scheme. **P4** is comparing multiple organic charge extraction layers and correlates between structural properties of these materials and their performance improvement. In addition, the ties found between structure and stability were not as strong as in the case of structure and performance. Especially the device performance was connected to the very complex nature of the many interlinking processes involved with OPV stability.

In **P5** a method is presented for analyzing IV characteristics in a new fashion and extracting in-depth knowledge which allows for a more focused and faster analysis of OPV device performance limitations. The principle of this analysis concept is the combination of electrical simulation and the second derivative of the IV curve. On the basis of this investigation it is possible to quickly gain understanding how either fresh devices are limited in their performance or aged devices are degrading. For example, we obtain information about which kind of defects it is worth to look for with more sophisticated methods. Furthermore, this method can be applied in order to pause ageing experiments shortly before or during a period in time where a sample undergoes a specific point in its degradation pathway.

P1 Agrivoltaics – the Perfect Fit for the Future of Organic Photovoltaics

Photovoltaics nowadays is mostly dominated by silicon based solar modules, as was already stated in the introduction to this thesis. This is due to its high efficiency, abundance of the element itself, experience with its processing and a large established industry by now that pushed its price to very low costs. Any new technology that wants to enter the photovoltaics market has to carve out a niche for itself, which has to have two important properties, these are: The technology has to offer a benefit no other competing technology can have and the chosen niche, has to have the potential for

P1 Agrivoltaics – the Perfect Fit for the Future of Organic Photovoltaics

scaling in the high GW to TW demands, else there can be no benefit from economies of scale and therefore none of the necessary cost reductions to compete with silicon PV can be achieved.

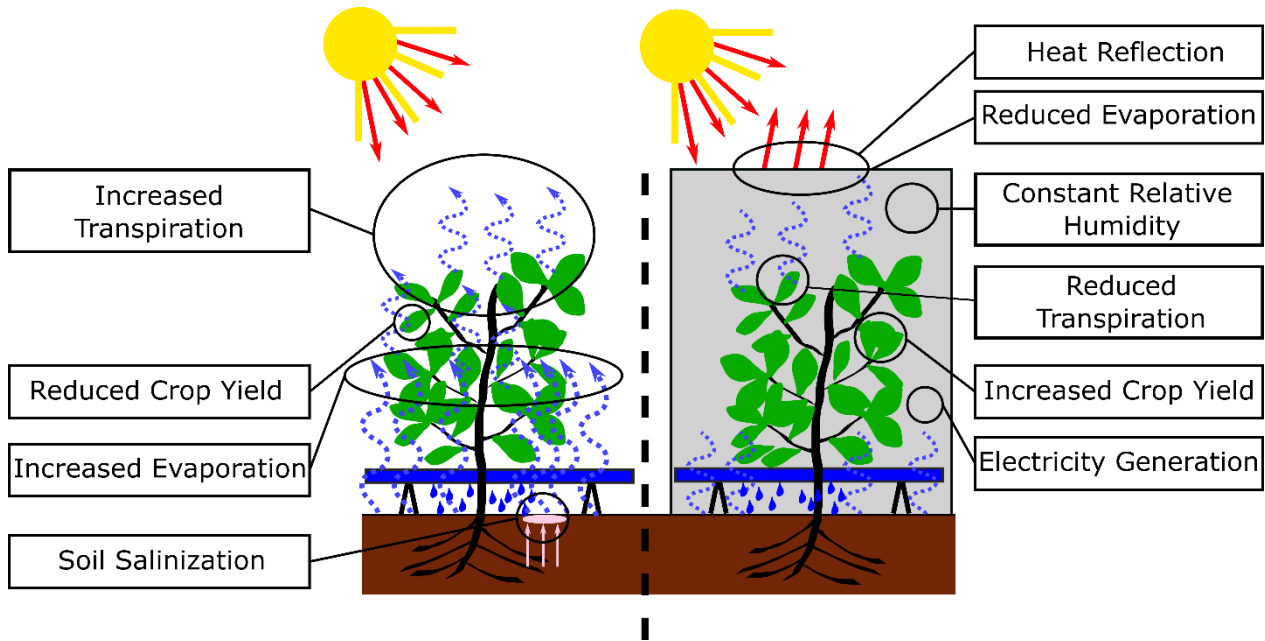


Figure 11: Comparison between plant growth in arid and semi-arid climates, on the left without photovoltaic polytunnels and on the right with photovoltaic polytunnels.

So, a niche has to be found for OPV where it can rely on its unique properties. Nowadays the most unique property of OPV, which it shares with no other PV technology is the ability to only absorb within a narrow spectral window^[16b, 68], usually this property is a downside, as it limits the absorption of solar radiation. Though in the proposed deployment scenario of OPV as hull structure for photovoltaic polytunnels, it precisely can be an asset, as it can allow to make use of the 50% of energy contained in near infrared part of the solar spectrum not used by plants, while being mostly transmissive in the spectral part, where plants are photosynthetically active. Besides that, there are other advantages and synergies to be gained from such an application. These are summarized in Figure 11, as can be seen such an application can be especially beneficial in arid and semi-arid climates, where it can help with water conservation, which is a critical resource. Further it can reduce soil salinization, which is a common problem for irrigation agriculture. The more easily controllable humidity around plants can also increase the overall yield^[69], as plants do not have to shut down photosynthesis as often to prevent critical water loss. Although silicon PV^[69-70] is also already applied in agrivoltaic settings, it comes with two massive drawbacks, on the one hand it has to be deployed well-spaced out, as otherwise it would entirely shade the ground and only very shade resistant plants could be grown underneath. And the more cumbersome restriction is due to its relatively large weight and rigid nature the support structures have to be quite massive, if agricultural machines have to pass underneath it. These constraints are not applicable to flexible OPV modules, which in the case of a polytunnel could simply be quickly folded together and unfolded again to allow access for a large machine.

P1 Agrivoltaics – the Perfect Fit for the Future of Organic Photovoltaics

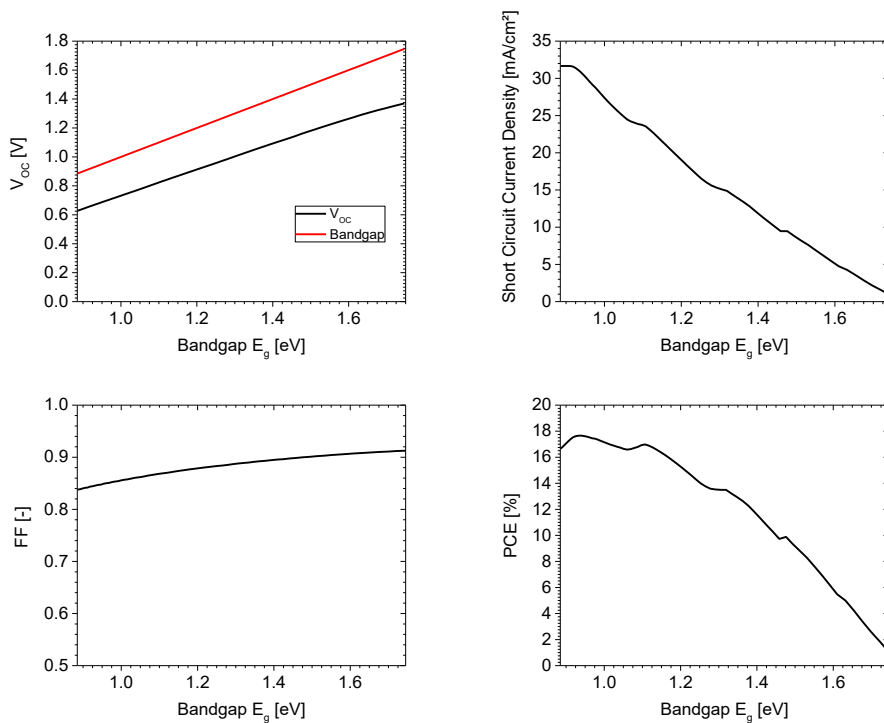


Figure 12: Schockley-Queisser-limit applied to organic solar cells with complete transparency in photosynthetically active energy range of plants.

With the mutual benefits presented another important factor is the question of the achievable performance for such an application. In Figure 12 the result of a detailed balance^[71] calculation is shown with the additional constraints that absorption is only allowed below an energy of 1.75 eV , corresponding with the onset of photosynthetic activity in plants. There are two peaks around 0.9 eV and around 1.1 eV with nearly identical achievable PCEs of 18% and 17.5% . As OPV so far is suffering from an increased photovoltage loss compared to other PV technologies^[72], the peak at higher energies is preferable as a development goal. The currently best performance reported for an organic solar cell is 19% PCE^[50a] and for a small module this best performance so far is 14% PCE^[73], when that ratio is taken and one assumes a similar scaling lag between lab cell and large scale a performance of up to 13% PCE on a large scale might be achievable, but a more conservative estimate of 10% PCE should be given the theoretical maximum of 17.5% PCE a goal that should be targeted for applications.

In Figure 13 the UV/Vis absorbance of several published low bandgap materials for OPV devices is compared with the photosynthetic action spectrum of plants. And in Figure 14 the chemical structures for these compounds is shown^[74]. These are polymer donors, small molecule donors, as well as small molecule acceptors, i.e. non-fullerene acceptors. In general, it can be seen that there is already a broad sample of active layer materials for donors as well as acceptors that are showing a low overlap of absorbance with plants. On the donor side the three diketopyrrolopyrrole (DPP) based donor polymers C3-DPPTT-T, C3-DPPTT-Se and C3-DPPTT-Te are especially well suited for solar cells with a high transmissivity in the photosynthetically active region. In combination with fullerenes as acceptor efficiencies of up to 9% have been reported for these compounds, though the fullerene used was PC₇₁BM, which already has an appreciable absorption in the blue

P1 Agrivoltaics – the Perfect Fit for the Future of Organic Photovoltaics

region of the visible spectrum. In regards to NFAs the choice in materials is even larger thanks to the development of low and ultra-low bandgap acceptors over the last few years. The most interesting are IEICO-4F, IEICO-4Cl, IXIC-4Cl, CO₈DFIC, INPIC-4F and DTPC-DFIC. For all of these NFAs efficiencies above 10% are reported, but so far not when paired with low bandgap donors. Hence the potential for highly UV/Vis transparent OPV devices is clearly there though so far not realized. With a moderate efficiency of 10% as already stated the potential for cumulative OPV in the application of agrivoltaics is for only the land used for vegetables, roots and tubers already 2 orders of magnitude larger than the so far deployed PV capacity worldwide, offering a very exciting case as application and to realize economies of scale.

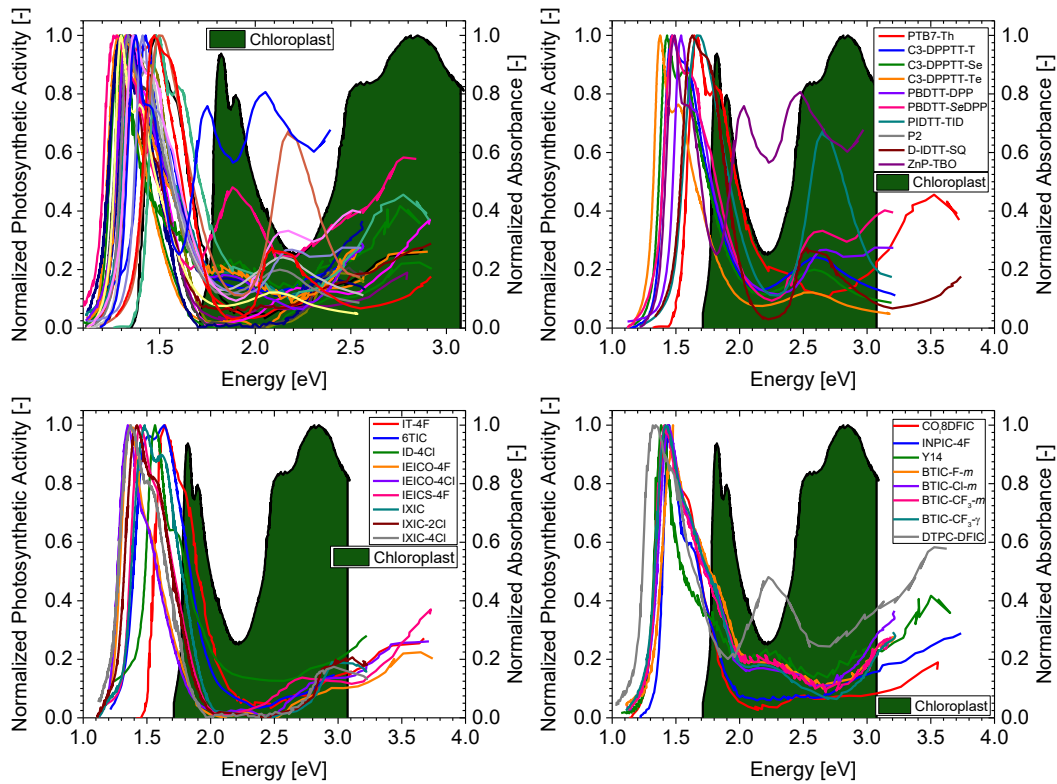


Figure 13: Comparison between the photosynthetically active spectral region of plants and the absorbance spectra of different low bandgap active layer materials used in OPV devices that have been published in the scientific literature.

P1 Agrivoltaics – the Perfect Fit for the Future of Organic Photovoltaics

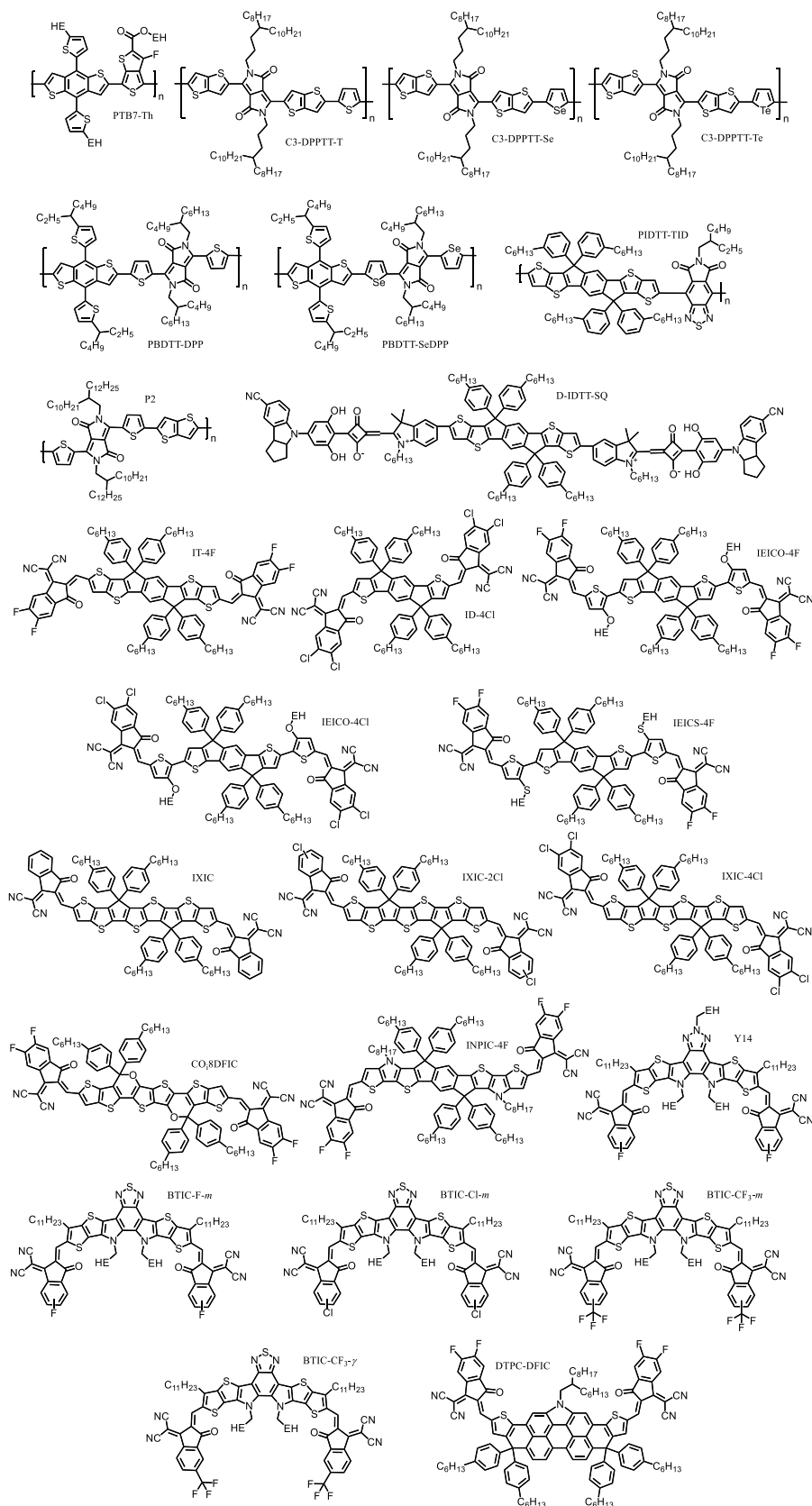


Figure 14: Structures of published low bandgap materials with absorption windows that are partially compatible with agrivoltaics applications.

P2 Transmission Windows of Charge Transport Layers and Electrodes in Highly Transparent Organic Solar Cells for Agrivoltaic Application

P2 Transmission Windows of Charge Transport Layers and Electrodes in Highly Transparent Organic Solar Cells for Agrivoltaic Application

Besides the active layer materials also charge transport layers are playing a critical role in the application of agrivoltaics. They have to be highly transparent in the full spectral range from 1.1 eV to up to 3.5 eV, as they do not only have to transmit light for the active layer of the PV device, but also for the underlying plants. In Table 1 published of energy levels and bandgaps are shown for various materials used as charge transport or extraction layers. For the metal oxides used as ETLs their conduction bands are well suited as electron selective layer in conjunction with fullerenes and most NFAs, as their LUMOs are in general around 4 eV. For PDINO the published value of the LUMO is actually a bit too high for efficient electron extraction. The same is true for hydrogenated nanodiamonds (H-NDs)

Table 1: Energy Levels and bandgaps in various published and commonly used charge transport/extraction layer materials for organic solar cells.

Material	HOMO /VB (eV)	LUMO /CB (eV)	Band Gap (eV)	Reference
ETL/EEL				
SnO ₂	-8.0	-4.5	3.5	[75]
TiO _x	-8.1	-4.4	3.7	[76]
ZnO	-7.5	-4.2	3.3	[77]
PDINO	-6.21	-3.63	2.58	[56]
H-NDs	-5.5	-3.0	2.5	[78]
HTL/HEL				
MoO _x	-5.6	-2.3	3.3	[55]
WO ₃	-5.7	-2.2	3.5	[47]
PTAA (poly(triaryl amine))	-5.1	-1.8	3.3	[79]
NPB (N,N'-diphenyl-1,1'-biphenyl-4,4'-diamine)	-5.4	-2.3	3.1	[80]
P VP Al4083	-5.2	/	/	[81]

For the materials commonly used as hole transport or extraction layers the two metal oxides valence band is too deep for most donors to show efficient hole extraction, though in general the literature states for these materials that they are actually more acting like recombination layers, at whose surface to the active layer, electrons injected from the electrode recombine with holes from the

P3 Robustness of polymer solar cell stability against semiconductor properties and its susceptibility towards layer stack variations

donor^[82]. For the organic materials PTAA and NPB, which are commonly used as HELs in perovskite solar cells both show values for the HOMO which are well suitable for most commonly used donor materials in OPV. P VP Al4083, which is a commercial formulation of PEDOT:PSS, is commonly used as a HTL and shows a HOMO also well suited for efficient hole transport.

In Figure 15 the UV/Vis absorbance spectra of various CTLs is depicted. Figure 15 a) shows the ETLs and EELs compared against the photosynthetic activity of plants and expect for PDINO all the ETLs/EELs show a low absorption in that range. The best suited candidates of the whole range from 400 nm to 1100 nm are TiO_x, SnO₂ nano particles and PEI. ZnO though not showing the lowest absorption has an added benefit of being a partial UV blocker, which is beneficial as UV radiation is well documented in being damaging to the active layer of OSCs as well as producing stress on plants, due to damage it causes to the photosystem^[83]. Figure 15 b) shows the absorptance common HTLs and HELs compared with the photosynthetic activity of plants, the two least suitable materials are PEDOT:PSS, as well as tungsten oxide, as both show increased absorptance either in the spectral range of plants or in the spectral range of the solar cell. Best suited would be NPB and PTAA, as both have a very low absorptance over the whole range, while again showing some absorptance on the UV range, which would be beneficial to either protect the active layer of the solar cell and/or plants grown underneath the photovoltaic polytunnel.

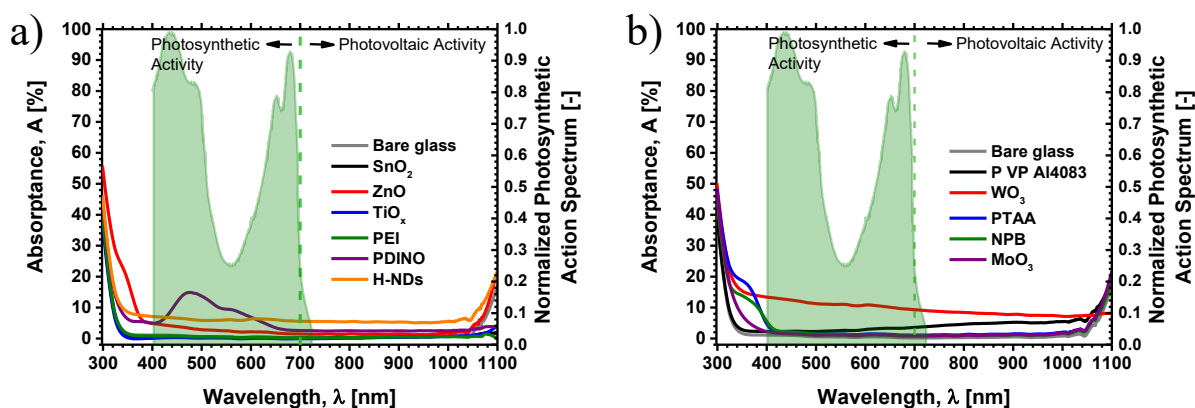


Figure 15: Absorbance of different commonly used charge transport and charge extraction layers used in organic solar cells, a) electron extraction/transport layers, b) hole extraction/transport layers.

P3 Robustness of polymer solar cell stability against semiconductor properties and its susceptibility towards layer stack variations

In this chapter the results of a large collaborative study between several European institutions is presented. In the study different batches of P3HT which was commercially available were used to produce OPV devices based on P3HT:PCBM active layers with different layer stacks, which were chosen by the individual labs based on familiarity with these layer stacks. The initial manufacturing and distribution procedures are shown in Figure 16. As is shown 5 different batches of P3HT were selected with 5 different labs manufacturing solar cells from each P3HT batch. Beside the solar cell manufacture the different P3HT batches were also physically and chemically analyzed in regards to properties like molecular weight, dispersity, radical content, trace metal content and the concentration of sub-bandgap states, though this part of the work is not the main focus of this

P3 Robustness of polymer solar cell stability against semiconductor properties and its susceptibility towards layer stack variations

chapter for further interest the reader shall be referred to the published manuscript this chapter is based on. As the focus of this chapter is on the impact of the CTLs.

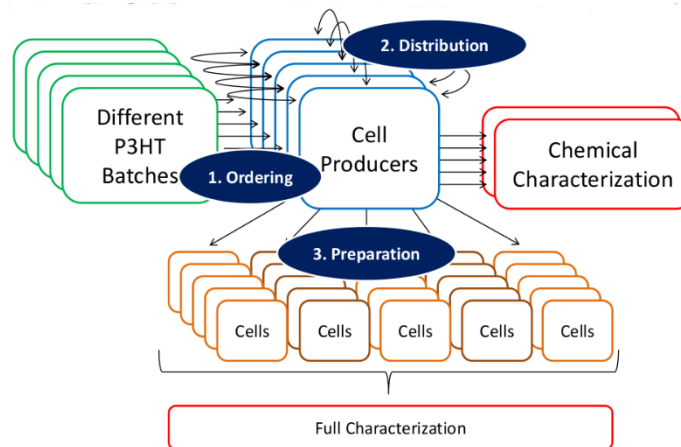


Figure 16: Design of the initial production process for the OPV devices that were tested in the experiments.

Following the manufacture and characterization at the manufacturing labs the cells were sent out to four different locations for ageing tests, see Figure 17 for the procedure taken. Upon arrival at each lab involved with the ageing another characterization was done. The substrates were then placed under the different ageing conditions which were performed in accordance to the ISOS protocols^[84]. At CEEC Jena devices were aged ISOS-L2 conditions, i.e. under simulated AM1.5 solar irradiation of 100 mW/cm² and at a temperature of 55°C in the shade, which is equivalent to a cell temperature of 65°C. ISOS-D2, which is ageing in the dark at 85°C was performed by Solliance in Eindhoven. While the samples under ISOS-O1, i.e. outdoor ageing with regular lab characterization, was done at the J. Blaustein Institutes for Desert Research of the Ben-Gurion-University of the Negev at Midreshet Ben Gurion in the Negev desert.

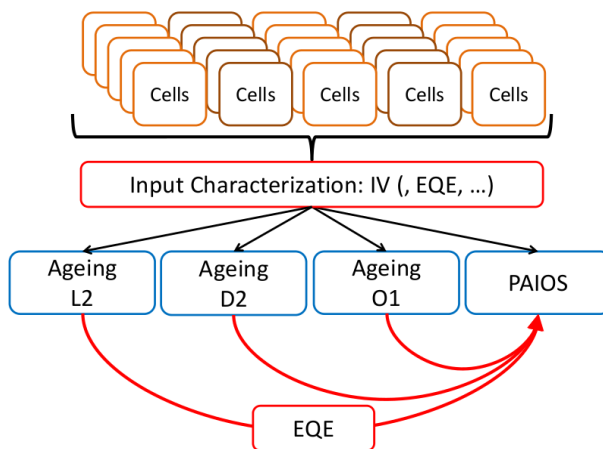


Figure 17: Schematic depiction of the experimental design in regards to the ageing experiments performed.

For the various layer stacks used by the different labs they are shown in Figure 18, there were 4 labs that choose inverted architectures, while one lab went with a conventional architecture. The charge transport layers chosen by the labs represented some of the most widely chosen ETLs and

P3 Robustness of polymer solar cell stability against semiconductor properties and its susceptibility towards layer stack variations

HTLs especially with zinc oxide as ETL and molybdenum oxide and PEDOT:PSS as commonly chosen HTLs. TEIC choose a very moisture sensitive ETL with calcium, which is easily corroded and therefore requires very good encapsulation. CEA choose a flexible substrate and a flexible encapsulation scheme. CEA choose a flexible substrate and a flexible encapsulation scheme. The different devices also had different substrate layouts, with e.g. CEA only having one cell per substrate, while UTV had 8 cells per substrate.

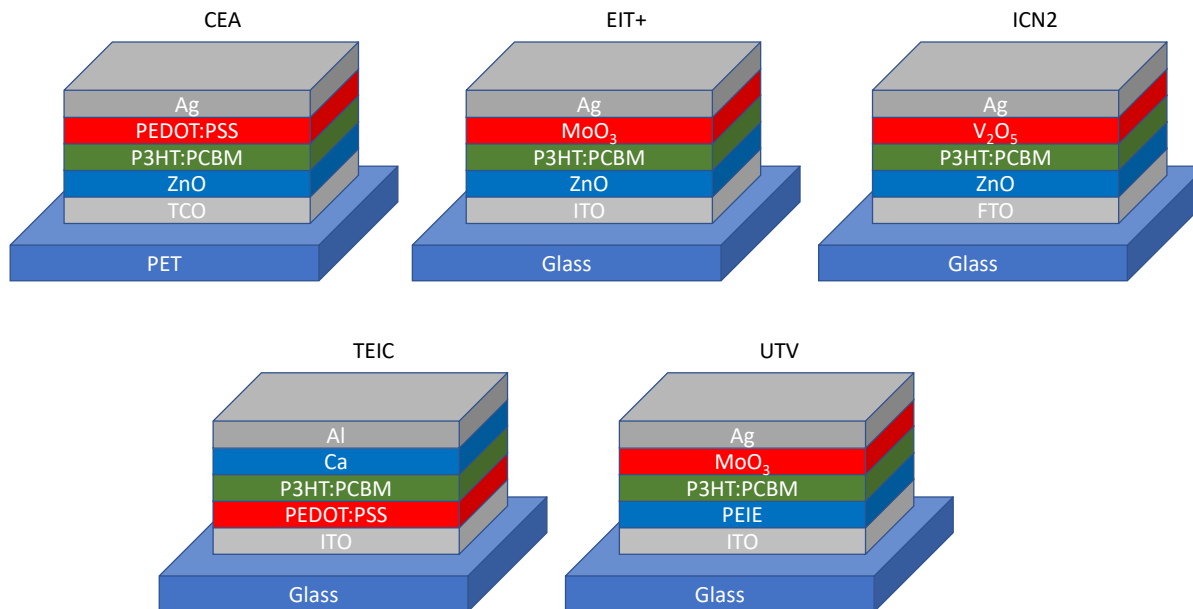


Figure 18: Layer stacks for the different solar cells from the participating European labs.

In Figure 19 the ageing curves from the ISOS-L2 experiment performed at CEEC Jena are shown. There is a large variation between the different manufacturers in regard to the device stability, as well within one and the same manufacturer, as well as between them. The devices from UTV all showed early catastrophic failures due to a break of encapsulation. Similar there were also breaks of encapsulation for ICN2 samples, though they did not result in catastrophic failures, where devices quickly decayed to zero percent efficiency. Though UTV devices quickly degraded they showed the highest initial performance of all the manufacturers. This improved performance stems mostly from an increased fill factor in comparison to the other manufacturers. As UTV being the only manufacturer using PEIE as EEL the likely reason for this improved fill factor can be seen in this EEL.

There is a well-established light soaking effect, where light soaking results in a performance increase for ZnO when used as an ETL^[63]. This effect can be nicely seen in the course of the short circuit current density over time during ISOS-L2 ageing seen in Figure 20 for devices processed by EIT+. The initial increase in J_{sc} results from a change in work function upon UV illumination^[65]. A similar effect is just not seen for the fill factor and open circuit voltage of these devices, as the shunt resistance is degrading at the same time and more quickly than the improvement in the work function. This reduction in open circuit voltage and fill factor is due to a reduction in charge carrier selectivity, as oxygen from the surface of the ZnO gets desorbed, creating defect states^[63, 65]. A similar effect for the CEA cells is not seen due to the UV cut-off

P3 Robustness of polymer solar cell stability against semiconductor properties and its susceptibility towards layer stack variations

filter used for these cells, while ICN2 showed an effect similar to the EIT+ cells, but only for P3HT-II, as the other cells were performing too poorly in other metrics to clearly see an impact from this light soaking.

For the samples of TEIC there is an initial reduction in performance for all devices, i.e. a burn-in, followed by a relatively constant, nearly linear decay rate. This secondary decay rate is likely dominated by the degradation of the calcium layer between active layer and anode^[85], which is easily oxidized by moisture ingress.

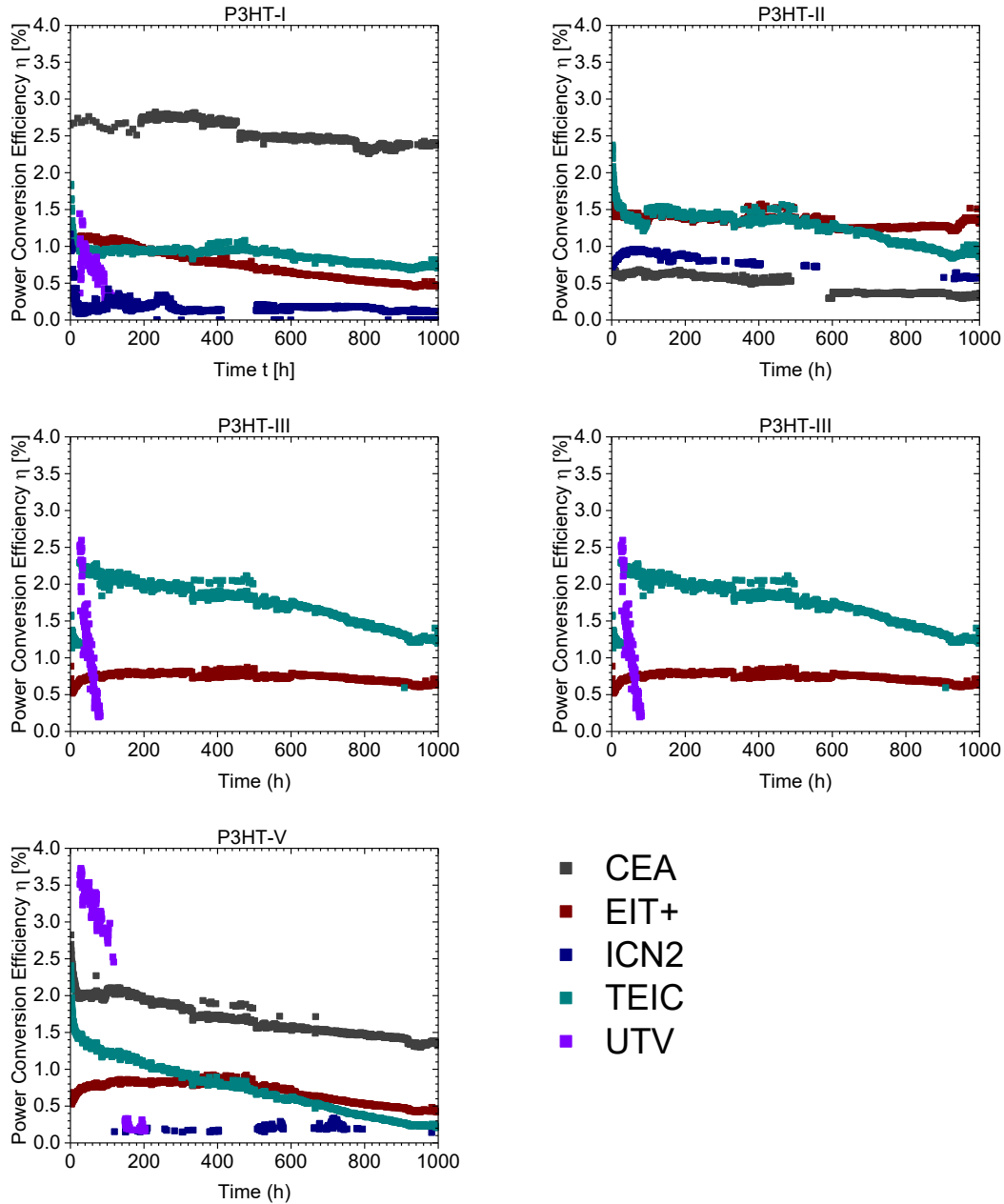


Figure 19: Ageing results of the different solar cells aged under ISOS-L2 conditions from the different manufacturers. As can be seen the shape of the ageing curve is dominated by the layer stack and not by the properties of the P3HT used for the active layer.

P3 Robustness of polymer solar cell stability against semiconductor properties and its susceptibility towards layer stack variations

In general, it can be stated that the shape of the ageing curve is strongly dominated by the overall layer stack. This shows that for light ageing interfacial effects between active layer and the CTLs and CELs determines the burn-in depth, as well as the degradation rate.

For all the manufacturers it was observed that they achieved the highest performance and lifetimes with the P3HT batches they contributed themselves. Showing that the experience of the processor with the respective batch is one of the most important factors to achieve a stable and well performing device.

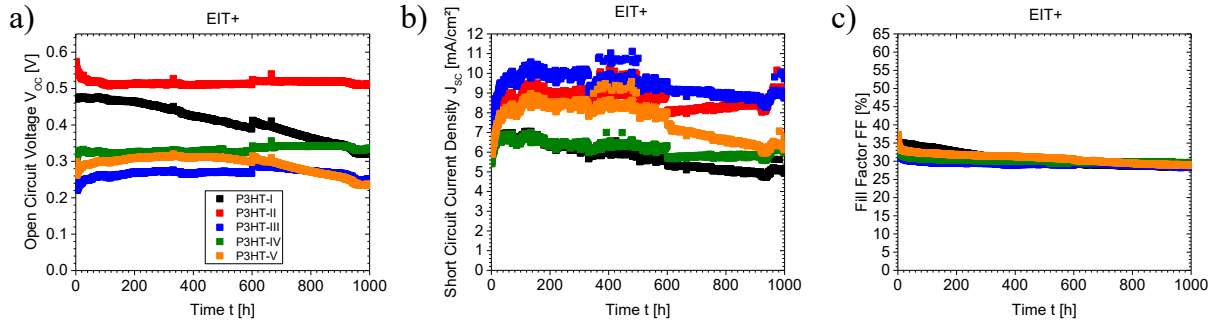


Figure 20: Solar cell parameters of samples from EIT+ from ISOS-L2 ageing, a) V_{oc} , b) J_{sc} , c) Fill Factor.

The overall lifetime parameters from the ISOS-L2 experiments are shown in Table 2. The by far largest lifetime energy yield (LEY) was achieved by the cell from CEA with the P3HT batch CEA itself provided. With a value of 53 kWh/m^2 it more than doubles the next best device, which was from EIT+. Hence the highest achieved outputs of any device were from the devices using the inverted structure. Clearly showing the superior stability under ISOS-L2 conditions for this layer stack. The TEIC cells, which were the only ones using a conventional architecture show only a LEY of less than a fifth of the best device.

The very fast and linear degradation of the UTV devices suggest the degradation process being mostly dominated by photooxidation of the active layer, due to the already stated encapsulation break. For all TEIC devices the burn-in is happening within the first 24 h of the ageing process, this suggests a strong impact of the charge transport layer on this process. There is a documented UV sensitivity for PEDOT:PSS^[86], as these are the only cells using PEDOT:PSS in a conventional layer stack, this is the most likely reason for this initial burn-in, as for the CEA devices using PEDOT:PSS it is on the one hand protected by the UV blocker in the device as well as by the active layer if front of it.

Figure 21 shows the ageing kinetics of the solar cells aged at Solliance under ISOS-D2 conditions. Except for the devices from EIT+ all the others degrade quite severely over the course of the experiment. The origin of this degradation is mostly in a massive reduction of the J_{sc} , which is connected to the well-known morphological degradation of P3HT:PCBM blends under elevated temperatures^[36, 87]. Where P3HT and PCBM start to crystallize and therefore de-mix, resulting in a coarser phase separation, and less interfacial area with a reduction in exciton separation.

The results of EIT+ are interesting, as it is known that the charge transport layers can have an effect on the vertical phase separation of the active layer blend^[22a, 22c, 88]. The free surface energy of the

P3 Robustness of polymer solar cell stability against semiconductor properties and its susceptibility towards layer stack variations

CTLs is controlling which active layer component is preferentially separating towards which electrode. From the results seen for the different blends this does not only seem to have an impact on the surface, but can also restrain the horizontal phase separation in the bulk, at least at the given thermal energies and over the time spans observed in the experiment.

The devices from TEIC also show a less severe degradation in J_{SC} than the devices of the other 3 manufacturers, i.e. CEA, ICN2 and UTV. And in contrast to these they do not show a fast bi-exponential decay in J_{SC} , suggesting a different degradation mechanism. The degradation in J_{SC} for the TEIC cells is nearly linear, which was reported in the past for a loss of electrode area^[85], which is well in line with a degradation of the Ca layer, which is very sensitive to moisture ingress. The lack of burn-in these cells are showing under dark ageing, also strongly high lights that the likely culprit for the burn-in seen for these cells in ISOS-L1 experiments is indeed the degradation of the PEDOT:PSS layer by UV irradiation.

P3 Robustness of polymer solar cell stability against semiconductor properties and its susceptibility towards layer stack variations

Table 2: Calculated lifetime metrics for the various solar cells aged under ISOS-L2 conditions. LEY: Lifetime energy yield. (* - lifetime was limited to the tenfold of the stressing time as experimental data showed constant low output, # catastrophic failure)

Manufacturer	P3HT Batch	Fit function	E_S (%)	T_S (h)	$E_{S,80}$ or E_{80} (%)	$T_{S,80}$ or T_{80} (h)	LEY (kWh/m^2)
CEA	P3HT-I	Exp	-	-	2.32	2241	52.9
	P3HT-II	Lin	-	-	0.55	355	2.16
	P3HT-III						
	P3HT-IV	BiExp	0.56	172	0.44	826	4.44
	P3HT-V	BiExp	1.84	24	1.47	509	9.56
EIT+	P3HT-I	Exp	-	-	0.93	229	2.39
	P3HT-II	BiExp	1.44	16	1.15	1594	20.5
	P3HT-III	Lin	-	-	0.65	1088	8.01
	P3HT-IV	Lin	-	-	0.53	1547	9.18
	P3HT-V	LogLin	0.85	180	0.56	784	5.81
ICN2	P3HT-I	BiExp	0.22	35.9	0.17	10000*	14.6
	P3HT-II	Exp	-	-	0.76	458	3.9
	P3HT-III	-	-	-	-	-	-
	P3HT-IV	Exp	-	-	0.55	114 [#]	0.70 [#]
	P3HT-V	BiExp	0.15	437	0.12	7248	9.83
TEIC	P3HT-I	BiExp	1.02	21	0.81	733	6.71
	P3HT-II	BiExp	1.6	24	1.27	454	6.56
	P3HT-III	Lin	-	-	1.79	458	9.23
	P3HT-IV	BiExp	1.47	11	1.26	546	7.71
	P3HT-V	BiExp	1.46	22	1.16	155	2.11
UTV	P3HT-I	Lin	-	-	0.91	34 [#]	0.35
	P3HT-II	-	-	-	-	-	0
	P3HT-III	Lin	-	-	2.43	17 [#]	0.45
	P3HT-IV	Lin	-	-	0.67	14 [#]	0.1
	P3HT-V	Lin	-	-	3.62	40 [#]	1.61

P3 Robustness of polymer solar cell stability against semiconductor properties and its susceptibility towards layer stack variations

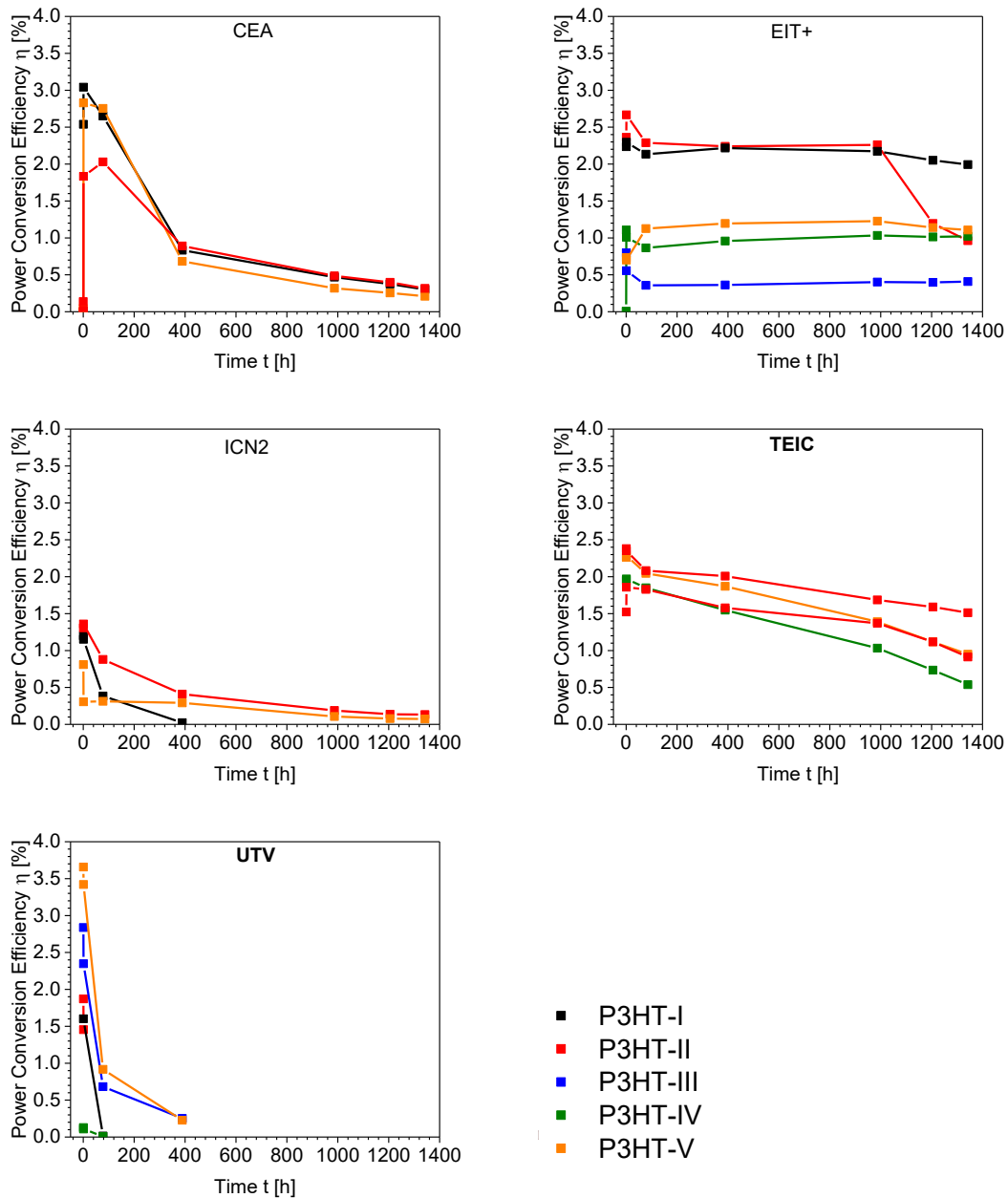


Figure 21: Ageing curves from ISOS-D2 experiments performed by Solliance.

The ageing curves of the ISOS-O1 experiment are shown in Figure 22. This experiment was performed during the winter time and to reduce degradation due to moisture ingress, cells were placed indoor during the night. Under the O1 conditions EIT+ cells are the most stable, showing a constant performance throughout the experiment. Interestingly their behavior is similar than under L2, as they also show an increase in J_{SC} , combined with a reduction in FF . This strongly reinforces the conclusions from the ISOS-L2 experiment, especially as a similar degradation was not observed under ISOS-D2, where no UV light was present.

P3 Robustness of polymer solar cell stability against semiconductor properties and its susceptibility towards layer stack variations

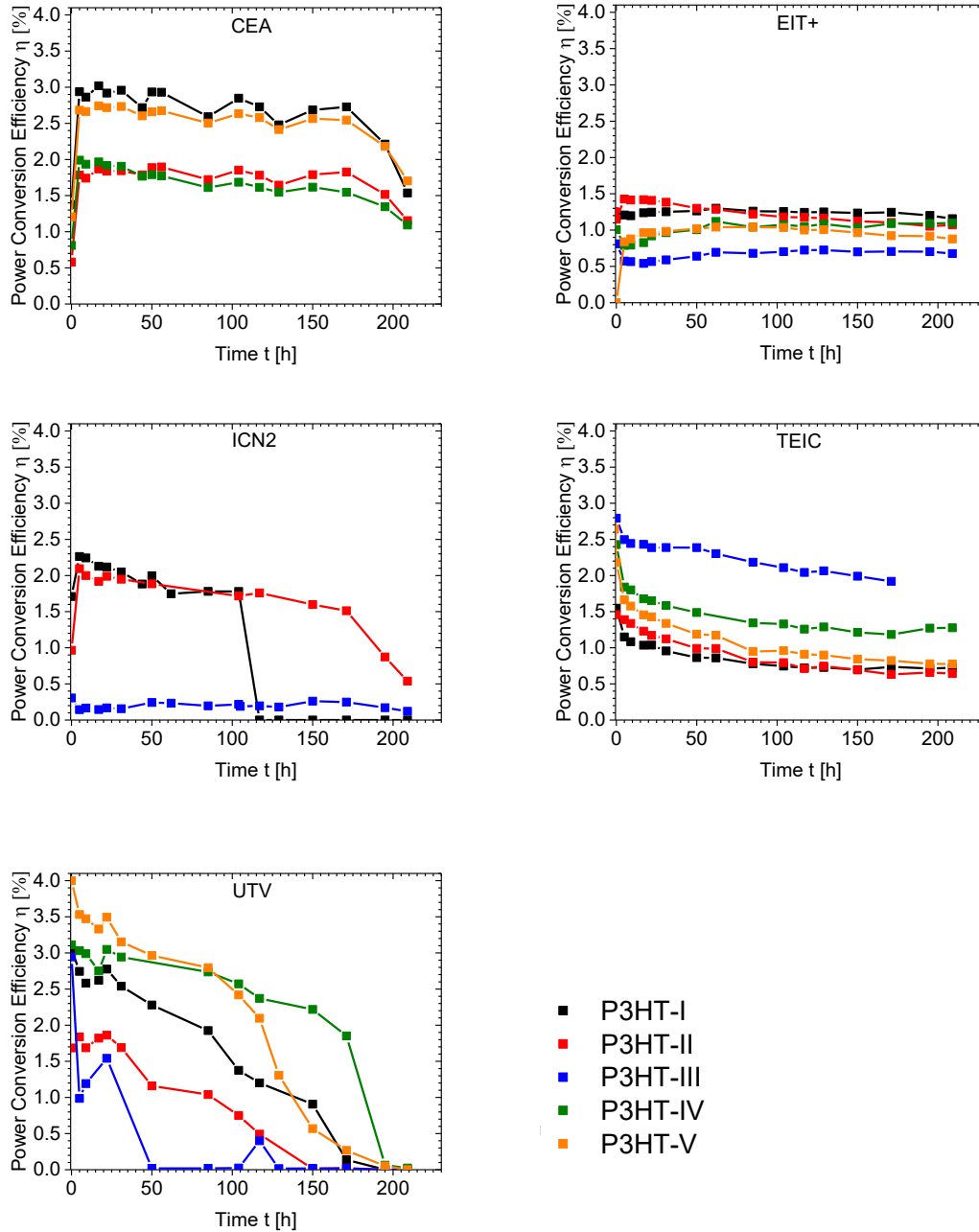


Figure 22: Ageing curves for solar cells aged outdoor at the Negev desert campus of BGU.

The cells from TEIC also show a very similar behavior as in the ISOS-L2 experiment, with a fast initial loss of performance, which stems from a reduction in J_{SC} and FF and afterwards slow and steady decay. As the degradation is again occurring so quickly and again light is involved the likely culprit is the UV sensitivity of PEDOT:PSS. This generally shows that PEDOT:PSS clearly performs very poorly in a conventional layer stack, where it is immediately exposed to UV light and induces a fast reduction in performance. In an inverted layer stack, like for the devices

P4 Performance and Stability of Organic Solar Cells bearing Nitrogen Containing Electron Extraction Layers

produced by CEA the same effect cannot be seen, due to the UV filtering of the barrier material that was used, as well as the UV filtering effect ZnO and the active layer would have additionally.

P4 Performance and Stability of Organic Solar Cells bearing Nitrogen Containing Electron Extraction Layers

The focus of this study were various organic nitrogen bearing molecules and polymers as EELs and to understand their structure-property-relationships and how these affect the performance and stability of OPV devices. As stated in the introduction PEI is a commonly used EEL in organic solar cells^[55]. Its working mechanism is explained via its dipole moment, lowering the work function of the electrode and therefor allowing for efficient electron extraction^[57]. An advantage of PEI is that it is a widely available polymer already in commercial use^[57], a downside is its cellular toxicity.

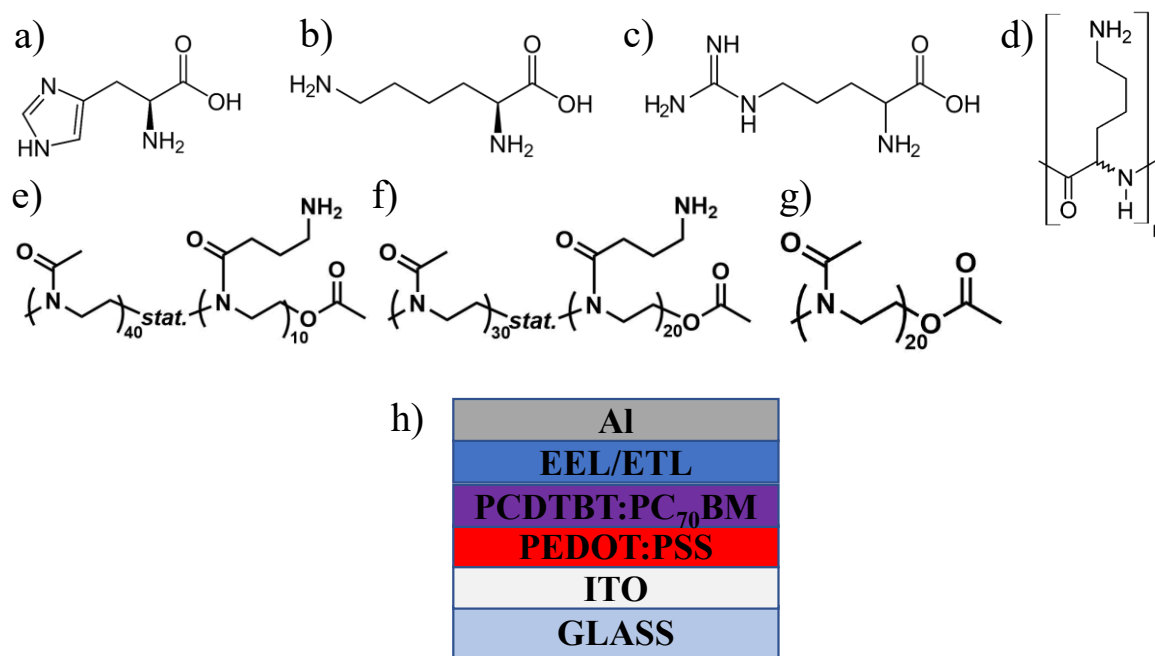


Figure 23: Chemical structures of the organic electron extraction layers used in the study (a), (b) layer stack of the solar cells that were processed.

Therefore compounds were chosen for this study, which are non-toxic and actually are biodegradable and which also contain nitrogen bearing groups like amine groups, guanidine groups and pyrrole rings, these compounds are shown in Figure 23. The OPV devices studied used a conventional layer stack with PCDTBT:PC₇₀BM. Especially interesting were the amino acids studied, as in contrast to polymers they are circumventing the issue of batch to batch variations. Further different variations of TiO_x as ETL and devices without an ETL were studied as references.

In Table 1 the solar cell parameters for the OPV devices processed with the various EELs and ETLs can be seen. The best performing devices were the ones using L-Arginine as EEL. A simple methanol overcast, which was done, to be able to differentiate the impact from the nitrogen

P4 Performance and Stability of Organic Solar Cells bearing Nitrogen Containing Electron Extraction Layers

containing EELs, which were all prepared from methanol solutions and the effect of the EEL itself, resulted on its own already in a significant performance improvement. The different TiO_x layers studied as reference system for stability and efficiency all performed worse than the best nitrogen containing organic compound L-Arginine. Interestingly the Polylysine and the Lysine both performed similarly well.

Table 3: Initial photovoltaic parameters of the solar cells processed with different electron extraction and electron transport layers.

EEL	V_{OC} (mV)	J_{SC} (mA/cm ²)	FF (%)	PCE (%)	R_S (Ω)	R_{Sh} (k Ω)
L-Histidine	832±19	11.12±0.33	48.3±0.5	4.46±0.23	16.0±1.8	1.05±0.06
L-Lysine	858±12	11.27±0.15	49.0±0.8	4.73±0.09	15.3±3.2	0.90±0.25
L-Arginine	869±7	10.99±0.34	51.3±1.0	4.89±0.12	12.0±0.0	1.30±0.09
Poly-L-Lysine	850±22	11.06±0.37	49.8±1.7	4.68±0.42	13.3±1.5	1.26±0.06
P(MeOx ₄₀ -stat-AmOx ₁₀)	857±9	10.11±0.20	46.5±2.4	4.02±0.17	13.8±1.5	0.98±0.13
P(MeOx ₃₀ -stat-AmOx ₂₀)	854±18	10.65±0.50	50.0±0.0	4.55±0.26	14.0±3.6	1.22±0.06
PMeOx ₂₀	795±16	10.20±0.12	44.8±0.5	3.62±0.03	16.3±1.3	0.92±0.05
No EEL	656±18	10.53±0.24	43.8±0.5	2.94±0.16	184.5±72.9	0.68±0.03
Methanol overcast on PAL (No EEL)	772±9	10.80±0.20	45.8±0.5	3.81±0.14	10.3±0.5	0.98±0.05
TiO _x , Reference	670±315	9.75±0.73	41.0±10.7	3.00±1.77	11.3±1.0	0.69±0.49
TiO _x , diluted	842±5	9.14±0.08	44.5±1.0	3.45±0.07	17.5±1.3	0.97±0.05
TiO _x , unannealed	784±12	10.45±0.26	47.8±1.3	3.92±0.13	9.8±1.0	1.04±0.08

To gain an understanding how the variations in material properties of the EELs used, were affecting the performance of the devices they were made with, these variations were compared with each PV performance parameter. For the polyoxazolines, which varied in the amount of amine containing side chains, this dependency is shown in Figure 24. The polymer with the 40% amine content in side chains showed a 33% improvement in performance overall over the polymer without any amine groups in the side chain, which is a quiet remarkable improvement. All solar cell parameters improved with an increase in amine content in the side chains of the polymers. The increase was smallest for the J_{SC} , as to be expected as it mostly stems from the capability of the active layer to absorb photons and separate the resulting excitons into free charge carriers to be transported to the

P4 Performance and Stability of Organic Solar Cells bearing Nitrogen Containing Electron Extraction Layers

CTLs. A bigger impact was seen on V_{OC} , FF and R_s , which are expectedly more affected by an EEL, as an EEL might improve the contact to the electrodes, through helping to form an ohmic contact, as well as that an EEL could passivate surface defects at the interface with the electrode.

Further, the impact of material properties of the amino acids and how they affected the device performance was studied. The relevant varying parameter determined for the amino acids were the dissociation constants of their nitrogen containing functional groups, especially of these groups not attached to the alpha carbon, as these varied significantly.

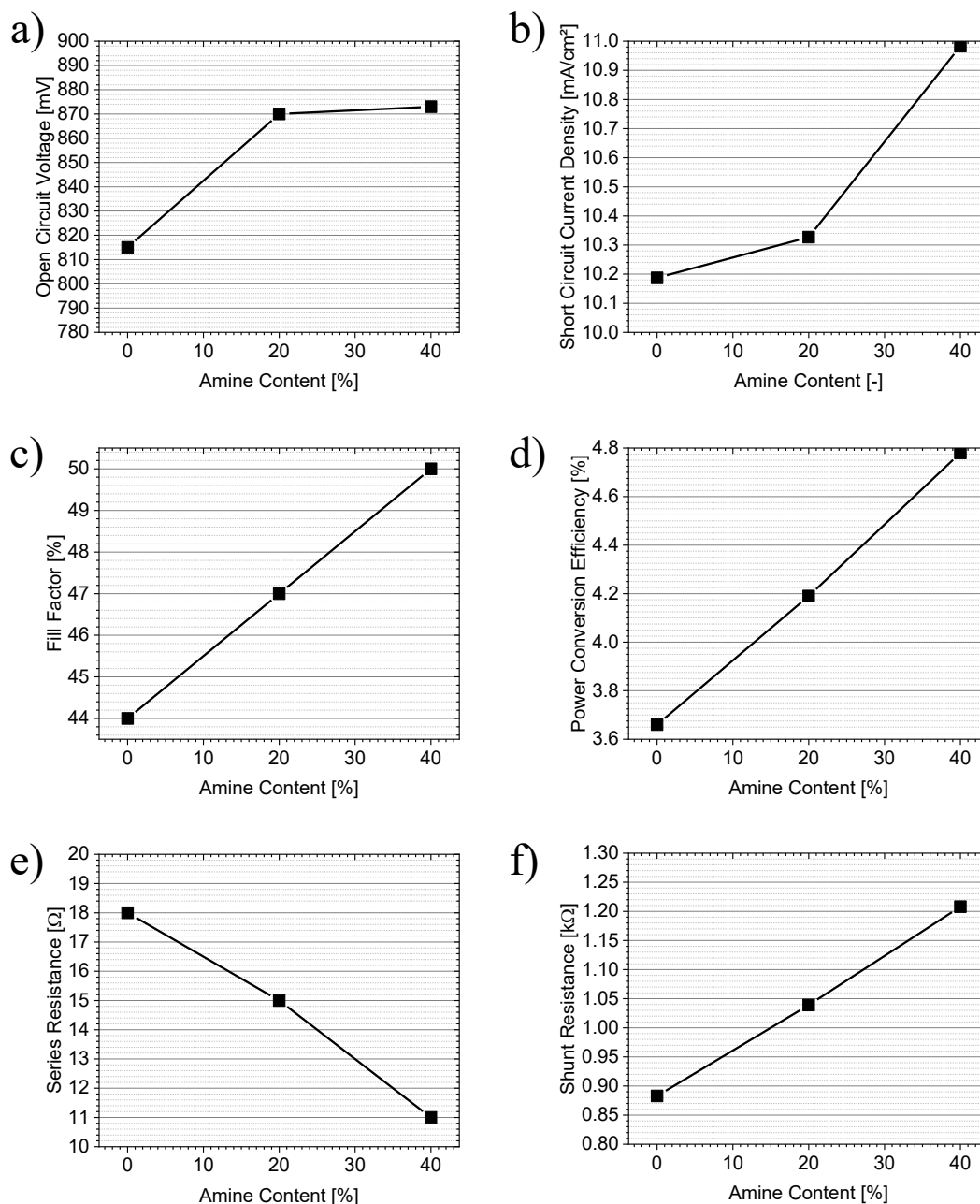


Figure 24: Photovoltaic parameters for the devices processed with the different polyoxazoline polymers with varying amine content in the side chain.

P4 Performance and Stability of Organic Solar Cells bearing Nitrogen Containing Electron Extraction Layers

These correlations between dissociation constants and photovoltaic parameters are shown in Figure 25. The depicted photovoltaic parameters are the ones for which there was a clear correlation between pK and the respective parameter. For J_{SC} and R_{Sh} there were none, though especially for J_{SC} a correlation was also not expected. The pK was chosen as a property to compare against, as it is a proxy for two interesting molecular properties, it is already tabulated for many compounds and if not tabulated it can be easily measured. On the one hand it indicates the strength of the molecular dipole, on the other hand it indicates the strength as a Lewis acid/base, which can be relevant in terms of surface defect passivation.

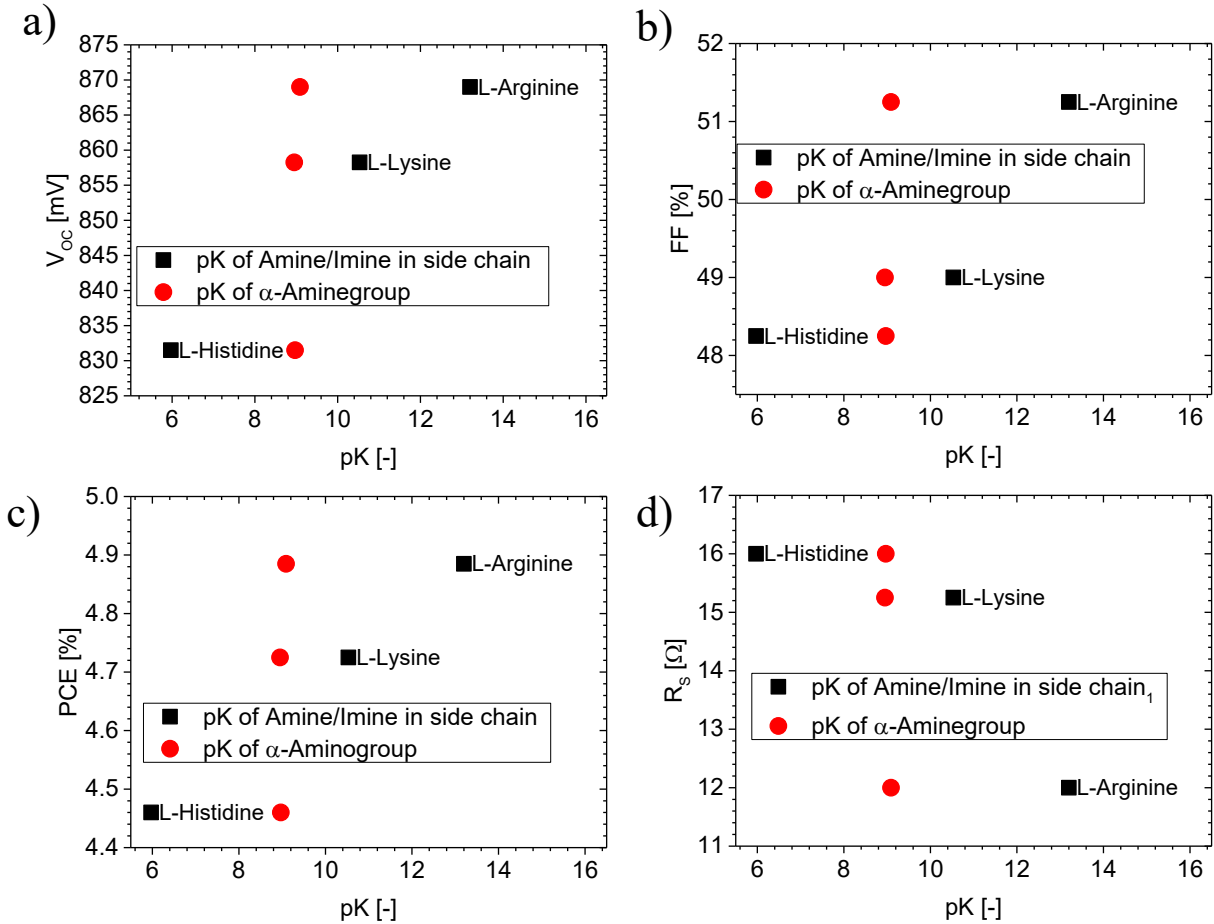


Figure 25: Correlation between dissociation constants of the various amine groups in the amino acids used for the EELs and their respective photovoltaic parameters.

From Figure 25 correlations are clearly visible between the dissociation constant of the nitrogen containing group on the side chain of the amino acids and the given photovoltaic parameters. For the V_{OC} , which follows the following equation:

$$V_{OC} = \frac{nk_B T}{q} \ln \left(\frac{J_{SC}}{J_0} + 1 \right), \quad (1)$$

with n being the diode ideality factor, k_B the Boltzmann constant, T the absolute temperature, q the elementary charge and J_0 the dark saturation current density. As there was no significant increase in J_{SC} for

P4 Performance and Stability of Organic Solar Cells bearing Nitrogen Containing Electron Extraction Layers

the different amino acid EELs either n increased or J_0 got reduced. Though n and J_0 are not entirely independent parameters, as the diode ideality factor represents the dominant mode of recombination and any deviation from 1 by necessity means there are additional recombination mechanisms beyond band to band recombination, which cannot be turned off and is therefore the absolute baseline for recombination. This requires that for any real solar cell an n different from one will also result in an increase in J_0 . As literature is generally considering values between 0.6 and 2 as physically meaningful values^[89] for the diode ideality factor a change in J_0 will affect the V_{OC} more strongly than a change in n . As J_0 can vary over a larger space than n . Therefore the increase in V_{OC} is likely due to a reduction in J_0 . For the FF there is also a clear increase in FF with increase in pK , the fill factor is representing the equilibrium between generation and recombination and follows the following equation:

$$FF = \frac{V(P'=0) \cdot (I_L - I_0 \exp(q \frac{V(P'=0) + IR_S}{nk_B T}) - \frac{V + IR_S}{R_{Sh}})}{\frac{nk_B T}{q} \ln(\frac{J_{SC} + 1}{J_0}) \cdot J_{SC}}, \quad (2)$$

with I_L being the photocurrent. As in the case of the V_{OC} already mentioned there is no significant change in J_{SC} , hence this cannot be the relevant factor. There is no significant change in shunt resistance either, but there is a significant change in series resistance, with a reduction, i.e. improvement, of it with an increase in pK . As I_0 is likely also reducing for increasing pK , as already stated for the V_{OC} , this is likely also a contributing factor in this case. The series resistance as already stated also sees a clear improvement, this suggests a better contact between active layer and electrode with an increase in pK .

From the observations so far and what is reported in literature the increasing pK should coincide with an increasing molecular dipole^[24d]. A stronger molecular dipole should result in a larger shift of work function, hence the work function was measured, for these results see the original manuscript. There was no significant shift in work function with the increase in pK . Hence this is likely not the mechanism that played a major role for the effect seen. The alternative explanation is the ability of the different amino acids to function as electron pair donors, i.e. Lewis bases. With an increase in pK their ability to donate an electron pair increases. Therefore they can more efficiently interact with the Al electrode and passivate defect states at the interface between Al and active layer, see Figure 10.

Finally, in Figure 26 the ageing curves of the hero devices are shown, as well as in Table 4 their lifetime parameters are given. All devices showed a very quick burn-in phase on a scale of 100 h, this basically identical burn-in time suggests the burn-in is only weakly influenced by interfacial processes at the anode. As for PCDTBT:PC₇₁BM it is documented in literature that under ageing a broadening of the density of states (DoS) occurs^[90], which is connected to a burn-in in the open circuit voltage, which is precisely what can be seen in the experimental data, this is the most likely culprit also for the burn-in observed by the devices. For all the devices with TiO_x as an ETL an increased long-term stability can be observed. For all these samples especially FF , V_{OC} and for both of the annealed devices also the R_{SH} showed a significantly increased stability over all the organic EELs and no EEL. As these parameters are all sensitive to changes in I_0 , an increase in stability of the interface between active layer and electrode is the likely origin of the improved lifetime^[37].

P4 Performance and Stability of Organic Solar Cells bearing Nitrogen Containing Electron Extraction Layers

Another interesting observation is that a sole overcast with MeOH already results in significant increase in overall lifetime by 14.5% with an even larger increase in *LEY* due to the boost in initial performance. This overall increase is due to a slight reduction in burn-in, as MeOHs mechanism of action during the washing step with it could stem from a removal of impurities, this could also explain the reduction in burn-in. The device with the MeOH treatment also shows the lowest overall increase in series resistance during the burn-in suggesting a very stable interface between anode and active layer.

The organic EELs all performed more poorly than the inorganic ones, though of the amino acids, histidine, which showed the lowest performance improvement, showed the longest lifetime, as well as the largest *LEY*. Suggesting a potential stabilization effect from the reduced *pK*. As for the amino acids and their lifetime the exactly different effect can be seen between lifetime and *pK* as can be seen between performance and *pK*. A possible explanation for this observation is that the carboxylic group of the amino acids reacts with the Al to form H_2 and Al^{3+} ions. For such a case the stronger Lewis acid would also present the stronger ligand for said ions, this could result in an easier mobility of the complexed ions into the active layer. Beyond that the polylysine performed very similar in stability to its monomeric counterpart, suggesting no significant advantage for the polymer in such a case.

P4 Performance and Stability of Organic Solar Cells bearing Nitrogen Containing Electron Extraction Layers

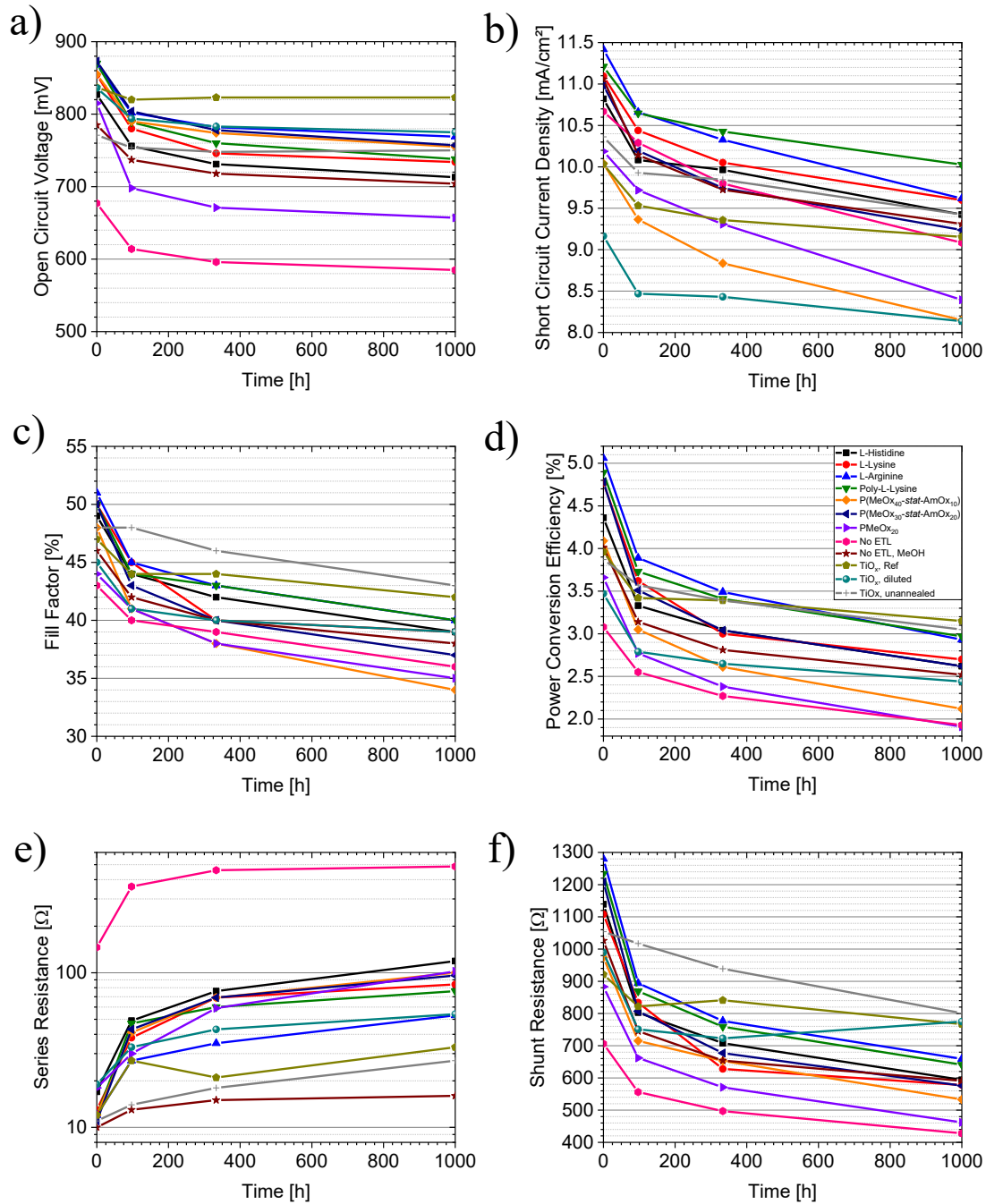


Figure 26: Ageing curves of the OPV devices with various EELs and ETLs under ISOS-L1 conditions.

Concluding it can be stated that amino acids, though not showing the same stabilizing effect as TiO_x, can still be an interesting alternative to it for cheaper and disposable applications. Where their superiority in easy processing as well as low price and biodegradability can be of advantage. Also, there is a clear anti-correlation between stability and performance in regards to the Lewis basicity of the given organic compounds used in this study, suggesting at least in case of amino acids a compromise has to be chosen between these parameters.

P5 An effective method of reconnoitering current-voltage (IV) characteristics of organic solar cells

Table 4: Lifetime parameters of OPV devices with various EELs and ETLs aged under ISOS-L1 conditions.

ETL/EEL	Burn-In Time [h]	Lifetime, $t_{s,80}$ [h]	Standard Deviation [h]	LEY [kWh/m ²]	Standard Deviation [kWh/m ²]
L-Histidine	~100	1966	847	59.8	34.7
L-Lysine	~100	1614	614	49.6	17.6
L-Arginine	~100	1187	162	38.5	6.7
Poly-L-Lysine	~100	1434	188	45.8	4.9
P(MeOx ₄₀ - stat- AmOx ₁₀)	~100	1084	184	25.7	5.9
P(MeOx ₃₀ - stat- AmOx ₂₀)	~100	1546	270	45.3	6.5
PMeOx ₂₀	~100	1409	291	36.4	8.5
No EEL	~100	1347	257	29.4	5.2
Methanol overcast on PAL (No EEL)	~100	1542	284	42.8	8.4
TiO _x , Reference	~100	2703	1235	81.9	31.1
TiO _x , diluted	~100	1812	434	44.6	9.8
TiO _x , unannealed	~100	1226	398	39.4	12.6

P5 An effective method of reconnoitering current-voltage (IV) characteristics of organic solar cells

In the following chapter a newly developed analytical tool for the interpretation of current-voltage (*IV*) curves is presented. It was developed from the work presented in this thesis, the initial encouragement for this method came from the experiments done for the manuscript presented in the previous chapter. The *IV* curves of devices treated only with methanol showed a peculiar

P5 An effective method of reconnoitering current-voltage (IV) characteristics of organic solar cells

feature, seen in Figure 27 a) for the cast while spinning the device, the feature is marked with a green oval. Further follow up experiments were done to see the effect of longer methanol treatment, i.e. methanol was not only dropped on the active layer during spinning, but was dropped on the PAL, while the device was resting and after the respective time was spun off. Also, a reference without any methanol treatment was manufactured. All these IV curves are shown in Figure 27 a). For the untreated device there is a very obvious S-shape in the IV curve for the 30 s and 1 min treated devices there is no S-Shape at all visible, while the spinning while casting device shows a subtler feature with a weak change in curvature. To obtain a clearer picture the IV curves were derived two times, as any S-shape, i.e. inflection point, would show a crossing of the voltage axis in the second derivative. Hence in Figure 27 b) the second derivative of the IV curves is shown. And indeed, only the device without any methanol treatment shows a crossing of the voltage axis, while all other show no such crossing. For the 30 s and 1 min methanol treated devices the second derivative shows only a peak, which than starts to level off towards larger forward biases. The device that was obtained via methanol treatment during spinning showed a peculiar double peak feature.

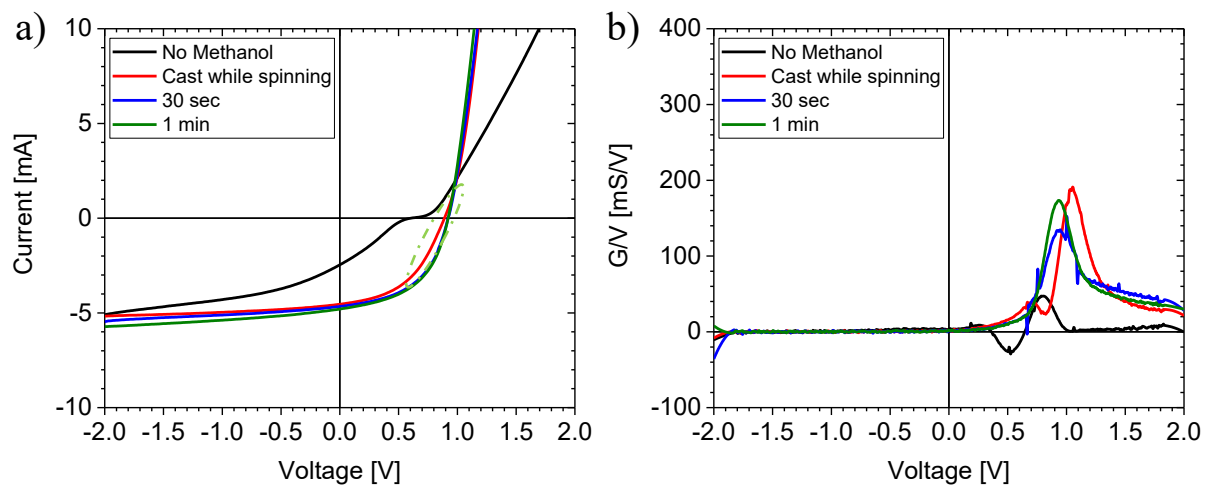


Figure 27: The active layer of OPV devices was treated with Methanol, by dropping Methanol on the active layer and spinning it off; a) shows their IV curves and b) the second derivatives of the IV curves shown in a). The green oval marks the region, whose curvature is deviating from the rest of the exponential equation for the “cast while spinning” device.

As the investigation of defective behavior in the IV curve via the usage of its second derivative was not reported in the literature so far and to further understand and study simulations via Simulation Program with Integrated Circuit Emphasis (SPICE) were performed. SPICE is any easy to learn tool to simulate the Shockley Diode equation very quickly, this allows for a broad accessibility. The Shockley equation with series resistance and shunt resistance is:

$$I = I_L - I_0 \exp\left(q \frac{V + IR_S}{nk_B T}\right) - \frac{V + IR_S}{R_{Sh}} \quad (3)$$

The equivalent circuits used for these simulations can be seen in Figure 28. The generally most basic equivalent circuit for any solar cell is shown in Figure 28 a) and consists of a current source (I1) representing the photocurrent, a diode (D1) representing the junction, a shunt resistance (R1) representing the resistance against recombination across the active layer of the solar cell and a

P5 An effective method of reconnoitering current-voltage (IV) characteristics of organic solar cells

series resistance (R_2) representing the ohmic resistivities of the individual layer plus the contact resistances between the individual layers. The circuits shown in Figure 28 b), c) and d) are the respective circuits used to study the impact of the dark saturation current I_0 , the diode ideality factor n , the series resistance R_S and the shunt resistance R_{Sh} on the second derivative.

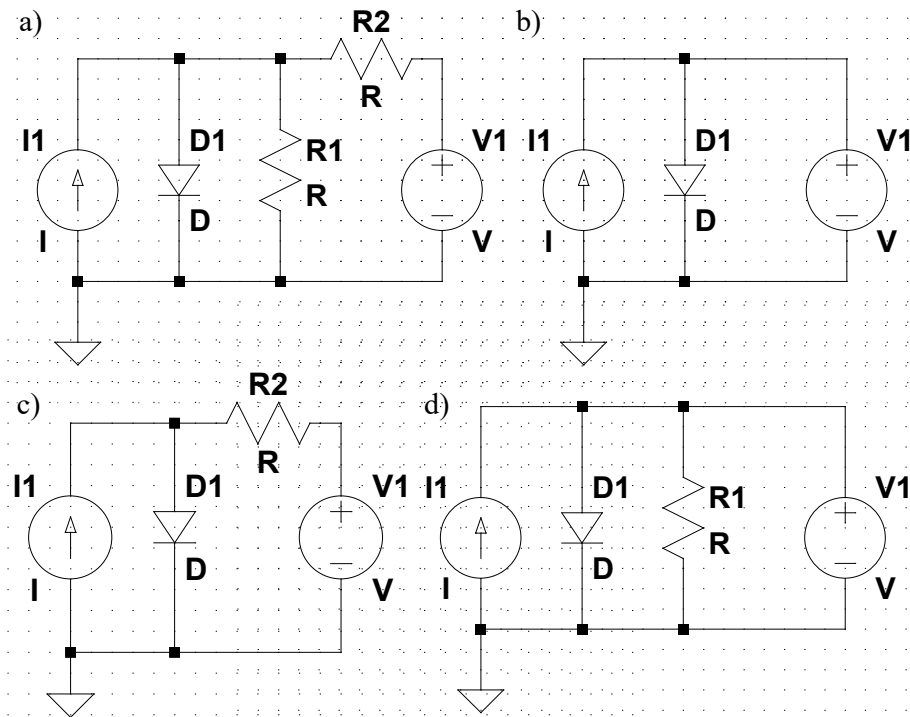


Figure 28: Equivalent circuits used for the SPICE simulations done to understand the impact of individual parameters of the Shockley-Diode-Equation, a) Most basic equivalent circuit for a solar cell, b) equivalent circuit used to study the impact of I_0 and n , c) equivalent circuit used to study the impact of the series resistance, d) equivalent circuit used to study the impact of the shunt resistance.

The simulation results of the aforementioned equivalent circuits seen in Figure 28 b) to d) are shown in Figure 29. In Figure 29 a) the simulation results for the variation of I_0 are shown. With a reduction of I_0 the diode opens up at larger voltages, as does the second derivative which also just increase at larger forward biases. As the Shockley equation without resistive terms remains a simple exponential equation its second derivative will also remain an exponential equation though with a different pre-factor, i.e. with different scaling. For b) where n was varied, an increase in n results in opening of the diode at larger forward biases and again in conjunction with this the second derivative also only starts to increase at larger forward biases. Again, in this case the Shockley equation does not contain any additional resistive terms, i.e. it is also a simple exponential equation and the same will be true as for the I_0 variation. Next the R_S was varied and these results can be seen in Figure 29 c) the second derivative shows here a very interesting feature, as a peak is appearing resembling the features seen in Figure 27 b). This can be easily understood by considering what the second derivative represents. The second derivative presents the change in conductivity with applied bias. A diode is showing increasing conductivity with increasing bias. On the other hand, an ohmic resistor shows no change in conductivity with changing bias, as its conductivity is a constant value. The peak can then be easily understood as the interaction between

P5 An effective method of reconnoitering current-voltage (IV) characteristics of organic solar cells

the diode in the circuit with the series resistance, representing an ohmic resistor, while the diode is turning on the conductivity starts to rise with increasing bias. At a certain point the ohmic resistance starts limiting this increasing conductivity and when the ohmic resistor starts to entirely takeover the device resistance the second derivative has to return to zero. Finally, in Figure 29 d) the results for the simulation where shunt resistance was varied is shown. For the shunt resistance variation, no change in the second derivative is visible at all. This can be easily understood when looking at Equation 3, as the shunt resistance is just a part of a linear term, it will disappear after deriving the equation twice.

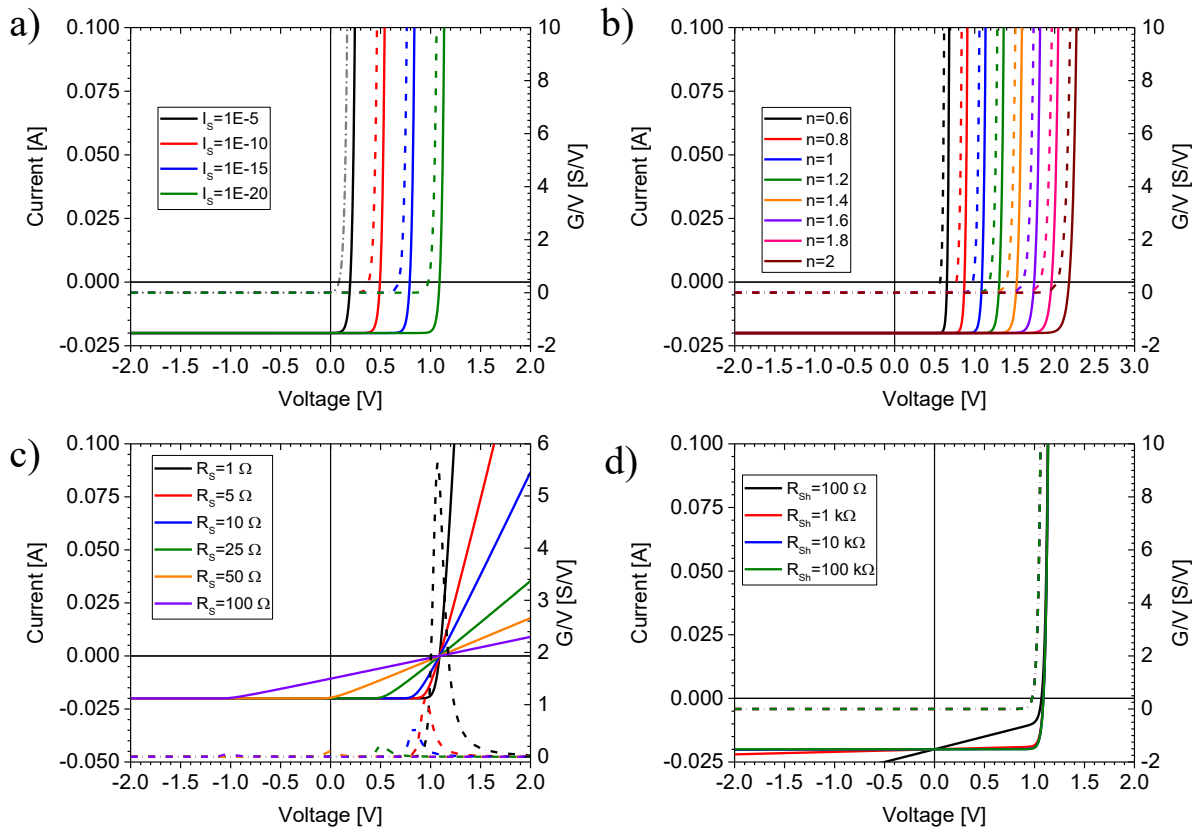


Figure 29: Results of SPICE simulation of the basic circuits shown in Figure 28 b) to d). a) Impact of I_0 , b) Impact of n , c) Impact of R_s , d) Impact of R_{sh} .

From the addition of a R_s to the circuit interesting interactions were seen, which were able to qualitatively reproduce the results obtained experimentally in Figure 27. This spawned interest in studying how the diode parameters interact when a series resistance is present in the circuit, hence further simulations were done using the circuit shown in Figure 28 c), though keeping R_s constant, while varying I_0 and n independently. The results of these simulations are shown in Figure 30, with a) showing the variation of the n and b) the variation of I_0 . For the variation in n one can observe two major effects on the second derivative a smaller n results in a more narrow and higher peak. This peak also is at lower voltage for a smaller n , the increase of n than shows three effects, the broadness of the peak increases, its height reduces and the peak position moves toward higher voltages. For the dark saturation current variation only one effect is visible, the peak position moves towards larger forward biases, besides this effect the peaks are identical.

P5 An effective method of reconnoitering current-voltage (IV) characteristics of organic solar cells

As some basic understanding was gained how simple equivalent circuits affect the second derivative of solar cells and being able to qualitatively reproduce the effects seen in the well working solar cells seen in Figure 27. Another model of an equivalent circuit was developed to understand the origin of certain defects seen on the experimental solar cells. This model can be seen in Figure 31 and shows a model with two diodes with associated contact resistances (R1 and R2). The parameters of the diodes were chosen in a way, that one diode behaves well, i.e. low I_0 and an n of 1, while the other performs poorly, i.e. larger I_0 and an n of 2. Additionally, the ratio between R1 and R2 was varied to modify how well each of the parallel diodes has contact with the electrodes, with the well performing diode always having a lower resistance than the defective one.

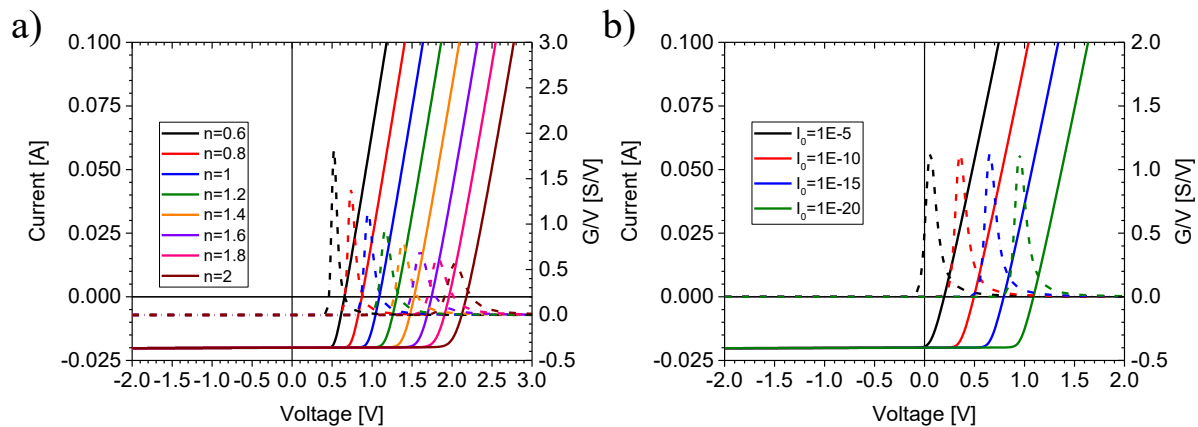


Figure 30: Simulations to study the combined impact of diode parameters and series resistance, a) constant series resistance and dark saturation current, but variation of diode ideality factor, b) constant series resistance and diode ideality factor, but variation of the dark saturation current.

Figure 32 shows the simulation results for the defective devices. In a) the IV curves for the simulations where the contact resistance of the defect inducing diode was varied are shown. The IV curves containing a defective diode are nearly all identical, except for around the maximum power point (MPP), the inset shows the region around the MPP enlarged and it can be seen that the IV curves for the devices with a lower contact resistance start to lose more and more FF , i.e. more and more current is recombining over the defective diode. Figure 32 b) shows the respective second derivatives for these IV curves and every device which was modeled with a defective diode shows a double peak, where the second peak towards lower voltages is represented as a shoulder to a main peak. With an increase in resistance ratio, i.e. an increasing contact resistance of the defective diode in respect to the contact resistance of the good diode, the shoulder peak reduced more and more in size and moved more towards lower voltages. Also, the main peak increased in size, while staying at the same position.

P5 An effective method of reconnoitering current-voltage (IV) characteristics of organic solar cells

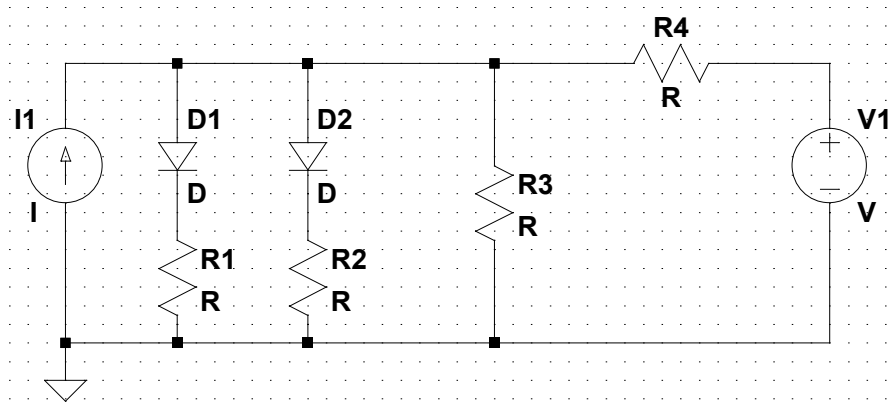


Figure 31: Equivalent circuit used to understand how defects and aberrative behavior in solar cells might be modelled in SPICE and what causes the effects seen in Figure 27.

The IV curves shown in Figure 32 c) are for the simulations where the contact resistance ratio between the two diodes was kept the same, but the I_0 of the defective diode was increased. The curves show two main effects, first the increase in I_0 results in a loss of V_{OC} , second also the FF is reducing more and more. The respective second derivative can be seen in Figure 32 d), where also a main peak with a shoulder can be seen. Though this shoulder only really forms when the I_0 increases to a value of $1E-10 A$, i.e. 10 orders of magnitude larger than the I_0 of the good diode. With increasing I_0 of the defective diode the shoulder moves further and further towards lower voltages.

P5 An effective method of reconnoitering current-voltage (IV) characteristics of organic solar cells

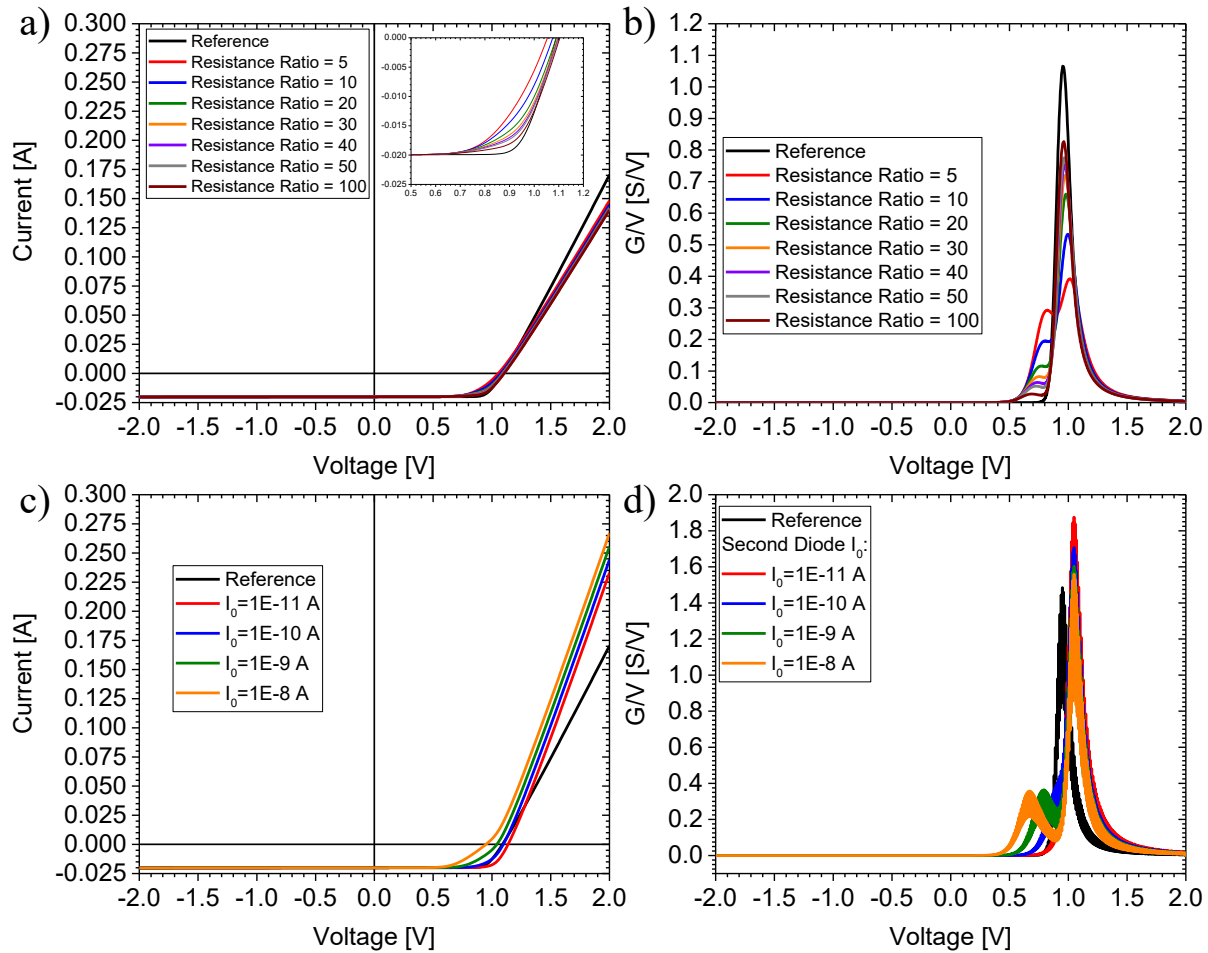


Figure 32: Simulation of defective IV curves with the equivalent circuit shown in Figure 31, a) IV curves for the variation of the contact resistance associated with the defective diode, b) second derivatives of the IV curves from a), c) IV curves for the variation of the I_0 of the defective diode, d) second derivatives of the IV curves from c).

With the simulations so far, it was quiet well possible to qualitatively reproduce the IV curves seen in Figure 27. Though there are still two major issues, the first issue is the values do not agree quantitatively, to address this issue various equivalent circuits were simulated consisting of multiple sub-solar cells shorted with each other, to represent on the one hand the distributed nature of the series resistance of a real solar cell. On the other hand, it also allows to look for effects of inhomogeneity within the device, as not every spot on the solar cell will behave exactly the same. The second effect so far not seen in the simulations but appearing in the experimental data, is that the second derivative does not entirely return to zero, but tends towards a constant value at increased forward biases. A possible reason for this effect could be limitation by space charge limited current, but further investigations on this effect are ongoing.

P5 An effective method of reconnoitering current-voltage (IV) characteristics of organic solar cells

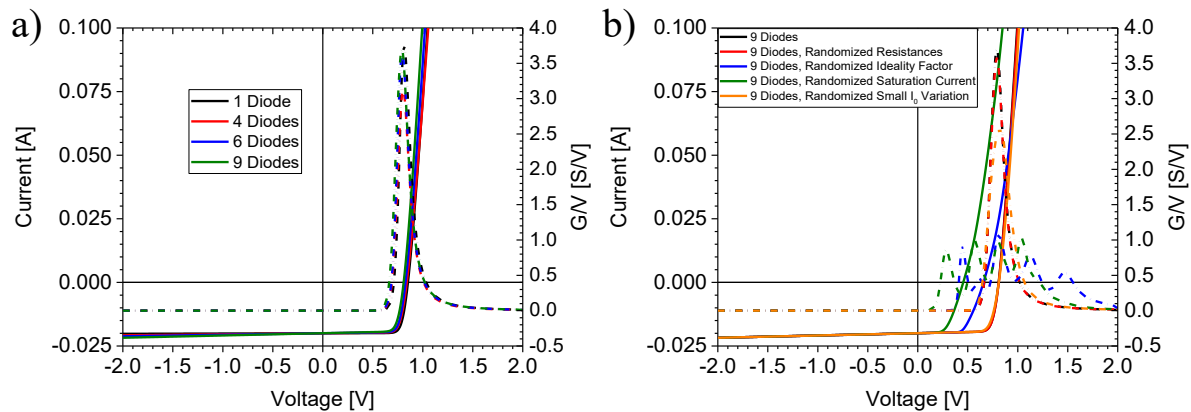


Figure 33: SPICE simulations of OPV devices with distributed solar cell parameters, i.e. multiple sub-solar cells shorted with each other, presenting the distributed nature of the series resistance and other parameters of the device. a) IV curves (solid lines) and second derivatives (dashed lines) for the variation of the number of diodes in the model. The global series resistance was kept constant. b) IV curves (solid lines) and second derivative (dashed lines) for the various 9 diode models where individual parameters of the sub-solar cells were varied.

In Figure 33 the results for the SPICE simulations with multiple sub-solar cells can be seen. In a) the number of sub-solar cells was steadily increased. One can see from this simulation, as long as the chosen parameters are basically resulting in the same global IV curve, the overall peak height, position and width barely changes, as the peak height is significantly higher than any height measured, this suggests that in a real device the values are more broadly distributed. So, in b) a broader distribution of parameters for the sub-solar cells was chosen. The variation of series resistances was chosen in a rather narrow window, as this is mostly dominated by the electrodes and should therefore usually not differ over many orders of magnitude. And the chosen variation indeed did not result in a large change in the IV curve and the second derivative. For the I_0 and n much larger variations were chosen and the resulting second derivative showed a multitude of peaks with a generally also way reduced peak height. Though this multitude of peaks did not resemble any of the measured devices, this still allows for some interesting insights. It shows that the distribution of values is more continuous in a real device, as to be expected, and that it usually does not vary over a large range, except for cases with defects, which seem to usually be far away in values of the here studied parameters from the main distribution. For the last pair of IV curve and second derivative seen in b) a smaller variation of I_0 was chosen. And indeed, a slight broadening, as well as a reduction in peak size is visible in this case, suggesting that for real devices, which can be treated as thousands of shorted equivalent circuits, a broad and continuous distribution of series resistances and diode parameters, would sufficiently reduce and broaden the peak.

For some further applications of the here presented method IV curves of devices aged under ISOS-L1^[84] conditions are shown in Figure 34. The two devices shown already have had slight differences in their initial behavior, which is well visible by looking at their respective second derivatives seen in b) and d). The device in b) already shows some blocking behavior at the beginning of the experiment. Such partial or total blocking behavior was also simulated and these simulations are shown in Figure 35 and will be explained in detail later on. The device shown in Figure 34 a) is developing an S-shape at around 15 h ageing time, this can be easily seen in the

P5 An effective method of reconnoitering current-voltage (IV) characteristics of organic solar cells

second derivative in b), though as all devices show at higher forward biases a bias dependent increase in conductivity, the IV curve slopes up again, which is seen in the second derivative as a constant value larger than zero. On the other hand, the device whose IV curves and their second derivatives are shown in c) and d) are only showing the bias dependent conductivity increase at large forward biases visible in the second derivative as a constant value again, though there is no dip in the second derivative between the peak and the plateau. This dip visible in b) is the already existing partial blocking contact, which will be further discussed.

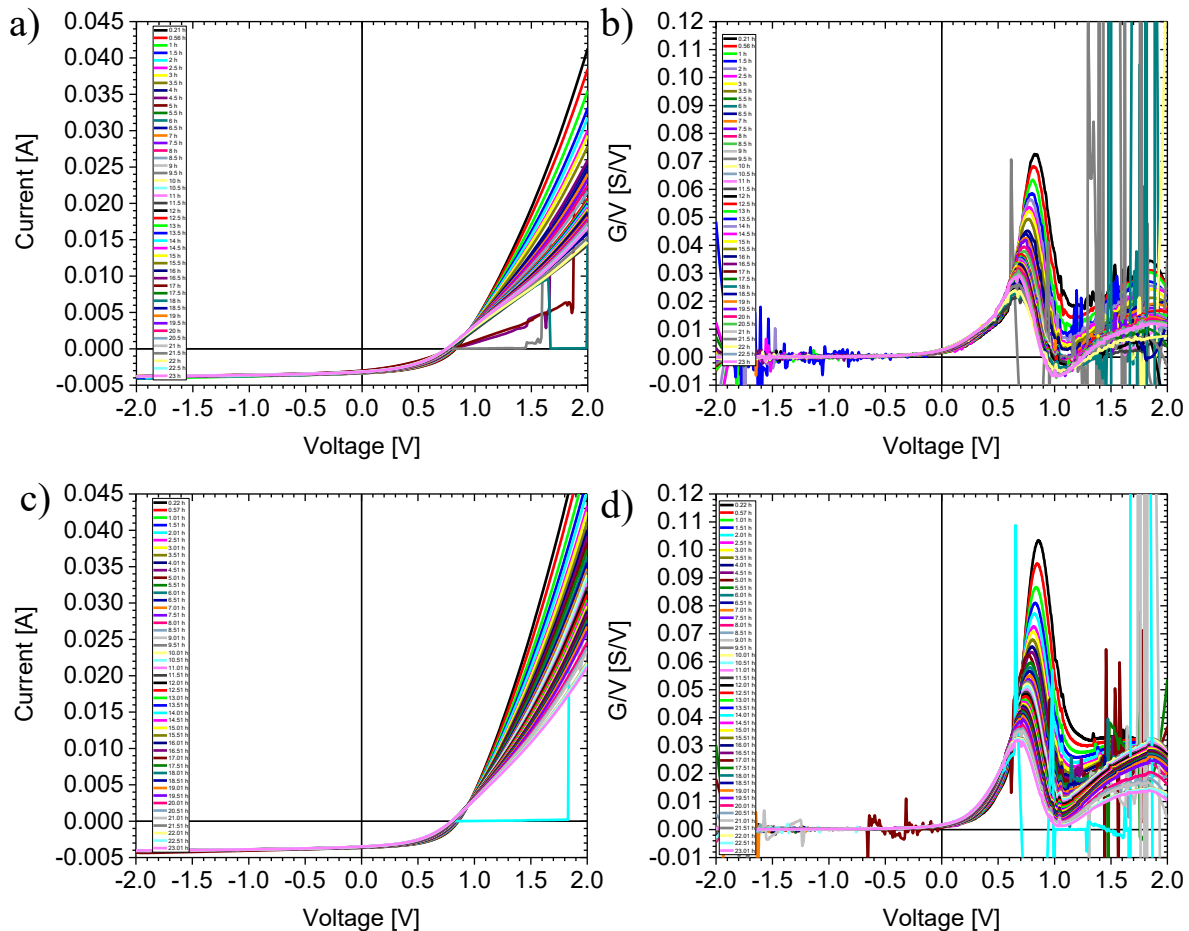


Figure 34: IV curves and their respective second derivative for PCDTBT:PC₇₁BM devices with a conventional layer stack that were aged under ISOS-L1 conditions via the usage of white light LEDs. The whole measurement time was the first 24 hours of a longer experiment, the interval between each curve was 30 minutes. For the second derivative some of the curves are depicted with 90% transparency to better see the general trend, as due to the increase in noise upon numerical derivation underlying curves were hardly visible. a) Example of solar cell developing an S-shape within the first 24 hours of ageing, b) the respective second derivatives to a). c) Example of a solar cell remaining free of an S-shape within the first 24 hours of ageing, d) respective second derivatives to c).

Additional simulations were performed and are shown in Figure 35. For these simulations an equivalent circuit containing a current source, a series resistance, a shunt resistance and 4 diodes were modelled, to each diode one by one another diode was placed in series in blocking direction, this second diode had a significantly larger I_0 value, i.e. showed much poorer blocking properties. In a) the respective IV curves are shown and one can see that for a device with only a quarter or even half of the diodes being blocked by counter diodes a deviation of the IV curve in forward

Summary

direction from the device without any counter diode is barely visible, especially without any comparison to a device without any counter diode properties. Though when comparing this to b) where the second derivative of the IV curves from a) are presented the blocking properties for a) in the case of 1 and 2 counter diodes is already easily visible. Returning now to the IV curves of the aged devices seen in Figure 34 a dip in the second derivative at large forward biases can be well explained with the formation of a partial counter diode, this counter diode can either be explained with the formation of a blocking layer or with a detrimental doping profile, which would result in an unfavorable energy landscape for charge carrier extraction^[28a].

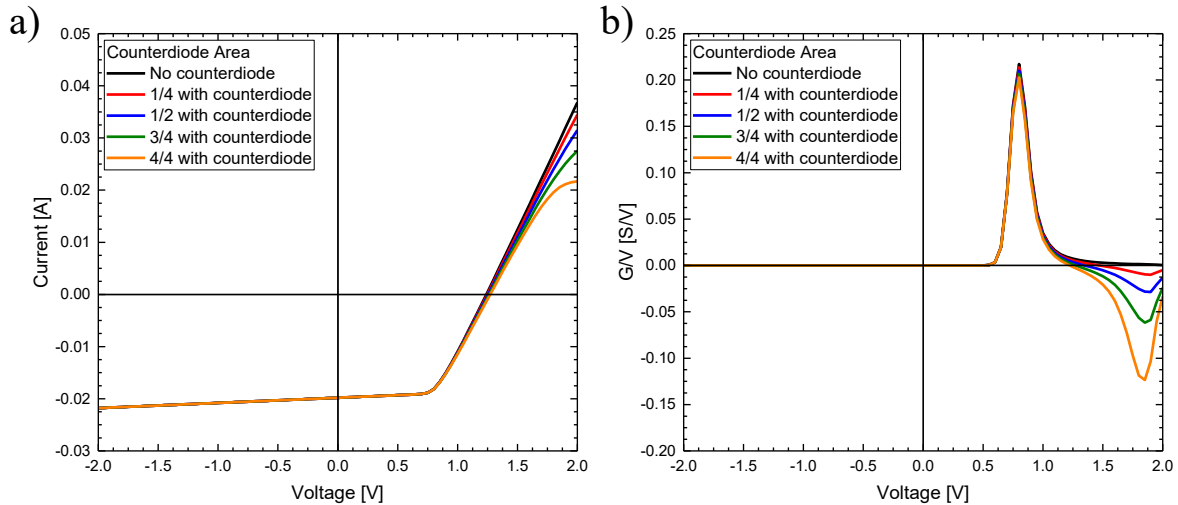


Figure 35: Results of SPICE simulations with counter diodes. Equivalent circuit consisted of 4 parallel diodes with identical parameters, which were one by one put into a series connection with diodes in reverse direction, which showed a very poor blocking behavior. a) the IV curves for each equivalent circuit, b) the respective second derivatives.

Such behaviors as described in this chapter are often connected with the interfacial layers, by either these layers themselves showing degradation, which for example is known for PEDOT:PSS, which on the one hand is sensitive to UV irradiation, but can generate additional doping, via the etching of adjacent layers^[59b, 86]. Also, metal oxides with known properties as photocatalysts, like zinc oxide or titanium oxide, can result in an increase in traps at the interface^[65], altering the n of the device, which would be more strongly visible in the second derivative. Though the aforementioned effects are not resulting in a unique signature in the second derivative of the IV curve, it is based on data already collected in any way and the analysis of it can allow for a faster and more focused decision on which methods to further apply, to gain a better insight on where degradation occurred.

7 Summary

Organic photovoltaics present a great opportunity to decarbonize the world's energy generation. Due to their versatility in terms of colors, mechanical flexibility, light weight, containing abundant elements and the inherent flexibility of organic chemistry, on which they are based, they could allow for fast deployment of photovoltaics in hitherto not seen scenarios and at massive scales in potentially very short times. They have by now reached efficiencies of 14% on the scale of small modules though they are unfortunately still lacking behind other PV technologies, though a-Si

Summary

modules, which still have niche applications like semi-transparent glassing actually has lower efficiencies. Beyond efficiency long lifetimes have been presented even for the latest high performing materials extrapolated under illumination of up to 30 years. This is especially important as manufacturers of silicon solar modules, which are the current industry standard, give warranties for 25 year, against which any newcomer will be evaluated against.

By now there is also a broad understanding of the fundamental processes in organic solar cells. This applies to how charges are generated, as well as how they degrade. Though the broad strokes are well understood, there are many fine details still to be etched out, which will be important to further develop OPV in a more focused manner. As at present much of their development is still primarily driven by serendipitous exploration of new materials and processing methods. Especially in terms of the active layer materials. But beyond active layer materials also charge transport layers have gained a lot of focus in the recent years, as they can greatly impact stability and performance as well.

In the first two chapters covered in this thesis a way forward for the commercialization of OPV is presented. This suggested path, which is the application of OPV in semi-transparent photovoltaic polytunnels. Such an application would bring several synergies for energy and food production. As solar energy is not very concentrated it requires a large footprint, when it is possible to make the same land usable for agriculture and energy generation, without any compromises for the food production, land can be easily and cheaply accessible. OPV can allow for this with its possibility to mostly collect the NIR portion of the solar spectrum, while leaving the visible portion for the plants. This comes with the added advantage of a more efficient water household for the plants, as well as a potentially higher photosynthetic yield. Further a calculation for the potentially achievable efficiency is presented, which can reach up to 18%. Also, it is shown that there are potentially already many active layer compounds presented in the literature, which have a sufficient transmissivity in the visible portion of the spectrum to be well suitable for agrivoltaics applications. Following this chapter, the second one builds on this idea and is presenting for a bunch of widely used charge transport layers how well they are suited for agrivoltaics applications. And is able to show that a few of the well-known transport layers from the OPV as well as the perovskite PV field are well suitable for such an application. Some are especially suited, like ZnO due to their UV filtering ability, which can reduce stress on plants and therefore increase yields.

Chapter three is presenting the results of a large international interlaboratory study, where a broad array of OPV layer stacks was compared with each other in various ageing experiments. The results of this study are showing that in general packaging of OPV is very important, as several devices had shown encapsulation breaches which resulted in premature failures of the devices. In case of a good packaging the devices with the highest lifetime energy yield were the ones with inverted layer stacks, which is partially not all too surprising as inverted layer stacks were originally introduced to increase the stability of OPV devices. The study showed also the importance of the choice of CTLs in regard to stability, as CTLs can even affect the long-term morphological stability of the active layer, as variations in the surface free energy of the CTLs will have an impact on vertical active layer stratification. For metal oxide ETLs the study again showed, for the case of zinc oxide, that UV filtering positively impacts the stability, as this reduces the photocatalytic ability of metal oxides like zinc oxide, but also titanium oxide.

Summary

In chapter four an array of various nitrogen containing organic electron extraction layers were studied and compared with a more standard electron transport layer the metal oxide titanium dioxide. The various organic EELs were the basic amino acids L-Histidine, L-Lysine and L-Arginine, as well as the polymer Poly-L-Lysine and three different Polyoxazolines. It was possible to show that the amino acids as EELs actually performed very well and in the case of L-Arginine performed even better than the TiO_x ETLs. Several correlations were found between material characteristics and solar cell performance. For the Polyoxazolines, which varied in their amine group content a correlation between said amine group content and the solar cell performance was found. While for the amino acids a correlation between the pK of the nitrogen containing functional groups in their side chain and the solar cell parameters were found. These two findings combined indicated that stronger Lewis bases perform better as EELs, as the stronger the Lewis basicity, the better the passivation of surface states at the interface between active layer and electrode. Also, the stability of devices with said ETLs and EELs were studied. The highest lifetime energy yield was achieved with the TiO_x reference ETL, though the L-Histidine achieved a value that was also respectable. For the Polyoxazolines no clear correlation between material parameters and stability was found, though that is usually complicated in polymers, as their properties also depend on measures like dispersity and molecular weight. For the amino acids on the other hand a reduced stability was found for increasing pK, i.e., an anti-correlation in regard to their performance. Suggesting that a higher Lewis basicity might also lead to a lower stability, due to the potentially higher reactivity. Nonetheless it was possible to show that the in general environmentally friendly and bio-compatible organic EELs chosen in this study, can perform well in OPV devices and might present a cheap and environmentally friendly option for certain applications.

In the fifth and final chapter a new method is presented, which allows for a quick and easy analysis of already existing current-voltage(IV)-characteristics, which represents the most basic characterization for any solar cell. Studying the second derivative of the IV curve can easily reveal aberrations in the device characteristics, easily overseen in the IV curve itself. The second derivative itself represents the bias dependent change in conductivity of a device. Via connecting said measurements with simulation results from SPICE performed on various equivalent circuits it was possible to show that different defects can only be well modelled by various diodes in parallel with different diode parameters, suggesting different and parallel contact conditions between active layer and the electrodes. Other defects were well recreated by combining multiple diodes in parallel, where some were successively blocked by counter diodes, while others remained undisturbed. Due to the simplicity of the method and the wide availability of data it can be easily employed to quickly analyze defects and allow for a more focused and through study of the involved mechanisms. It can also be used as an early warning system during degradation experiments to interrupt them and give devices a more thorough study shortly before and after for example the formation of blocking contacts.

In the course of this thesis a strategy for the commercialization of organic photovoltaics was presented, which makes optimal use of its properties. A certain topic of this strategy, i.e. the development of suitable charge transport layers was selected. Following the impact of various charge transport layers on solar cell performance and stability were discussed and for certain categories of these materials general properties could be extracted, which can be used to predict their suitability in regard to performance and stability. Last a new method was developed and

Zusammenfassung

shown for several examples, which should help reducing the time required to thoroughly study OPV devices and the factors limiting their performance and stability. Though still there is much to do in the future to optimize various processes and materials there is potentially a bright future ahead, which can result in a more environmentally friendly generation of energy, while not entirely wrecking natural habitats or having to give up the comforts of civilization.

8 Zusammenfassung

Die organische Photovoltaik bietet eine große Chance zur Dekarbonisierung der weltweiten Energieerzeugung. Aufgrund ihrer Vielseitigkeit in Bezug auf Farben, mechanische Flexibilität, geringes Gewicht, reichlich vorhandene Elemente und die inhärente Flexibilität der organischen Chemie, auf der sie beruhen, könnten sie einen schnellen Einsatz der Photovoltaik in bisher unbekanntem Szenarien und in großem Maßstab in potenziell sehr kurzer Zeit ermöglichen. Sie haben inzwischen Wirkungsgrade von 14 % bei kleinen Modulen erreicht, auch wenn sie leider noch hinter anderen PV-Technologien zurückbleiben. Über den Wirkungsgrad hinaus wurden selbst für die neuesten Hochleistungsmaterialien lange Lebensdauern von bis zu 30 Jahren unter Beleuchtung extrapoliert. Dies ist besonders wichtig, da die Hersteller von Silizium-Solarmodulen, die derzeit der Industriestandard sind, eine Garantie von 25 Jahren gewähren, an der sich jeder neue Marktteilnehmer messen lassen muss.

Inzwischen gibt es auch ein breites Verständnis der grundlegenden Prozesse in organischen Solarzellen. Dies gilt sowohl für die Erzeugung von Ladungen als auch für ihre Zersetzung. Obwohl die groben Züge gut verstanden sind, gibt es noch viele feine Details, die wichtig sind, um OPV gezielter weiterzuentwickeln. Gegenwärtig wird ein Großteil ihrer Entwicklung noch durch die zufällige Erforschung neuer Materialien und Verarbeitungsmethoden vorangetrieben. Dies gilt insbesondere für die Materialien der aktiven Schicht. Neben den Materialien für die aktive Schicht sind in den letzten Jahren aber auch die Ladungstransportschichten in den Blickpunkt gerückt, da sie ebenfalls einen großen Einfluss auf die Stabilität und Leistung haben können.

In den ersten beiden Kapiteln dieser Arbeit wird ein Weg für die Kommerzialisierung von OPV vorgestellt. Dieser vorgeschlagene Weg ist die Anwendung von OPV in halbtransparenten photovoltaischen Polytunneln. Eine solche Anwendung würde mehrere Synergien für die Energie- und Nahrungsmittelproduktion bringen. Da die Solarenergie nicht sehr konzentriert ist, benötigt sie eine große Fläche. Wenn es möglich ist, dieselbe Fläche für die Landwirtschaft und die Energieerzeugung zu nutzen, ohne Kompromisse bei der Lebensmittelproduktion einzugehen, kann die Fläche leicht und kostengünstig zugänglich sein. Die OPV kann dies ermöglichen, da sie hauptsächlich den NIR-Anteil des Sonnenspektrums auffängt und den sichtbaren Teil für die Pflanzen übrig lässt. Dies hat den zusätzlichen Vorteil eines effizienteren Wasserhaushalts für die Pflanzen sowie eines potenziell höheren photosynthetischen Ertrags. Ferner wird eine Berechnung des potenziell erreichbaren Wirkungsgrads vorgestellt, der bis zu 18 % betragen kann. Es wird auch gezeigt, dass es in der Literatur bereits viele aktive Schichtverbindungen gibt, die eine ausreichende Transmissivität im sichtbaren Bereich des Spektrums haben, um für Anwendungen in der Agro-Photovoltaik gut geeignet zu sein. Das zweite Kapitel baut auf dieser Idee auf und zeigt für eine Reihe von weit verbreiteten Ladungstransportschichten, wie gut sie für Anwendungen in der

Zusammenfassung

Agrovoltaik geeignet sind. Und kann zeigen, dass einige der bekannten Transportschichten aus dem OPV- sowie dem Perowskit-PV-Bereich gut für eine solche Anwendung geeignet sind. Einige sind besonders geeignet, wie z.B. ZnO aufgrund ihrer UV-Filtereigenschaften, die den Stress für die Pflanzen reduzieren und somit die Erträge erhöhen können.

In Kapitel drei werden die Ergebnisse einer großen internationalen Ringversuchsstudie vorgestellt, bei der eine breite Palette von OPV-Schichtstapeln in verschiedenen Alterungsexperimenten miteinander verglichen wurde. Die Ergebnisse dieser Studie zeigen, dass die Verpackung von OPV im Allgemeinen sehr wichtig ist, da mehrere Geräte Verletzungen der Verkapselung aufwiesen, die zu einem vorzeitigen Versagen der Geräte führten. Im Falle einer guten Verpackung waren die Geräte mit der höchsten Lebensdauerenergieausbeute diejenigen mit invertierten Schichtstapeln, was teilweise nicht allzu überraschend ist, da invertierte Schichtstapel ursprünglich eingeführt wurden, um die Stabilität von OPV-Geräten zu erhöhen. Die Studie zeigte auch, wie wichtig die Wahl der CTLs im Hinblick auf die Stabilität ist, da die CTLs sogar die langfristige morphologische Stabilität der aktiven Schicht beeinflussen können, da Schwankungen in der freien Oberflächenenergie der CTLs Auswirkungen auf die vertikale Schichtung der aktiven Schicht haben. Für Metalloxid-ETLs zeigte die Studie im Fall von Zinkoxid erneut, dass sich die UV-Filterung positiv auf die Stabilität auswirkt, da sie die photokatalytische Fähigkeit von Metalloxiden wie Zinkoxid, aber auch Titanoxid verringert.

In Kapitel vier wurde eine Reihe von verschiedenen stickstoffhaltigen organischen Elektronenextraktionsschichten untersucht und mit einer Standard-Elektronentransportschicht, dem Metalloxid Titandioxid, verglichen. Die verschiedenen organischen EELs waren die basischen Aminosäuren L-Histidin, L-Lysin und L-Arginin sowie das Polymer Poly-L-Lysin und drei verschiedene Polyoxazoline. Es konnte gezeigt werden, dass die Aminosäuren als EELs tatsächlich sehr gut abschnitten und im Falle von L-Arginin sogar besser als die TiO_x-ELs. Es wurden mehrere Korrelationen zwischen den Materialeigenschaften und der Solarzellenleistung festgestellt. Bei den Polyoxazolinen, die sich in ihrem Amingruppengehalt unterschieden, wurde eine Korrelation zwischen dem Amingruppengehalt und der Solarzellenleistung festgestellt. Bei den Aminosäuren wurde eine Korrelation zwischen dem pK-Wert der stickstoffhaltigen funktionellen Gruppen in der Seitenkette und den Solarzellenparametern festgestellt. Diese beiden Ergebnisse deuten darauf hin, dass stärkere Lewis-Basen als EELs besser funktionieren, denn je stärker die Lewis-Basizität, desto besser die Passivierung von Oberflächenzuständen an der Schnittstelle zwischen aktiver Schicht und Elektrode. Außerdem wurde die Stabilität von Bauelementen mit den genannten ETLs und EELs untersucht. Die höchste Lebensdauerenergieausbeute wurde mit dem TiO_x-Referenz-EL erzielt, obwohl das L-Histidin einen ebenfalls respektablen Wert erreichte. Bei den Polyoxazolinen wurde keine eindeutige Korrelation zwischen den Materialparametern und der Stabilität festgestellt, obwohl dies bei Polymeren normalerweise kompliziert ist, da ihre Eigenschaften auch von Größen wie Dispersität und Molekulargewicht abhängen. Bei den Aminosäuren hingegen wurde eine geringere Stabilität bei steigendem pK-Wert festgestellt, d. h. eine Anti-Korrelation in Bezug auf ihre Leistung. Dies deutet darauf hin, dass eine höhere Lewis-Basizität aufgrund der potenziell höheren Reaktivität auch zu einer geringeren Stabilität führen könnte. Nichtsdestotrotz konnte gezeigt werden, dass die in dieser Studie ausgewählten umweltfreundlichen und biokompatiblen organischen EELs in OPV-Geräten gut funktionieren und für bestimmte Anwendungen eine kostengünstige und umweltfreundliche Option darstellen könnten.

Zusammenfassung

Im fünften und letzten Kapitel wird eine neue Methode vorgestellt, die eine schnelle und einfache Analyse der bereits vorhandenen Strom-Spannungs-Kennlinien (IV) ermöglicht, die die grundlegendste Charakterisierung für jede Solarzelle darstellen. Die Untersuchung der zweiten Ableitung der IV-Kurve kann leicht Abweichungen in den Geräteeigenschaften aufdecken, die in der IV-Kurve selbst leicht zu übersehen sind. Die zweite Ableitung selbst stellt die von der Vorspannung abhängige Änderung der Leitfähigkeit eines Bauelements dar. Durch die Verknüpfung dieser Messungen mit Simulationsergebnissen aus SPICE, die an verschiedenen Ersatzschaltungen durchgeführt wurden, konnte gezeigt werden, dass verschiedene Defekte nur durch verschiedene Dioden in Parallelschaltung mit unterschiedlichen Diodenparametern gut modelliert werden können, was auf unterschiedliche und parallele Kontaktbedingungen zwischen aktiver Schicht und den Elektroden schließen lässt. Andere Defekte wurden durch die Kombination mehrerer Dioden in Parallelschaltung gut nachgebildet, wobei einige nacheinander durch Gegendiode blockiert wurden, während andere ungestört blieben. Aufgrund der Einfachheit der Methode und der breiten Verfügbarkeit von Daten kann sie leicht zur schnellen Analyse von Defekten eingesetzt werden und ermöglicht eine gezieltere und gründlichere Untersuchung der beteiligten Mechanismen. Sie kann auch als Frühwarnsystem während Degradationsexperimenten eingesetzt werden, um diese zu unterbrechen und den Bauelementen kurz vor und nach der Bildung von z. B. blockierenden Kontakten eine gründlichere Untersuchung zu ermöglichen.

Im Rahmen dieser Arbeit wurde eine Strategie für die Kommerzialisierung der organischen Photovoltaik vorgestellt, die deren Eigenschaften optimal nutzt. Ein bestimmter Bereich dieser Strategie, nämlich die Entwicklung geeigneter Ladungstransportschichten, wurde ausgewählt. Anschließend wurden die Auswirkungen verschiedener Ladungstransportschichten auf die Leistung und Stabilität von Solarzellen diskutiert, und für bestimmte Kategorien dieser Materialien konnten allgemeine Eigenschaften extrahiert werden, die zur Vorhersage ihrer Eignung in Bezug auf Leistung und Stabilität verwendet werden können. Schließlich wurde eine neue Methode entwickelt und an mehreren Beispielen demonstriert, die dazu beitragen dürfte, die für eine gründliche Untersuchung von OPV-Bauelementen und der Faktoren, die ihre Leistung und Stabilität einschränken, erforderliche Zeit zu verkürzen. Auch wenn es in Zukunft noch viel zu tun gibt, um verschiedene Prozesse und Materialien zu optimieren, steht uns möglicherweise eine vielversprechende Zukunft bevor, die zu einer umweltfreundlicheren Energieerzeugung führen kann, ohne die natürlichen Lebensräume völlig zu zerstören oder auf die Annehmlichkeiten der Zivilisation verzichten zu müssen.

Abbreviations

Abbreviations

CTL: Charge Transport Layer

EEL: Electron Extraction Layer

ETL: Electron Transport Layer

FF: Fill Factor

HEL: Hole Extraction Layer

HTL: Hole Transport Layer

NIR: near-infrared

NREL: National Renewable Energies Laboratory

PAL: Photoactive Layer

PCE: Power Conversion Efficiency

Symbols

Symbols

I_0 : Dark Saturation Current

I_L : Photocurrent

I_{SC} : Short Circuit Current

J_0 : Dark Saturation Current Density

J_{SC} : Short Circuit Current Density

k_B : Boltzmann Constant

n : Diode Ideality Factor

q : Elementary Charge

R_S : Series Resistance

R_{Sh} : Shunt Resistance

T : Absolute Temperature

V_{OC} : Open Circuit Voltage

References

References

- [1] a B. L. Drake, *Journal of Archaeological Science* **2012**, *39*, 1862-1870; b D. Kaniewski, E. Van Campo, J. Guiot, S. Le Burel, T. Otto, C. Baeteman, *PloS one* **2013**, *8*, e71004; c M. Finné, K. Holmgren, C.-C. Shen, H.-M. Hu, M. Boyd, S. Stocker, *PloS one* **2017**, *12*, e0189447.
- [2] a P. M. Douglas, A. A. Demarest, M. Brenner, M. A. Canuto, *Annual Review of Earth and Planetary Sciences* **2016**, *44*, 613-645; b D. J. Kennett, S. F. Breitenbach, V. V. Aquino, Y. Asmerom, J. Awe, J. U. Baldini, P. Bartlein, B. J. Culleton, C. Ebert, C. Jazwa, *Science* **2012**, *338*, 788-791.
- [3] M. Child, O. Koskinen, L. Linnanen, C. Breyer, *Renewable and Sustainable Energy Reviews* **2018**, *91*, 321-334.
- [4] Fraunhofer ISE, Photovoltaics Report **2021**, <https://www.ise.fraunhofer.de/content/dam/ise/de/documents/publications/studies/Photovoltaics-Report.pdf>, accessed 15.01.2021.
- [5] a N. Glanemann, S. N. Willner, A. Levermann, *Nature communications* **2020**, *11*, 1-11; b S. Baruch-Mordo, J. Kiesecker, C. Kennedy, J. Oakleaf, J. Opperman, *Environmental Research Letters* **2019**, *14*, 024013; cS. Teske, *Achieving the Paris climate agreement goals: Global and regional 100% renewable energy scenarios with non-energy GHG pathways for + 1.5 C and + 2 C*, Springer Nature, **2019**.
- [6] P. Verlinden, *Journal of Renewable and Sustainable Energy* **2020**, *12*, 053505.
- [7] a N. Espinosa, M. Hosel, D. Angmo, F. C. Krebs, *Energy & Environmental Science* **2012**, *5*, 5117-5132; b M. D. Chatzidisideris, N. Espinosa, A. Laurent, F. C. Krebs, *Solar Energy Materials and Solar Cells*; cR. Vidal, J.-A. Alberola-Borràs, N. Sánchez-Pantoja, I. Mora-Seró, *Advanced Energy and Sustainability Research* **2021**, *2*, 2000088.
- [8] a Z. Wang, H. Jiang, X. Liu, J. Liang, L. Zhang, L. Qing, Q. Wang, W. Zhang, Y. Cao, J. Chen, *Journal of Materials Chemistry A* **2020**, *8*, 7765-7774; b R. Søndergaard, M. Hösel, D. Angmo, T. T. Larsen-Olsen, F. C. Krebs, *Materials Today* **2012**, *15*, 36-49; c H. W. Ro, J. M. Downing, S. Engmann, A. A. Herzing, D. M. DeLongchamp, L. J. Richter, S. Mukherjee, H. Ade, M. Abdelsamie, L. K. Jagadamma, A. Amassian, Y. Liu, H. Yan, *Energy & Environmental Science* **2016**, *9*, 2835-2846; d D. I. Kutsarov, E. New, F. Bausi, A. Zoladek-Lemanczyk, F. A. Castro, S. R. P. Silva, *Solar Energy Materials and Solar Cells* **2017**, *161*, 388-396.
- [9] a F. Machui, M. Hosel, N. Li, G. D. Spyropoulos, T. Ameri, R. R. Søndergaard, M. Jorgensen, A. Scheel, D. Gaiser, K. Kreul, D. Lenssen, M. Legros, N. Lemaitre, M. Vilkmann, M. Valimaki, S. Nordman, C. J. Brabec, F. C. Krebs, *Energy & Environmental Science* **2014**, *7*, 2792-2802; b J. Zhang, N. Chang, C. Fagerholm, M. Qiu, L. Shuai, R. Egan, C. Yuan, *Renewable and Sustainable Energy Reviews* **2022**, *158*, 112146.
- [10] P. Cheng, Y. Yang, *Accounts of Chemical Research* **2020**, *53*, 1218-1228.
- [11] N. Espinosa, M. Hosel, M. Jorgensen, F. C. Krebs, *Energy & Environmental Science* **2014**, *7*, 855-866.
- [12] N. Espinosa, Y.-S. Zimmermann, G. A. dos Reis Benatto, M. Lenz, F. C. Krebs, *Energy & Environmental Science* **2016**, *9*, 1674-1680.
- [13] a C. W. Tang, *Applied Physics Letters* **1986**, *48*, 183-185; b R. A. J. Janssen, J. C. Hummelen, K. Lee, K. Pakbaz, N. S. Sariciftci, A. J. Heeger, F. Wudl, *The Journal of Chemical Physics* **1995**, *103*, 788-793.
- [14] A. J. Heeger, A. G. MacDiarmid, Springer Berlin Heidelberg, Berlin, Heidelberg, **1979**, pp. 359-383.

References

- [15] a N. Cho, J. Kim, K. Song, J. K. Lee, J. Ko, *Tetrahedron* **2012**, *68*, 4029-4036; b J. N. de Freitas, R. W. C. Li, A. F. Nogueira, J. Gruber, *Materials Chemistry and Physics* **2011**, *130*, 223-230; c R. Kroon, M. Lenes, J. C. Hummelen, P. W. M. Blom, B. de Boer, *Polymer Reviews* **2008**, *48*, 531-582; d D. Mühlbacher, M. Scharber, M. Morana, Z. Zhu, D. Waller, R. Gaudiana, C. Brabec, *Advanced Materials* **2006**, *18*, 2884-2889; e M. C. Scharber, N. S. Sariciftci, *Advanced Materials Technologies* **2021**, *6*, 2000857.
- [16] a Y. Li, G. Xu, C. Cui, Y. Li, *Advanced Energy Materials* **2018**, *8*, 1701791; b S. Han, Y. Deng, W. Han, G. Ren, Z. Song, C. Liu, W. Guo, *Solar Energy* **2021**, *225*, 97-107.
- [17] a M. C. Scharber, *Advanced Materials* **2016**, *28*, 1994-2001; b M. C. Scharber, D. Mühlbacher, M. Koppe, P. Denk, C. Waldauf, A. J. Heeger, C. J. Brabec, *Advanced Materials* **2006**, *18*, 789-794; c L. J. A. Koster, S. E. Shaheen, J. C. Hummelen, *Advanced Energy Materials* **2012**, *2*, 1246-1253; d V. Dirlikov, M. S. C. J., J. R. A. J., *Advanced Functional Materials* **2009**, *19*, 1939-1948; e K. Vandewal, K. Tvingstedt, A. Gadisa, O. Inganäs, J. V. Manca, *Nature Materials* **2009**, *8*, 904.
- [18] V. Koen, G. Abay, O. W. D., B. Sabine, B. Fateme, V. S. Ineke, L. Laurence, C. T. J., V. Dirk, M. J. V., *Advanced Functional Materials* **2008**, *18*, 2064-2070.
- [19] a A. Classen, C. L. Chochos, L. Lüer, V. G. Gregoriou, J. Wortmann, A. Osvet, K. Forberich, I. McCulloch, T. Heumüller, C. J. Brabec, *Nature Energy* **2020**, *5*, 711-719; b K. Leo, *Nature Reviews Materials* **2016**, *1*, 16056.
- [20] H. Hoppe, N. Arnold, D. Meissner, N. S. Sariciftci, *Thin Solid Films* **2004**, *451*, 589-592.
- [21] a M. Ghasemi, N. Balar, Z. Peng, H. Hu, Y. Qin, T. Kim, J. J. Rech, M. Bidwell, W. Mask, I. McCulloch, W. You, A. Amassian, C. Risko, B. T. O'Connor, H. Ade, *Nature Materials* **2021**, *20*, 525-532; b J. Peet, A. J. Heeger, G. C. Bazan, *Accounts of Chemical Research* **2009**, *42*, 1700-1708; c C. Yang, S. Zhang, J. Ren, M. Gao, P. Bi, L. Ye, J. Hou, *Energy & Environmental Science* **2020**, *13*, 2864-2869.
- [22] a B. Xue, B. Vaughan, C.-H. Poh, K. B. Burke, L. Thomsen, A. Stapleton, X. Zhou, G. W. Bryant, W. Belcher, P. C. Dastoor, *The Journal of Physical Chemistry C* **2010**, *114*, 15797-15805; b L. Huang, G. Wang, W. Zhou, B. Fu, X. Cheng, L. Zhang, Z. Yuan, S. Xiong, L. Zhang, Y. Xie, A. Zhang, Y. Zhang, W. Ma, W. Li, Y. Zhou, E. Reichmanis, Y. Chen, *ACS Nano* **2018**, *12*, 4440-4452; c M. Kim, J. Lee, S. B. Jo, D. H. Sin, H. Ko, H. Lee, S. G. Lee, K. Cho, *Journal of Materials Chemistry A* **2016**, *4*, 15522-15535.
- [23] a H. Hoppe, N. S. Sariciftci, *J. Mater. Res.* **2004**, *19*, 1924-1945; b C. J. Brabec, J. R. Durrant, *MRS Bulletin* **2008**, *33*, 670-675.
- [24] a W. C. H. Choy, D. Zhang, *Small* **2016**, *12*, 416-431; b W. Tress, K. Leo, M. Riede, *Advanced Functional Materials* **2011**, *21*, 2140-2149; c R. Xue, J. Zhang, Y. Li, Y. Li, *Small* **2018**, *14*, 1801793; d R. Steim, F. R. Kogler, C. J. Brabec, *Journal of Materials Chemistry* **2010**, *20*, 2499-2512.
- [25] a K. Zilberberg, T. Riedl, *Journal of Materials Chemistry A* **2016**, *4*, 14481-14508; b J. Huang, X. Liu, Y. Lu, Y. Zhou, J. Xu, J. Li, H. Wang, J. Fang, Y. Yang, W. Wang, R. Tan, W. Song, *Solar Energy Materials and Solar Cells* **2018**, *184*, 73-81.
- [26] K. Anagnostou, M. M. Stylianakis, K. Petridis, E. Kymakis, *Energies* **2019**, *12*, 2188.
- [27] S. K. Hau, H.-L. Yip, A. K. Y. Jen, *Polymer Reviews* **2010**, *50*, 474-510.
- [28] a A. G. Suren, H. Iлона Maria, B. Eva, C. Michael, H. Markus, R. S. Roar, B. Gisele Alves dos Reis, J. Mikkel, C. K. Frederik, *Journal of Physics D: Applied Physics* **2017**, *50*, 103001; b J. U. Lee, J. W. Jung, J. W. Jo, W. H. Jo, *Journal of Materials Chemistry* **2012**, *22*, 24265-24283.

References

- [29] NREL Solar Cell Efficiency Chart, **2022**, <https://www.nrel.gov/pv/assets/pdfs/cell-pv-eff-emergingpv-rev211214.pdf>, accessed 16.01.2022.
- [30] a A. K. Ghosh, T. Feng, *Journal of Applied Physics* **1978**, *49*, 5982-5989; b D. L. Morel, A. K. Ghosh, T. Feng, E. L. Stogryn, P. E. Purwin, R. F. Shaw, C. Fishman, *Applied Physics Letters* **1978**, *32*, 495-497; c V. Y. Merritt, H. J. Hovel, *Applied Physics Letters* **1976**, *29*, 414-415.
- [31] a G. Yu, J. Gao, J. C. Hummelen, F. Wudl, A. J. Heeger, *Science* **1995**, *270*, 1789-1791; b C. Yang, A. Heeger, *Synthetic metals* **1996**, *83*, 85-88.
- [32] F. Padinger, D. Gebeyehu, C. J. Brabec, T. Fromherz, N. S. Sariciftci, J. C. Hummelen, *MRS Online Proceedings Library (OPL)* **1999**, 598.
- [33] A. C. Mayer, S. R. Scully, B. E. Hardin, M. W. Rowell, M. D. McGehee, *Materials today* **2007**, *10*, 28-33.
- [34] H. W. Kroto, J. R. Heath, S. C. O'Brien, R. F. Curl, R. E. Smalley, *Nature* **1985**, *318*, 162-163.
- [35] C. B. Nielsen, S. Holliday, H.-Y. Chen, S. J. Cryer, I. McCulloch, *Accounts of Chemical Research* **2015**, *48*, 2803-2812.
- [36] M. T. Dang, L. Hirsch, G. Wantz, *Advanced Materials* **2011**, *23*, 3597-3602.
- [37] R. Roesch, K.-R. Eberhardt, S. Engmann, G. Gobsch, H. Hoppe, *Solar Energy Materials and Solar Cells* **2013**, *117*, 59-66.
- [38] Y. Liang, Z. Xu, J. Xia, S.-T. Tsai, Y. Wu, G. Li, C. Ray, L. Yu, *Advanced Materials* **2010**, *22*, E135-E138.
- [39] S. Beaupré, M. Leclerc, *Journal of Materials Chemistry A* **2013**, *1*, 11097-11105.
- [40] Y. Liang, L. Yu, *Polymer Reviews* **2010**, *50*, 454-473.
- [41] a Y. Liu, J. Zhao, Z. Li, C. Mu, W. Ma, H. Hu, K. Jiang, H. Lin, H. Ade, H. Yan, *Nature communications* **2014**, *5*, 1-8; b J. Zhao, Y. Li, G. Yang, K. Jiang, H. Lin, H. Ade, W. Ma, H. Yan, *Nature Energy* **2016**, *1*, 15027.
- [42] a W. Zhao, D. Qian, S. Zhang, S. Li, O. Inganäs, F. Gao, J. Hou, *Advanced Materials* **2016**, *28*, 4734-4739; b S. Li, L. Ye, W. Zhao, S. Zhang, S. Mukherjee, H. Ade, J. Hou, *Advanced Materials* **2016**, *28*, 9423-9429.
- [43] a J. Hou, O. Inganäs, R. H. Friend, F. Gao, *Nature Materials* **2018**, *17*, 119; b P. Cheng, G. Li, X. Zhan, Y. Yang, *Nature Photonics* **2018**, *12*, 131-142; c S. Li, W. Liu, C.-Z. Li, M. Shi, H. Chen, *Small* **2017**, *13*, 1701120; d J. Zhang, H. S. Tan, X. Guo, A. Facchetti, H. Yan, *Nature Energy* **2018**, *3*, 720-731.
- [44] a D. Qian, Z. Zheng, H. Yao, W. Tress, T. R. Hopper, S. Chen, S. Li, J. Liu, S. Chen, J. Zhang, *Nature materials* **2018**, *17*, 703-709; b X.-K. Chen, D. Qian, Y. Wang, T. Kirchartz, W. Tress, H. Yao, J. Yuan, M. Hülsbeck, M. Zhang, Y. Zou, *Nature Energy* **2021**, *6*, 799-806.
- [45] a W. Gao, T. Liu, C. Zhong, G. Zhang, Y. Zhang, R. Ming, L. Zhang, J. Xin, K. Wu, Y. Guo, W. Ma, H. Yan, Y. Liu, C. Yang, *ACS Energy Letters* **2018**, *3*, 1760-1768; b Z. Zhong, H. Qin, Z. Shaoqing, Z. Dongyang, W. Jianqiu, X. Shenkun, W. Rong, Q. Yunpeng, L. Wanning, H. Ling, L. Ningning, L. Feng, Z. Yuan, W. Zhixiang, T. Zhiyong, R. T. P., H. Jianhui, Z. Huiqiong, *Advanced Materials*, *0*, 1801801.
- [46] a W. Zhao, S. Li, H. Yao, S. Zhang, Y. Zhang, B. Yang, J. Hou, *Journal of the American Chemical Society* **2017**, *139*, 7148-7151; b H. Zhang, H. Yao, J. Hou, J. Zhu, J. Zhang, W. Li, R. Yu, B. Gao, S. Zhang, J. Hou, *Advanced Materials* **2018**, *30*, 1800613.
- [47] T.-Y. Tsai, P.-R. Yan, S.-H. Yang, *Nanoscale Research Letters* **2016**, *11*, 516.

References

- [48] N. Gasparini, M. Salvador, S. Strohm, T. Heumueller, I. Levchuk, A. Wadsworth, J. H. Bannock, J. C. de Mello, H.-J. Egelhaaf, D. Baran, I. McCulloch, C. J. Brabec, *Advanced Energy Materials* **2017**, *7*, 1700770.
- [49] S. Li, C.-Z. Li, M. Shi, H. Chen, *ACS Energy Letters* **2020**, *5*, 1554-1567.
- [50] a Y. Cui, Y. Xu, H. Yao, P. Bi, L. Hong, J. Zhang, Y. Zu, T. Zhang, J. Qin, J. Ren, Z. Chen, C. He, X. Hao, Z. Wei, J. Hou, *Advanced Materials* **2021**, *33*, 2102420; b Q. Liu, Y. Jiang, K. Jin, J. Qin, J. Xu, W. Li, J. Xiong, J. Liu, Z. Xiao, K. Sun, S. Yang, X. Zhang, L. Ding, *Science Bulletin* **2020**, *65*, 272-275.
- [51] a Y. Li, X. Huang, K. Ding, H. K. M. Sheriff, L. Ye, H. Liu, C.-Z. Li, H. Ade, S. R. Forrest, *Nature Communications* **2021**, *12*, 5419; b X. Xu, J. Xiao, G. Zhang, L. Wei, X. Jiao, H.-L. Yip, Y. Cao, *Science Bulletin* **2020**, *65*, 208-216.
- [52] W. R. Mateker, M. D. McGehee, *Advanced Materials* **2017**, *29*, n/a-n/a.
- [53] T. Heumueller, W. R. Mateker, I. T. Sachs-Quintana, K. Vandewal, J. A. Bartelt, T. M. Burke, T. Ameri, C. J. Brabec, M. D. McGehee, *Energy & Environmental Science* **2014**, *7*, 2974-2980.
- [54] J. Luke, E. M. Speller, A. Wadsworth, M. F. Wyatt, S. Dimitrov, H. K. H. Lee, Z. Li, W. C. Tsoi, I. McCulloch, D. Bagnis, J. R. Durrant, J.-S. Kim, *Advanced Energy Materials* **2019**, *9*, 1803755.
- [55] Z. Yin, J. Wei, Q. Zheng, *Adv. Sci.* **2016**, *3*, 1500362.
- [56] Z.-G. Zhang, B. Qi, Z. Jin, D. Chi, Z. Qi, Y. Li, J. Wang, *Energy & Environmental Science* **2014**, *7*, 1966-1973.
- [57] Y. Zhou, C. Fuentes-Hernandez, J. Shim, J. Meyer, A. J. Giordano, H. Li, P. Winget, T. Papadopoulos, H. Cheun, J. Kim, M. Fenoll, A. Dindar, W. Haske, E. Najafabadi, T. M. Khan, H. Sojoudi, S. Barlow, S. Graham, J.-L. Brédas, S. R. Marder, A. Kahn, B. Kippelen, *Science* **2012**, *336*, 327-332.
- [58] a S. Huang, L. Duan, D. Zhang, *Journal of Materials Chemistry A* **2020**, *8*, 18792-18801; b B. A. E. Courtright, S. A. Jenekhe, *ACS Appl. Mater. Interfaces* **2015**, *7*, 26167-26175; c H. Zhou, Y. Zhang, J. Seifert, S. D. Collins, C. Luo, G. C. Bazan, T.-Q. Nguyen, A. J. Heeger, *Advanced Materials* **2013**, *25*, 1646-1652; d R. Meitzner, J. Essomba, S. Alam, A. Anand, N. Engel, K. Fulbert, K. Kuma, F. Ayuyasmin, M. M. Islam, C. Ugokwe, U. S. Schubert, H. Hoppe, *Energy Technology* **2020**, *8*, 2000117.
- [59] a P. Cheng, X. Zhan, *Chemical Society Reviews* **2016**, *45*, 2544-2582; b A. Anand, J. P. Madalaimuthu, M. Schaal, F. Otto, M. Gruenewald, S. Alam, T. Fritz, U. S. Schubert, H. Hoppe, *ACS Applied Electronic Materials* **2021**, *3*, 929-943.
- [60] M. P. d. Jong, L. J. v. IJzendoorn, M. J. A. d. Voigt, *Applied Physics Letters* **2000**, *77*, 2255-2257.
- [61] L. Duan, A. Uddin, *Adv. Sci.* **2020**, *7*, 1903259.
- [62] C.-Y. Chi, C.-H. Shih, E. Sauter, S. K. Das, Y.-H. Liang, H.-T. Lien, S.-T. Chang, M. Zharnikov, Y. Tai, *Journal of Materials Chemistry A* **2018**, *6*, 6542-6550.
- [63] S. R. Cowan, P. Schulz, A. J. Giordano, A. Garcia, B. A. MacLeod, S. R. Marder, A. Kahn, D. S. Ginley, E. L. Ratcliff, D. C. Olson, *Advanced Functional Materials* **2014**, *24*, 4671-4680.
- [64] A. Sundqvist, O. J. Sandberg, M. Nyman, J.-H. Smått, R. Österbacka, *Advanced Energy Materials* **2016**, *6*, 1502265.
- [65] S. Trost, T. Becker, A. Polywka, P. Görrn, M. F. Oszajca, N. A. Luechinger, D. Rogalla, M. Weidner, P. Reckers, T. Mayer, T. Riedl, *Advanced Energy Materials* **2016**, *6*, 1600347.

References

- [66] a L. Hu, Y. Liu, L. Mao, S. Xiong, L. Sun, N. Zhao, F. Qin, Y. Jiang, Y. Zhou, *Journal of Materials Chemistry A* **2018**, *6*, 2273-2278; b Y. Wang, J. Han, L. Cai, N. Li, Z. Li, F. Zhu, *Journal of Materials Chemistry A* **2020**, *8*, 21255-21264.
- [67] X. Xu, J. Xiao, G. Zhang, L. Wei, X. Jiao, H.-L. Yip, Y. Cao, *Science Bulletin* **2020**, *65*, 208-216.
- [68] a S. Chen, H. Yao, B. Hu, G. Zhang, L. Arunagiri, L.-K. Ma, J. Huang, J. Zhang, Z. Zhu, F. Bai, W. Ma, H. Yan, *Advanced Energy Materials* **2018**, *8*, 1800529; b P. Shen, G. Wang, B. Kang, W. Guo, L. Shen, *ACS Appl. Mater. Interfaces* **2018**, *10*, 6513-6520; c Q. Xue, R. Xia, C. J. Brabec, H.-L. Yip, *Energy & Environmental Science* **2018**, *11*, 1688-1709; d D. Wang, H. Liu, Y. Li, G. Zhou, L. Zhan, H. Zhu, X. Lu, H. Chen, C.-Z. Li, *Joule* **2021**, *5*, 945-957; e R. Xia, H. Gu, S. Liu, K. Zhang, H.-L. Yip, Y. Cao, *Solar RRL* **2019**, *3*, 1800270.
- [69] S. Amaducci, X. Yin, M. Colauzzi, *Applied Energy* **2018**, *220*, 545-561.
- [70] a A. S. Pascaris, C. Schelly, J. M. Pearce, *Agronomy* **2020**, *10*, 1885; b T. Sekiyama, A. Nagashima, *Environments* **2019**, *6*, 65.
- [71] W. Shockley, H. J. Queisser, C. D. M., F. C. S., P. G. L., *Journal of Applied Physics* **1961**, *32*, 510-519.
- [72] a J. Liu, S. Chen, D. Qian, B. Gautam, G. Yang, J. Zhao, J. Bergqvist, F. Zhang, W. Ma, H. Ade, O. Inganäs, K. Gundogdu, F. Gao, H. Yan, *Nature Energy* **2016**, *1*, 16089; b J. Benduhn, K. Tvingstedt, F. Piersimoni, S. Ullbrich, Y. Fan, M. Tropiano, K. A. McGarry, O. Zeika, M. K. Riede, C. J. Douglas, S. Barlow, S. R. Marder, D. Neher, D. Spoltore, K. Vandewal, **2017**, *2*, 17053; c D. Qian, Z. Zheng, H. Yao, W. Tress, T. R. Hopper, S. Chen, S. Li, J. Liu, S. Chen, J. Zhang, X.-K. Liu, B. Gao, L. Ouyang, Y. Jin, G. Pozina, I. A. Buyanova, W. M. Chen, O. Inganäs, V. Coropceanu, J.-L. Bredas, H. Yan, J. Hou, F. Zhang, A. A. Bakulin, F. Gao, *Nature Materials* **2018**, *17*, 703-709.
- [73] S. Dong, T. Jia, K. Zhang, J. Jing, F. Huang, *Joule* **2020**, *4*, 2004-2016.
- [74] a S. Zhang, L. Zuo, J. Chen, Z. Zhang, J. Mai, T.-K. Lau, X. Lu, M. Shi, H. Chen, *Journal of Materials Chemistry A* **2016**, *4*, 1702-1707; b L. Ye, X. Jiao, S. Zhang, H. Yao, Y. Qin, H. Ade, J. Hou, *Advanced Energy Materials* **2017**, *7*, 1601138; c Y. Yang, W. Chen, L. Dou, W.-H. Chang, H.-S. Duan, B. Bob, G. Li, Y. Yang, *Nature Photonics* **2015**, *9*, 190; d L. Yang, S. Zhang, C. He, J. Zhang, Y. Yang, J. Zhu, Y. Cui, W. Zhao, H. Zhang, Y. Zhang, Z. Wei, J. Hou, *Chemistry of Materials* **2018**, *30*, 2129-2134; e D. Yang, H. Sasabe, T. Sano, J. Kido, *ACS Energy Letters* **2017**, *2*, 2021-2025; f C. Wang, X. Xu, W. Zhang, J. Bergqvist, Y. Xia, X. Meng, K. Bini, W. Ma, A. Yartsev, K. Vandewal, M. R. Andersson, O. Inganäs, M. Fahlman, E. Wang, *Advanced Energy Materials* **2016**, *6*, 1600148; g G. Li, W.-H. Chang, Y. Yang, *Nature Reviews Materials* **2017**, *2*, 17043; h H. Choi, S.-J. Ko, T. Kim, P.-O. Morin, B. Walker, B. H. Lee, M. Leclerc, J. Y. Kim, A. J. Heeger, *Advanced Materials* **2015**, *27*, 3318-3324; i R. S. Ashraf, I. Meager, M. Nikolka, M. Kirkus, M. Planells, B. C. Schroeder, S. Holliday, M. Hurhangee, C. B. Nielsen, H. Sirringhaus, I. McCulloch, *Journal of the American Chemical Society* **2015**, *137*, 1314-1321; j Y. Liu, P. Cheng, T. Li, R. Wang, Y. Li, S.-Y. Chang, Y. Zhu, H.-W. Cheng, K.-H. Wei, X. Zhan, B. Sun, Y. Yang, *ACS Nano* **2019**, *13*, 1071-1077; k Z. Yao, X. Liao, K. Gao, F. Lin, X. Xu, X. Shi, L. Zuo, F. Liu, Y. Chen, A. K. Y. Jen, *Journal of the American Chemical Society* **2018**, *140*, 2054-2057; l Y. Chen, R. Cao, H. Liu, M. L. Keshtov, E. N. Koukaras, H. Dahiya, Y. Zou, G. D. Sharma, *Sustainable Energy & Fuels* **2020**; m H. Yao, Y. Cui, R. Yu, B. Gao, H. Zhang, J. Hou, *Angewandte Chemie International Edition* **2017**, *56*, 3045-3049; n J. Sun, X. Ma, Z. Zhang, J. Yu, J. Zhou, X. Yin, L. Yang, R. Geng, R. Zhu, F. Zhang, W. Tang, *Advanced Materials*, *0*, 1707150; o Z. Xiao, X. Jia, D. Li, S. Wang, X.

References

- Geng, F. Liu, J. Chen, S. Yang, T. P. Russell, L. Ding, *Science Bulletin* **2017**, *62*, 1494-1496; p S. Dai, T. Li, W. Wang, Y. Xiao, T. K. Lau, Z. Li, K. Liu, X. Lu, X. Zhan, *Advanced Materials* **2018**, *30*, 1706571; q Y. Cui, C. Yang, H. Yao, J. Zhu, Y. Wang, G. Jia, F. Gao, J. Hou, *Advanced Materials* **2017**, *29*, 1703080.
- [75] J. Song, E. Zheng, J. Bian, X.-F. Wang, W. Tian, Y. Sanehira, T. Miyasaka, *Journal of Materials Chemistry A* **2015**, *3*, 10837-10844.
- [76] A. R. b. Mohd Yusoff, H. P. Kim, J. Jang, *Solar Energy Materials and Solar Cells* **2013**, *109*, 63-69.
- [77] L. Safriani, Risdiana, Fitriawati, M. Manawan, A. Bahtiar, A. Aprilia, D. P. Sari, J. Angel, I. Watanabe, *Journal of Physics: Conference Series* **2018**, *1080*, 012011.
- [78] A. Nagata, T. Oku, K. Kikuchi, A. Suzuki, Y. Yamasaki, E. Osawa, *Progress in Natural Science: Materials International* **2010**, *20*, 38-43.
- [79] C.-C. Chueh, C.-Z. Li, A. K. Y. Jen, *Energy & Environmental Science* **2015**, *8*, 1160-1189.
- [80] Y. Wang, Q. Liang, J. Huang, D. Ma, Y. Jiao, *RSC Advances* **2017**, *7*, 28494-28498.
- [81] X. Fan, W. Nie, H. Tsai, N. Wang, H. Huang, Y. Cheng, R. Wen, L. Ma, F. Yan, Y. Xia, *Adv. Sci.* **2019**, *6*, 1900813.
- [82] J. Meyer, A. Kahn, *Journal of Photonics for Energy* **2011**, *1*, 011109.
- [83] S. Takahashi, S. E. Milward, W. Yamori, J. R. Evans, W. Hillier, M. R. Badger, *Plant Physiology* **2010**, *153*, 988-993.
- [84] a M. O. Reese, S. A. Gevorgyan, M. Jørgensen, E. Bundgaard, S. R. Kurtz, D. S. Ginley, D. C. Olson, M. T. Lloyd, P. Morvillo, E. A. Katz, A. Elschner, O. Haillant, T. R. Currier, V. Shrotriya, M. Hermenau, M. Riede, K. R. Kirov, G. Trimmel, T. Rath, O. Inganäs, F. Zhang, M. Andersson, K. Tvingstedt, M. Lira-Cantu, D. Laird, C. McGuinness, S. Gowrisanker, M. Pannone, M. Xiao, J. Hauch, R. Steim, D. M. DeLongchamp, R. Rösch, H. Hoppe, N. Espinosa, A. Urbina, G. Yaman-Uzunoglu, J.-B. Bonekamp, A. J. J. M. van Breemen, C. Girotto, E. Voroshazi, F. C. Krebs, *Solar Energy Materials and Solar Cells* **2011**, *95*, 1253-1267; b M. V. Khenkin, E. A. Katz, A. Abate, G. Bardizza, J. J. Berry, C. Brabec, F. Brunetti, V. Bulović, Q. Burlingame, A. Di Carlo, R. Cheacharoen, Y.-B. Cheng, A. Colmann, S. Cros, K. Domanski, M. Duszka, C. J. Fell, S. R. Forrest, Y. Galagan, D. Di Girolamo, M. Grätzel, A. Hagfeldt, E. von Hauff, H. Hoppe, J. Kettle, H. Köbler, M. S. Leite, S. Liu, Y.-L. Loo, J. M. Luther, C.-Q. Ma, M. Madsen, M. Manceau, M. Matheron, M. McGehee, R. Meitzner, M. K. Nazeeruddin, A. F. Nogueira, Ç. Odabaşı, A. Osherov, N.-G. Park, M. O. Reese, F. De Rossi, M. Saliba, U. S. Schubert, H. J. Snaith, S. D. Stranks, W. Tress, P. A. Troshin, V. Turkovic, S. Veenstra, I. Visoly-Fisher, A. Walsh, T. Watson, H. Xie, R. Yıldırım, S. M. Zakeeruddin, K. Zhu, M. Lira-Cantu, *Nature Energy* **2020**, *5*, 35-49.
- [85] M. Seeland, R. Roesch, H. Hoppe, *Journal of Applied Physics* **2011**, *109*.
- [86] A. Elschner, *Solar Energy Materials and Solar Cells* **2011**, *95*, 1333-1338.
- [87] a M. V. Madsen, T. Tromholt, A. Böttiger, J. W. Andreasen, K. Norrman, F. C. Krebs, *Polymer Degradation and Stability* **2012**, *97*, 2412-2417; b d. Z. M. A. Diaz, M. Armantas, R. Stephan, B. Olof, N. Lars, E. Paul, O. Eva, A. T. D., I. Olle, M. Christian, *Advanced Materials* **2015**, *27*, 7325-7331.
- [88] I. T. Sachs-Quintana, T. Heumüller, W. R. Mateker, D. E. Orozco, R. Cheacharoen, S. Sweetnam, C. J. Brabec, M. D. McGehee, *Advanced Functional Materials* **2014**, *24*, 3978-3985.
- [89] a T. Kirchartz, F. Deledalle, P. S. Tuladhar, J. R. Durrant, J. Nelson, *The Journal of Physical Chemistry Letters* **2013**, *4*, 2371-2376; b T. Kirchartz, B. E. Pieters, J. Kirkpatrick, U. Rau,

References

- J. Nelson, *Physical Review B* **2011**, *83*, 115209; c T. Kirchartz, J. Nelson, *Physical Review B* **2012**, *86*, 165201.
- [90] a C. H. Peters, I. T. Sachs-Quintana, W. R. Mateker, T. Heumueller, J. Rivnay, R. Noriega, Z. M. Beiley, E. T. Hoke, A. Salleo, M. D. McGehee, *Advanced Materials* **2012**, *24*, 663-668; b T. Heumueller, T. M. Burke, W. R. Mateker, I. T. Sachs-Quintana, K. Vandewal, C. J. Brabec, M. D. McGehee, *Advanced Energy Materials* **2015**, *5*, 1500111.

Publication List

Publication List

Peer-reviewed publications

- [1] 2016 R. Meitzner, S.-H. Schulze, Method for determination of parameters for moisture simulations in photovoltaic modules and glass laminates, *Solar Energy Materials and Solar Cells*, in *Solar Energy Materials and Solar Cells*, 144, 23-28
- [2] 2017 S.-H. Schulze, C. Ehrich, R. Meitzner, M. Pander, Helium permeation as a fast quality indicator for barrier properties of solar cell encapsulates, *Progress in Photovoltaics*, 1-8
- [3] 2018 S. Alam, R. Meitzner, C. Kästner, C. Ulbricht, S. Höppener, D. A. M. Egbe, U. S. Schubert, H. Hoppe, Controlling donor crystallinity and phase separation in bulk heterojunction solar cells by the introduction of orthogonal solvent additives, *MRS Advances*, 2018, 1891-1900, DOI: 10.1557/adv.2018.436
- [4] 2018 P. Apilo, M. Välimäki, R. Po, K.-L. Väisänen, H. Richter, M. Ylikunnari, M. Vilkmann, A. Bernardi, G. Corso, H. Hoppe, R. Roesch, R. Meitzner, U. S. Schubert, J. Hast, Fully Roll-to-Roll Printed P3HT/Indene-C60-Bisadduct Modules with High Open-Circuit Voltage and Efficiency, *Solar RRL*, 1700160, DOI: 10.1002/solr.20170016
- [5] 2018 S. Alam, R. Meitzner, O. V. Nwadiaru, C. Friebe, J. Cann, J. Ahner, C. Ulbricht, Z. Kan, S. Höppener, M. D. Hager, D. A. M. Egbe, G. C. Welch, F. Laquai, H. Hoppe, Organic solar cells based on anthracene-containing PPE-PPVs and non-fullerene acceptors, *Chemical Papers*, DOI: 10.1007/s11696-018-0466-y
- [6] 2019 S. Alam, A. Gavrik, R. Meitzner, S. Hoepfener, V. Dyankonov, A. Baumann, U. S. Schubert, H. Hoppe, Thermally Induced Degradation of PBDTTT-CT:PCBM Based Polymer Solar Cells, *Journal of Physics D: Applied Physics*, Accepted Manuscript
- [7] 2019 R. Meitzner, T. Faber, S. Alam, A. Anand, R. Roesch, M. Büttner, F. Hermann-Westendorf, M. Presselt, L. Ciammaruchi, I. Visoly-Fisher, S. Veenstra, A. Diaz de Zerio, X. Xu, E. Wang, C. Müller, P. Troshin, M. D. Hager, S. Köhn, M. Dusza, M. Krassas, S. Züfle, E. Kymakis, E. A. Katz, S. Bersonn, F. Granek, M. Manceau, F. Brunetti, G. Polino, U. S. Schubert, M. Lira-Cantu, H. Hoppe, Impact of P3HT materials properties and layer architecture on OPV device stability, *Solar Energy Materials and Solar Cells*, November 2019, Volume 202, 110151
- [8] 2020 Mark V. Khenkin, Eugene A. Katz, Antonio Abate, Giorgio Bardizza, Joseph J. Berry, Christoph J. Brabec, Francesca Brunetti, Vladimir Bulović, Quinn Burlingame, Aldo Di Carlo, Rongrong Cheacharoen, Yi-Bing Cheng, Alexander Colsmann, Stephane Cros, Konrad Domanski, Michał Dusza, Christopher J. Fell, Stephen R. Forrest, Yulia Galagan, Diego Di Girolamo, Michael Grätzel, Anders Hagfeldt, Elizabeth von Hauff, Harald Hoppe, Jeff Kettle, Hans Köbler, Marina S. Leite, Shengzhong (Frank) Liu, Yueh-Lin Loo, Joey M. Luther, Chang-Qi Ma, Morten Madsen, Matthieu Manceau, Muriel Matheron, Michael McGehee, Rico Meitzner, Mohammad Khaja Nazeeruddin, Ana Flavia Nogueira, Çağla Odabaşı, Anna Osherov, Nam-Gyu Park, Matthew O. Reese, Francesca De Rossi, Michael

Publication List

- Saliba, Ulrich S. Schubert, Henry J. Snaith, Samuel D. Stranks, Wolfgang Tress, Pavel A. Troshin, Vida Turkovic, Sjoerd Veenstra, Iris Visoly-Fisher, Aron Walsh, Trystan Watson, Haibing Xie, Ramazan Yıldırım, Shaik Mohammed Zakeeruddin, Kai Zhu and Monica Lira-Cantu, Consensus statement for Stability Assessment and Reporting for Perovskite Photovoltaics based on ISOS procedures, *Nature Energy*, 2020, 5, 35-49
- [9] 2020 Shahidul Alam, Md. Moidul Islam, Shadia Chowdhury, Rico Meitzner, Christian Kästner, Ulrich S. Schubert and Harald Hoppe, Disentanglement of Degradation Mechanisms by Analyzing Aging Dynamics of Environmentally Friendly Processed Polymer Solar Cells, *Energy Technology*, 2020, 8, 2000116
- [10] 2020 Rico Meitzner, Juliette Essomba, Shahidul Alam, Aman Anand, Nora Engel, Kevin Fulbert, Krisna Kuma, Fernanda Ayuyasmin, Md Moidul Islam, Chikezie Ugokwe, Ulrich S. Schubert, Harald Hoppe, Performance and Stability of Organic Solar Cells bearing Nitrogen Containing Electron Extraction Layers, *Energy Technology*, 2020, 8, 12, 2000117
- [11] 2021 Rico Meitzner, Ulrich S. Schubert, Harald Hoppe, Agrivoltaics—The Perfect Fit for the Future of Organic Photovoltaics, *Advanced Energy Materials*, 2021, 11, 2002551
- [12] 2021 Aman Anand, Md Moidul Islam, Rico Meitzner, Ulrich S. Schubert, Harald Hoppe, Introduction of a Novel Figure of Merit for the Assessment of Transparent Conductive Electrodes in Photovoltaics: Exact and Approximate Form, *Advanced Energy Materials*, 2021, 2100875
- [13] 2021 Andrew J Clarke, Joel Luke, Rico Meitzner, Jiaying Wu, Yuming Wang, Harrison KH Lee, Emily M Speller, Helen Bristow, Hyojung Cha, Michael J Newman, Katherine Hooper, Alex Evans, Feng Gao, Harald Hoppe, Iain McCulloch, Ulrich S Schubert, Trystan M Watson, James R Durrant, Wing C Tsoi, Ji-Seon Kim, Zhe Li, Non-fullerene acceptor photostability and its impact on organic solar cell lifetime, *Cell Reports Physical Science*, 2021, 7, 100498
- [14] 2021 Shahidul Alam, Vojtech Nádaždy, Tomáš Váry, Christian Friebe, Rico Meitzner, Johannes Ahner, Aman Anand, Safakath Karuthedath, Catherine SP De Castro, Clemens Göhler, Stefanie Dietz, Jonathan Cann, Christian Kästner, Alexander Konkin, Wichard Beenken, Arthur Markus Anton, Christoph Ulbricht, Andreas Sperlich, Martin D Hager, Uwe Ritter, Friedrich Kremer, Oliver Brüggemann, Ulrich S Schubert, Daniel AM Egbe, Gregory C Welch, Vladimir Dyakonov, Carsten Deibel, Frédéric Laquai, Harald Hoppe, Uphill and downhill charge generation from charge transfer to charge separated states in organic solar cells, *Journal of Materials Chemistry C*, 2021, 40, 14463-14489
- [15] 2021 Aurelien Sokeng Djoumessi, Shahidul Alam, Jose Prince Madalaimuthu, Aman Anand, Josef Slowik, Theo Pflug, Rico Meitzner, Roland Roesch, Enrico Gnecco, Alexander Horn, Ulrich S. Schubert, Harald Hoppe, Improved Hole Extraction Selectivity of Polymer Solar Cells by Combining PEDOT:PSS with WO₃, *Energy Technology*, 2021, 12, 2100474

Publication List

- [16] 2022 Rico Meitzner, Jose Prince Madalaimuthu, Shahidul Alam, Md Moidul Islam, Sebastian Peiler, Aman Anand, Johannes Ahner, Martin D. Hager, Ulrich S. Schubert, Yingping Zou, Frédéric Laquai, Harald Hoppe, An effective method of reconnoitering current-voltage (IV) characteristics of organic solar cells, *Journal of Applied Physics D*, 2022, 132, 015001
- [17] 2022 Shahidul Alam, Aman Anand, Md Moidul Islam, Rico Meitzner, Aurelien Sokeng Djoumessi, Josef Slowik, Zekarias Teklu, Peter Fischer, Christian Kästner, Jafar I Khan, Ulrich S Schubert, Frédéric Laquai, Harald Hoppe, P3HT: PCBM polymer solar cells from a didactic perspective, *Journal of Photonics for Energy*, 2022, 12, 035501
- [18] Zhuo Xu, Jose Prince Madalaimuthu, Josef Bernd Slowik, Rico Meitzner, Aman Anand, Shahidul Alam, Héctor Corte, Steffi Stumpf, Ulrich S Schubert, Harald Hoppe, Compatible Solution-Processed Interface Materials for Improved Efficiency of Polymer Solar Cells, *Advanced Materials Interfaces*, 2023, 2201740

Poster Presentation & Conference Proceedings

- [1] 2013 S.-H. Schulze, A. Apel, R. Meitzner, M. Schak, C. Ehrich, J. Schneider, Influence of Polymer Properties on Potential Induced Degradation of PV-Modules, in *Proceedings of the 28th European Photovoltaic Solar Energy Conference and Exhibition*, S. 503-507, DOI: 10.4229/28thEUPVSEC2013-1CV.2.21
- [2] 2014 S.-H. Schulze, M. Wendt, C. Ehrich, S. Henning, R. Meitzner, Correlation of Morphological and Physical Properties of Encapsulation and Back Sheet Materials After Aging, in *Proceedings of the 29th European Photovoltaic Solar Energy Conference and Exhibition*, DOI: 10.4229/EUPVSEC20142014-5BV.4.11
- [3] 2022 Rico Meitzner, Aurelien Sokeng Djoumessi, Aman Anand, Chikezie Ugokwe, Anastasia Sichwardt, Zhou Xu, Daria Miliaieva, Jan Čermák, Theo Pflug, Arthur Markus Anton, Shahidul Alam, Štěpán Stehlík, Alexander Horn, Ulrich S Schubert, Harald Hoppe, Transmission windows of charge transport layers and electrodes in highly transparent organic solar cells for agrivoltaic application, *AIP Conference Proceedings*, 2022, 2635, 080001

Acknowledgements

Acknowledgements

I would like to thank all my colleagues in AG Hoppe that supported me throughout these rough years via providing me with devices, helping me out with measurements when it was time critical, helping me out coding, when I was running into a brick wall and many other issues. Also, I want to thank all the support by the various technical staff at CEEC and ZAF, that were always very generous with repairing and manufacturing experimental setups, as well as helping out with construction and tools.

I want to thank my supervisor Dr. Hoppe for providing me the chance to do my PhD with him, as well as Prof. Schubert for the opportunity of having access to all the facilities provided by CEEC and ZAF.

Additionally, I want to thank Ulrike Kaiser and Franca Frister with helping me navigating my way in university bureaucracy, as well as Stefanie Brockel for the time when we had to cope with the labs at Zeiss.

I also wanted to thank all my friends that had to endure my complaints at how my work is driving me insane sometimes. And helped me to stay sane and gave me encouragement to stick with my thesis.

Finally, I want to thank my parents that were always willing to support me, no matter what, without their support I would not have been able to make it so far.

Declaration of Authorship / Selbstständigkeitserklärung

Declaration of Authorship / Selbstständigkeitserklärung

I certify that the work presented here is, to the best of my knowledge and belief, original and the result of my own investigations, except as acknowledged, and has not been submitted, either in part or whole, for a degree at this or any other university.

Ich erkläre, dass ich die vorliegende Arbeit selbstständig und unter Verwendung der angegebenen Hilfsmittel, persönlichen Mitteilungen und Quellen angefertigt habe.

Jena, der 11.01.2023

.....

Rico Meitzner

Publications P1 to P5

Publications P1 to P5

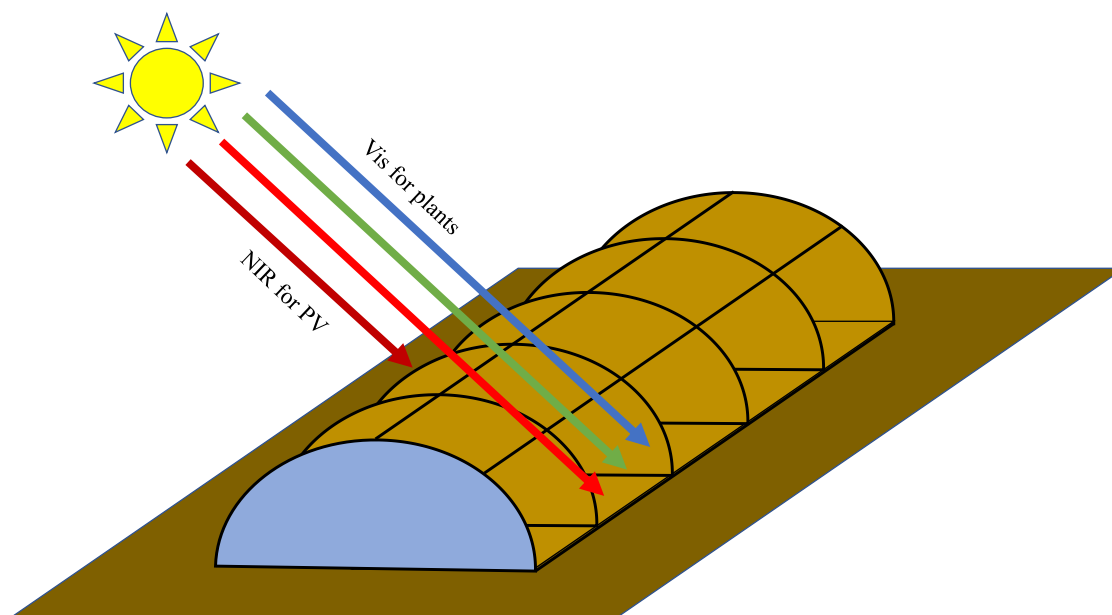
Publications P1 to P5

Publication P1

Agrivoltaics – the Perfect Fit for the Future of Organic Photovoltaics

Rico Meitzner, Ulrich S. Schubert, Harald Hoppe

Adv. Energ. Mater. **2021**, 11, 2002551



Reproduced with permission of John Wiley & Sons, Inc., Copyright © 2021.

Agrivoltaics—The Perfect Fit for the Future of Organic Photovoltaics

Rico Meitzner, Ulrich S. Schubert, and Harald Hoppe*

This Essay presents a possible pathway for the advancement of organic photovoltaics toward broader commercial success and enlarged market size. This vision aims at broad scale applications in photovoltaic greenhouses and polytunnels, which harvest those portions of the solar spectrum that are not used or required by plants. Based on the assumptions of the Shockley–Queisser–Limit, respectively detailed balance, and the additional postulation of using no absorption in the visible part of the AM 1.5G solar spectrum a power conversion efficiency of $\approx 17\%$ is theoretically predicted. The suggestion is supported by the existence of a number of organic compounds, which already exhibit a good spectral compatibility with the typical photosynthetic action spectrum of chloroplasts. It is hoped that more suitable materials development shall be triggered and fertilized as a result of this Essay.

1. Introduction

Organic photovoltaics (OPV) combines advantages like usage of earth-abundant materials, compatibility with high-throughput roll-to-roll (R2R) processing, as well as a low energy demand in production (low embedded energy cost) and thus short energy pay-back times. OPV panels can be fitted to any size, and shape (flexibility and conformity) and—evenly important—many colors. While OPV has been long-term considered as a game changer due to its potentially low prices, so far this promise did not successfully come to fruition and even might never do so with the advent of perovskite photovoltaics, which can still promise close to the same features (except for being colorful), but with significantly higher efficiencies. However, one big advantage of OPV is that it may not only be processed from environmentally friendly

R. Meitzner, Prof. U. S. Schubert, Dr. H. Hoppe
Center for Energy and Environmental Chemistry Jena (CEEC Jena)
Friedrich Schiller University Jena
Philosophenweg 7a, Jena 07743, Germany
E-mail: harald.hoppe@uni-jena.de

R. Meitzner, Prof. U. S. Schubert, Dr. H. Hoppe
Laboratory of Organic and Macromolecular Chemistry (IOMC)
Friedrich Schiller University Jena
Humboldtstrasse 10, Jena 07743, Germany

 The ORCID identification number(s) for the author(s) of this article can be found under <https://doi.org/10.1002/aenm.202002551>.

© 2020 The Authors. Advanced Energy Materials published by Wiley-VCH GmbH. This is an open access article under the terms of the Creative Commons Attribution-NonCommercial-NoDerivs License, which permits use and distribution in any medium, provided the original work is properly cited, the use is non-commercial and no modifications or adaptations are made.

The copyright line for this article was changed on 27 May 2021 after original online publication.

DOI: 10.1002/aenm.202002551

solvents but also the constituting materials do not necessarily display any harm for health or environment. On the other side, alternative existing photovoltaic technologies involve considerably more environmentally questionable and toxic chemicals in the layer stacks and their production.^[1] And such a factor may play out for applications in buildings or anywhere within reach of intelligent lifeforms or food production.

Thus, to achieve market penetration within a wide-scale and high-volume application for OPV, which would be the necessary precondition for any economies of scale and therefore major price reductions, requires finding an application, where its specific properties offer clear advantages over any other technology in the market. The internet-of-things applications could be viewed as one potential market for increased usage of OPV. However, this very market lacks behind the expectations, and thus there might be considerable doubts in the overall market size. Second, IoT may require rather small devices as compared to power applications. Hence, IoT might not offer the chance for scaling up OPV sufficiently, to obtain competitive prices for penetration into other markets. Furthermore, it is required to address the question where does OPV display an advantage over the application of silicon PV in IoT, even if costs do not matter? Thus, even though there are plenty of applications foreseeable for IoT or smart buildings, it remains a question, whether these markets could provide a breakthrough for OPV. For the latter, sheer quantity or rather sheer area of photovoltaic modules may be required. At the same time, besides silicon PV, also perovskite PV provides comparable performances with efficiencies of roughly 25% power conversion efficiency (PCE) for very small devices in the lab^[2] and 16% PCE for small modules^[3] (which may approach the size of a standard silicon solar cell). Currently, OPV is still lagging behind these numbers with above 18% for small lab-scale devices^[4] and 12% for small modules.^[3] Under such strong competition and difficult markets, the question is, what then to do with OPV?

2. The Strategy for a Way Forward

While traditional photovoltaic applications might not be in reach for a competitive product based on OPV, the situation changes, when carefully selecting an application in line with the specific advantages of OPV. At this point, we could even go one step further: what generally needs to be considered as a downside for reaching high-level power-conversion efficiencies, namely the incomplete absorption throughout a

broad wavelength range severely limiting the photocurrent generation, can even be turned into a blessing. In contrast to any inorganic semiconductor and hybrid perovskites, organic semiconductors or conjugated molecules and polymers do show over the wavelength (respectively photon energy) limited absorption bands, leaving room for the absorption of the plants below/above ≈ 730 nm/1.7 eV. The simple solution is to use this semi-transparent window of non-absorption for a combination with agriculture. Thus, using transmitted light for plant growth may essentially turn the weakness of a limited absorption band into an advantage for dual use on the same land.

In order to leave as much light as possible for the plants growing underneath the photovoltaic modules, it will be necessary to move the absorption window of the active layer material entirely away from the visible into the near-infrared (NIR) part of the electromagnetic spectrum.

The benefits from such an approach can be manifold for both sides of the equation: at first, the costs of the PV system would not need to include costs for land acquisition anymore, as the land already is in use for agriculture. Besides the immediate costs of land acquisition, which mostly impact more developed nations, there are also zoning issues that can be circumvented, as countries might forbid installation of PV on agricultural land, therefore making more land available for PV applications, which are not hundreds of kilometers away from habitation, like in entirely uninhabited deserts. As next, such a photovoltaic installation would replace traditional greenhouses as well as polytunnels, swapping these investment costs directly, by which the PV system would be made more competitive or even make the usage of greenhouses or polytunnels financially viable, where they would have been not viable before. On top of that, there is a manifold of benefits for the agricultural side of the equation that come along with a precise control of the climatic conditions for the plants. For example, in semi-arid and arid climates, where irrigation is essential for doing any agriculture, greenhouses, and polytunnels can strongly reduce evaporation losses and therefore reduce watering requirements. In addition, the electricity generation could be used to keep humidity at a stable level by the application of active ventilation systems with humidity recuperation.

Such effort is usually not done for greenhouses or polytunnels due to the additional costs for energy that would have to be provided from the outside. In turn, better controlled humidity is enabling a higher crop yield, especially for those plants, which stop photosynthesis at too low moisture levels, to prevent drying out. Such conditions normally occur in the middle of the day in warm and arid or semi-arid climates when solar irradiation is at its peak. Furthermore, a reduction in evaporation reduces the risk of soil salinization, which is till date a major problem of many areas requiring irrigation for agriculture.

These points make a deployment of transparent photovoltaic polytunnels especially attractive for developing nations in semi-arid and arid climate like Africa's countries along its and in its large deserts like the Sahara and the Namib. The same should apply also for the dryer regions of the Indian subcontinent.

Also, temperature control in these greenhouses or polytunnels would be easier, as on the one hand, the solar modules already reduce the heat influx from absorbing part of the solar irradiation, and on the other hand, part of the generated electricity could be employed for air ventilation.

In such a scenario, the photovoltaic modules would actually upgrade the value of land by its double usage. On the other hand, this application thus would also increase the available land area for utility-scale PV installations by multiples of its current amount. **Figure 1** summarizes a number of the mentioned aspects in a schematic depiction. Even if the double use is not in the focus of the consideration, locally generated electricity may provide sufficient benefit for upgrading existing greenhouses and consumers nearby.

Currently, the interest in this topic is rising and there are by now a few reports^[5] on the use of Si-PV for agrivoltaics. The challenge Si-PV is facing in this context is connected with it being in-transparent, rigid, and brittle in nature. Such installations obviously cannot cover the full area, or are only compatible with crops that require low light intensities. Furthermore, such installations are by necessity quite heavy, as they have to bear the load of full-size Si-PV modules and are thus not as quickly installable or removable. We on the other hand are advocating for installations that can be quickly installed or removed., that

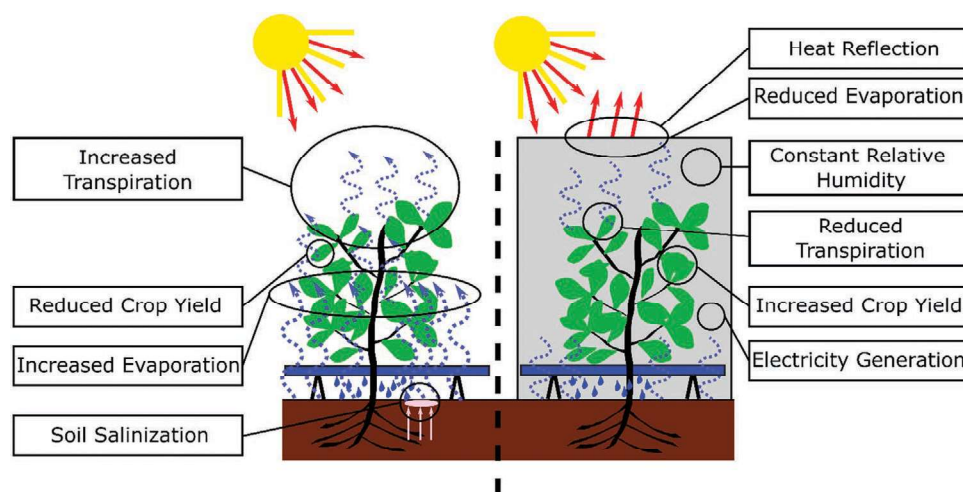


Figure 1. Schematic depiction of the advantages of the proposed agrivoltaics approach. The current situation in scenarios of irrigation dependent agriculture (left) versus the situation of an agrivoltaic application scenario (right), in which specific properties of organic photovoltaics provide a perfect match.

is, in the case of dryland agriculture, whereupon sowing irrigation is deployed and upon deployment large OPV polytunnels could be installed, that cover these fields and which can be quickly removed before harvest is due. Therefore, as the first step for OPV agrivoltaics, we advocate for deployment of OPV-polytunnels in arid and semi-arid climates to re-green deserts and other drylands and make them arable for a long-term and sustainable agriculture. The added value will be to provide access to cheap electricity to rural communities inhabiting such areas. Thus, OPV agrivoltaics could be considered as one major step toward the sustainable development goals (SDGs) of the United Nations. Due to the combination of the benefits of sustainable agriculture, reduced irrigation and water consumption as well as sustainable energy generation, obviously not only the elimination of hunger (SDG 2) and the provision of clean energy (SDG 7) follow as a direct consequence, but indirectly also most other SDGs will be positively and sustainably influenced.

The benefits from a specific OPV development for agrivoltaics could then—in a second step—be transferred toward the building-integrated OPV (BIO-PV) sector. The aforementioned transparency for plants in the visible spectrum range is obviously a benefit for energy producing building glazing.

However, since most glazing is vertical, the angle of incidence is somewhat unfavorable leading to a reduced potential in power generation. Though organic solar cells exhibit only a minor dependence of the performance on the angle of incidence as all thin film photovoltaic technologies,^[6] when the angle of incidence is basically parallel during the most sun intense hours of the day, as is the case in latitudes between

the tropic of Cancer and tropic of Capricorn, still only indirect irradiation can be collected in the middle of the day. There are also two targets for a sustainable city development, which are in direct opposition to efficient usage of any PV technology, these are densification, that is, closely built as well as taller buildings, resulting in mutual shading between buildings. The other target is vertical gardens along facades of buildings,^[7] these obviously would compete with space for solar energy generation, though this actually could be alleviated with the developments that have to be made for organic agrivoltaics. While in dense cities potentially compromises will have to be made, BIO-PV applications will certainly benefit from the herein promoted agrivoltaics with OPV.

3. Limits, Current Status, and Next Steps

As we have now laid out our vision for a bright future of OPV, it is time to assess, which parameters such technology should have. The properties are largely determined by the necessities of plants to be able to have as much light as possible for photosynthesis. This requires high transparency of the photovoltaic module in the range between 1.77 to 3.55 eV, as this is the region of the solar spectrum where the photosynthetic activity takes place. Based on the general idea of the Shockley–Queisser–Limit for photovoltaics, that is, a box-shaped external quantum efficiency, we calculated the maximally obtainable efficiency for such given limitations. A very encouraging efficiency of $\approx 17\%$ at a bandgap of 1.125 eV displays a local theoretical limit, see **Figure 2**.

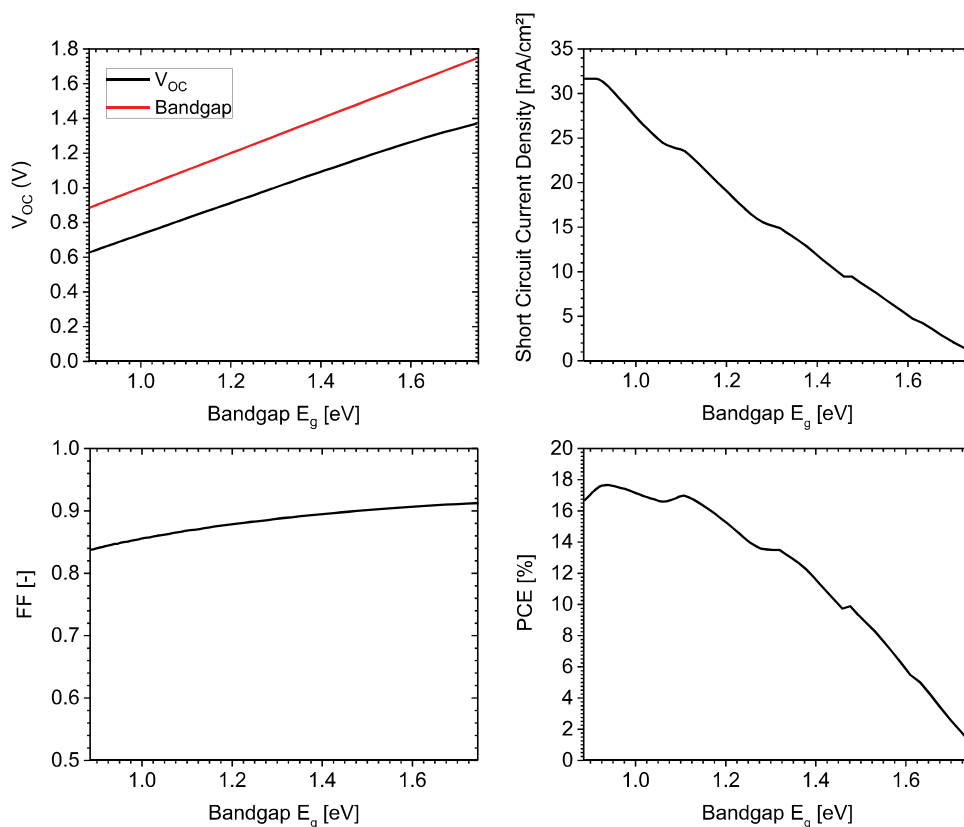


Figure 2. Photovoltaic parameters (short circuit photocurrent, open circuit voltage, fill factor) and resulting power conversion efficiency for a solar cell based on the Shockley–Queisser–Limit for an absorption window starting with an onset energy (band gap) given by the x-axis of the graph and ending at 1.77 eV.

Note that this is not the global maximum, but since smaller bandgap organic semiconductors should exhibit a higher relative energy loss, it should be the more smart choice. These results were obtained by using the following equations for calculation.

$$J_{SC} = q \int_{E_g}^{1.77\text{eV}} \phi_{\text{Sun}}(E) dE \quad (1)$$

$$J_0 = q \int_{E_g}^{1.77\text{eV}} \phi_{\text{bb}}(E, T = 300\text{ K}) dE \quad (2)$$

$$V_{OC} = \frac{kT}{q} \ln \left(\frac{J_{SC}}{J_0} + 1 \right) \quad (3)$$

$$J = J_0 \left[\exp \left(\frac{qV}{kT} \right) - 1 \right] - J_{SC} \quad (4)$$

While the Shockley–Queisser–Limit has to be regarded as the ultimate limit for application of photovoltaics in agriculture, it should be mentioned here that additional losses may apply for OPV due to the specific properties of organic semiconductors. This performance loss by in total few absolute percent does originate from energy, respectively open circuit voltage (V_{OC}), losses which may be attributed to a) considerable exciton binding energies, which have to be overcome for successful charge generation processes and to b) increased recombination losses in organic solar cells of smaller bandgap, due to the overlap of the vibronic energy levels of the ground state, which may interfere more severely with the charge transfer state at the decisive charge separating step (compare with Benduhn et al.).^[8] While the first may result either in smaller photocurrent or photovoltage, the latter adds to the non-radiative losses of solar cells and thus to a reduced V_{OC} .

With these given constraints, where are we at the moment? In **Figure 3** the chemical structures of various low bandgap active layer materials are shown and in **Figure 4** their normalized absorbance is plotted in comparison to the normalized photosynthetic activity of a chloroplast of a green plant. Among these are a few candidates that already show a very minor overlap with the spectrum of chloroplasts: only one is found among the electron donors: C3-DPPTT-Te.^[9] In case of electron acceptors, there are indeed several candidates that are suitable: IEICO-4F,^[10] IEICO-4Cl,^[11] IXIC-4Cl,^[12] Y14,^[13] and DTPC-DFIC.^[14] The latter represents an interesting special case, as it exhibits a second absorption peak matching closely to the spectral region where chloroplasts have an activity minimum. This might allow for a correspondingly higher photocurrent and performance, with only minor detriment to plant growth. As all of these materials exhibit a small spectral overlap with the chloroplast absorption, they do not yet present a perfect fit. Thus, organic chemists are invited and invoked to develop new electron donors and acceptors, which will fulfill the requirement of exhibiting a sufficiently large absorption window to be employed for plant growth.

Besides the optical requirements for the photoactive layer, it will be of high importance to develop semi-transparent

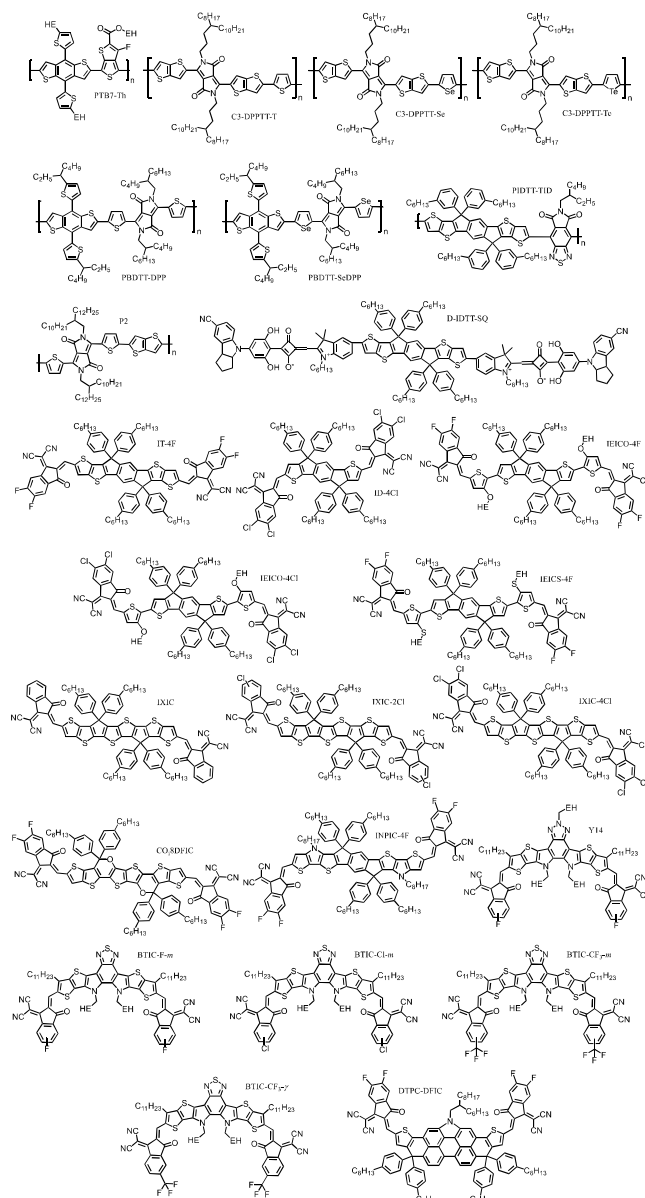


Figure 3. Chemical structures of various low bandgap donors and acceptors reported throughout the literature.^[9–15] EH: Ethylhexyl.

electrode materials which provide significantly increased transmission in the NIR spectral range (specifically between 1.13 and 3.5 eV) as compared to the existing ones. Hence, we see the development of such materials that fulfill these requirements as an important additional challenge, which should be tackled to reach a bright future for OPV.

In summary, three important design parameters result from the above consideration:

1. Active layer materials ideally show an absorption window between 1.13 to 1.77 eV
2. Charge transport layers and transparent electrodes should be transmitting the light in the range of 1.13 to 3.5 eV
3. Transparent electrodes have to replace opaque ones and current collectors are to be minimized in area

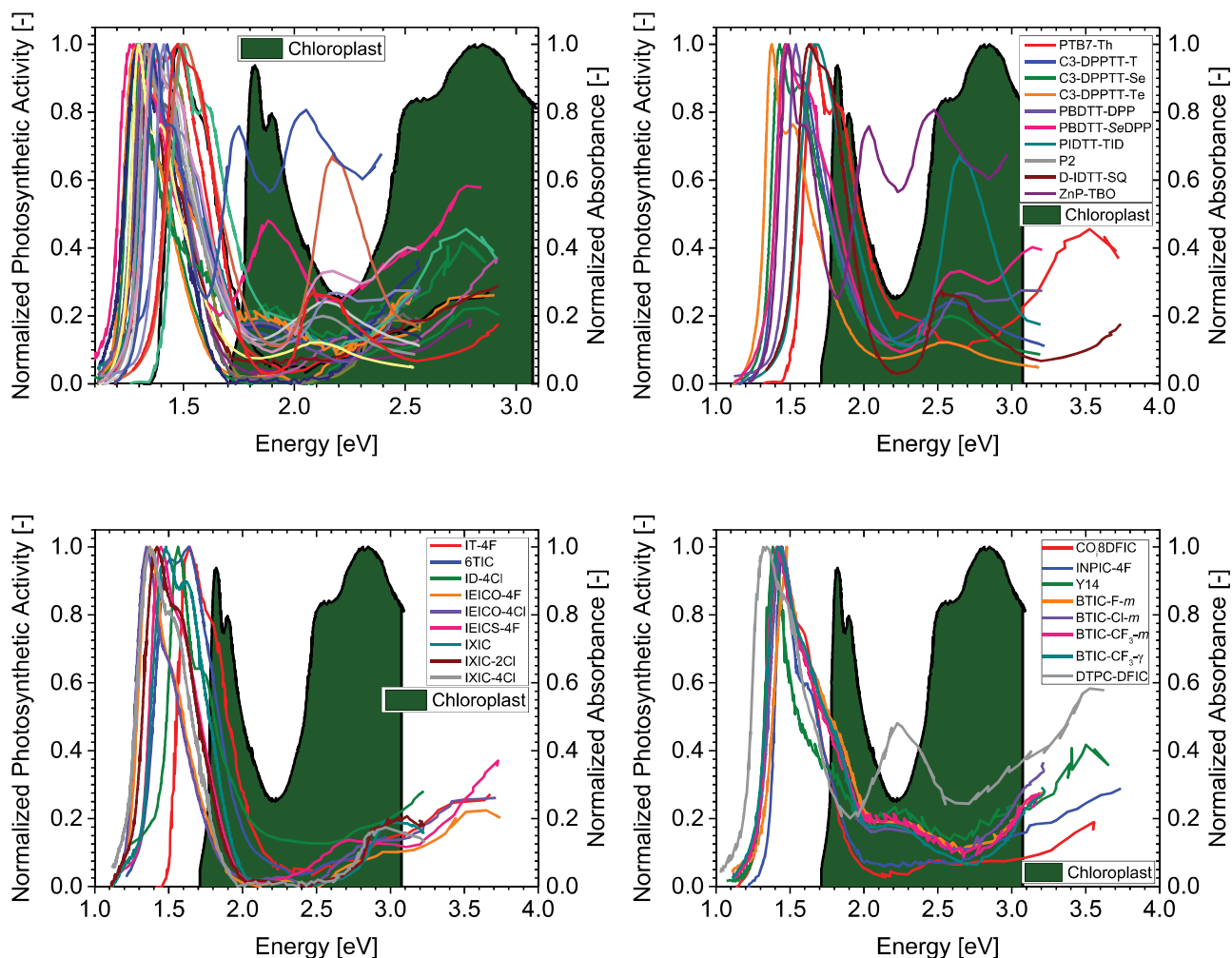


Figure 4. Photosynthetic action spectrum of a Chloroplast (dark green) and normalized absorbance spectra of different low bandgap donors and non-fullerene acceptors that are reported in the literature.^[9–16]

4. Conclusion

In conclusion, employing OPV for agricultural greenhouses and polytunnels may be the key for a proper market development of this PV-technology, since all the properties—may it official be an advantage or disadvantage—of organic solar modules could be played outright: The device flexibility resulting from the low total thickness of the layer stack will enable its application in a similar way as polytunnels, being used today in agriculture. If the absorption range of such active layer materials is placed properly around those of the plants, the situation shifts from competition to synergism, as part of the energy provided by the photovoltaic system could be used to have better controlled humidity levels and temperatures inside greenhouses and polytunnels. Finally, such easy to install agrivoltaic units could contribute beyond the means of food production toward sustainable development in rural areas that suffer from aridity, by providing clean energy to the communities around.

Acknowledgements

Open access funding enabled and organized by Projekt DEAL.

Conflict of Interest

The authors declare no conflict of interest.

Keywords

agriculture, agrivoltaics, efficiency limit, organic photovoltaics, sustainability

Received: August 7, 2020
Revised: October 15, 2020
Published online: November 17, 2020

[1] a) NIH evaluation of CdTe, https://ntp.niehs.nih.gov/ntp/htdocs/chem_background/exsumpdf/cdte_508.pdf (accessed: September 2020); b) *MSDS Cadmium Telluride*, <https://www.fishersci.com/store/msds?partNumber=AA1436703&productDescription=CADMIUM+TELLURIDE%2C+99.999%25+1G&vendorId=VN00024248&countryCode=US&language=en> (accessed: September 2020);

- c) *MSDS Hydrofluoric Acid*, <https://www.nano.pitt.edu/sites/default/files/MSDS/Acids/Hydrofluoric%20Acid.pdf> (accessed: September 2020); d) *MSDS Arsine*, <https://www.airgas.com/msds/001217.pdf> (accessed: September 2020); e) *MSDS Phosphine*, https://produkte.linde-gas.at/sdb_konform/PH3_10021727EN.pdf (accessed: September 2020); f) *Phosphorous Oxychloride*, <https://www.sigmaaldrich.com/MSDS/MSDS/DisplayMSDSPage.do?country=DE&language=EN-generic&productNumber=262099&brand=ALDRICH&PageToGoToURL=https%3A%2F%2Fwww.sigmaaldrich.com%2Fcatalog%2Fproduct%2Faldrich%2F262099%3Flang%3Dde> (accessed: November 2020); g) N. Hadrup, A. K. Sharma, K. Loeschner, *Regul. Toxicol. Pharmacol.* **2018**, *98*, 257; h) Z. Ferdous, A. Nemmar, *Int. J. Mol. Sci.* **2020**, *21*, 2375.
- [2] NREL Solar Cell Chart: <https://www.nrel.gov/pv/assets/pdfs/best-research-cell-efficiencies.20200925.pdf> (accessed: May 2020).
- [3] NREL Module Efficiency Chart: <https://www.nrel.gov/pv/assets/pdfs/champion-module-efficiencies.20200708.pdf> (accessed: May 2020).
- [4] Q. Liu, Y. Jiang, K. Jin, J. Qin, J. Xu, W. Li, J. Xiong, J. Liu, Z. Xiao, K. Sun, S. Yang, X. Zhang, L. Ding, *Sci. Bull.* **2020**, *65*, 272.
- [5] a) E. H. Adeh, S. P. Good, M. Calaf, C. W. Higgins, *Sci. Rep.* **2019**, *9*, 11442; b) E. Hassanpour Adeh, J. S. Selker, C. W. Higgins, *PLoS One* **2018**, *13*, e0203256; c) www.agrophotovoltaik.de (accessed: May 2020).
- [6] a) M. S. S. Rahman, M. K. Alam, *AIP Adv.* **2017**, *7*, 065101; b) T. Adrada Guerra, J. Amador Guerra, B. Orfao Tabernero, G. De La Cruz García, *Energies* **2017**, *10*, 772.
- [7] C. Abel, *Counc. Tall Build. Urban Habitat* **2010**, *5*, 20.
- [8] J. Benduhn, K. Tvingstedt, F. Piersimoni, S. Ullbrich, Y. Fan, M. Tropicano, K. A. McGarry, O. Zeika, M. K. Riede, C. J. Douglas, S. Barlow, S. R. Marder, D. Neher, D. Spoltore, K. Vandewal, *Nat. Energy* **2017**, *2*, 17053.
- [9] R. S. Ashraf, I. Meager, M. Nikolka, M. Kirkus, M. Planells, B. C. Schroeder, S. Holliday, M. Hurhangee, C. B. Nielsen, H. Siringhaus, I. McCulloch, *J. Am. Chem. Soc.* **2015**, *137*, 1314.
- [10] H. Yao, Y. Cui, R. Yu, B. Gao, H. Zhang, J. Hou, *Angew. Chem., Int. Ed.* **2017**, *56*, 3045.
- [11] Y. Cui, C. Yang, H. Yao, J. Zhu, Y. Wang, G. Jia, F. Gao, J. Hou, *Adv. Mater.* **2017**, *29*, 1703080.
- [12] Y. Chen, T. Liu, H. Hu, T. Ma, J. Y. L. Lai, J. Zhang, H. Ade, H. Yan, *Adv. Energy Mater.* **2018**, *8*, 1801203.
- [13] M. Luo, C. Zhao, J. Yuan, J. Hai, F. Cai, Y. Hu, H. Peng, Y. Bai, Z. Tan, Y. Zou, *Mater. Chem. Front.* **2019**, *3*, 2483.
- [14] Z. Yao, X. Liao, K. Gao, F. Lin, X. Xu, X. Shi, L. Zuo, F. Liu, Y. Chen, A. K.-Y. Jen, *J. Am. Chem. Soc.* **2018**, *140*, 2054.
- [15] a) S. Chen, H. Yao, B. Hu, G. Zhang, L. Arunagiri, L.-K. Ma, J. Huang, J. Zhang, Z. Zhu, F. Bai, W. Ma, H. Yan, *Adv. Energy Mater.* **2018**, *8*, 1800529; b) H. Choi, S.-J. Ko, T. Kim, P.-O. Morin, B. Walker, B. H. Lee, M. Leclerc, J. Y. Kim, A. J. Heeger, *Adv. Mater.* **2015**, *27*, 3318; c) H. Lai, Q. Zhao, Z. Chen, H. Chen, P. Chao, Y. Zhu, Y. Lang, N. Zhen, D. Mo, Y. Zhang, F. He, *Joule* **2020**, *4*, 688; d) X. Li, H. Meng, F. Shen, D. Su, S. Huo, J. Shan, J. Huang, C. Zhan, *Dyes Pigm.* **2019**, *166*, 196; e) J. Sun, X. Ma, Z. Zhang, J. Yu, J. Zhou, X. Yin, L. Yang, R. Geng, R. Zhu, F. Zhang, W. Tang, *Adv. Mater.* **2018**, *30*, 1707150; f) C. Wang, X. Xu, W. Zhang, J. Bergqvist, Y. Xia, X. Meng, K. Bini, W. Ma, A. Yartsev, K. Vandewal, M. R. Andersson, O. Inganäs, M. Fahlman, E. Wang, *Adv. Energy Mater.* **2016**, *6*, 1600148; g) Z. Xiao, X. Jia, D. Li, S. Wang, X. Geng, F. Liu, J. Chen, S. Yang, T. P. Russell, L. Ding, *Sci. Bull.* **2017**, *62*, 1494; h) D. Yang, H. Sasabe, T. Sano, J. Kido, *ACS Energy Lett.* **2017**, *2*, 2021; i) L. Yang, S. Zhang, C. He, J. Zhang, Y. Yang, J. Zhu, Y. Cui, W. Zhao, H. Zhang, Y. Zhang, Z. Wei, J. Hou, *Chem. Mater.* **2018**, *30*, 2129; j) Y. M. Yang, W. Chen, L. Dou, W.-H. Chang, H.-S. Duan, B. Bob, G. Li, Y. Yang, *Nat. Photonics* **2015**, *9*, 190.
- [16] S.-Y. Chang, P. Cheng, G. Li, Y. Yang, *Joule* **2018**, *2*, 1039.



Rico Meitzner is currently doing his Ph.D. in the group of Dr. Harald Hoppe at the Friedrich-Schiller-University Jena. His interests are in the stability and application of organic solar cells. He further focuses on the destruction-free characterization of organic semiconductor devices. Before he joined the group of Dr. Hoppe to do his Ph.D. he did research at the Fraunhofer Center for Silicon Photovoltaics in Halle on encapsulation materials for solar modules.



Ulrich S. Schubert studied chemistry in Frankfurt and Bayreuth (both Germany). His Ph.D. studies were performed at the Universities of Bayreuth and South Florida. After a post-doctoral training with J.-M. Lehn at the University of Strasbourg (France), he moved to the TU Munich (Germany) and obtained his Habilitation in 1999. During 2000–2007 he was Full-Professor at the TU Eindhoven (the Netherlands). Since 2007, he has been a Full-Professor at the Friedrich Schiller University Jena, Germany.



Harald Hoppe received his Ph.D. in 2004 from the Johannes-Kepler-University Linz, where he started his work in organic photovoltaics (OPV) by investigation of material and phase morphologies within organic bulk heterojunction blends and their impact on device properties. Thereafter he built up a research group at Ilmenau University of Technology. In 2015 he joined the Friedrich-Schiller-University of Jena at the Center for Energy and Environmental Chemistry Jena (CEEC Jena). His current research interests are materials and strategies for improved solution processing, device performance and long-term stability of OPV, as well as imaging methods for offline and inline inspection.

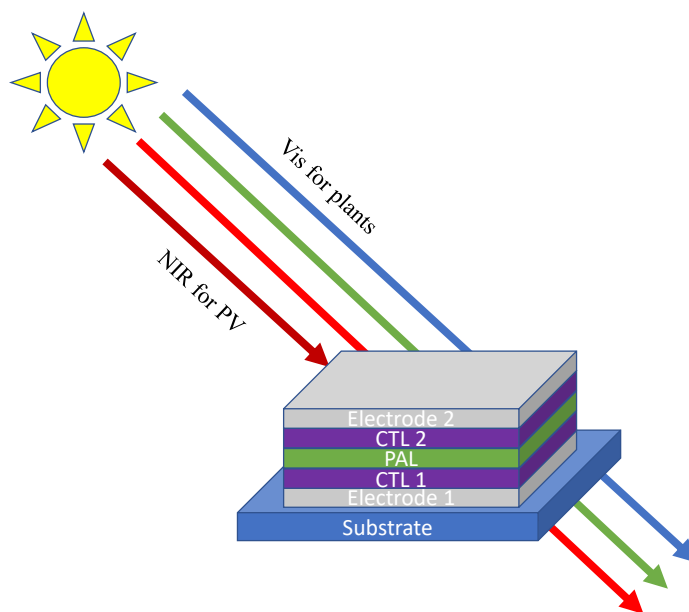
Publications P1 to P5

Publication P2

Transmission Windows of Charge Transport Layers and Electrodes in Highly Transparent Organic Solar Cells for Agrivoltaic Application

Rico Meitzner, Aurelien Sokeng Djoumessi, Aman Anand, Chikezie Ugokwe, Anastasia Sichwardt, Zhou Xu, Daria Miliiaeva, Jan Čermák, Theo Pflug, Arthur Markus Anton, Shahidul Alam, Štěpán Stehlík, Alexander Horn, Ulrich S. Schubert, Harald Hoppe

AIP Conference Proceedings **2022**, 2635, 080001



With the permission of AIP Publishing, Copyright © 2022.

Transmission Windows of Charge Transport Layers and Electrodes in Highly Transparent Organic Solar Cells for Agrivoltaic Application

Rico Meitzner^{1, 2, a)}, Aurelien Sokeng Djoumessi^{1, 2}, Aman Anand^{1, 2}, Chikezie Ugokwe^{1, 2}, Anastasia Sichwardt^{1, 2}, Zhou Xu^{1, 2}, Daria Miliaieva³, Jan Čermák³, Theo Pflug^{4, 5}, Arthur Markus Anton^{1, 2}, Shahidul Alam^{1, 2}, Štěpán Stehlík³, Alexander Horn⁴, Ulrich S. Schubert^{1, 2}, Harald Hoppe^{1, 2 b)}

¹Laboratory of Organic and Macromolecular Chemistry (IOMC), Friedrich Schiller University Jena, Humboldtstrasse 10, 07743 Jena, Germany

²Center for Energy and Environmental Chemistry Jena (CEEC Jena), Friedrich Schiller University Jena, Philosophenweg 7a, 07743 Jena, Germany

³Institute of Physics of the Czech Academy of Sciences, Na Slovance 1999/2, 182 21 Prague 8, Czech Republic

⁴Laserinstitut Hochschule Mittweida, Hochschule Mittweida Schillerstraße 10, 09648 Mittweida, Germany

⁵Institute of Physics, Chemnitz University of Technology Reichenhainer Straße 70, 09126 Chemnitz, Germany

^{a)} Corresponding author: rico.meitzner@uni-jena.de

^{b)} harald.hoppe@uni-jena.de

Abstract. Organic semiconducting materials provide only narrow absorption bands, in contrast to classical, inorganic semiconductors. Concerning photovoltaic applications this is considered as a drawback; however, in combination with plant cultivation the narrow-band absorption provides a unique advantage: Organic solar cell devices with high transparency between 1.75 and 3.5 eV can be designed, being translucent exactly in the spectral range where chlorophyll is predominantly active in natural photosynthesis. These organic photovoltaic-based agrivoltaics are called “AgrOPV”. Common active layer materials already fulfill the requirements for AgrOPV application; the suitability of the other materials used in the photovoltaic layer stack, instead, is hardly investigated and widely uncertain. In order to provide guidance for future developments, we will discuss the suitability of charge transport and electrode materials for AgrOPV applications, mainly on the basis of their absorbance.

INTRODUCTION

Organic photovoltaics (OPV) represent a promising technology with maximum lab efficiencies reaching 18%¹ and small module performances yielding up to 12%² by now, also recently extrapolated lifetimes of up to 30'000 hours have been shown³. A meaningful breach into the market has not been made so far and steep challenges are facing OPV when doing so, as we have recently argued⁴. However, this situation will change dramatically if this technology is introduced into a particular market where the capabilities of OPV are simply unrivaled. This condition is indeed satisfied for the simultaneous utilization of the same area of land when power is generated at greenhouses and polytunnels equipped with OPV in agrivoltaics (AgrOPV)⁵. According to an adapted Shockley-Queisser-Limit calculation, a maximum theoretical power conversion efficiency (PCE) of about 17.5% is within reach^{4, 6}, even though a considerable portion of the solar spectrum is not intended to be used for photovoltaics but rather for the

plants. However, the performances achievable in practice will be lower than the calculated maximum for AgrOPV, since non-radiative losses usually occur here quite severely, too. Recently we have shown that there are a lot of potential active layer materials which absorb in the range of the solar spectrum relevant for agrivoltaics, while still being highly transparent in the range of the photosynthetic action spectrum. An example for these suitable photoactive layer materials is given in the following FIGURE 1:

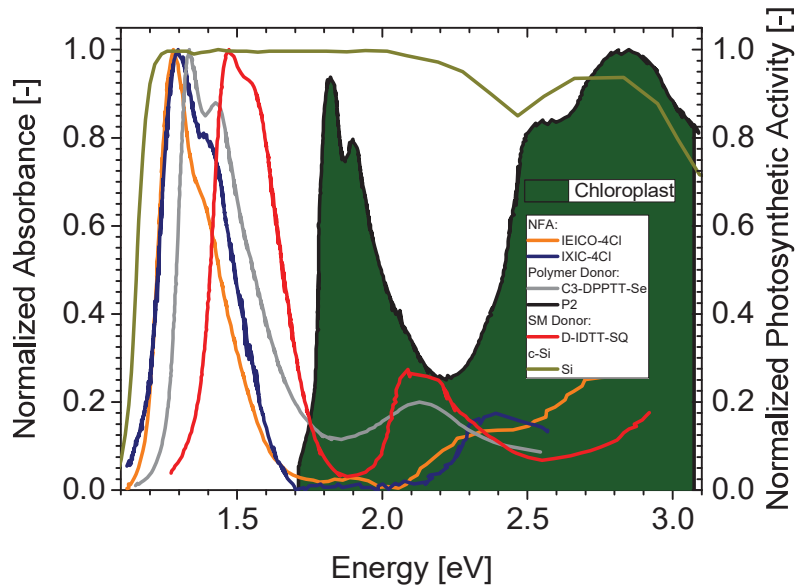


FIGURE 1. Absorbance of different low bandgap organic semiconductors, which are usable for photoactive layers in organic solar cells, as well as for silicon, compared to the photosynthetic action spectrum. (compare with Meitzner *et al.*⁴; IEICO-4CL⁷)

In addition to optical transparency of the active layer in the desired spectral range the sheet resistances of the transparent conductive electrodes (TCEs) play a major role for the device performance⁶. In contrast to well-performing organic photovoltaic devices (OPV), being assembled of an efficient active layer between a transparent front electrode (the TCE) and a highly reflective, and therefore non-transparent, back electrode, devices for AgrOPV application have to be transparent *as a whole*. In fact, all layers in the photovoltaic stack must be highly translucent in the range from 1.1 to 3.5 eV. Furthermore, for an AgrOPV module it is preferable to have a reduced transparency above 3.1 eV. At higher energies than 3.1 eV the photosystem II, which is in fact a protein complex important for photosynthesis, might be damaged. This will result in stress for the plants and, therefore, in potentially reduced crop yields. To summarize, the ideal electrode material for AgrOPV will exhibit a bandgap of 3.1 eV and hence absorb radiation of this energy or greater while being transparent for radiation of lower energy.

TABLE 1 gives a summary of the work functions of various materials for transparent electrodes and TABLE 2 lists the electronic and optoelectronic properties of various materials used as charge transport/extraction layers or as transparent electrodes for OPV. While most of these materials have been extensively used in the field of OPV, though their optical properties have not been reported over the whole range of interest for AgrOPV applications so far.

TABLE 1. Work function of commonly used materials for transparent conductive electrodes.

Transparent conductive electrode material	Work function (eV)	Reference
ITO	-4.7	8
PH1000	-5.08	9
Silver nanowires	-4.8	10
Clevios HYE	-4.85	11

TABLE 2. Electronic and optoelectronic properties of commonly used electron and hole transport/extraction layer materials.

Material	HOMO (eV)	LUMO (eV)	Band Gap (eV)	Reference
ETL/EEL				
SnO ₂	-8.0	-4.5	3.5	12
TiO _x	-8.1	-4.4	3.7	13
ZnO	-7.5	-4.2	3.3	14
PDINO	-6.21	-3.63	2.58	15
H-NDs	-5.5	-3.0	2.5	16
HTL/HEL				
MoO _x	-5.6	-2.3	3.3	17
WO ₃	-5.7	-2.2	3.5	18
PTAA (poly(triaryl amine))	-5.1	-1.8	3.3	19
NPB (<i>N,N'</i> -diphenyl-1,1'- biphenyl-4,4'-diamine)	-5.4	-2.3	3.1	20
P VP A14083	-5.2	/	/	9

Kim *et al.*²¹ reported about a composite electrode of silver nanowires (AgNWs) and aluminum-doped zinc oxide (AZO) with high transparency in the range from 1.1 to 2.75 eV and a sheet resistance of around 11 Ω/sq. Though the transparency window of this composite is smaller compared to that of the reference electrode of indium doped tin oxide (ITO) with an intrinsic zinc oxide layer (i-ZnO) (transparent in-between 1.1 and 3.1 eV), the AgNW/AZO electrode is fully solution-processable, whereas the reference is not. Wang *et al.*²² presented a similar combination of solution-processable AgNWs and AZO. They varied the AgNWs surface coverage and thereby modified the transparency as well as sheet resistance of the TCE between 10 and 150 Ω/sq. Despite the difference in transparency was rather small, the authors determined for the the lowest and highest transparency of TCEs sheet resistances of 10 and 150 Ω/sq, respectively. The authors achieved their best performing solar cells using the composite electrode with 20 Ω/sq, representing the best compromise between transmittance and conductance.

Kuwahata *et al.*²³ compared AZO/ZnO electrodes with aluminum-doped Zn_{1-x}Mg_xO (AZMO) with varying magnesium content. The authors reported an increase in the alloy AZMO bandgap ranging between 3.5 to 4.4. eV due to rising magnesium contents from nothing ($x = 0$) to $x = 0.24$. At the same time, an enhanced magnesium content gave rise to a dramatic increase in sheet resistance (from $\sim 4 \cdot 10^1$ up to $1 \cdot 10^6$ Ω/sq).

We therefore herewith provide an overview of materials commonly used for charge transport layers and transparent electrodes, reporting their optical and electrical properties for studying their suitability in agrivoltaic applications.

EXPERIMENTAL

Materials

Transparent Conducting Electrodes

ITO coated glass was purchased from Xinyan Technology Ltd (Hong Kong). The different PEDOT:PSS formulations, Clevios PH1000 and Clevios HYE were purchased from Heraeus (Germany). In order to reach high conductivity, PH1000 were mixed with 5-wt % of dimethyl sulfoxide (DMSO). Silver nanowires (AgNWs) ClearOhm® Ink-Y were purchased from Cambrios Film Solutions (China) and used as received.

Electron Transport Layers

SnO₂ solution was diluted to 2.67% v/v in distilled water from the stock solution containing Tin(IV) oxide, 15% in H₂O colloidal dispersion liquid purchased from Thermo Fisher GmbH (Germany). In order to prepare the zinc

oxide (ZnO) solution, we used a sol-gel method and mixed zinc acetate dihydrate 99,5+% (274.6 mg) purchased from Chempur (Germany) with 2-methoxyethanol (2.5 mL) and 2-aminoethanol (78 μ L) purchased from Sigma-Aldrich (Germany). The final solution was stirred vigorously overnight. The Titanium oxide (TiO_x) solution was prepared from a precursor solution and then diluted in isopropanol to 15% v/v. The polyethylenimine (PEI) solution was prepared by dissolving branched polyethylenimine (Sigma-Aldrich, Germany) in butanol for a final solution concentration of 2 mg/mL. Perylene diimide amino *N*-oxide (PDINO) was dissolved in methanol to a final concentration of 2 mg/mL. Commercially monocrystalline nanodiamonds (NDs) powder were purchased from Microdiamant AG (Switzerland). The NDs were then oxygenated through annealing in ambient air at 450 °C for 2 hours. Afterward, the annealed NDs were mixed with deionized water to a final solution concentration of 20 mg/L and ultrasonicated and centrifuged. The such-obtained O-NDs pellets were annealed in a hydrogen atmosphere at 700 °C for 3 hours to get the hydrogenated nanodiamonds (H-NDs).

Hole Transport Layers

The PEDOT:PSS formulation Clevis P VP Al4083 was purchased from Heraeus (Germany). A tungsten oxide precursor solution was prepared from tungsten(VI) ethoxide (Alfa Aesar) and methoxy ethanol. Tungsten (VI) ethoxide (270 mg) was dissolved in methoxy ethanol (75 mL) through vigorous stirring and filled into a three-necked round bottom flask, both under inert atmosphere. Next, the solution was stirred at 80 °C and 120 °C successively. Between each of these steps, heating or cooling phases of 30 minutes each were necessary, and the obtained solution was stored under an inert atmosphere. Poly[bis(4-phenyl)(2,4,6-trimethylphenyl)amine] (PTAA) was purchased from Luminescence Technology Corp. (France) and dissolved in toluene to a concentration of 2.5 mg/mL at room temperature. *N,N'*-Di-1-naphthyl-*N,N'*-diphenylbenzidine (NPB, >98% purity, Tokyo Chemical Industry Co. Ltd, Japan) was dissolved in chlorobenzene to a concentration of 2.5 mg/mL at room temperature. Molybdenum oxide pellets (MoO₃, 99.95% purity) were purchased from Kurt J. Lesker (USA) and deposited by physical vapor deposition at less than 10⁻⁶ mbar.

Film Preparation

The fabrication of the films started with cleaning bare or indium tin oxide (ITO) coated glasses (sheet resistance 8.35 Ω /sq) in an ultrasonic bath successively using toluene and isopropanol for 15 minutes each. Subsequently, the substrates were dried with a nitrogen-air blowing gun followed by argon-plasma treatment for 10 minutes before the different TCE and charge extraction materials were deposited by spin-coating. An overview of the different processing conditions and resulting film thicknesses can be found in TABLE 3. As an exception, MoO₃ was processed via physical vapor deposition (PVD).

Film Characterization

Transmittance and reflectance spectra of the films were measured using two Avantes AvaSpec-ULS3648-USB2-UA-25 fiber spectrometer. The sheet resistance was measured using a SURAGUS sheet resistance tester (EddyCus® TF lab 2020SR). While the film thickness does not necessarily have to represent the optimal conditions, it was determined by using a laser scanning microscope. In some cases, the exact film thickness could not be determined and was estimated instead (see above, Table 1).

TABLE 3. Processing parameters for different layers studied and the resulting layer thickness.

	Material	Spin condition	Annealing condition	Layer thickness (nm)	Roughness (nm)
Electrodes	PH1000	1000 rpm for 60s	120°C for 15 mins	138.0	5.4
	AgNWs	1000 rpm for 60s	120°C for 15 mins	17.8	16.0**
	HYE	1000 rpm for 60s	120°C for 15 mins	68.3	11.0
Electron transport layers (ETLs)	SnO ₂	3000 rpm for 60s	150°C for 30 mins	57.3	17.5
	ZnO	3000 rpm for 60s	170°C for 40 mins	62.0	7.0
	TiO _x	3000 rpm for 60s	110°C for 10 mins	≥10*	17.1
	PEI	3000 rpm for 60s	110°C for 5 mins	≥10*	6.1
	PDINO	3000 rpm for 60s	N/A	≥10*	3.7
	H-NDs	1500 rpm for 120s	120°C for 15 mins	23.1	44.4**
Hole transport layers (HTLs)	P VP A14083	3000 rpm for 60s	178°C for 15 mins	52.7	12.6
	WO ₃	1000 rpm for 60s	90°C for 15 mins	21.9	97.2**
	PTAA	5000 rpm for 60s	100°C for 10 mins	15.5	6.7
	NPB	5000 rpm for 60s	100°C for 10 mins	14.9	6.9
	MoO ₃ ~ 10 nm	/	/	14.8	4.6

* In some cases the films could not successfully be completely removed and the thickness was estimated.
 ** Incomplete coverage by the material, not a closed film. Hence film roughness surpassed the film thickness.

RESULTS AND DISCUSSION

Among all transparent conductive electrode (TCE) materials, silver nanowires (AgNWs) did show the highest suitability by the lowest overall absorbance in the range of photovoltaic activity (besides the base glass itself).

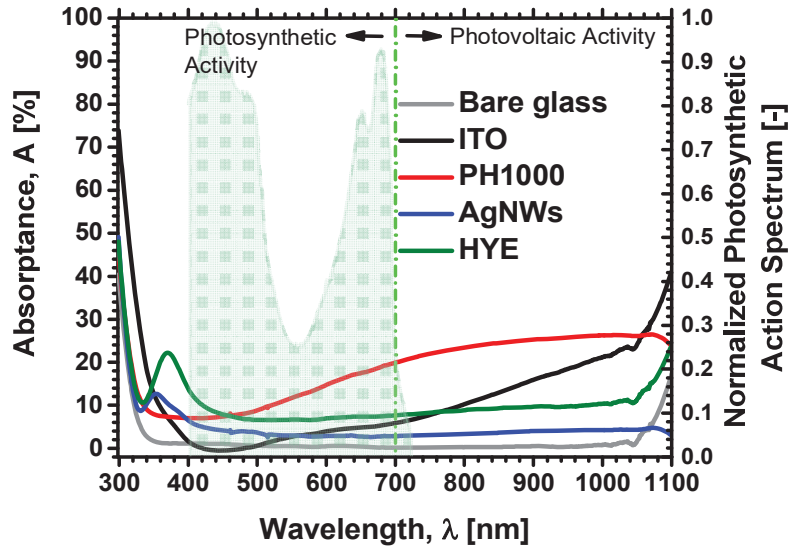


FIGURE 2. Absorbance spectra of commonly used transparent electrodes for organic solar cells. Most of the photosynthetic activity of plants occurs in the range from 400 to 700 nm, whereas in the range from 700 to 1100 nm the activity of the photovoltaic device is located.

The absorbance spectra of different commonly used TCE materials are presented in FIGURE 2. ITO shows a low absorbance in the range of the photosynthetic activity of plants (0.0 to 5.9%) but an increasing absorbance towards longer wavelengths (up to 41.2% at 1100 nm), where the OPV shall be collecting energy. PH1000 – a highly conductive formulation of poly(3,4-ethylenedioxythiophene) polystyrene sulfonate (PEDOT:PSS) – already exhibits stronger absorption than ITO in the range from 400 to 700 nm (7.0 to 19.9%), which is even larger in the range from 700 to 1100 nm (up to 26.5%). In addition AgNWs and HYE (formulation of AgNWs together with highly conductive PEDOT:PSS) have a very similar absorbance spectrum. Below 700 nm their absorbance is slightly larger than that of ITO (AgNWs: 2.8 to 6.1%, HYE: 6.5 to 13.0), whereas above 700 nm their absorbance values are remarkably lower than that from ITO (AgNWs: up to 4.8%, HYE: up to 23.9%).

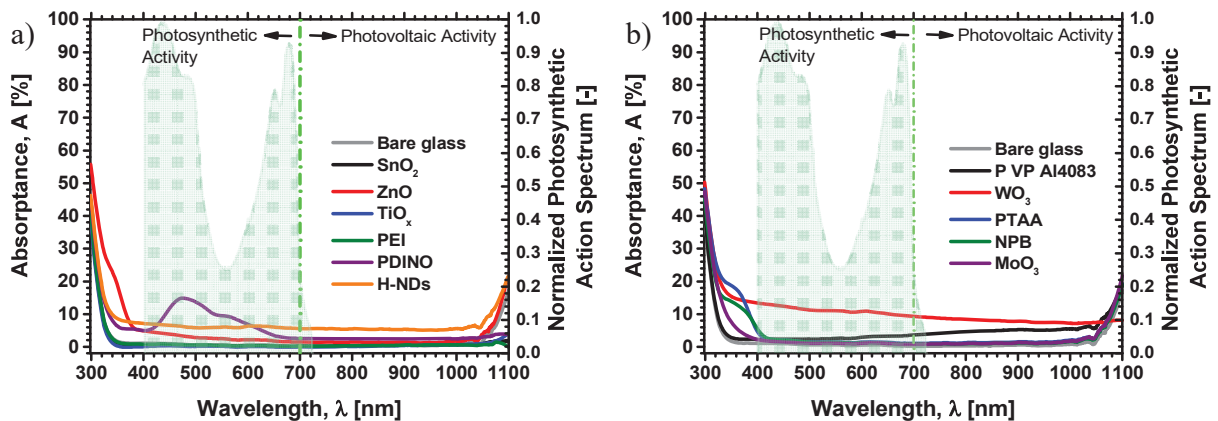


FIGURE 3. Absorbance spectra of (a) electron transport/extraction layers, as well as (b) hole transport/extraction layers used for organic solar cells and evaluated for AgrOPV.

FIGURE 3 a) is presenting the absorbance spectra of different electron transport layers (ETL), respectively electron extraction layers (EEL), used for OPV. The two metal oxides, tin oxide and titanium oxide, and the organic dielectric polyethyleneimine (PEI) reveal very similar absorbance spectra and very low values between 400 and 1100 nm (TiO_x: 0.0 – 0.3%, ZnO: 1.4 – 4.8%, PEI: 0.2 – 0.9%), which is beneficial for both agriculture and OPV. In addition, zinc oxide provides a very suitable bandgap, as the absorption increases strongly below 400 nm (slightly above 3 eV). Although the organic semiconductor PDINO shows a low absorbance in the range of 700 to 1100 nm (2.4 – 3.8%), which makes this material in principle suitable for AgrOPV, its own absorbance (2.6 – 14.8%) overlaps with nearly the whole photosynthesis action spectrum.

The absorbance of different hole transport layers (HTL), respectively hole extraction layers (HEL), are depicted in FIGURE 3 b). Clevios P VP AL4083 is a formulation of PEDOT:PSS used for HTLs in organic solar cells. This formulation has a low absorbance in the range of 400 to 700 nm (2.2 – 3.6%), similar to PH1000 from FIGURE 2 though in contrast to PH1000 the absorbance does not increase as much in the range of 700 to 1050 nm (up to 6.4%, at 1100 nm up to 18.9%). Tungsten oxide (WO₃) has a rather high absorbance in the range of 400 to 700 nm (13.4 – 9.3%), which is further reduced beyond 700 nm (down to 7.1% at 1000 nm). Therefore, this material shows the highest absorbance in the photosynthesis action range of all investigated HTLs and HELs. Nanodiamonds reduced in hydrogen atmosphere (H-NDs) have an absorbance below 10% (5.6 – 7.1%) over the whole range of 400 to 1050 nm (increase to 21.6% at 1100 nm) and are therefore very similar to the P VP AL4083. PTAA and NPB show a very low absorbance, below 5% for most of the spectral range from 400 to 1050 nm (PTAA: 1.1 – 4.5%, NPB: 0.8 – 5.4%). They only show a significant increase in absorbance below 400 nm (PTAA up to 46.9% and NPB up to 43.5% at 300 nm) and above 1050 nm (PTAA up to 19.3% and BPB up to 19.0% at 1100 nm). Molybdenum oxide (MoO₃) also exhibits an absorbance of below 5% (0.8 – 3.5%) over the whole spectral range from 400 to 1050 nm and shows an increase in absorbance below 400 nm (up to 45.9% at 300 nm) and above 1050 nm (up to 21.8% at 1100 nm).

It can be summarized for charge transport materials, that most of them are highly suitable for AgrOPV and some may additionally offer protection from UV-light. For the current film data, only PDINO and WO₃ seems to be less applicable.

FIGURE 4 shows the values of the sheet resistance of the different electrode materials. It is evident that all materials are suited for the application as TCEs in OSCs. Among the tested materials, AgNWs show the lowest sheet resistance with 29.1 Ω/sq (HYE: 48.5 Ω/sq, PH1000: 64.0 Ω/sq, TABLE 4). The figure of merit (FOM) for rating electrodes was carried out using the following equation⁶

$$\Phi_{TCE,exact} = \frac{P_{MPP}(E_G, T(\lambda), R_{\square}, L)}{P_{MPP}(E_G, T=100\% \forall \lambda, R_{\square}=0.0001 \Omega/\square, L)} \quad (1)$$

The FOM (Equation 1) is defined as the ratio of the power generated by an ideal OPV device having a bandgap E_G (between 700 – 1100 nm) and a solar cell length $l^{24, 25}$ for a *particular* TCE (with a material-specific sheet resistance R_{\square} and transmittance T) to the power generated by the same ideal solar cell with an *ideal* TCE ($R_{\square} = 0.0001 \Omega/\square$ and $T = 100\%$ throughout the whole spectral range). The FOM values of the studied transparent electrode materials are presented in FIGURE 5 and summarized together with the average transmittance and the sheet resistance in TABLE 4. The FOM demonstrates that AgNWs slightly outperform ITO, which in turn surpasses HYE. However, all three materials are well-suited for TCEs application, with AgNWs and HYE having the advantage of being easily solution-processable at low temperatures.

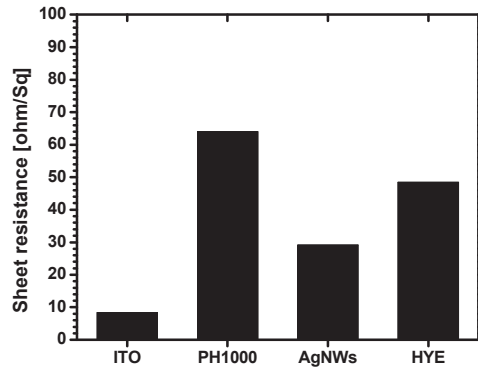


FIGURE 4. Sheet resistances of the transparent conducting films studied as potential electrodes for agrivoltaic applications.

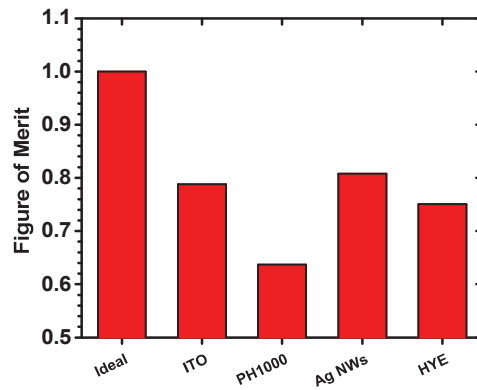


FIGURE 5. Figure of merit values for the transparent conducting electrodes.

TABLE 4. Average transmittance (700 to 1100 nm), sheet resistance, and figure of merit for different transparent conducting electrodes.

Material Name	Average Transmittance (700 to 1100 nm) [%]	Sheet Resistance [Ohm/square]	Figure of Merit
Ideal	100.00	0.0001	1.000
ITO	79.29	8.35	0.788
PH1000	70.78	64.00	0.637
AgNWs	85.80	29.11	0.808
HYE	82.70	48.46	0.751

The results from the absorbance measurements show that there is a large variety of materials for (semi)transparent conductive electrodes, as well as electron and hole transport/extraction layers which are well suited for application in agrivoltaic devices. In particular, AgNWs and HYE are very appropriate electrode

materials, as they show a low absorptance throughout the whole range from 400 to 1050 nm and considerable absorptance above 1100 nm and below 400 nm. Especially the latter is important in order to protect plants from photo damage.

PEI, SnO₂, and TiO_x are excellent choices for ETLs/EELS, because they exhibit very low absorptance over the whole spectral range considered. Even though ZnO shows an increased absorptance in the range of photosynthesis, it provides a strong cutoff below 400 nm and therefore protects plants from photodamage²⁶. Potentially increased and accelerated degradation of OPV as a result of UV irradiation in combination with photocatalytic ZnO has to be investigated in further detail in the future work.

In the case of the HTLs/HELs, NPB represents an attractive possibility, because it has a low absorptance in the range from 400 to 1100 nm but an increased absorptance below 400 nm and, thus, the potential to reduce photodamage to the plant.

CONCLUSION

In conclusion, a variety of conducting electrodes and charge extraction materials were investigated in terms of optical and electric properties for their suitability in application for organic solar cells in agrivoltaic applications (AgrOPV). Besides the requirement of having sufficient or rather maximized transmittance in the two ranges of operation, photosynthetic and photovoltaics, some materials provide the ability to protect plants from photodamage by UV-light reduction, and therefore might contribute to reducing stress on plants and increasing the crop yield.

ACKNOWLEDGMENTS

HH and ASD are grateful for financial support from the Deutsche Forschungsgemeinschaft (DFG) via the DFG project number 431903417. USS is grateful to the Thüringer Ministerium für Wirtschaft, Wissenschaft und Digitale Gesellschaft (TMWWDG) for funding the CEEC Jena. AH and TP thank the European Social Fund for Germany (ESF) for funding the project EilaSax (n° 100339506). SS, JC and DM thank the Czech Science Foundation (GACR) via the project 20-20991J for the support. AMA highly acknowledges financial support from the DFG via the return fellowship AN 1523/2-1. AA acknowledges financial support by DAAD (Deutscher Akademischer Austauschdienst).

REFERENCES

1. NREL Solar Cell Efficiency Chart, (<https://www.nrel.gov/pv/cell-efficiency.html>, 2021).
2. NREL Solar Module Efficiency Chart, (<https://www.nrel.gov/pv/module-efficiency.html>, 2021).
3. X. Xu, J. Xiao, G. Zhang, L. Wei, X. Jiao, H.-L. Yip and Y. Cao, *Science Bulletin* **65** (3), 208-216 (2020).
4. R. Meitzner, U. S. Schubert and H. Hoppe, *Advanced Energy Materials* **11** (1), 2002551 (2021).
5. C. J. M. Emmott, J. A. Röhr, M. Campoy-Quiles, T. Kirchartz, A. Urbina, N. J. Ekins-Daukes and J. Nelson, *Energy & Environmental Science* **8** (4), 1317-1328 (2015).
6. A. Anand, Md. M. Islam, R. Meitzner, U. S. Schubert, H. Hoppe, *Advanced Energy Materials*, 202100875 (2021).
7. 2,2'-((2Z,2'Z)-(((4,4,9-tris(4-hexylphenyl)-9-(4-pentylphenyl)-4,9-dihydro-s-indaceno[1,2-b:5,6-b dithiophene-2,7-diyl)bis(4-((2-ethylhexyl)oxy)thiophene 5,2-diyl))bis(methanylylidene))bis(5,6-dichloro-3-oxo-2,3-dihydro-1H-indene-2,1-diylidene))dimalononitrile.
8. T. Hori, H. Moritou, N. Fukuoka, J. Sakamoto, A. Fujii and M. Ozaki, *Materials* **3** (11), 4915-4921 (2010).
9. X. Fan, W. Nie, H. Tsai, N. Wang, H. Huang, Y. Cheng, R. Wen, L. Ma, F. Yan and Y. Xia, *Adv. Sci.* **6** (19), 1900813 (2019).
10. M. Raïssi, S. Vedraïne, R. Garuz, T. Trigaud and B. Ratier, *Solar Energy Materials and Solar Cells* **160**, 494-502 (2017).
11. H. Zhou, Y. Wang, J. Zhang, Z. Yu, Y. Li, L. Tan and Y. Chen, *Journal of Materials Chemistry C* **6** (2), 312-319 (2018).
12. J. Song, E. Zheng, J. Bian, X.-F. Wang, W. Tian, Y. Sanehira and T. Miyasaka, *Journal of Materials Chemistry A* **3** (20), 10837-10844 (2015).
13. A. R. b. Mohd Yusoff, H. P. Kim and J. Jang, *Solar Energy Materials and Solar Cells* **109**, 63-69 (2013).

14. L. Safriani, Risdiana, Fitriawati, M. Manawan, A. Bahtiar, A. Aprilia, D. P. Sari, J. Angel and I. Watanabe, [Journal of Physics: Conference Series](#) **1080**, 012011 (2018).
15. Z.-G. Zhang, B. Qi, Z. Jin, D. Chi, Z. Qi, Y. Li and J. Wang, [Energy & Environmental Science](#) **7** (6), 1966-1973 (2014).
16. A. Nagata, T. Oku, K. Kikuchi, A. Suzuki, Y. Yamasaki and E. Osawa, [Progress in Natural Science: Materials International](#) **20**, 38-43 (2010).
17. Z. Yin, J. Wei and Q. Zheng, [Adv. Sci.](#) **3** (8), 1500362 (2016).
18. T.-Y. Tsai, P.-R. Yan and S.-H. Yang, [Nanoscale Research Letters](#) **11** (1), 516 (2016).
19. C.-C. Chueh, C.-Z. Li and A. K. Y. Jen, [Energy & Environmental Science](#) **8** (4), 1160-1189 (2015).
20. Y. Wang, Q. Liang, J. Huang, D. Ma and Y. Jiao, [RSC Advances](#) **7** (45), 28494-28498 (2017).
21. A. Kim, Y. Won, K. Woo, S. Jeong and J. Moon, [Advanced Functional Materials](#) **24** (17), 2462-2471 (2014).
22. M. Wang and K.-L. Choy, [ACS Appl. Mater. Interfaces](#) **8** (26), 16640-16648 (2016).
23. Y. Kuwahata and T. Minemoto, [Renewable Energy](#) **65**, 113-116 (2014).
24. H. Hoppe, M. Seeland and B. Muhsin, [Solar Energy Materials and Solar Cells](#) **97**, 119-126 (2012).
25. M. Seeland and H. Hoppe, [Phys. Status Solidi A-Appl. Mat.](#) **212** (9), 1991-2000 (2015).
26. S. Takahashi, S. E. Milward, W. Yamori, J. R. Evans, W. Hillier and M. R. Badger, [Plant Physiology](#) **153** (3), 988-993 (2010).

Publications P1 to P5

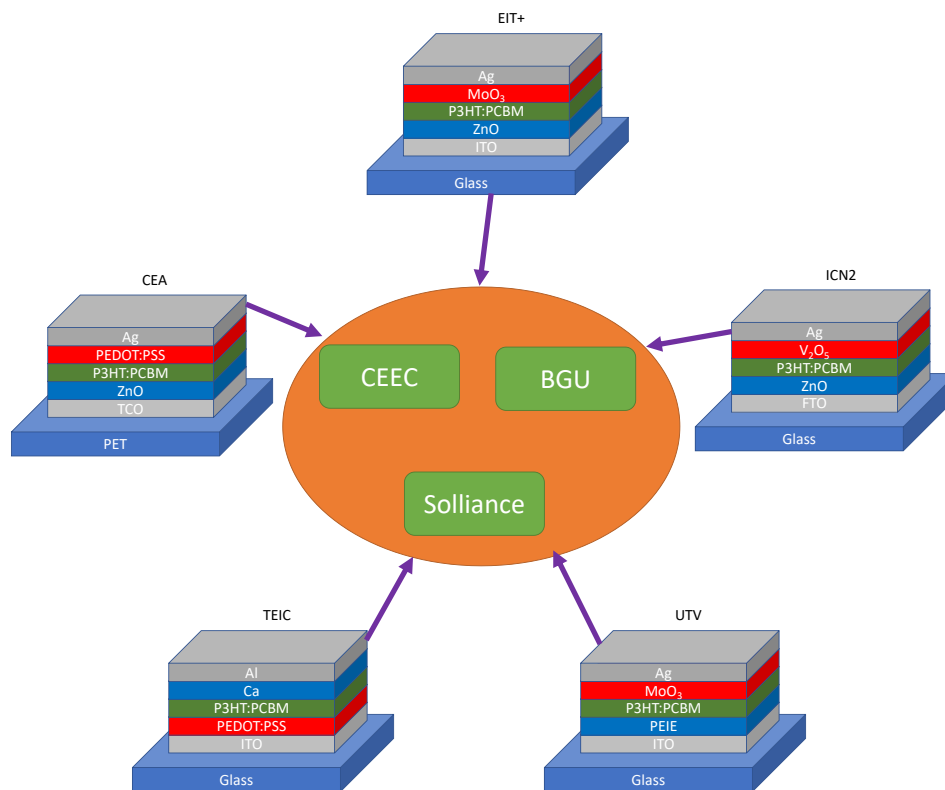
Publication P3

Impact of P3HT Materials Properties and Layer architecture on OPV Device

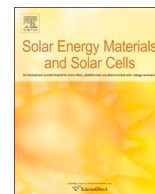
Stability

Rico Meitzner, Tobias Faber, Shahidul Alam, Aman Anand, Roland Roesch,
Mathias Büttner, Felix Herrmann-Westendorf, Martin Presselt, Laura Ciammaruchi,
Iris Visoly-Fisher, Sjoerd Veenstra, Amaia Diaz de Zerio, Xiaofeng Xu, Ergang Wang,
Christian Müller, Pavel Troshin, Martin D. Hager, Sandra Köhn, Michal Dusza,
Miron Krassas, Simon Züfle, E. Kymakis, Eugene A. Katz, Solenn Berson, Filip Granek,
Matthieu Manceau, Francesca Brunetti, Giuseppina Polino, Ulrich S. Schubert,
Monica Lira-Cantu, Harald Hoppe,

Solar Energy Materials and Solar Cells **2019**, 202, 110151



Reproduced with permission of Elsevier B.V., Copyright © 2019.



Impact of P3HT materials properties and layer architecture on OPV device stability



Rico Meitzner^{a,b,*}, Tobias Faber^c, Shahidul Alam^{a,b}, Aman Amand^{a,b}, Roland Roesch^{a,b}, Mathias Büttner^c, Felix Herrmann-Westendorf^{cd}, Martin Presselt^{a,d,s,t}, Laura Ciammaruchi^e, Iris Visoly-Fisher^{e,f}, Sjoerd Veenstra^g, Amaia Diaz de Zerio^h, Xiaofeng Xu^h, Ergang Wang^h, Christian Müller^h, Pavel Troshin^{i,j}, Martin D. Hager^{a,b}, Sandra Köhn^{a,b}, Michal Dusza^{k,l}, Miron Krassas^m, Simon Züfle^{q,r}, E. Kymakis^m, Eugene A. Katz^{e,f}, Solenn Bersonⁿ, Filip Granek^k, Matthieu Manceauⁿ, Francesca Brunetti^o, Giuseppina Polino^o, Ulrich S. Schubert^{a,b}, Monica Lira-Cantu^p, Harald Hoppe^{a,b}

^a Center for Energy and Environmental Chemistry Jena (CEEC Jena), Friedrich Schiller University Jena, Philosophenweg 7a, 07743, Jena, Germany

^b Laboratory of Organic and Macromolecular Chemistry (IOMC), Friedrich Schiller University Jena, Humboldtstrasse 10, 07743, Jena, Germany

^c Institute of Physics, Technische Universität Ilmenau, Weimarer Straße 32, 98693, Ilmenau, Germany

^d Institute of Physical Chemistry (IPC), Friedrich Schiller University Jena, Helmholtzweg 4, 07743, Jena, Germany

^e Department of Sol. Energ. and Environmental Physics, Swiss Inst. for Dryland Environmental and Energy Research, J. Blaustein Institutes for Desert Research, Ben-Gurion University of the Negev, Midreshet Ben-Gurion, 8499000, Israel

^f Ilse Katz Institute for Nanoscale Science and Technology, Ben-Gurion University of the Negev, Beersheva, 8410501, Israel

^g Eindhoven University of Technology, High Tech Campus 21, 5656 AE, Eindhoven, the Netherlands

^h Department of Chemistry and Chemical Engineering, Chalmers University of Technology, 41296, Göteborg, Sweden

ⁱ Skolkovo Institute of Science and Technology, Nobel St. 3, Moscow, 121205, Russia

^j IPCP RAS, Semenov Prospect 1, Chernogolovka, 141432, Russia

^k Wrocław Research Centre EIT+, Stabłowicka 147, 54-066, Wrocław, Poland

^l Institute of Low Temperature and Structure Research, Polish Academy of Science, Okolna 2, 50-422, Wrocław, Poland

^m Center of Materials Technology and Photonics, Electrical Engineering Department, School of Applied Technology, Technological Educational Institute (TEI) of Crete, Heraklion, 71004, Crete, Greece

ⁿ CEA, LITEN/DTS, Laboratoire des Technologies pour Les Modules Photovoltaïques, Savoie Technolac, BP 332, 50 Avenue Du Lac Léman, 73377, Le Bourget-du-Lac, France

^o CHOSE (Centre for Hybrid and Organic Sol. Energ.), Department of Electronic Engineering, University of Rome Tor Vergata, Via Del Politecnico 1, 00133, Rome, Italy

^p Catalan Institute of Nanoscience and Nanotechnology (ICN2), CSIC and the Barcelona Institute of Science and Technology (BIST), Building ICN2, Campus UAB, E-08193, Bellaterra, Barcelona, Spain

^q Institute of Computational Physics, Zurich University of Applied Sciences (ZHAW), Wildbachstrasse 21, 8400, Winterthur, Switzerland

^r Fluxim AG, Katharina-Sulzer-Platz 2, 8400, Winterthur, Switzerland

^s Leibniz Institute of Photonic Technology (IPHT), Albert-Einstein-Str. 9, 07745, Jena, Germany

^t Sciclus GmbH & Co. KG, Moritz-von-Rohr-Str. 1a, 07745, Jena, Germany

ARTICLE INFO

Keywords:

Organic solar cells
P3HT
Stability
ISOS

ABSTRACT

We report a cooperative study conducted between different laboratories to investigate organic solar cell degradation with respect to P3HT material properties and different solar cell architectures. Various batches of P3HT were collected from different suppliers reflecting commercial availability as well as properties variability. Among the materials properties explicitly considered were the molar mass, dispersity, regio-regularity, impurities by trace metals and intrinsic doping evaluated from radical concentrations. Each of the participating laboratories contributing test devices applied their own layer stack, *i.e.* their own device architecture and layout. This variation was appreciated as another parameter for evaluation. Even though a large amount of devices failed due to extrinsic degradation effects, indeed, some materials properties were found to be more important than others for obtaining long lifetimes and high stability of P3HT-based polymer solar cells.

* Corresponding author. Center for Energy and Environmental Chemistry Jena (CEEC Jena), Friedrich Schiller University Jena, Philosophenweg 7a, 07743 Jena, Germany.

E-mail address: rico.meitzner@uni-jena.de (R. Meitzner).

<https://doi.org/10.1016/j.solmat.2019.110151>

Received 6 August 2018; Received in revised form 5 June 2019; Accepted 24 August 2019

Available online 02 September 2019

0927-0248/© 2019 Published by Elsevier B.V.

1. Introduction

With increasing depletion of fossil fuels and growing strain on the environment due to emission of greenhouse gases and thereby accelerating global warming, it is necessary to switch to more renewable and sustainable ways of energy generation. As the most abundant renewable energy source on earth is sunlight, a very attractive technology for providing of sustainable energy is photovoltaics. Of these a very interesting subcategory is represented by organic photovoltaics (OPV) with its ability to rely on abundant materials, being easily scalable and bearing the potential of very high speeds in roll-to-roll processing.

Recently a significant progress was made in this field with regards to efficiency and stability. Power conversion efficiencies of 13–14% were obtained in single junction, bulk-heterojunction organic solar cells (BHJ OSC) [1,2] and operational lifetimes in the range of 10 years [3–5] were estimated on the basis of exclusively intrinsic degradation processes. Roll-to-roll processed flexible modules have already demonstrated outdoor stabilities of several years [6]. While this is very encouraging and promising, more understanding is required in terms of how materials properties impact the device stability.

Various published reports demonstrated extrapolated operational lifetimes of OPV for several years [4,5,7,8,11]. A recently published review [3,6,9] revealed an increase in publication activities on OPV stability research and an increase in average reported lifetimes over the recent years, clearly demonstrating progress in the field. The observed experimental lifetimes range up to 2 years [8,10], when no extrapolations to T_{80} (corresponding to efficiency drop to 80% of the initial efficiency value) or $T_{S,80}$ (corresponding to efficiency drop to 80% after stabilization) were considered [11,12].

An important factor to be taken into account when evaluating the lifetime of an OPV device is the so-called burn-in phase. The burn-in is described as the initial rapid decay of the solar cell performance followed by a stabilized performance [7,11]. In some more recent reports devices seemed to show no burn-in Refs. [7,13], but even with a burn-in, very long lifetimes are attainable [4]. After all, a limited performance loss during burn-in does not harm long-term energy harvesting if the performance decay thereafter is very low.

In general, degradation can be divided into intrinsic and extrinsic mechanisms [3,14,15]. Extrinsic mechanisms are those that can be avoided by a proper sealing of the device. Most common examples are photo-oxidation due to oxygen ingress [16,17] and electrode corrosion from ingress of moisture [14]. These modes of degradation can be successfully prevented with a robust encapsulation of the device and they can be further alleviated by an inverted solar cell architecture, where low-workfunction metals [18], which are prone to corrosion due to oxygen or moisture ingress, can be avoided. Intrinsic mechanisms, however, cannot be prevented by employing encapsulation, as they originate from the materials used in the solar cell layer stack, and are triggered by unavoidable factors such as temperature (heat) [15,19,20] and electromagnetic radiation (including UV-light) [21–23]. Some examples are an increased phase separation of donor and acceptor in the active layer blend [24], the formation of traps and increased energetic disorder [25,26], the formation of fullerene dimers [27–29] and electro-migration of e.g. silver from printed electrodes [30]. Charge transport layers may also induce effects leading to degradation, e.g. doping of the photoactive layer via MoO_3 [31,32]. Furthermore, impurities inherently connected to the materials used, e.g. remnants from synthesis such as catalyzing agents (metal impurities) or low molar mass components may also be responsible for electronic trap formation [33–35].

Besides the mentioned doping effect, transport layers degradation can also have a large impact on the overall stability of organic solar

cells [36–39]. Degradation of the transport layers or of their interfaces can induce an extraction barrier to charge carriers [40]. Transport layers can be quite diverse, ranging from small molecules to polymers to amorphous or nanocrystalline metal oxides to hybrids of these materials [41]. A commonly used hole transport layer, PEDOT:PSS, is well known to be a potential weak point for stability, due to its hygroscopic and acidic properties [6,42]. Metal oxides have become very common as transport layers due to their capability to be solution processable [36] and their rather good stability [37,43–45].

The most commonly studied material in OPV is poly(3-hexylthiophene) (P3HT) [46], as it is relatively cheap to produce and readily available in kilogram amounts, due to easy synthetic upscaling [47]. In order to enable wide comparability among the researchers working in the field, in this study solar cells based on the classical material combination P3HT:PCBM ([6,6]-phenyl- C_{61} -butyric acid methyl ester) were explored under variation of P3HT batches in order to assess the impact of the material parameters of P3HT on device stability. Five labs were involved in providing solar cells according to their optimized layer stack architecture and device layout, constituting the second parameter space.

The phase behavior of P3HT:PCBM blends is not only controlled by miscibility, which is strongly enhanced in amorphous P3HT domains, but also by the ability of each of the two constituents to crystallize. Upon prolonged heating this may lead to crystallization induced large-scale (micron-sized) phase separation. Hence material purity and regio-regularity are expected to play an important role concerning morphological stability [48,49]. For P3HT:PCBM solar cells also a minor voltage loss during burn-in has been observed, which was assigned to the formation of less ordered phases [50].

P3HT with higher regio-regularity is reported to be relatively stable against photo-oxidation, as crystallinity hampers both the in-diffusion of reactants (oxygen) as well as conformational changes required for oxidation [3,48]. Molecular weight does not always seem to have an impact on photostability [48], but certainly impacts the crystallization temperature [51]. Though there are conflicting reports about other polymers as PCDTBT [15] and PTB7[52] where a higher molar mass resulted in a longer lifetime, this can be most likely associated to smaller electronic trap formation at chain ends. A higher glass transition temperature (T_g) or a higher melting point (T_m), as described by the dispersity (PDI), were reported to exhibit a positive impact on thermal stability [24,53–56]. Countermeasures against morphological degradation include the application of polymers exhibiting higher T_g [57], the application of phase-locked diblock-copolymers [58], acceptor alloys [59,60] as well as crosslinking of organic semiconductors [61–64].

Furthermore, trace metals in the active layer could catalyze reactions or act as traps and therefore as recombination centers. Several reports [33,65] mention the impact of impurities on device performance – and hence studying their impact on stability is required.

Finally, upon analyzing all results, several recommendations could be derived for obtaining long-term stability with organic solar cells based on P3HT and potentially beyond.

2. Experimental

Five different commercial P3HT samples were acquired from 1 M, BASF, Merck, Plextronics and Rieke Metals Inc. and named P3HT-I through P3HT-V, without following the producer order above. Commercial P3HTs were chosen to study the viability of these materials available from suppliers broadly used labs within the OPV community. Their intrinsic properties were evaluated in detail via chemical, thermal and optical analysis. Thus their properties, reported in the results section, are the only parameters to enter into the evaluation. PC_{61}BM of

99% purity or better was used in all cases for the suppliers of the used PC₆₁BM see Table 2.

In Fig. 1 the procedure of the initial experimental phase, including ordering and distribution of P3HTs, manufacturing of the solar cells and characterization, is depicted. Chemical characterization including ¹H nuclear magnetic resonance spectroscopy, size exclusion chromatography, induction coupled plasma optical emission spectroscopy, electron spin resonance spectroscopy, thermal characterization like differential scanning calorimetry and thermogravimetric analysis, as well as optical characterization methods like UV/Vis spectroscopy and photothermal deflection spectroscopy, were performed. Additionally, electronic characterization including current-voltage (IV) and external quantum efficiency (EQE) measurements, as well as different characterization methods performed with PAIOS by Fluxim (see section 2.7.3), were done. The results of these experiments are reported in Sections 2.6 and 2.7.

In Fig. 2 the experimental procedure after cell manufacturing and initial characterization is shown. The produced solar cell devices (see section 2.1) were distributed to the respective labs for aging (see section 2.3) and some were sent to Fluxim for characterization with the PAIOS instrument. Aging was performed at different labs according to ISOS-L2, ISOS-D2 and ISOS-O1 protocols [12], as explained in detail in Section 2.3. Samples aged at L2, D2 and O1 were also sent to Fluxim after aging to determine their electrical properties.

At the end of the experiment the polymer properties determined from chemical and thermal analysis were correlated with the extracted lifetime parameters. For ease of reading the results, a unified color code for the different P3HT batches was defined and is shown in Table 1.

2.1. Materials and layer stacks

We deliberately allowed a large variation in layer stacks/device layout— including substrates – providing additional parameters impacting device stability. This was made possible by the fact that each cell producer prepared devices based on all the different P3HT batches using their preferred device layout. Five different labs served as cell producers: Commissariat à l'énergie atomique et aux énergies alternatives (CEA), Wrocław Research Centre EIT+ (EIT+), Institut Català de Nanociència i Nanotecnologia (ICN2), Technological Educational Institute Crete (TEIC) and University Tor Vergata Rome (UTV). The different P3HT batches were contributed by different collaborators of the experiment. Three of the cell producers used ITO coated glass as substrates, one lab used FTO coated glass (ICN2), and one lab used ITO coated PET foil (CEA); suppliers can be found in the Table 2. Further variations were in the device architecture, including mainly inverted layer stacks (electron extraction *via* semi-transparent electrode) as well as one example for conventional layer stack (hole extraction *via* semi-transparent electrode). The charge extraction layers were varied as well: ZnO, MoO₃, V₂O₅, PEIE, and PEDOT:PSS were used. Calcium, aluminum and silver served as opaque back electrodes. Physical vapor deposition was used for evaporation which will be called evaporation for short from here on. Three producers used epoxy as sealant for cell encapsulation (EIT+, TEIC and ICN2), while CEA used a fully flexible encapsulation and UTV used Parafilm for sealing. All layer stacks as well as device layouts are reported in detail in Table 3. A more detailed description of the manufacture of the solar cells is presented in the [supplementary information section 1 and 2](#).

2.2. Processing of active layer solutions

The active layer solutions were provided by various labs involved in the study and were distributed including detailed preparation recipes among all cell producers. These recipes were followed largely, though small adaptations were allowed concerning processing temperatures in order to incorporate for specific layer stack requirements. In general, solutions were handled around 50 °C for storage and processing; details

can be found in the Supporting Information.

2.3. Aging methods

Aging of the photovoltaic devices was performed following largely the published ISOS recommendations. Three different aging protocols were applied: laboratory weathering (L2), outdoor aging (O1) and dark aging (D2). This allowed us to investigate the impact of different stress conditions on the device stability.

2.3.1. ISOS-L2 degradation

Samples were aged at the CEEC Jena under conditions close to ISOS-L2. The setup in Jena consists of a metal halide lamp, whose illumination spectrum is close to AM 1.5G, as can be seen in Fig. 3. The light intensity was set to 1000 W/m² with help of a pyranometer. The intensity was logged by a silicon sensor at all times, demonstrating that the operation of the lamp was very stable. The temperature was set to 55 °C in a shady region of the chamber and monitored as well. Unfortunately, a higher temperature could not be reached and therefore remained 10 K below the ISOS recommendations. However, the acceleration for 10 K higher temperature can be estimated to be roughly a factor of two [66]. Furthermore, as the devices were illuminated, their temperature was considerably higher than in the shadow, yielding 65 °C or higher inside the cells. Humidity was monitored and remained constant at around 5% r.H within the setup due to the elevated temperature. The samples were electrically connected *via* crocodile clamps to a multiplexing unit (Keithley 2700). Periodic current-voltage (IV) characterization was performed automatically every 30 min with a Keithley 2400 *via* computer control. When multiple cells on a substrate were available, the innermost cells were chosen for aging, as they were considered to be least affected by extrinsic degradation mechanisms.

2.4. ISOS-D2 degradation

Dark storage degradation was carried out Solliance in Eindhoven under a solar simulator equipped with a sulphur plasma light source (Solaronix), under which the samples were shaded by a metal plate. The samples were occasionally uncovered, computer-controlled automated IV measurements took place during the whole aging process every hour and the collected data was stored in a database. The IV measurements recorded under one sun illumination were later filtered from the complete data set. During the aging process the temperature was set to 65 °C and relative humidity stayed at around 5% at that temperature. The setup used and the device connections can be seen in Fig. S4. Solar cells on substrates with more than one device were chosen based on maximum performance.

2.5. ISOS-O1 degradation

The cells were mounted on a fixed angle (30° to horizontal) stand (as shown in Fig. S3) and the global intensity of incident sunlight was measured with a calibrated thermopile pyranometer (Eppley PSP) mounted on the same plane. It should be noted that the spectrum measured at noon time ± 2–3 h of a cloudless day at Sede Boqer, Israel (Lat. 30.8°N, Lon. 34.8°E, Alt. 475 m), matches almost perfectly to the standardized AM 1.5G spectrum [67], see Fig. S2. The cells were

Table 1
Color coding for the materials used in the experiment.

Material	Color Code
P3HT-I	Black
P3HT-II	Red
P3HT-III	Blue
P3HT-IV	Green
P3HT-V	Orange

Table 2
List of layer stacks and materials applied in the solar cells.

Supplier	CEA	EIT +	ICN2	TEIC	UTV
Type of architecture	Inverted	Inverted	Inverted (No UV filter)	Conventional	Inverted
Substrate	PET/TCO (visiontek)	Glass/ITO (Ossila)	Glass/FTO (SOLEMS)	Glass/ITO	Glass/ITO (Kintec)
ETL	ZnO (Sigma Aldrich)	ZnO (Sigma Aldrich)	ZnO (Sigma Aldrich)	Ca (Kurt J. Lesker Company)	PEIE (Sigma Aldrich)
HTL	PEDOT:PSS (Heraeus)	MoO ₃ (Sigma Aldrich)	V ₂ O ₅ (home made, vanadium ethoxide from Sigma-Aldrich))	PEDOT:PSS (Heraeus)	MoO ₃ (5 nm evaporated) (Sigma Aldrich)
PCBM	PC ₆₁ BM (Merck)	PC ₆₁ BM (Lumtec)	PC ₆₁ BM (Solenne)	PC ₆₁ BM (Solenne)	PC ₆₁ BM (Solenne)
Solvents	CB (Sigma Aldrich)	o-DCB (Poch S.A.)	CB (Sigma-Aldrich)	o-DCB (Sigma Aldrich)	CB
Metal Electrode	Ag, evaporated	Ag, evaporated (Kurt J. Lesker Company)	Ag, evaporated (Kurt J. Lesker Company)	Aluminum, evaporated (Kurt J. Lesker Company)	Ag, 100 nm evaporated (Kurt J. Lesker Company)
Adhesive	Thermoplastic	Epoxy (Ossila)	Epoxy (Ossila)	Epoxy (Ossila)	Parafilm (Heathrow Scientific)
Encapsulation	Flexible transparent barrier film	Glass	Glass	Glass (Ossila)	Glass (PEARL)

PET: polyethylene terephthalate; TCO: transparent conducting oxide; ITO: indium tin oxide; FTO: fluorine doped tin oxide; PEDOT:PSS: poly(3,4-ethylenedioxythiophene) polystyrene sulfonate; PC₆₁BM: Phenyl-C61-butiric acid methyl ester; CB: chlorobenzene; o-DCB: ortho-dichlorobenzene.

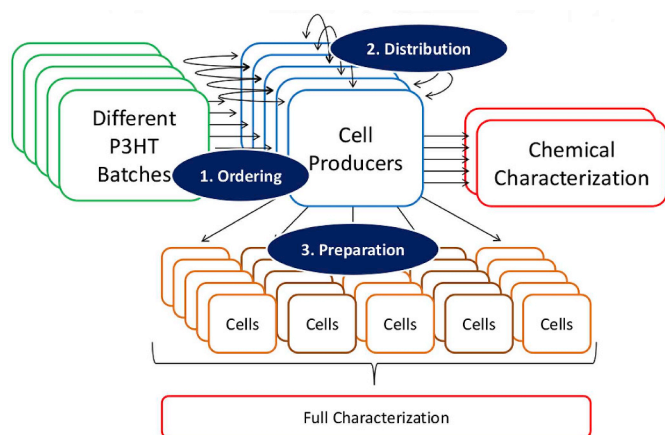


Fig. 1. Schematic of the experimental proceedings before aging.

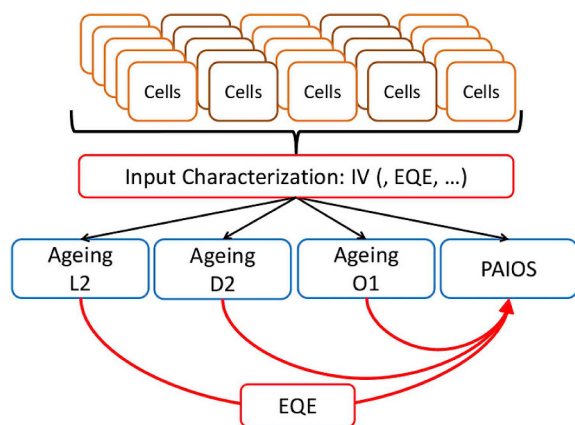


Fig. 2. Further experimental procedure after production and initial characterization of the devices.

exposed between November 2015 and February 2016 and only during light hours (between \pm 9:30 and 15:30) for a total of \sim 210 h, in order to avoid potential encapsulation breaking or contact oxidation problems due to night-time humidity. After the daily exposure the cells were stored in the dark at shelf life conditions (lab environment).

The photovoltaic parameters of the solar cells were periodically monitored indoor with an AM1.5 class AAA Newport Oriel Verasol LSH-7520 solar simulator (70 mW/cm²) and a Keithley 2410 source-measure unit. Before aging the cells were kept in the dark inside a glove box (O₂ < 0.1 ppm).

2.6. Materials characterization

2.6.1. Dynamic scanning calorimetry (DSC), size exclusion chromatography (SEC), nuclear magnetic resonance spectroscopy (NMR)

Differential scanning calorimetry (DSC) was carried out under nitrogen between -20 to 300 °C at a scan rate of 10 °C/min using a Mettler Toledo DSC2 calorimeter equipped with a HSS7 sensor and a TC-125MT intracooler. DSC was used to determine the peak melting and crystallization temperature as well as the enthalpy of melting. Thermogravimetric analysis (TGA) was carried out under nitrogen between 20 to 550 °C at a scan rate of 10 °C/min using a Mettler Toledo TGA/DSC 3 + instrument. TGA was used to determine the decomposition temperature. The molar mass was measured with size exclusion chromatography (SEC) on an Agilent PL-GPC 220 Integrated High Temperature GPC/SEC System in 1,2,4-trichlorobenzene at 150 °C using relative calibration with polystyrene standards. SEC was used to determine the molar mass and the dispersity (PDI) of the polymers. ¹H nuclear magnetic resonance (NMR) spectroscopy was measured on a Varian Inova 400 MHz NMR spectrometer by using chloroform-*d* (CDCl₃) as solvent and tetramethylsilane (TMS) as internal reference. The head-to-tail (HT) and head-to-head (HH) protons from α -CH₂ on the hexyl side chain give a peak at around $\delta = 2.8$ ppm and $\delta = 2.6$ ppm, respectively. The regioregularity of P3HT was calculated from the ¹H NMR integral of the different α -CH₂ protons on the hexyl of P3HT by following the equation (1) below [68]:

$$RR_{P3HT}(\%) = \frac{Integral_{HT}}{Integral_{HT} + Integral_{HH}} \quad (1)$$

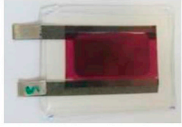
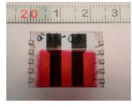
2.6.2. Inductively coupled plasma optical emission spectroscopy (ICP-OES)

ICP-OES was used to determine the trace metal content of the polymers. 200–250 mg polymer were digested in nitric acid (65%, purity p.A., Merck Schuchardt OHG) and hydrogen peroxide (33%) in a microwave (Biotage Initiator +, instrument settings 15 min, 180 °C, vial 0.5–2 mL, absorption level very high, fixed hold time OFF). This process was repeated three times with altogether 2 mL nitric acid and 400 μ L hydrogen peroxide. The combined solutions were refilled to 25 mL with water and filtered through nylon syringe filter (0.45 μ m, Applichrom). The resulting solution was utilized for the measurements with the ICP-OES (Varian 725-ES) to determine the trace metal contents.

2.6.3. Electron spin resonance (ESR)

Standard 5 mm OD NMR tubes (which are ESR silent within the $g = 2.00$ region) were loaded with the P3HT powder (10–20 mg) inside the argon glovebox and tightly closed under inert atmosphere before taking them out for measurements. The weights of the empty sample tubes and those with the introduced material were determined with a

Table 3
Producers of OPV devices, layer stack, layout (photo) and single device area.

Manufacturer	Layer Stack	Photo	Active Area (mm ²)
CEA, France	Ag		140
	PEDOT:PSS		
	P3HT:PCBM		
	ZnO		
	TCO		
	PET		
EIT+, Poland	Ag		4.5
	MoO ₃		
	P3HT:PCBM		
	ZnO		
	ITO		
ICN2, Spain	Ag		20
	V ₂ O ₅		
	P3HT:PCBM		
	ZnO		
	FTO		
TEIC, Greece	Glass		4
	Al		
	Ca		
	P3HT:PCBM		
	PEDOT:PSS		
UTV, Italy	ITO		10
	Glass		
	Ag		
	MoO ₃		
	P3HT:PCBM		
	PEIE		

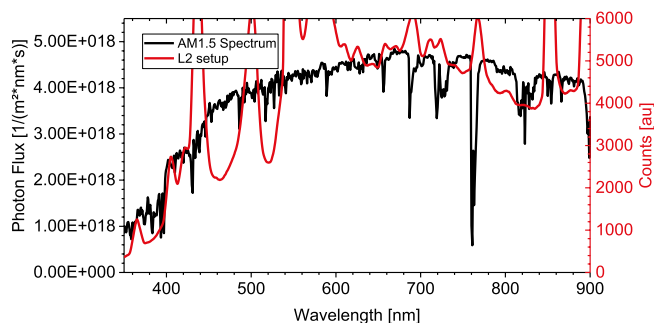


Fig. 3. Comparison of the spectrum of the metal halide lamp used in the L2 aging setup at CEEC Jena with AM 1.5G showing a good match. The full intensity range is shown in Fig. S1 (Supplementary Information).

high accuracy (± 0.01 mg). The ESR spectra were recorded using a benchtop Adani CMS8400 spectrometer. Integration of the signals in the ESR spectra was performed using EPR4K software developed by National Institute of Environmental Health Science (NIEHS). Each sample was characterized by average number of spins per repeating unit following the previously published approach [65].

2.6.4. Optical spectroscopy – ultraviolet/visible-spectroscopy (UV/Vis), photothermal deflection spectroscopy (PDS)

A custom-made spectroscopy setup was used to determine UV/Vis spectra. In the setup a glass fiber above the sample, which captures light reflected from the sample, is surrounded by a ring of several other fibers which carry the light from a white light source containing a halogen lamp and a deuterium arc lamp. Below the sample there is another glass fiber collecting the light transmitted through the device. The fibers are connected to two spectrometers from Avantes AvaSpec-ULS3648,

which record the spectra.

A custom-made setup for photothermal deflection spectroscopy (PDS) was used to determine the sub-bandgap absorption of all investigated P3HT films as done in previous works [69–71]. The measurement principle and basic setup of PDS is described elsewhere [72]. The used monochromatic light source (obtained from LOT-Quantum Design) contains a 450 W Xenon lamp and a monochromator with a focal length of 260 mm). The monochromator is equipped with three gratings providing maximum intensity from 300 to 2000 nm, while the resolution is kept at 10 nm up to 1000 nm and 20 nm above 1000 nm. The light is modulated by a chopper operating at a frequency of 5 Hz. Deflection of a 0.7 mW HeNe-laser is measured by a 10×10 mm² lateral effect sensor obtained from Thorlabs. The measured deflection is frequency selective and amplified by a SR850 Lock-In amplifier. The samples are dispersed in perfluorohexane and graphite is used as standard to calibrate the data. A self-written Labview program automatically collects and calibrates the data.

2.7. Device characterization

2.7.1. Current-voltage-characterization (IV)

Devices were initially IV characterized upon arrival e.g. at CEEC Jena under a solar simulator using a metal halide lamp. The metal halide lamp was calibrated to 1000 W/m² with a pyranometer. The setup uses a computer-controlled Keithley 2400 SMU. Samples were connected using crocodile clamps.

2.7.2. External quantum efficiency (EQE)

EQE characterization of the samples was done at CEEC Jena upon arrival and after aging. The EQE setup used is a BENTHAM PVE300. EQE measurements were generally performed without additional bias light. Hence, if the device performance decays during aging, but the

EQE remains constant, the loss mechanism could be due to increased bimolecular recombination or series resistance losses, only showing under higher excitation densities. On the other hand, if EQE decreased upon ageing, but photocurrent remained on a higher level within the L2-setup, the low light level conditions within the EQE measurement point to extraction problems, e.g. due to insufficient trap filling.

2.7.3. PAIOS characterization

2.7.3.1. JV, CELIV, TPC, TPV, DIT, impedance, C-V, temperature dependence and numerical simulation details. Transient and impedance techniques can help to characterize charge transport. Qualitative comparison of nominally identical devices, and between fresh and aged cells may contribute to the understanding of the underlying degradation processes. Current-voltage (IV), charge extraction by linearly increasing voltage (CELIV), transient photocurrent (TPC), transient photovoltage (TPV), double injection transient (DoIT), impedance spectroscopy, capacitance -voltage curves (C-V), and further optoelectrical characterization methods were performed at Fluxim AG using their All-in-one characterization platform Paivos for Solar Cells [73,74]. For this purpose, Fluxim received a batch of fresh devices as well as aged cells from the L2 and O1 tests. The devices were illuminated with a high-power white LED (with an intensity above 1 sun illumination) allowing for pulsed and light-intensity dependent experiments.

2.8. Analysis method for L2 aging results: lifetime energy yield (LEY)

After the experiments were finished the aging data was analyzed to extract different relevant parameters, like the end of the burn-in period (at stabilized efficiency E_S) (T_S), the lifetime (T_{80}) or lifetime after stabilization ($T_{S,80}$) and the lifetime energy yield (LEY) [4,11]. The procedure to determine the LEY was introduced by Roesch et al. [4]. It was considered useful here due to its capability to depict a relevant parameter for an energy producing device, i.e. its energy output throughout its nominal lifetime. In the case of an ISOS-L2 experiment the LEY is straightforward as the light intensity is stable throughout the whole experiment.

In case of O1 and D2 aging we restricted ourselves to analyze the performance decay as is.

3. Results and discussion

3.1. Polymer properties characterization

The initial characterization concerned polymer materials properties and the corresponding parameters obtained for the different P3HT batches investigated are summarized in Table 4. The molar masses varied roughly by a factor of three, whereas the dispersity (\bar{M}_w/\bar{M}_n or polydispersity index – PDI) exhibited smaller variations with values between 2.0 and 2.7. The lowest molar mass, P3HT-III exhibited also the lowest PDI – together with P3HT-I. Concerning the regio-regularity (RR) generally all samples showed high values between 94% and 96%; only the sample with the highest molar mass and the highest PDI, P3HT-IV, had a rather low value with 90%. Also for crystallization (T_C) and melting temperatures (T_M) the same sample differed considerably

from the others, exhibiting the second lowest value of $T_C = 189^\circ\text{C}$ and the lowest value of $T_M = 222^\circ\text{C}$. In accordance with its low RR, P3HT-IV exhibits the lowest melting enthalpy (ΔH_M) of all samples, indicating and confirming that it is less ordered. The decomposition temperatures were – as expected for the same chemical structure – almost identical for the different P3HT batches.

3.2. Trace metal content analysis of the P3HT batches

The results for the trace metal content determined by ICP-OES are summarized in Table 5. They show a certain variation between the different polymer samples, which might stem from different synthetic approaches used for the polymerization, the equipment used to handle them and the purification methods applied. The standard synthetic procedures for regioregular P3HT include the McCullough method, which is a Kumada coupling, as well as the Rieke method based on activated zinc (Rieke zinc) [75,76]. Moreover, the Grignard metathesis reaction (GRIM) was developed by McCullough [77]. All these reactions are based on nickel catalysts. Furthermore, also palladium-catalyzed reactions have been applied: Stille coupling, Suzuki coupling as well as the dehydrogenative polycondensation [78,79].

For a very ubiquitous element like sodium, which is basically everywhere, there are barely any variations between the different P3HT samples. Palladium content was below the detection limit for all samples (Pd-catalyst are only used for the non-standard polymerizations). Residual palladium is known to cause shunting problems [80]. The nickel content, the main catalyst for the standard polymerizations (e.g., in the GRIM [51]) is also very low for all polymer samples. Only P3HT-I exhibited a comparably high magnesium content, which might be caused by residual magnesium salts from utilized Grignard reagents. Noteworthy, the zinc content was also rather low for all polymers. On the other hand, P3HT-IV exhibited the highest iron (Fe) content but otherwise did not differ much from all other batches. The iron could originate from the catalyst (dppf as phosphine ligand), however, this ligand is rather unusual. Alternatively, the synthesis might also have been performed in steel reactors.

3.3. Optical spectroscopy

Optical spectroscopy can yield information about the crystallinity of the different P3HT batches used. In this case films were cast from pristine P3HT solutions and characterized as is. In Fig. 4 P3HT-III stands out as the most crystalline batch as can be seen by the multiple distinct peaks near the absorption onset. This is consistent with its material properties as stated in Table 4, specifically the low PDI, high regio-regularity (RR) and the high melting enthalpy [51]. However, the overall correlation between spectroscopic information and structural parameters reported above is not strong. In general it could be expected that more crystalline materials would be more stable and exhibit a slower degradation [3], in case blend stability dominates the degradation.

Photothermal deflection spectroscopy, of which results are depicted in Fig. 5, showed an increased absorption below the bandgap for P3HT-II, in agreement with the results from electron spin resonance spectroscopy (see below). The sub-bandgap absorption of the P3HT batches

Table 4

Polymer properties of the P3HT batches determined by GPC, TGA and DSC at Chalmers University.

Polymer	M_n (kg/mol)	M_w (kg/mol)	\bar{M}_w/\bar{M}_n (PDI)	RR (%)	T_D ($^\circ\text{C}$)	T_M ($^\circ\text{C}$)	T_C ($^\circ\text{C}$)	ΔH_M (J/g)
P3HT-I	30	59	2.0	96	455	237	201	18
P3HT-II	24	54	2.3	94	455	227	184	17
P3HT-III	11	22	2.0	96	455	227	197	20
P3HT-IV	26	71	2.7	90	456	222	189	14
P3HT-V	25	60	2.4	95	455	236	198	21

Table 5

Trace metal content of the different P3HTs used in the experiment. Determined by ICP-OES (nn = below detection limit).

P3HT Batch	Ca mg/L	Cu mg/L	Fe mg/L	K mg/L	Mg mg/L	Na mg/L	Ni mg/L	Pd mg/L	Sn mg/L	Zn mg/L
Blind Values	0.115	0.009	0.116	0.115	0.013	0.51	nn	nn	0.06	0.015
	0.101	0.008	0.092	nn	0.009	0.49	nn	nn	0.06	0.013
P3HT-I	0.806	0.024	0.083	0.33	0.481	3.158	0.046	nn	0.182	0.037
	0.789	0.025	0.084	0.347	0.487	3.135	0.057	nn	0.177	0.038
P3HT-II	1.077	0.014	0.153	0.145	0.131	3.081	0.045	nn	0.132	0.024
	1.085	0.014	0.15	0.168	0.132	3.082	0.043	nn	0.144	0.024
P3HT-III	1.051	0.01	0.179	0.173	0.107	3.41	0.013	nn	0.091	0.072
	1.035	0.01	0.188	0.177	0.106	3.367	0.014	nn	0.078	0.072
P3HT-IV	1.116	0.01	0.512	0.155	0.112	3.183	0.045	nn	0.068	0.072
	1.124	0.01	0.521	0.159	0.113	3.185	0.044	nn	0.076	0.073
P3HT-V	0.934	0.014	0.203	0.257	0.093	3.588	0.031	nn	0.133	0.021
	0.949	0.014	0.203	0.224	0.094	3.591	0.029	nn	0.155	0.022

show several known features. The first one is the peak centered at around 1000 nm which can be assigned to the P2 polaron transition [70], indicating minor p-doping of all batches of the pristine P3HT. It seems that this is most pronounced for P3HT-IV, and least pronounced for P3HT-I and -III. While P3HT-I contained relatively high content of trace metal impurities, P3HT-III had fewer impurities making an assignment of the polaron peak to trace metal contents difficult. However, P3HT-IV exhibited the highest content of Iron. Furthermore, we see an unstructured absorption between 700 and 900 nm which is most prominent in P3HT-II and -V. This might be caused by amorphous morphology resulting in increased tail absorption [71]. However, interestingly, the most disordered P3HT-IV batch exhibits a lower absorption in this range. A shallow defect state arising e.g. from chemical impurities could also explain this feature, which might increase the recombination rate in P3HT.

3.4. Electron spin resonance spectroscopy

Electron spin resonance is a useful method for determining radical concentrations in the material under investigation. In this study, radicals might originate from defects at the chain capping groups, some structural defects (e.g., stabilized tri(hetaryl)amine type radicals) or certain impurities possibly stemming from the synthesis and insufficient purification. Alternatively, radicals can belong to the polymer polaronic state formed as a result of the material oxidation (oxidative doping) while handling it in air. The concentrations of persistent radical species for the P3HT-batches was estimated using ESR spectroscopy (Table 6)

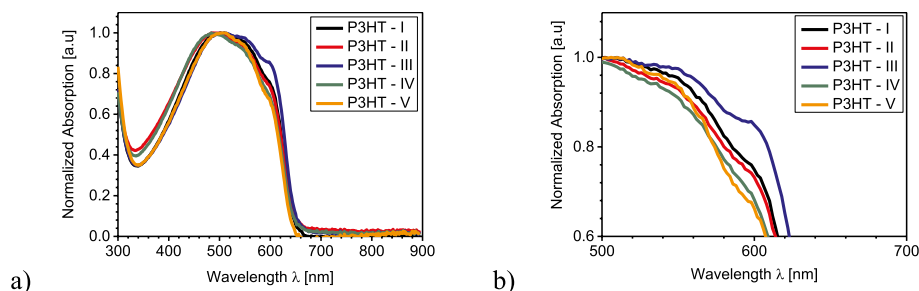


Fig. 4. UV/Vis spectroscopy results for pristine P3HT thin films of the respective P3HT batches, a) overview and b) details of the films. P3HT-III shows the highest crystallinity.

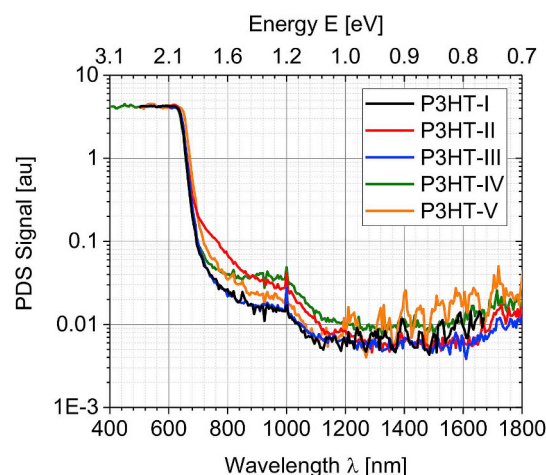


Fig. 5. Results of the photothermal deflection spectroscopy measurement on pristine P3HT films. All of them show some signature of doping, visible by the peak around 1000 nm.

following previously reported procedures [34,65,81,82]. We did not find any correlation with the molar masses of the polymer samples, which would be a reasonable expectation if the radicals are mostly induced by defected chain capping groups. The obtained radical concentrations could also not be related with the findings from the ICP-OES measurements (Table 5), as P3HT-II generally showed relatively small

Table 6

Experimental results of the ESR measurements on the pristine P3HT films.

P3HT Batch	Concentration of the radicals (spin/r.u.)
P3HT-I	7.94E-6
P3HT-II	3.98E-5
P3HT-III	1.45E-6
P3HT-IV	4.82E-6
P3HT-V	3.13E-6

levels of trace metals, but exhibits the highest radical concentration by ESR. However, some correlation could be found when comparing radical concentrations with PDS data: here P3HT-II showed the highest radical concentration in ESR, and also exhibited the strongest absorption between 700 – 900 nm in the sub-bandgap region of the PDS spectrum. On the other hand, P3HT-III exhibited not only the lowest sub-bandgap absorption, but also showed the lowest radical concentration obtained *via* ESR. However, the correlation does not hold very well for the other batches, *e.g.* P3HT-I, exhibiting the lowest concentration of polarons as by PDS (like P3HT-III), had a relatively high radical concentration. These observations suggest that radical

species identified in different samples of P3HT apparently have different origins.

Finally, it should be emphasized that concentration of radical species in all investigated P3HT samples is relatively low and should not impair the efficiency of the photovoltaic devices based on these materials as per previous findings [65]. The results of other characterization methods applied to the P3HT batches are displayed in the Supplementary Information, sections 5-8.

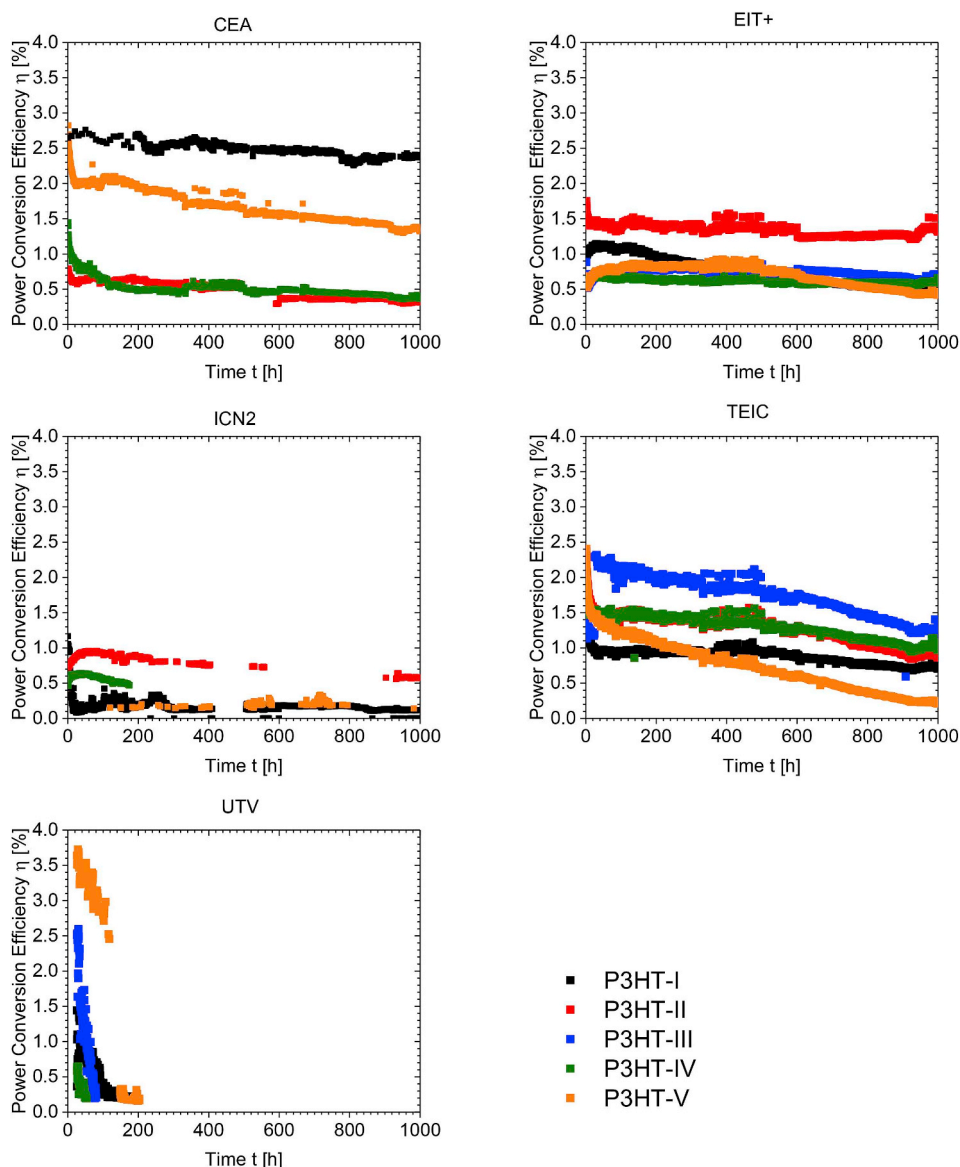


Fig. 6. Aging curves for organic solar cells of the different manufacturers (indicated in the title of each panel) from the ISOS-L2 measurements performed at CEEC Jena, with different P3HT-batches.

3.5. Results of controlled aging

3.5.1. ISOS-L2 degradation

3.5.1.1. Performance over time versus P3HT batches. The ISOS-L2 protocol provides an efficient way of accelerated testing of lifetimes. Stress factors like heat (here 55 °C in the shadow) and light (including UV-light) reveal operational weaknesses of photovoltaic devices. Due to space constraints here only the power conversion efficiency (PCE) over time curves are being displayed; see section 3.5.1.4, and the Supporting Information, section 9, for the time development of the other photovoltaic parameters.

Considering the characterization data from above, it might be expected that P3HT-I (for metal contamination) and P3HT-II batches (for radical concentration and sub-bandgap absorption) would lead to the fastest decay in performance. However, specifically these two batches yielded the best values for stability. Similarly, if we consider the extreme cases of the molecular properties, P3HT-III representing one of the most highly ordered, and P3HT-IV representing the least ordered among all, we can find a layer stack (TEIC) in which both perform similarly well and better than all others. These results – and the fact that there was no agreement among the different sets of devices originating from different cell producers concerning which P3HT batches lead to slower or faster degradation, makes correlating the lifetime data and the P3HT properties difficult.

The performance decay for the different cell producers, respectively their layer stacks applied, are shown in Fig. 6, while the corresponding ageing parameters based on various fit functions are summarized in Table 7. In order to check whether P3HT-batches do yield similar decay curves in different layer stacks, the ageing data is replotted with respect to the materials itself (Fig. 7). However, no clear correlation is found

between P3HT-batch and ageing slopes, thus the decay slopes generally seem to depend more on the layer stack (*i.e.*, cell producer) than on the actual P3HT-batch used.

A more consistent behavior was found for the rather stable (but sometimes at lower performance) operation of P3HT-I and P3HT-V, which seemed to degrade generally faster (smaller lifetime) than the other batches. Unfortunately, this behavior could not be related to any P3HT property, as the latter batch had no distinct properties under all of the characterization methods reported above.

It is interesting to note that cell producers who provided their own active layer material, obtained the most stable operation with exactly these materials. Thus, we may conclude here that experience with the material system seems to play a more dominant role in obtaining stable devices than the actual choice of P3HT-batch.

The most consistent ageing behavior was found for the devices made by TEIC, which always showed a bi-exponential decay function under ISOS-L2. Furthermore, TEIC cells demonstrated that with a sufficiently good encapsulation it is also possible to reach a relatively high lifetime with conventional architecture. The outstandingly highest device stability was reached by CEA with the self-provided P3HT batch (P3HT-I), leading to similar LEY values as reported in the literature [7]. It is interesting to note that also poorly encapsulated inverted devices failed faster than the conventional devices, which was most pronounced in the case of the UTV and ICN2 devices. This observation suggests the need to re-assess the inverted layer stacks concerning their inherent intrinsic stability problems.

The low stability observed for the UTV devices might be connected with the encapsulant Surlyn, as its glass transition temperature (T_g) is below 60 °C. Though the heating in the chamber was set to 55 °C in the shadow, the cell temperature can be expected to be considerably higher

Table 7

Results of curve fitting of the performance decay over time. Given are the fit function, the burn-in time T_s , efficiency after burn-in E_s , operational lifetime $T_{s,80}$ (or T_{80}) and efficiency at the end of nominal lifetime $E_{s,80}$ (or E_{80}). Finally the calculated lifetime energy yields (LEYs) for the L2 aged solar cells are given. See S59–S80 for the respective fits. (* - lifetime from data is infinite and thus was limited to the tenfold stressing time, # denotes catastrophic failure).

Manufacturer	P3HT Batch	Fit function	E_s (%)	T_s (h)	$E_{s,80}$ or E_{80} (%)	$T_{s,80}$ or T_{80} (h)	LEY (kWh/m ²)
CEA	P3HT-I	Exp	-	-	2.32	2241	52.9
	P3HT-II	Lin	-	-	0.55	355	2.16
	P3HT-III						
	P3HT-IV	BiExp	0.56	172	0.44	826	4.44
	P3HT-V	BiExp	1.84	24	1.47	509	9.56
EIT+	P3HT-I	Exp	-	-	0.93	229	2.39
	P3HT-II	BiExp	1.44	16	1.15	1594	20.5
	P3HT-III	Lin	-	-	0.65	1088	8.01
	P3HT-IV	Lin	-	-	0.53	1547	9.18
	P3HT-V	LogLin	0.85	180	0.56	784	5.81
ICN2	P3HT-I	BiExp	0.22	35.9	0.17	10000*	14.6
	P3HT-II	Exp	-	-	0.76	458	3.9
	P3HT-III	-	-	-	-	-	-
	P3HT-IV	Exp	-	-	0.55	114 [#]	0.70 [#]
	P3HT-V	BiExp	0.15	437	0.12	7248	9.83
TEIC	P3HT-I	BiExp	1.02	21	0.81	733	6.71
	P3HT-II	BiExp	1.6	24	1.27	454	6.56
	P3HT-III	Lin	-	-	1.79	458	9.23
	P3HT-IV	BiExp	1.47	11	1.26	546	7.71
	P3HT-V	BiExp	1.46	22	1.16	155	2.11
UTV	P3HT-I	Lin	-	-	0.91	34 [#]	0.35
	P3HT-II	-	-	-	-	-	0
	P3HT-III	Lin	-	-	2.43	17 [#]	0.45
	P3HT-IV	Lin	-	-	0.67	14 [#]	0.1
	P3HT-V	Lin	-	-	3.62	40 [#]	1.61

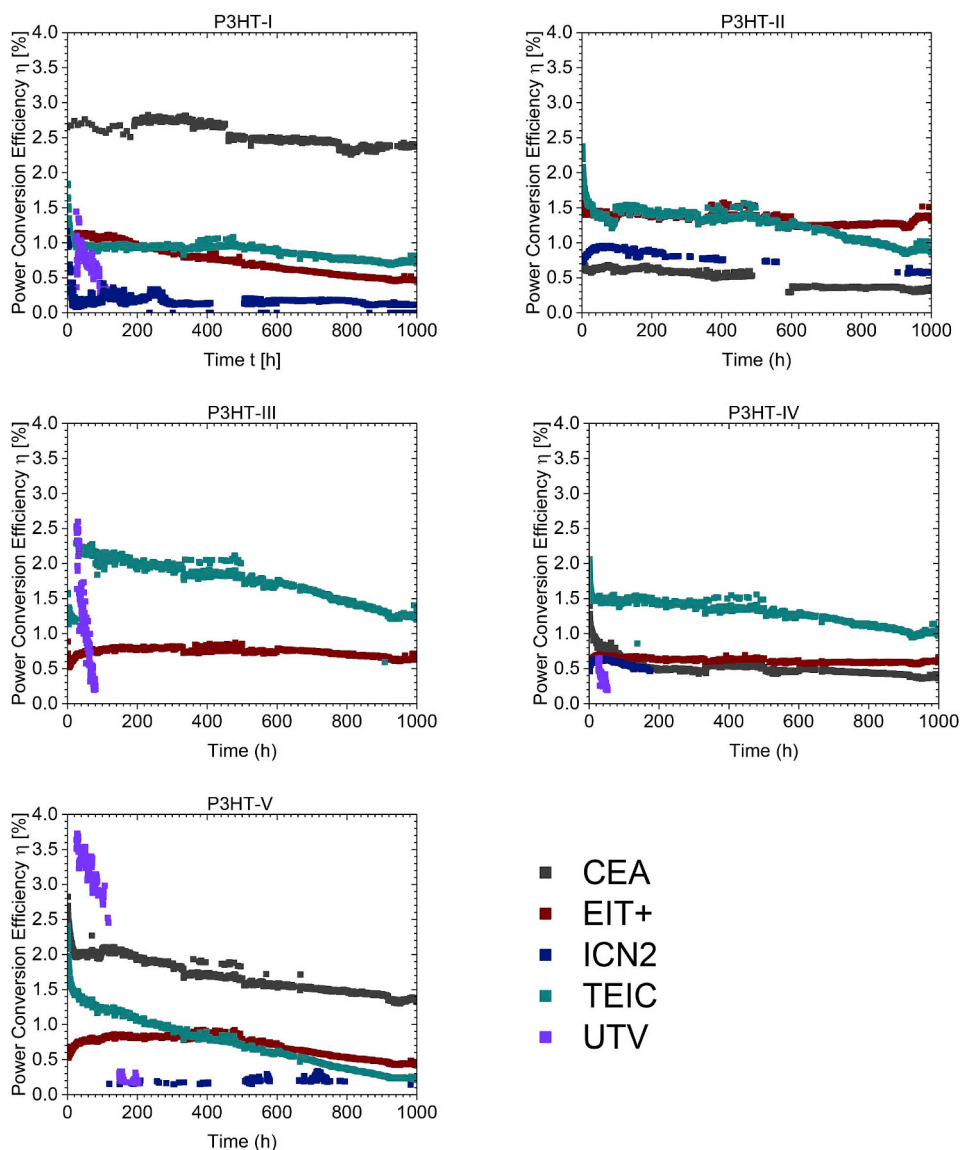


Fig. 7. ISOS-L2 aging data plotted for individual P3HT-batches (indicated in the title of each panel) for solar cell producer, respectively, their device layout.

owing to direct exposure to full light spectrum and associated heating effects. As diffusivity suddenly increases above T_g , especially oxygen ingress might have happened at an increased rate. This assumption is supported by the fact that the Surlyn encapsulation layer is thicker than the epoxy layers used and thus can lead to higher ingress rates and then serve as a larger reservoir for oxygen [83,84].

3.5.1.2. Performance over time versus cell producer. In Fig. 7 it is clearly visible that the cell producer, *i.e.* the device layout, is more dominating the aging behavior than the P3HT. The same P3HT batch exhibits strongly varying aging behavior for the different producers, like P3HT-I which shows a nearly linear decay for EIT+, though showing a bi-exponential decay behavior for TEIC and a more or less constant operation in case of CEA. The burn-in behavior for the individual P3HTs is independent of the P3HT batch used as can be seen from the aging curves of each producer. Hence the degradation of the interfaces and interfacial and electrode materials (partially influenced by the sealing) have a larger impact, than the variation of polymer properties found in the P3HTs used for the experiment.

3.5.1.3. Evaluation of lifetime energy yield (LEY). CEA and EIT+ demonstrated record LEYs of $\sim 53 \text{ kWh/m}^2$ and 20 kWh/m^2

based on devices built with their self-provided material P3HT-I and P3HT-II, respectively (see Tables 2 and 7). This fact is unexpected, as P3HT-II exhibits considerably different material properties than P3HT-I, and the low performance in EIT+ devices cannot be explained. Among the other materials, maximum LEY values of ca. 10 kWh/m^2 were reached, for P3HT-III by TEIC, for P3HT-IV by EIT+ and for P3HT-V by ICN2. In general, the aging characteristics obtained by one producer were not identical for the different materials used. In case of P3HT-I based solar cells built by CEA the first 200 h are missing due to some contact problem observed only later. As no burn-in was observed, it may be highly probable that this device completed burn-in before reconnection occurred. From the best stabilities obtained for the record devices of CEA and EIT+ some further conclusion concerning the hole extraction layer can be made: CEA used inverted architecture with PEDOT:PSS, while EIT+ used MoO_3 for hole extraction. Thus, at least PEDOT:PSS cannot be claimed responsible for yielding insufficient OPV stability. For completeness it should be mentioned that the total device area is not a relevant parameter for stability, as these two cell producers delivered the largest and the (nearly) smallest solar cell areas. Further data of LEY analysis of L2 degradation experiments can be found in the Supplementary Information, section 13.

3.5.1.4. Remarkable exceptions. The highest stability in terms of lifetime was generally shown by P3HT-I cells. A remarkable exception was observed for P3HT-I cells provided by ICN2: while devices generally suffered from insufficient encapsulation, this device basically showed an “eternal” lifetime (no slope), however, at a very low performance level ($< 0.2\%$ PCE). We decided to cut the lifetime at 10000 h, as further extrapolation to longer lifetimes is not really supported by an about 1000 h lasting ageing experiment.

3.5.1.5. Photovoltaic parameters. In the following the photovoltaic parameters of L2-aged devices are briefly reviewed. All solar cells showed a short and very small burn-in of the open-circuit voltage under L2 conditions, which can be seen in [Figures S12, S15, S18, S21 and S24](#). This can be explained either by an increase in energetic disorder, which is rather unlikely due to the crystalline nature of P3HT²⁵, or more likely by a slight increase in crystallinity in the material due to light and heat stress and thereby a change of the energetic landscape along the donor/acceptor interface [85].

Except for a few devices, all showed the rather common burn-in with a bi-exponential decay behavior of the short circuit current density for P3HT, see [Figures S13, S16, S19, S22 and S25](#). This is a well-known feature for P3HT:PCBM solar cells and an important contributor to this decay is the increase in phase separation between P3HT and PCBM, which leads to a reduction of interfacial area where excitons could be separated and thereby to a reduction in photocurrent generated [6,86]. Notable exceptions are all of the devices by EIT+, see [Fig. S16](#), which initially show an increase in photocurrent followed by a nearly linear decay. This increase in photocurrent could indicate further annealing under light and elevated temperature. Another option for this initial increase might also be the necessity for photo-activation of the ETL material [87]. Interestingly, the most stable device of CEA [86] processed with P3HT-I was limited by a slowly decaying short circuit current, while the other photovoltaic parameters were virtually constant.

Finally, the fill factor showed some very interesting differences for some cases even among cells of one manufacturer. For CEA L2, [Fig. S14](#), P3HT-I showed a constant FF for the entire experiment. This might be connected to its high crystallinity and no further annealing occurring during the aging process, as well as no formation of major barriers between the different interface layers. P3HT-IV and P3HT-V, in contrast, showed a burn-in followed by a linear decay. A reason for this might be the formation of barrier layer for extraction, doping induced space-charge or an increase in disorder in the active layer material. For EIT+, see [Fig. S17](#), there was nearly an identical behavior in fill factor for all the different materials, which suggests that the behavior of the cells was fully determined by the device layout and the large series resistance. Interestingly, the fill factor of 30% constitutes the limiting parameter for the performance of the most stable device, processed from P3HT-II. There was a fast exponential burn-in followed by a nearly linear weak decay afterwards. There is a slight difference in the slope of the linear part of the decay curve, which might be due to differences in the P3HT-batches. ICN2 showed rather low fill factors already from the start, see [Fig. S20](#), but P3HT-II showed first an increase in FF followed by a linear decay. This might be related to an annealing process of the cell, which induces more crystallinity, followed by ingress of oxygen and trap formation [26]. However, the value of 25% found for several devices is due to a shunting problem. TEIC cells, see [Fig. S23](#), showed, with the exception of P3HT-I, a nearly constant linear decay of the fill factor. This is most likely connected with the oxidation of the low work function metal electrodes of this conventional device architecture.

The most durable solar cell exhibited – as expected – an inverted architecture, and reached a LEY above 52 kWh/m [2]. Due to avoiding low work-function metals, inverted architectures are less susceptible to moisture and oxygen ingress, which can corrode the low work function metal rapidly. The major issues found with proper encapsulation and resulting electrode corrosion as a reason for early failure, pronounce

again the importance of a) a good sealing and b) in an inverted architecture to be more resilient against any breach of encapsulation.

We found that with a proper encapsulation even conventional devices can be rather stable, which can be seen in the LEYs achieved by the TEIC devices. On the other hand, as stated earlier, with a sub-optimal encapsulation not even an inverted architecture can avoid drastic failures, as can be seen in the cases of ICN2 and UTV cells.

3.5.1.6. Usefulness of L2 for stability experiments. The ISOS-L2 protocol allows determining the photostability of devices in an accelerated way. In combination with ISOS-D2 characterization the effect of the elevated temperature can be deconvoluted in order to learn about the pure light stability. Hence the performance decay observed in L2 should be expected to be more than for O1 and D2, assuming a perfect encapsulation and a sufficiently long measurement period. L2 ageing might also allow for drawing conclusions about the lifetime of a device under realistic operation in the field (outdoors). It is assumed that a lifetime of 1000–2000 h under L2 roughly corresponds to a lifetime of 1 year in the field under stable sealing [5]. Thus the most stable devices of this study correspond to about 1–5 years operational stability in the field.

3.5.2. External quantum efficiency for L2-Ageing

Besides the pure stability and performance information, external quantum efficiency (EQE) measurements can yield additional information. In accordance with its high crystallinity, solar cells processed with P3HT-I commonly have an absorption onset towards longer wavelengths than those of the other P3HT batches (see [Fig. 8](#)). In case of the inverted device structure (here CEA, EIT+, and ICN2) the spectral response remains stable in its qualitative characteristics. However, for the only conventional device architecture (TEIC) an interesting effect is observed: upon aging the regions exhibiting highest absorption by P3HT-I show lower charge extraction for the L2 aged device. This may refer to an unfavorable vertical material gradient that inhibits charge extraction from a certain region of the device, where a higher P3HT-I concentration is present. This could be due to a build-up of a space charge region within the active layer, where a higher concentration of P3HT-I is present [88]. However, this effect takes place already early during aging, specifically during the burn-in process, and thereafter the performance remains fairly stable – in fact this was the most stable of all devices processed in conventional architecture. Thus this type of burn-in degradation might be best related to the relatively high number of metal impurities, as well as radical concentrations, as found by ICP-OES and ESR. However, in unprocessed pristine P3HT-I fairly low polaron densities (PDS) were found, indicating that only the combination of light and metal impurities may play a dominant role here for the generation of space charge. As the overall behavior of all

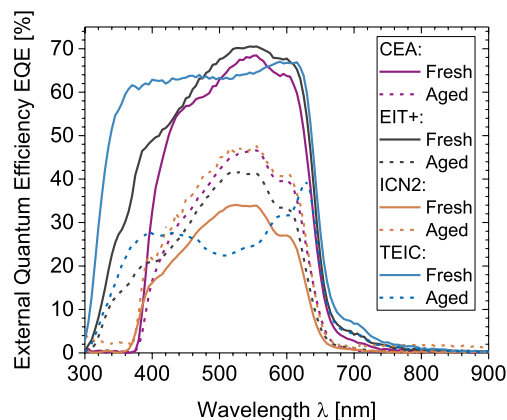


Fig. 8. EQE spectra for P3HT-I solar cells from different manufacturers before and after L2 aging.

devices cast from this P3HT-I is relatively stable (as seen by the long lifetimes), the observed losses should in all cases be related to space charge built up due to inherent impurities present in the material from the beginning. Thus, we may speculate that the same P3HT without the space charge would yield much higher performances for longer times. Further data of EQE measurements related to L2 degradation experiments can be found in the Supplementary Information, section 12.

Upon comparison of the EQE-data with the ageing data of the photocurrent from ISOS-L2 we can find a severe deviation for the CEA-P3HT-I sample between the photocurrent measured under the solar simulator ($\sim 8 \text{ mA/cm}^2$) and the one from integration of the EQE-curve and multiplication with a hypothetical AM 1.5 spectrum: the EQE-curve delivers only 5.72 mA/cm^2 . This deviation could be assigned to trap-assisted charge recombination or an extraction barrier in the low-light level case, which can be overcome by trap-filling for higher excitation densities. A similar effect was recently observed in P3HT-PCBM cells [89]. It is interesting to note that already in the beginning of the experiment, light bias yielded a gain in photocurrent for the same device, see Fig. 9. Unfortunately, no EQE with bias measurements were performed after the L2-ageing.

3.5.3. ISOS-D2 degradation

In contrast to our expectation, the photovoltaic devices suffered on average more degradation under dark storage at elevated temperatures (ISOS-D2), seen in Fig. 10, than under accelerated laboratory weathering (ISOS-L2). Notable exceptions were found only for EIT+ and TEIC devices, which showed higher performances than under L2. In case of the EIT+ solar cells drastic device failure is visible for P3HT-II, indicating breakage of the sealing. This hints that for these configurations the thermal stability is much more relevant than the light stability. However, even for the case presented here, where the L2 ageing took place at slightly lower temperatures of $55 \text{ }^\circ\text{C}$ in the shadow, similar temperatures are to be expected within the devices for L2, as the light absorption itself must inevitably lead to heating. Further this means that EIT+ cells show a good thermal stability, while their photo-stability is lower than those of the other cells. This might be connected to light-induced doping effects arising from the MoO_3 hole transport layer. On the other hand, devices produced by UTV and ICN2 exhibited similarly low stability as under L2, indicating degradation mechanisms to be independent of light. In general, it should be noted that insufficient sealing effects may have played a more important role under D2 than under L2 aging, as for D2 not the innermost devices were chosen, but rather the best performing ones.

An interesting deviation appeared for the TEIC solar cells, which did not show a fast burn-in, but rather a linear long-term decay. This hints to a light induced rather than a thermally induced process for the burn-in, independent of the P3HT batch used. Furthermore, the CEA cells degraded severely, independent of the P3HT batch, indicating a thermally driven process that might be prevented (at least for the most stable P3HT-I batch) under illumination. Finally, it should be noted that the highest performing devices (yielding also highest hypothetical LEYs) provided by EIT+ were obtained with the already identified superior P3HT-batches I and II. Further data of D2 degradation experiments can be found in the Supplementary Information, section 10.

3.5.4. ISOS-O1 degradation

The observations made for dark ageing under elevated temperatures could in part also be found for ISOS-O1, see Fig. 11. As a matter of fact, the EIT+ devices outperformed in terms of stability for this ageing condition those aged under L2. Again, the identified superior P3HT-batches, namely I and II, yielded the best performance over time here. Noteworthy are the devices provided by TEIC: although they showed considerable degradation following exponential decays, there was no indication of drastic failure. This confirms the superiority of the encapsulation used in this case over the other device layouts. In case of the remaining cell producers, drastic failure was observed in all cases,

independent of the P3HT batch used. Hence the conditions even under this modified outdoor ageing seemed to be dominated by environmental impacts such as water or oxygen ingress. Interestingly, ICN2 solar cells based on the P3HT-batches I and II also outperformed the other batches, confirming their superiority. However, such exceptions were not observed in case of CEA, TEIC and UTV, where rather a material independent degradation was found. Further data of O2 degradation experiments can be found in the Supplementary Information, section 11.

3.6. Païos results

It has been shown that by a combination of various transient and impedance experiments, and a complementary data analysis, certain aging mechanisms can be revealed by their specific signatures [73,74]. For example, an overshoot observed in the transient photocurrent is a trace of charge accumulation (space charge), which can occur due to trapping or an energetic barrier for charge extraction. The impedance signal of the two cases (trapping or energetic barrier), however, looks different, and therefore allows distinguishing between the two mechanisms. Another example is charging of the active layer (doping), which can be determined by combining impedance and CELIV measurements.

Unfortunately, no systematic behavior for devices of the same producer or using the same P3HT batch could be found. We identified two main reasons for this: i) the low reproducibility in cells obtained make a cell-to-cell comparison erroneous, ii) the significantly differing stack architectures and sample geometries turn out to have an enormous impact on the initial cell performances and their stability. Yet, several conclusions can be drawn from this supplementary experiment.

In order to perform transient measurements small devices with a low RC time constant are required. This is, however, not only a necessary condition for analytic models to be valid [90], but also impacts any electrical measurement on the device. Large resistance values have been found in all cells produced by EIT+ using the Osilla layout, which is mainly due to the un-metallized ITO contact. A series resistance of 200 Ohm already affects the steady-state performance of the device and should therefore be avoided. This observation nicely agrees with the observed low fill factors. The UTV layout, on the other hand, showed negligible contact resistances.

We further found shunting by leakage currents to be a major failure mechanism. Here devices by UTV, ICN2, and EIT+ were most sensitive, and the O1-aged devices showed more severe shunting than L2-aged ones. The underlying mechanisms for this behavior are however not understood.

Another important conclusion from the Païos measurements is that encapsulation failure, leading to the lateral in-diffusion of oxygen and water vapor, can superimpose to the degradation process of the active

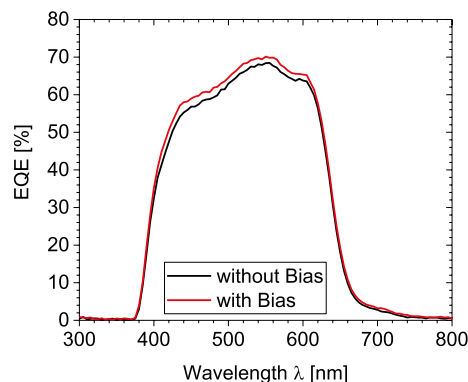


Fig. 9. EQE measurement with and without bias light for CEA-P3HT-I cell before L2 degradation determined at CEEC Jena.

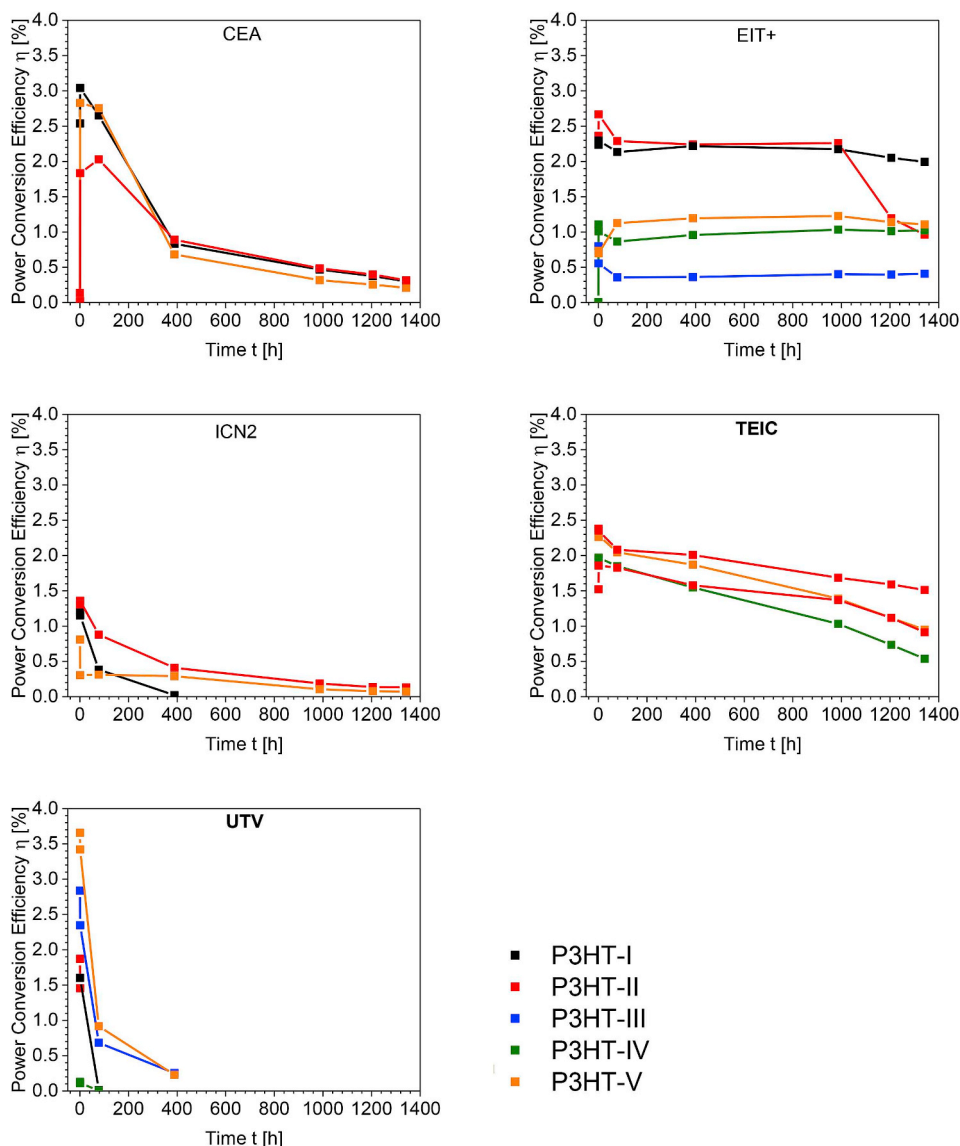


Fig. 10. Aging data from ISOS-D2 experiment done by Solliance in Eindhoven.

layer and will induce additional pathways for degradation which should be prevented. The inhomogeneous oxidation of the metal electrode from the sample edges forms an insulating oxide layer hampering charge extraction. A prominent signature of this process is a strong overshoot in the transient photocurrent signal [74].

Fig. 12 shows an example of a TEIC sample, where the outer devices show more severe degradation due to the failure of the encapsulation adhesive. The further to the edge the cells were, the weaker was the measured signal, which shows there was ingress of oxygen and moisture through the encapsulation. This effect was found more pronounced in cells aged under L2 at CEEC Jena than under O1 in the Negev. We therefore speculate that it is driven by the oxygen diffusion, supported by elevated temperatures under L2 conditions [91].

4. Discussion

Two P3HT-batches showed in several cases – however, not consistently over all cell producers – exceptional stability: P3HT-I and P3HT-II. However, these two batches exhibit significantly different materials properties:

P3HT-I, yielding the exceptionally high LEY of 53 kWh/m^2 under accelerated ISOS-L2 ageing, is distinguished from the other batches by

its high crystallinity; however, P3HT-III showed in the optical characterization the strongest aggregate absorption [92,93]. Furthermore, P3HT-III remained similarly inconspicuous concerning sub-bandgap absorption like P3HT-I. However, except for TEIC cells based on P3HT-III under outdoor degradation (ISOS-O1), this P3HT-batch rather underperformed in all stress tests compared to the other cell producers. The fact that P3HT-III exhibited the lowest radical and trace metal concentrations of all batches, seems to make this material property rather insignificant concerning its impact on yielding stable organic solar cells. Thus, the only remaining material parameter that could be blamed for the low stability can be the exceptionally low molar mass of this batch, roughly three times lower than all others. Microscopically, the low molar mass might be connected to an unfavorable phase behavior; either unsuitable crystallization leading to phase separation and thus loss in charge generation and diode characteristics, or vertical phase segregation reducing the fill factor and potentially the open-circuit voltage as well. It is known that lower molar mass P3HT samples lead to high crystallinity, while higher molar mass result in different crystallites due to chain backfolding [51,94,95]. Besides the fact that several devices based on P3HT-III were missing out from the studies, this batch gave usually the lowest open-circuit voltages, except for the UTV devices where it yielded the highest ones. The difference that UTV

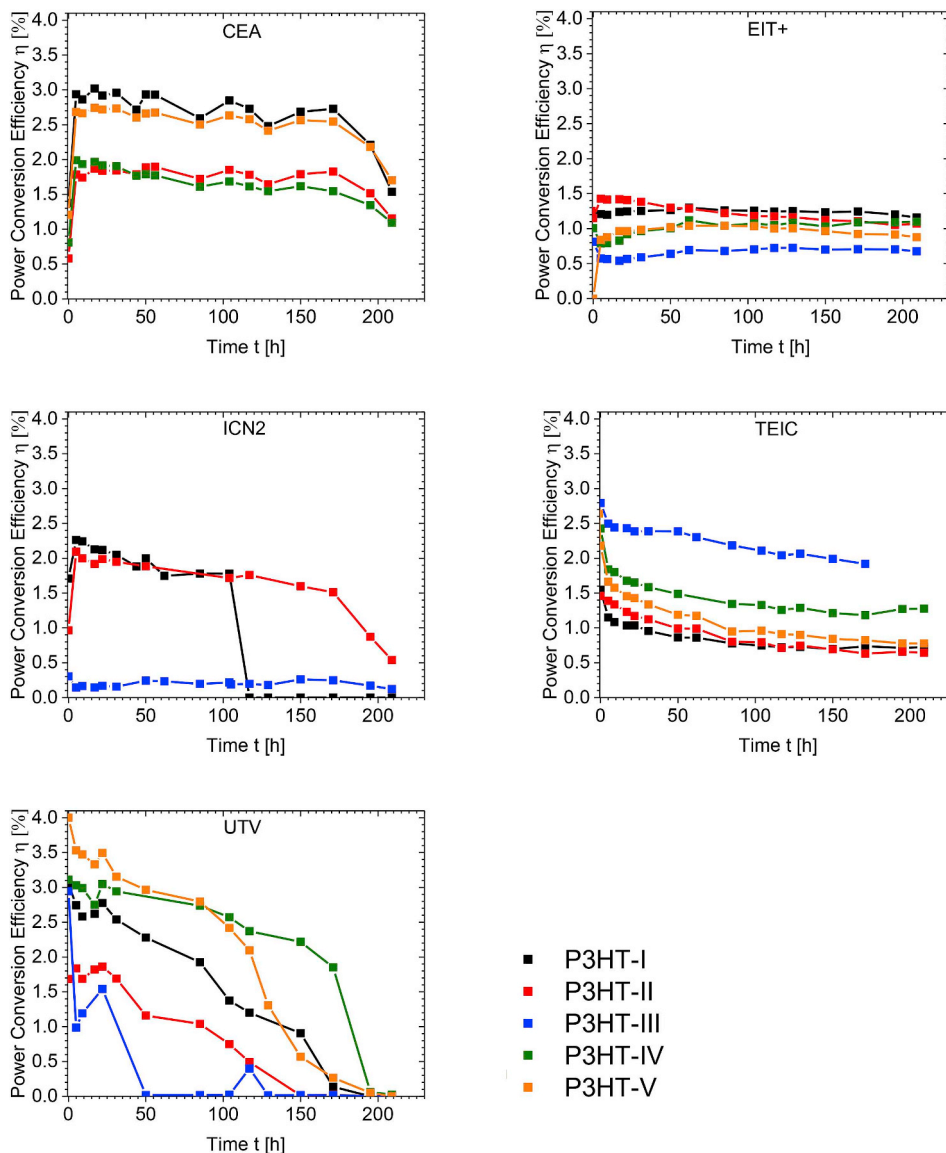


Fig. 11. Aging data for ISOS-O1 measurements performed at BGU in Sede Boqer in Israel.

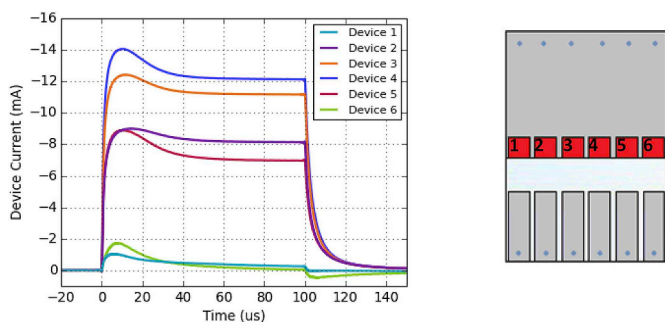


Fig. 12. Transient photocurrent results for TEIC solar cells after aging.

devices showed with respect to all others must be connected to its electron extraction layer, which consisted of PEIE. This seems to make a big difference, potentially preventing interfacial recombination otherwise leading to a reduction of the quasi-Fermi level splitting. Getting back to P3HT-I and its properties, we may take the sub-bandgap absorption as the only remaining factor to take into account. Thus, low intrinsic doping levels and well-ordered domains, while keeping the molar mass large enough, seem to display a necessity for reaching long

lifetimes at appreciable performances.

The second best result for lifetime energy yields was obtained with P3HT-II (by EIT+), although it exhibited rather opposite material properties than P3HT-I in all cases. However, its LEY remained below one half of that obtained by CEA with P3HT-I under ISOS-L2 conditions, clearly making this batch second choice. Part of the explanation for a LEY of $\sim 20 \text{ kWh/m}^2$ thus should be assigned to the experience by EIT+ with this material, as it was (as in the case of P3HT-I and CEA) provided by this lab. This reason might be also responsible for comparable performances between P3HT-I and -II obtained by EIT+ in the other ageing tests (D2, O1). Thus it may be concluded that experience with a material system plays a major role in getting stable performances.

Unfortunately, not all cell producers could reproduce these results: in two cases (ICN2, UTV) this was not possible due to insufficient encapsulation of the devices, leading to extrinsic degradation becoming dominant. However, concerning the layers involved it might be indicated that PEIE is less suitable than ZnO for long-term stable electron extraction and V_2O_5 might be less stable than MoO_3 and PEDOT:PSS. The most reliable sealing of samples could be demonstrated by EIT+ and TEIC, specifically for the ageing tests obtained under ISOS-D2 and ISOS-O1. This means that – at least for glass-glass sealing – also

conventional devices exhibiting PEDOT:PSS layers can reach substantially high intrinsic stabilities.

The experience gained from this collaboration experiment could be summarized as follows: if cell producers are confronted with new material systems with which they have no processing experience, a longer preparation and training time before providing devices for ageing tests is required. Of course a proper sealing method and corresponding encapsulation materials are required. Furthermore, improved statistics obtained by averaging over more devices may provide more reliability in ageing characteristics. The fewer devices take part in such an ageing experiment, the higher is the risk of losing devices due to catastrophic failures, which drastically lowers the chance for finding correlations between materials or layer stack properties. Finally, the design of the ageing experiments should be such that a sufficient amount of data points ($\gg 10$) over time to enable a reliable fitting procedure, leading to a well-predictable long-term behavior.

According to the data, large lifetimes alone seem not to be an appropriate way of expressing the stability, since severe performance losses during burn-in would be disregarded. Hence we have chosen to use the determination of the lifetime energy yield (LEY), as this parameter combines lifetime and performance into one figure of merit, which expresses the usefulness of the solar cells in applications. This analysis is also of vital importance for solar cells with reversible degradation, for instance for perovskite-based photovoltaics [96].

5. Conclusion

In conclusion, though the overall statistics in this experiment were challenging due to partially insufficient encapsulation and thus extrinsic degradation, some rules concerning the materials properties could be found, which can help to develop intrinsically more stable organic photovoltaic devices. In case of the semi-crystalline organic semiconductor poly(3-hexyl-thiophene), high crystallinity, sufficiently high molar mass and minimum intrinsic doping levels, as well as minimal disorder as found by photothermal deflection spectroscopy, are beneficial parameters contributing to stable photovoltaic operation. Interestingly, trace metal contents and radical concentrations seem to have no remarkable impact on device stability.

Furthermore, we found that the burn-in behavior of organic solar cells is mostly dependent on the layer stack. This means that part of the burn-in may stem from a) electrodes, b) transport layers, c) interfacial changes at the layer boundaries, d) differences in phase segregation of the active layer (i.e. stratification) due to different surface energies of the adjacent layers, or from e) a combination of the aforementioned factors.

In addition, experience with a certain material system seems to be an important parameter contributing to achieving relatively stable solar cells. Finally, the common suspect for insufficient organic solar cell stability, PEDOT:PSS, seems to perform better than its reputation, since the best devices in this comparison obtained with it in an inverted device architecture show competitive lifetime energy yields of more than 50 kWh/m [2].

Acknowledgements

All authors are grateful for support from COST Action MP 1307, “StableNextSol”. This article is based upon work from COST Action StableNextSol project MP1307, supported by COST (European Cooperation in Science and Technology). RM, TF, DF, RR and HH are grateful for financial support within the frame of “AIMS in OPV” junior research group by the BMBF, Germany. L.C. is thankful to ENEA (Ente Nazionale Energia e Ambiente) and the Italian Ministry of Foreign Affairs for a visitor post-doc fellowship to BGU. FG and MD are grateful for financial support by the National Center for Research and Development within the Project POSCIS under Grant No. LIDER/09/129/L-3/11/NCBR/2012). IVF and EAK acknowledge financial support

from Adelis Foundation. N. Blaubach is acknowledged for ICP measurements. MP thanks the Bundesministerium für Bildung und Forschung, Germany (BMBF FKZ 03EK3507).

Appendix A. Supplementary data

Supplementary data to this article can be found online at <https://doi.org/10.1016/j.solmat.2019.110151>.

References

- [1] W. Zhao, S. Li, H. Yao, S. Zhang, Y. Zhang, B. Yang, J. Hou, Molecular optimization enables over 13% efficiency in organic solar cells, *J. Am. Chem. Soc.* 139 (2017) 7148–7151.
- [2] Z. Xiao, X. Jia, L. Ding, Ternary organic solar cells offer 14% power conversion efficiency, *Sci. Bull.* 62 (2017) 1562–1564.
- [3] W.R. Mateker, M.D. McGehee, Progress in understanding degradation mechanisms and improving stability in organic photovoltaics, *Adv. Mater.* 29 (2017) 1603940.
- [4] R. Roesch, K.-R. Eberhardt, S. Engmann, G. Gobsch, H. Hoppe, Polymer solar cells with enhanced lifetime by improved electrode stability and sealing, *Sol. Energy Mater. Sol. Cells* 117 (2013) 59–66.
- [5] C.H. Peters, I.T. Sachs-Quintana, J.P. Kastrop, S. Beaupré, M. Leclerc, M.D. McGehee, High efficiency polymer solar cells with long operating lifetimes, *Adv. Energy Mater.* 1 (2011) 491–494.
- [6] S.A. Gevorgyan, I.M. Heckler, E. Bundgaard, M. Corazza, M. Hösel, R.R. Søndergaard, G.A. dos Reis Benatto, M. Jørgensen, F.C. Krebs, Improving, characterizing and predicting the lifetime of organic photovoltaics, *J. Phys. Appl. Phys.* 50 (2017) 103001.
- [7] N. Gasparini, M. Salvador, S. Strohm, T. Heumueller, I. Levchuk, A. Wadsworth, J.H. Bannock, J.C. de Mello, H.-J. Egelhaaf, D. Baran, I. McCulloch, C.J. Brabec, Burn-in free nonfullerene-based organic solar cells, *Adv. Energy Mater.* 7 (2017) 1700770.
- [8] S.A. Gevorgyan, N. Espinosa, L. Ciammaruchi, B. Roth, F. Livi, S. Tsopanidis, S. Zuffe, S. Queiros, A. Gregori, G.A.D. Benatto, M. Corazza, M.V. Madsen, M. Hoesel, M.J. Beliatas, T.T. Larsen-Olsen, F. Pastorelli, A. Castro, A. Mingorance, V. Lenzi, D. Fluhr, R. Roesch, M.M.D. Ramos, A. Savva, H. Hoppe, L.S.A. Marques, I. Burgess, E. Georgiou, L. Serrano-Lujan, F.C. Krebs, Baselines for lifetime of organic solar cells, *Adv. Energy Mater.* 6 (2016) 9.
- [9] S. Rafique, S.M. Abdullah, K. Sulaiman, M. Iwamoto, Fundamentals of bulk heterojunction organic solar cells: an overview of stability/degradation issues and strategies for improvement, *Renew. Sustain. Energy Rev.* 84 (2018) 43–53.
- [10] S.A. Gevorgyan, M.V. Madsen, H.F. Dam, M. Jørgensen, C.J. Fell, K.E. Anderson, B.C. Duck, A. Mescheloff, E.A. Katz, A. Elschner, R. Roesch, H. Hoppe, M. Hermenau, M. Riede, F.C. Krebs, Interlaboratory outdoor stability studies of flexible roll-to-roll coated organic photovoltaic modules: stability over 10,000 h, *Sol. Energy Mater. Sol. Cells* 116 (2013) 187–196.
- [11] R. Roesch, T. Faber, E. von Hauff, T.M. Brown, M. Lira-Cantu, H. Hoppe, Procedures and practices for evaluating thin-film solar cell stability, *Adv. Energy Mater.* 5 (2015) 24.
- [12] M.O. Reese, S.A. Gevorgyan, M. Jørgensen, E. Bundgaard, S.R. Kurtz, D.S. Ginley, D.C. Olson, M.T. Lloyd, P. Moryllo, E.A. Katz, A. Elschner, O. Haillant, T.R. Currier, V. Shrotriya, M. Hermenau, M. Riede, K.R. Kirov, G. Trimmel, T. Rath, O. Inganas, F.L. Zhang, M. Andersson, K. Tvingstedt, M. Lira-Cantu, D. Laird, C. McGuinness, S. Gowrisanker, M. Pannone, M. Xiao, J. Hauch, R. Steim, D.M. DeLongchamp, R. Rosch, H. Hoppe, N. Espinosa, A. Urbina, G. Yaman-Uzunoglu, J.B. Bonekamp, A. van Bremen, C. Grotto, E. Voroshazi, F.C. Krebs, Consensus stability testing protocols for organic photovoltaic materials and devices, *Sol. Energy Mater. Sol. Cells* 95 (2011) 1253–1267.
- [13] H. Cha, J. Wu, A. Wadsworth, J. Nagitta, S. Limbu, S. Pont, Z. Li, J. Searle, M.F. Wyatt, D. Baran, J.-S. Kim, I. McCulloch, J.R. Durrant, An efficient, “burn in” free organic solar cell employing a nonfullerene electron acceptor, *Adv. Mater.* 29 (2017) 1701156.
- [14] M.V. Madsen, K. Norrman, F.C. Krebs, Oxygen- and water-induced degradation of an inverted polymer solar cell: the barrier effect, *J. Photonics Energy* 1 (2011) 011104.
- [15] P. Cheng, X. Zhan, Stability of organic solar cells: challenges and strategies, *Chem. Soc. Rev.* 45 (2016) 2544–2582.
- [16] K. Norrman, F.C. Krebs, Lifetimes of organic photovoltaics: using TOF-SIMS and 18O 2 isotopic labelling to characterise chemical degradation mechanisms, *Sol. Energy Mater. Sol. Cells* 90 (2006) 213–227.
- [17] H. Hintz, H.J. Egelhaaf, H. Peisert, T. Chassé, Photo-oxidation and ozonization of poly(3-hexylthiophene) thin films as studied by UV VIS and photoelectron spectroscopy, *Polym. Degrad. Stab.* 95 (2010) 818–825.
- [18] M.S. White, D.C. Olson, S.E. Shaheen, N. Kopidakis, D.S. Ginley, Inverted bulk-heterojunction organic photovoltaic device using a solution-derived ZnO underlayer, *Appl. Phys. Lett.* 89 (2006) 87–90.
- [19] a) S. Bertho, G. Janssen, T.J. Cleij, B. Conings, W. Moons, A. Gadisa, J. D’Haen, E. Goovaerts, L. Lutsen, J. Manca, D. Vanderzande, Effect of temperature on the morphological and photovoltaic stability of bulk heterojunction polymer:fullerene solar cells, *Sol. Energy Mater. Sol. Cells* 92 (2008) 753–760;
b) D.E. Motaung, G.F. Malgas, C.J. Arendse, Insights into the stability and thermal degradation of P3HT:C60 blended films for solar cell applications, *J. Mater. Sci.* 46

- (2011) 4942–4952.
- [20] B. Gholamkhash, S. Holdcroft, Toward stabilization of domains in polymer bulk heterojunction films, *Chem. Mater.* 22 (2010) 5371–5376.
- [21] M. Manceau, A. Rivaton, J.-L. Gardette, S. Guillerez, N. Lemaître, Light-induced degradation of the P3HT-based solar cells active layer, *Sol. Energy Mater. Sol. Cells* 95 (2011) 1315–1325.
- [22] a) M. Manceau, E. Bundgaard, J.E. Carlé, O. Hagemann, M. Helgesen, R. Søndergaard, M. Jørgensen, F.C. Krebs, Photochemical stability of π -conjugated polymers for polymer solar cells: a rule of thumb, *J. Mater. Chem.* 21 (2011) 4132; b) M. Manceau, S. Chambon, A. Rivaton, J.L. Gardette, S. Guillerez, N. Lemaître, Effects of long-term UV-Visible light irradiation in the absence of oxygen on P3HT and P3HT: PCBM blend, *Sol. Energy Mater. Sol. Cells* 94 (2010) 1572–1577.
- [23] S. Holdcroft, A photochemical study of poly(3-hexylthiophene), *Macromolecules* 24 (1991) 4834–4838.
- [24] S. Bertho, G. Janssen, T.J. Cleij, B. Conings, W. Moons, A. Gadisa, J. D'Haen, E. Goovaerts, L. Lutsen, J. Manca, D. Vanderzande, Effect of temperature on the morphological and photovoltaic stability of bulk heterojunction polymer:fullerene solar cells, *Sol. Energy Mater. Sol. Cells* 92 (2008) 753–760.
- [25] T. Heumueller, T.M. Burke, W.R. Mateker, I.T. Sachs-Quintana, K. Vandewal, C.J. Brabec, M.D. McGehee, Disorder-induced open-circuit voltage losses in organic solar cells during photoinduced burn-in, *Adv. Energy Mater.* 5 (2015) 1500111.
- [26] H. Hintz, H.-J. Egelhaaf, L. Lüer, J. Hauch, H. Peisert, T. Chassé, Photodegradation of P3HT a systematic study of environmental factors, *Chem. Mater.* 23 (2011) 145–154.
- [27] T. Heumueller, W.R. Mateker, A. Distler, U.F. Fritze, R. Cheacharoen, W.H. Nguyen, M. Biele, M. Salvador, M. von Delius, H.-J. Egelhaaf, M.D. McGehee, C.J. Brabec, Morphological and electrical control of fullerene dimerization determines organic photovoltaic stability, *Energy Environ. Sci.* 9 (2016) 247–256.
- [28] A. Distler, T. Sauerbrey, H.-J. Egelhaaf, S. Rodman, D. Waller, K.-S. Cheon, M. Lee, D.M. Guldi, The effect of PCBM dimerization on the performance of bulk heterojunction solar cells, *Adv. Energy Mater.* 4 (2014) 1300693.
- [29] H.C. Wong, Z. Li, C.H. Tan, H. Zhong, Z. Huang, H. Bronstein, I. McCulloch, J.T. Cabral, J.R. Durrant, Morphological stability and performance of polymer–fullerene solar cells under thermal stress: the impact of photoinduced PC60BM oligomerization, *ACS Nano* 8 (2014) 1297–1308.
- [30] H.H. Khaligh, I.A. Goldthorpe, Failure of silver nanowire transparent electrodes under current flow, *Nanoscale Res. Lett.* 8 (2013) 235.
- [31] C.K. Chan, W. Zhao, S. Barlow, S. Marder, A. Kahn, Decamethylcobaltocene as an efficient n-dopant in organic electronic materials and devices, *Org. Electron.* 9 (2008) 575–581.
- [32] R. Steim, F.R. Kogler, C.J. Brabec, Interface materials for organic solar cells, *J. Mater. Chem.* 20 (2010) 2499–2512.
- [33] Ö. Usluer, M. Abbas, G. Wantz, L. Vignau, L. Hirsch, E. Grana, C. Brochon, E. Cloutet, G. Hadziioannou, Metal residues in semiconducting polymers: impact on the performance of organic electronic devices, *ACS Macro Lett.* 3 (2014) 1134–1138.
- [34] L.A. Frolova, N.P. Piven, D.K. Susarova, A.V. Akkuratov, S.D. Babenko, P.A. Troshin, ESR spectroscopy for monitoring the photochemical and thermal degradation of conjugated polymers used as electron donor materials in organic bulk heterojunction solar cells, *Chem. Commun. (J. Chem. Soc. Sect. D)* 51 (2015) 2242–2244.
- [35] L. Ciammaruchi, F. Brunetti, I. Visoly-Fisher, Solvent effects on the morphology and stability of PTB7:PCBM based solar cells, *Sol. Energy* 137 (2016) 490–499.
- [36] W.C.H. Choy, D. Zhang, Solution-processed metal oxides as efficient carrier transport layers for organic photovoltaics, *Small* 12 (2016) 416–431.
- [37] R. Betancur, Maymóc, X. Elias, Luat T. Vuong, J. Martorell, Sputtered NiO as electron blocking layer in P3HT:PCBM solar cells fabricated in ambient air, *Sol. Energy Mater. Sol. Cells* 95 (2011) 735–739.
- [38] M. Wang, F. Xie, W. Xie, S. Zheng, N. Ke, J. Chen, N. Zhao, J.B. Xu, Device lifetime improvement of polymer-based bulk heterojunction solar cells by incorporating copper oxide layer at Al cathode, *Appl. Phys. Lett.* 98 (2011) 2011–2014.
- [39] C.H. Hsieh, Y.-J. Cheng, P. Jung Li, C.H. Chen, M. Dubosc, R.M. Liang, C.S. Hsu, Highly efficient and stable inverted polymer solar cells integrated with a cross-linked fullerene material as an interlayer, *J. Am. Chem. Soc.* 132 (2010) 4887–4893.
- [40] L. Ciammaruchi, C. Wang, Y. Gao, C.W. Tang, Delineation of degradation patterns of C60-based organic solar cells under different environments, *J. Appl. Phys.* 117 (2015) 245504.
- [41] Z. Yin, J. Wei, Q. Zheng, Interfacial materials for organic solar cells: recent advances and perspectives, *Adv. Sci.* 3 (2016) 1500362.
- [42] A.M. Nardes, M. Kemerink, M.M. de Kok, E. Vinken, K. Maturova, R.A.J. Janssen, Conductivity, work function, and environmental stability of PEDOT:PSS thin films treated with sorbitol, *Org. Electron.* 9 (2008) 727–734.
- [43] C. Waldauf, M. Morana, P. Denk, P. Schilinsky, K. Coakley, S.A. Choulis, C.J. Brabec, Highly efficient inverted organic photovoltaics using solution based titanium oxide as electron selective contact, *Appl. Phys. Lett.* 89 (2006) 1–4.
- [44] D. Gao, M.G. Helander, Z.B. Wang, D.P. Puzzo, M.T. Greiner, Z.H. Lu, C60:LiF blocking layer for environmentally stable bulk heterojunction solar cells, *Adv. Mater.* 22 (2010) 5404–5408.
- [45] G. Teran-Escobar, J. Pampel, J.M. Caicedo, M. Lira-Cantu, Low-temperature, solution-processed, layered V2O5 hydrate as the hole-transport layer for stable organic solar cells, *Energy Environ. Sci.* 6 (2013) 3088–3098.
- [46] M.T. Dang, L. Hirsch, G. Wantz, P3HT:PCBM, best seller in polymer photovoltaic research, *Adv. Mater.* 23 (2011) 3597–3602.
- [47] D. Baran, R.S. Ashraf, D.A. Hanifi, M. Abdelsamie, N. Gasparini, J.A. Rohr, S. Holliday, A. Wadsworth, S. Lockett, M. Neophytou, C.J.M. Emmott, J. Nelson, C.J. Brabec, A. Amassian, A. Salleo, T. Kirchartz, J.R. Durrant, I. McCulloch, Reducing the efficiency-stability-cost gap of organic photovoltaics with highly efficient and stable small molecule acceptor ternary solar cells, *Nat. Mater.* 16 (2016) 363–369.
- [48] M.V. Madsen, T. Tromholt, A. Böttiger, J.W. Andreasen, K. Norrman, F.C. Krebs, Influence of processing and intrinsic polymer parameters on photochemical stability of polythiophene thin films, *Polym. Degrad. Stab.* 97 (2012) 2412–2417.
- [49] K. Sivula, C.K. Luscombe, B.C. Thompson, J.M.J. Fréchet, Enhancing the thermal stability of polythiophene:fullerene solar cells by decreasing effective polymer regularity, *J. Am. Chem. Soc.* 128 (2006) 13988–13989.
- [50] P. Kumar, C. Bilen, K. Feron, X. Zhou, W.J. Belcher, P.C. Dastoor, Enhanced regeneration of degraded polymer solar cells by thermal annealing, *Appl. Phys. Lett.* 104 (2014) 193905.
- [51] C.R. Singh, G. Gupta, R. Lohwasser, S. Engmann, J. Balko, M. Thelakktat, T. Thurn-Albrecht, H. Hoppe, Correlation of charge transport with structural order in highly ordered melt-crystallized poly(3-hexylthiophene) thin films, *J. Polym. Sci. B Polym. Phys.* 51 (2013) 943–951.
- [52] Z. Ding, J. Kettle, M. Horie, S.W. Chang, G.C. Smith, A.I. Shames, E.A. Katz, Efficient solar cells are more stable: the impact of polymer molecular weight on performance of organic photovoltaics, *J. Mater. Chem.* 4 (2016) 7274–7280.
- [53] L.H. Nguyen, H. Hoppe, T. Erb, S. Gunes, G. Gobsch, N.S. Sariciftci, Effects of annealing on the nanomorphology and performance of poly(alkylthiophene): fullerene bulk-heterojunction solar cells, *Adv. Funct. Mater.* 17 (2007) 1071–1078.
- [54] J. Zhao, A. Swinnen, G. Van Assche, J. Manca, D. Vanderzande, B. Van Mele, Phase diagram of P3HT/PCBM blends and its implication for the stability of morphology, *J. Phys. Chem. B* 113 (2009) 1587–1591.
- [55] I.T. Sachs-Quintana, T. Heumueller, W.R. Mateker, D.E. Orozco, R. Cheacharoen, S. Sweetnam, C.J. Brabec, M.D. McGehee, Electron barrier formation at the organic-back contact interface is the first step in thermal degradation of polymer solar cells, *Adv. Funct. Mater.* 24 (2014) 3978–3985.
- [56] C. Müller, On the glass transition of polymer semiconductors and its impact on polymer solar cell stability, *Chem. Mater.* 27 (2015) 2740–2754.
- [57] T. Heumueller, W.R. Mateker, I.T. Sachs-Quintana, K. Vandewal, J.A. Bartelt, T.M. Burke, T. Ameri, C.J. Brabec, M.D. McGehee, Reducing burn-in voltage loss in polymer solar cells by increasing the polymer crystallinity, *Energy Environ. Sci.* 7 (2014) 2974–2980.
- [58] J.U. Lee, J.W. Jung, J.W. Jo, W.H. Jo, Degradation and stability of polymer-based solar cells, *J. Mater. Chem.* 22 (2012) 24265–24283.
- [59] A.D. de Zerio, A. Melianas, S. Rossbauer, O. Bäcke, L. Nordstierna, P. Erhart, E. Olsson, T.D. Anthopoulos, O. Inganäs, C. Müller, High-entropy mixtures of pristine fullerenes for solution-processed transistors and solar cells, *Adv. Mater.* 27 (2015) 7325–7331.
- [60] A.D. de Zerio, C. Müller, Glass forming acceptor alloys for highly efficient and thermally stable ternary organic solar cells, *Adv. Energy Mater.* (2018) 1702741.
- [61] a) J.W. Rumer, R.S. Ashraf, N.D. Eisenmenger, Z. Huang, I. Meager, C.B. Nielsen, B.C. Schroeder, M.L. Chabiny, I. McCulloch, Dual function additives: a small molecule crosslinker for enhanced efficiency and stability in organic solar cells, *Adv. Energy Mater.* 5 (2015) 1401426. b) J.W. Rumer, I. McCulloch, Organic photovoltaics: crosslinking for optimal morphology and stability, *Mater. Today* 18 (2015) 425–435.
- [62] M. Drees, H. Hoppe, C. Winder, H. Neugebauer, N.S. Sariciftci, W. Schwinger, F. Schaffler, C. Topf, M.C. Scharber, Z.G. Zhu, R. Gaudiana, Stabilization of the nanomorphology of polymer–fullerene “bulk heterojunction” blends using a novel polymerizable fullerene derivative, *J. Mater. Chem.* 15 (2005) 5158–5163.
- [63] G. Wantz, L. Derue, O. Dautel, A. Rivaton, P. Hudhomme, C. Dagron-Lartigau, Stabilizing polymer-based bulk heterojunction solar cells via crosslinking, *Polym. Int.* 63 (2014) 1346–1361.
- [64] Q. Burlingame, B. Song, L. Ciammaruchi, G. Zanotti, J. Hankett, Z. Chen, E.A. Katz, S.R. Forrest, Reliability of small molecule organic photovoltaics with electron-filtering compound buffer layers, *Adv. Energy Mater.* 6 (2016) 1601094.
- [65] D.K. Susarova, N.P. Piven, A.V. Akkuratov, L.A. Frolova, M.S. Polinskaya, S.A. Ponomarenko, S.D. Babenko, P.A. Troshin, ESR spectroscopy as a powerful tool for probing the quality of conjugated polymers designed for photovoltaic applications, *Chem. Commun. (J. Chem. Soc. Sect. D)* 51 (2015) 2239–2241.
- [66] L. Ciammaruchi, S. Penna, A. Reale, T.M. Brown, A. Di Carlo, Acceleration factor for ageing measurement of dye solar cells, *Microelectron. Reliab.* 53 (2013) 279–281.
- [67] E.A. Katz, D. Faiman, S.M. Tuladhar, J.M. Kroon, M.M. Wien, T. Fromherz, F. Padinger, C.J. Brabec, N.S. Sariciftci, Temperature dependence for the photovoltaic device parameters of polymer–fullerene solar cells under operating conditions, *J. Appl. Phys.* 90 (2001) 5343–5350.
- [68] T.-A. Chen, X. Wu, R.D. Rieke, Regiocontrolled synthesis of poly(3-alkylthiophenes) mediated by Rieke zinc: their characterization and solid-state properties, *J. Am. Chem. Soc.* 117 (1995) 233–244.
- [69] a) S. Das, F. Herrmann-Westendorf, F.H. Schacher, E. Tauscher, U. Ritter, B. Dietzek, M. Presselt, Controlling electronic transitions in fullerene van der Waals aggregates via supramolecular assembly, *ACS Appl. Mater. Interfaces* 8 (2016) 21512–21521; b) F. Herrmann, S. Engmann, M. Presselt, H. Hoppe, S. Shokhovets, G. Gobsch, Correlation between near infrared-visible absorption, intrinsic local and global sheet resistance of poly(3,4-ethylenedioxy-thiophene) poly(styrene sulfonate) thin films, *Appl. Phys. Lett.* 100 (2012) 153301.
- [70] F. Herrmann, B. Muhsin, C.R. Singh, S. Shokhovets, G. Gobsch, H. Hoppe, M. Presselt, Influence of interface doping on charge-carrier mobilities and sub-bandgap absorption in organic solar cells, *J. Phys. Chem. C* 119 (2015) 9036–9040.
- [71] M. Presselt, F. Herrmann, S. Shokhovets, H. Hoppe, E. Runge, G. Gobsch, Sub-bandgap absorption in polymer–fullerene solar cells studied by temperature-

- dependent external quantum efficiency and absorption spectroscopy, *Chem. Phys. Lett.* 542 (2012) 70–73.
- [72] W.B. Jackson, N.M. Amer, A.C. Boccara, D. Fournier, Photothermal deflection spectroscopy and detection, *Appl. Optic.* 20 (1981) 1333–1344.
- [73] M.T. Neukom, S. Züfle, B. Ruhstaller, Reliable extraction of organic solar cell parameters by combining steady-state and transient techniques, *Org. Electron.* 13 (2012) 2910–2916.
- [74] S. Züfle, M.T. Neukom, S. Altazin, M. Zinggeler, M. Chrapa, T. Offermans, B. Ruhstaller, An effective area approach to model lateral degradation in organic solar cells, *Adv. Energ. Mater.* 5 (2015) 1500835.
- [75] R.D. McCullough, R.D. Lowe, Enhanced electrical conductivity in regioselectively synthesized poly(3-alkylthiophenes), *J. Chem. Soc., Chem. Commun.* (1992) 70–72.
- [76] T.A. Chen, R.D. Rieke, The first regioregular head-to-tail poly(3-hexylthiophene-2,5-diyl) and a regiorandom isopolymer: nickel versus palladium catalysis of 2(5)-bromo-5(2)-(bromozincio)-3-hexylthiophene polymerization, *J. Am. Chem. Soc.* 114 (1992) 10087–10088.
- [77] R.S. Loewe, S.M. Khersonsky, R.D. McCullough, A simple method to prepare head-to-tail coupled, regioregular poly(3-alkylthiophenes) using grignard metathesis, *Adv. Mater.* 11 (1999) 250–253.
- [78] A. Marrocchi, D. Lanari, A. Facchetti, L. Vaccaro, Poly(3-hexylthiophene): synthetic methodologies and properties in bulk heterojunction solar cells, *Energ. Environ. Sci.* 5 (2012) 8457–8474.
- [79] I. Osaka, R.D. McCullough, Advances in molecular design and synthesis of regioregular polythiophenes, *Accounts Chem. Res.* 41 (2008) 1202–1214.
- [80] C. Bracher, H. Yi, N.W. Scarratt, R. Masters, A.J. Pearson, C. Rodenburg, A. Iraqi, D.G. Lidzey, The effect of residual palladium catalyst on the performance and stability of PCDTBT:PC₇₀BM organic solar cells, *Org. Electron.* 27 (2015) 266–273.
- [81] A.I. Shames, L.N. Inasaridze, A.V. Akkuratov, A.E. Goryachev, E.A. Katz, P.A. Troshin, Assessing the outdoor photochemical stability of conjugated polymers by EPR spectroscopy, *J. Mater. Chem.* 4 (2016) 13166–13170.
- [82] L.N. Inasaridze, A.I. Shames, I.V. Martynov, B. Li, A.V. Mumyatov, D.K. Susarova, E.A. Katz, P.A. Troshin, Light-induced generation of free radicals by fullerene derivatives: an important degradation pathway in organic photovoltaics? *J. Mater. Chem.* 5 (2017) 8044–8050.
- [83] F. Matteocci, L. Cinà, E. Lamanna, S. Cacovich, G. Divitini, P.A. Midgley, C. Ducati, A. Di Carlo, Encapsulation for long-term stability enhancement of perovskite solar cells, *Nano Energy* 30 (2016) 162–172.
- [84] T.J. Wilderspin, F. De Rossi, T.M. Watson, A simple method to evaluate the effectiveness of encapsulation materials for perovskite solar cells, *Sol. Energy* 139 (2016) 426–432.
- [85] S. Sweetnam, K.R. Graham, G.O.N. Ndjawa, T. Heumüller, J.A. Bartelt, T.M. Burke, W. Li, W. You, A. Amassian, M.D. McGehee, Characterization of the polymer energy landscape in polymer:fullerene bulk heterojunctions with pure and mixed phases, *J. Am. Chem. Soc.* 136 (2014) 14078–14088.
- [86] A. Guerrero, G. Garcia-Belmonte, Recent advances to understand morphology stability of organic photovoltaics, *Nano-Micro Lett.* 9 (2016) 10.
- [87] F.C. Krebs, T. Tromholt, M. Jorgensen, Upscaling of polymer solar cell fabrication using full roll-to-roll processing, *Nanoscale* 2 (2010) 873–886.
- [88] G.F.A. Dibb, M.-A. Muth, T. Kirchartz, S. Engmann, H. Hoppe, G. Gobsch, M. Thelakkat, N. Blouin, S. Tierney, M. Carrasco-Orozco, J.R. Durrant, J. Nelson, Influence of doping on charge carrier collection in normal and inverted geometry polymer:fullerene solar cells, *Sci. Rep.* 3 (2013) 3335.
- [89] E.A. Katz, A. Mescheloff, I. Visoly-Fisher, Y. Galagan, Light intensity dependence of External Quantum Efficiency of fresh and degraded organic photovoltaics, *Sol. Energy Mater. Sol. Cells* 144 (2016) 273–280.
- [90] M.T. Neukom, N.A. Reinke, B. Ruhstaller, Charge extraction with linearly increasing voltage: a numerical model for parameter extraction, *Sol. Energy* 85 (2011) 1250–1256.
- [91] S. Züfle, Degradation Analysis and Parameter Extraction of Organic Semiconductor Devices : Investigation by Means of Complementary Measurement Techniques Combined with Numerical Simulation, PhD Thesis Karlsruhe Institute of Technology, 2017, <https://doi.org/10.5445/IR/1000078129> , Accessed date: 10 March 2018.
- [92] F. Panzer, H. Bässler, A. Köhler, Temperature induced order–disorder transition in solutions of conjugated polymers probed by optical spectroscopy, *J. Phys. Chem. Lett.* 8 (2017) 114–125.
- [93] H. Yamagata, F.C. Spano, Interplay between intrachain and interchain interactions in semiconducting polymer assemblies: the HJ-aggregate model, *J. Chem. Phys.* 136 (2012) 184901.
- [94] C. Müller, N.D. Zhigadlo, A. Kumar, M.A. Baklar, J. Karpinski, P. Smith, T. Kreouzis, N. Stingelin, Enhanced charge-carrier mobility in high-pressure-crystallized poly(3-hexylthiophene), *Macromolecules* 44 (2011) 1221–1225.
- [95] P. Kohn, S. Huettner, H. Komber, V. Senkovskyy, R. Tkachov, A. Kiriy, R.H. Friend, U. Steiner, W.T.S. Huck, J.-U. Sommer, M. Sommer, On the role of single regiodefects and polydispersity in regioregular poly(3-hexylthiophene): defect distribution, synthesis of defect-free chains, and a simple model for the determination of crystallinity, *J. Am. Chem. Soc.* 134 (2012) 4790–4805.
- [96] M.V. Khenkin, A.K. M, I. Visoly-Fisher, Y. Galagan, F. Di Giacomo, B.R. Patil, G. Sherafatipour, V. Turkovic, H.-G. Rubahn, M. Madsen, T. Merckx, G. Uytterhoeven, J.P.A. Bastos, T. Aernouts, F. Brunetti, M. Lira-Cantu, E.A. Katz, Reconsidering figures of merit for performance and stability of perovskite photovoltaics, *Energ. Environ. Sci.* 11 (2018) 739–743.

Publications P1 to P5

Publication P4

Performance and Stability of Organic Solar Cells Bearing

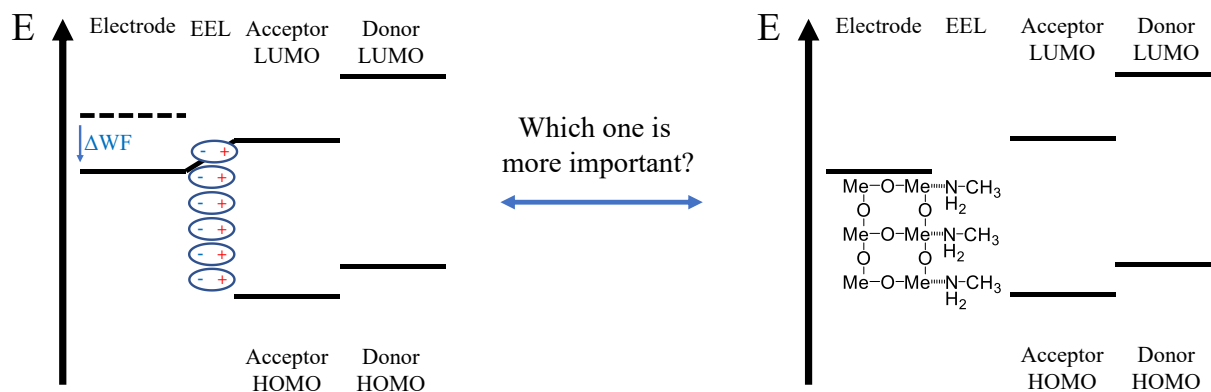
Nitrogen Containing Electron Extraction Layers

Rico Meitzner, Juliette Essomba, Shahidul Alam, Aman Anand, Nora Engel,

Kevin Fulbert, Krisna Kuma, Fernanda Ayuyasmin, Md Moidul Islam, Chikezie Ugokwe,

Ulrich S. Schubert, Harald Hoppe

Energy Technology **2020**, 8, 2000117



Reproduced with permission of John Wiley & Sons, Inc., Copyright © 2020.

Performance and Stability of Organic Solar Cells Bearing Nitrogen Containing Electron Extraction Layers

Rico Meitzner,* Juliette Essomba, Shahidul Alam, Aman Anand, Nora Engel, Kevin Fulbert, Krisna Kuma, Fernanda Ayuyasmin, Md Moidul Islam, Chikezie Ugokwe, Ulrich S. Schubert, and Harald Hoppe*

Charge extraction and transport layers represent an important component of organic solar cells. Many different material groups are reported for these layers. Two important classes are metal oxides and organic materials. Many of these organic materials which are used as electron extraction layers (EELs) are nitrogen containing. Therefore, it has been decided to study a broad array of—to the largest part so far not reported—amine and imine containing organic materials as EELs in organic solar cells and compare them with an archetypical metal oxide electron transport layer (ETL). It enables certain structure–property relationships to be obtained for the EELs and to understand what determines their performance to a large part. Furthermore, their effect on the stability of organic solar cells is studied and they are found to be reasonable replacements as a cheap, quickly processable, environmentally friendly, biocompatible, and biodegradable alternative as compared with ETLs.

1. Introduction

Organic solar cells (OSCs) are a promising solar energy conversion technology, due to their potential for fast processing via roll-to-roll manufacture, their usage of earth abundant materials, their small environmental footprint, and last but not least their flexibility and general freedom in design. By today there are already several examples of notably high performances because the power conversion efficiencies of OSCs surpassed 15% since the year 2019.^[1] The most commonly used design today for solution-processed

OSCs is the bulk-heterojunction,^[2] where an active layer, which is a blend of an organic semiconductor acting as donor and one acting as acceptor, is sandwiched between two charge transport (CTL) or charge extraction layers (CEL), which themselves are adjacent to electrodes, whereby one of these electrodes has to be transparent.

These CELs have a strong impact on both performance and stability of OSCs.^[3] They, thereby, have to possess an array of qualities such as high transparency, easy processability, a suitable work function (WF)/energy levels, high abundance, and a low price.^[3e] There are many different classes of CTLs/CELs; these include metal oxides, inorganic and organic semiconductors, organic molecules with high dipole moments, and hybrids of the aforementioned categories.^[3e]

From the standpoint of solution processability and high abundance, organic CTLs/CELs are in particular interesting and have been extensively studied.^[3c,e,4] Two well-known organic polymers used as electron extraction layer (EEL) in organic solar cells are poly(ethylene imine) (PEI) and ethoxylated poly(ethylene imine) (PEIE).^[4a,e,5] Both of these polymers are insulators and are used to modify the WF of the adjacent electrode through their large dipole moment.^[4a] It was shown that they do so in inverted OSCs by chemisorption to substrates such as indium tin oxide or zinc oxide and, thereby, align their dipole moment properly to

R. Meitzner, J. Essomba, Dr. S. Alam, A. Anand, K. Fulbert, K. Kuma, F. Ayuyasmin, M. M. Islam, C. Ugokwe, Prof. U. S. Schubert, Dr. H. Hoppe
Center for Energy and Environmental Engineering (CEEC Jena)
Friedrich Schiller University Jena
Philosophenweg 7a, 07743 Jena, Germany
E-mail: rico.meitzner@uni-jena.de; harald.hoppe@uni-jena.de

R. Meitzner, J. Essomba, Dr. S. Alam, A. Anand, N. Engel, K. Fulbert, K. Kuma, F. Ayuyasmin, M. M. Islam, C. Ugokwe, Prof. U. S. Schubert, Dr. H. Hoppe
Laboratory for Organic and Macromolecular Chemistry (IOMC)
Friedrich Schiller University Jena
Humboldtstrasse 10, 07743 Jena, Germany

N. Engel, Prof. U. S. Schubert
Jena Center for Soft Matter
Friedrich Schiller University Jena
Philosophenweg 7, 07743 Jena, Germany

K. Fulbert, K. Kuma, F. Ayuyasmin
Faculty of Industrial Engineering
Ernst-Abbe-Hochschule Jena
07745 Jena, Germany

K. Fulbert, K. Kuma, F. Ayuyasmin
Faculty of Life Sciences and Technology
Swiss German University
15143 Banten, Indonesia

 The ORCID identification number(s) for the author(s) of this article can be found under <https://doi.org/10.1002/ente.202000117>.

© 2020 The Authors. Published by Wiley-VCH GmbH. This is an open access article under the terms of the Creative Commons Attribution License, which permits use, distribution and reproduction in any medium, provided the original work is properly cited.

Correction added on 6 January 2021, after first online publication: Rico Meitzner was designated as corresponding author.

DOI: 10.1002/ente.202000117



adjust the WF of the electrode to enable an improved contact and efficient charge carrier extraction.^[4a]

Recently, α -poly-L-lysine^[4c] was reported as an efficient EEL in conjunction with different active layer blends, fullerene- and nonfullerene-based alike. In this study, the materials derived from an amino acid outperformed other organic electron transport materials such as PDINO (3,3'-(1,3,8,10-tetraoxo-1,3,8,10-tetrahydroantra[2,1,9-def:6,5,10-d'e'f']diisoquinoline-2,9-diyl)bis(*N,N*-dimethylpropan-1-amine oxide)), PFN (poly[(9,9-bis(3'-(*N,N*-dimethylamino)propyl)-2,7-fluorene)-*alt*-2,7-(9,9-dioctylfluorene)]), and PFN-Br (poly[(9,9-bis(3'-(*N,N*-dimethyl-*N*-ethylammonium)-propyl)-2,7-fluorene)-*alt*-2,7-(9,9-dioctylfluorene)]). Also, the amino acid serine^[6] was reported as an EEL and resulted in a good performance. More recently, the use of a simple amino acid (glycine) for modification of the EEL ZnO has been demonstrated. Indeed, the WF shifted slightly upward ($-4.11 \rightarrow -4.02$ eV), improving the performance.^[7]

On the contrary, such amine/imine compounds are also able to improve the contact by reducing surface recombination at the interface between active layer and electrode. Between organic semiconductors and reactive metals like aluminum, interfacial states can be formed; these states can help to form an ohmic contact between the semiconductor and the metal.^[8] These interfacial states can result in injection of charge carriers from the electrode into the organic semiconductor; this can limit the achievable fill factor of such devices.^[9] Also, surface recombination has a pronounced impact on the open-circuit voltage.^[10] For nonconducting materials such as poly(methyl methacrylate) (PMMA), Hu et al. reported no change in WF upon metal deposition, which they interpreted as no interaction between metal and polymer, but for polymers such as polyethylene oxide (PEO) and polyvinylpyrrolidone (PVP) they observed a change in WF, which they explained with coordinative interactions between these polymers and the electrode.^[11] Kim et al.^[12] described several strategies used in the field of perovskite solar cells used to passivate defect states based on the Lewis basicity of materials, for example, nitrogen atoms in pyridine were used to passivate defects. They also described the usage of PVP for both

defect passivation and reduction of interfacial recombination due to the Lewis base nature of PVP.^[12]

Another important factor is the stability of devices built with such interfacial layers. Courtright et al.^[5d] used PEI with different molar masses as part of a double-layer ETL in conjunction with ZnO and obtained a stability improvement over only ZnO, which was dependent on the molar mass of the PEI and improved with the same. Kim et al.^[5a] reported the stability of inverted OSCs containing PEIE as the sole EEL and retained above 80% of the initial performance after 30 days of storage under ambient conditions. This indicates potential for nitrogen containing organic materials as efficient electrode modifiers for organic solar cells.

We investigated several amine and/or imine containing organic molecules and polymers in CELs, to learn about structure–property relations. The organic compounds used as EELs and the layer stack used for all devices used for the experiments are shown in **Figure 1**. Furthermore, we investigated the stability of solar cells processed with the same and compared this with our reference material for the ETL, which is sol-gel-processed TiO_x .^[13]

2. Results and Discussion

First, a layer thickness optimization for the EELs was performed. The results of this optimization are shown in Figure S1, Supporting Information. Some of the materials showed only a weak dependence on the spin frequency, such as L-lysine and L-arginine, which may indicate low film thickness in general. However, others revealed a strong dependence such as L-histidine and especially the amine-rich polyoxazoline copolymer. The highest performance could be achieved with L-arginine, even in comparison with various differently processed TiO_x layers, as shown in **Table 1**. Due to the relatively large device area of 0.42 cm^2 , the devices showed in general a performance distribution at the intermediate range of the values reported for this material system.^[14]

The devices with L-arginine as EEL showed an open-circuit voltage which got closest to the maximum reported for this

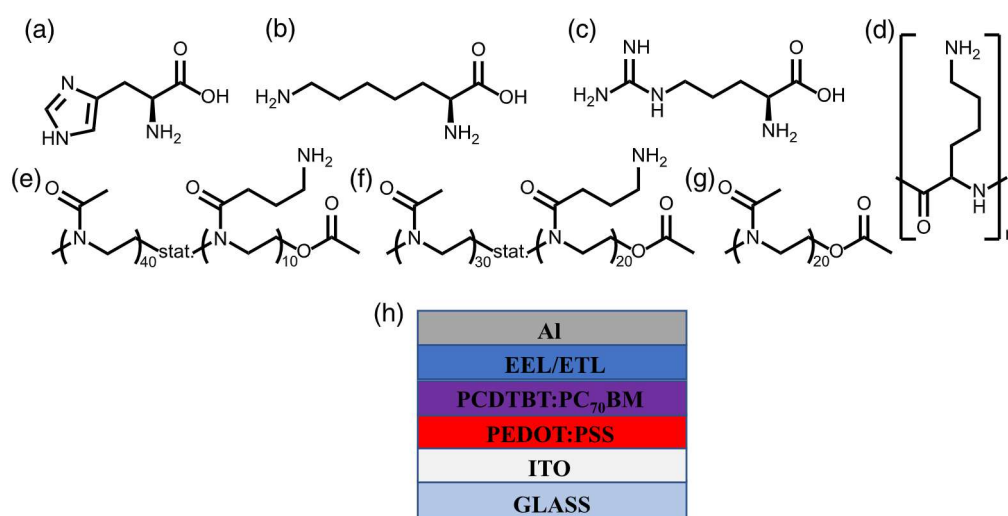


Figure 1. Schematic representation of organic materials used as EELs: a) L-histidine, b) L-lysine, c) L-arginine, d) poly-L-lysine, e) P(MeOx₄₀-stat-AmOx₁₀), f) P(MeOx₃₀-stat-AmOx₂₀) and g) PMeOx₂₀. h) The active layer stack used for the devices used for the experiments, which was a conventional layer stack.

Table 1. Photovoltaic parameters of the solar cells with different layer stacks. All values are averages with the respective standard deviation.

EEL	V_{OC} [mV]	J_{SC} [mA cm^{-2}]	FF [%]	PCE [%]	R_S [Ω]	R_{Sh} [$\text{k}\Omega$]
L-Histidine	832 ± 19	11.12 ± 0.33	48.3 ± 0.5	4.46 ± 0.23	16.0 ± 1.8	1.05 ± 0.06
L-Lysine	858 ± 12	11.27 ± 0.15	49.0 ± 0.8	4.73 ± 0.09	15.3 ± 3.2	0.90 ± 0.25
L-Arginine	869 ± 7	10.99 ± 0.34	51.3 ± 1.0	4.89 ± 0.12	12.0 ± 0.0	1.30 ± 0.09
Poly-L-lysine	850 ± 22	11.06 ± 0.37	49.8 ± 1.7	4.68 ± 0.42	13.3 ± 1.5	1.26 ± 0.06
P(MeOx_{40} -stat-AmOx ₁₀)	857 ± 9	10.11 ± 0.20	46.5 ± 2.4	4.02 ± 0.17	13.8 ± 1.5	0.98 ± 0.13
P(MeOx_{30} -stat-AmOx ₂₀)	854 ± 18	10.65 ± 0.50	50.0 ± 0.0	4.55 ± 0.26	14.0 ± 3.6	1.22 ± 0.06
PMeOx ₂₀	795 ± 16	10.20 ± 0.12	44.8 ± 0.5	3.62 ± 0.03	16.3 ± 1.3	0.92 ± 0.05
No EEL	656 ± 18	10.53 ± 0.24	43.8 ± 0.5	2.94 ± 0.16	184.5 ± 72.9	0.68 ± 0.03
Methanol overcast on PAL (no EEL)	772 ± 9	10.80 ± 0.20	45.8 ± 0.5	3.81 ± 0.14	10.3 ± 0.5	0.98 ± 0.05
TiO _x reference	670 ± 315	9.75 ± 0.73	41.0 ± 10.7	3.00 ± 1.77	11.3 ± 1.0	0.69 ± 0.49
TiO _x diluted	842 ± 5	9.14 ± 0.08	44.5 ± 1.0	3.45 ± 0.07	17.5 ± 1.3	0.97 ± 0.05
TiO _x unannealed	784 ± 12	10.45 ± 0.26	47.8 ± 1.3	3.92 ± 0.13	9.8 ± 1.0	1.04 ± 0.08

system, which is around 900 mV for all of the devices.^[15] The short-circuit current density of most devices was between 10 and 11 mA cm^{-2} , which is close to the maximum for this system, which is around 12 mA cm^{-2} . Only if devices were processed with TiO_x photocurrent densities were lower, which might be due to induced aggregation of the PC₇₁BM.^[16] The fill factor of the L-arginine-based device reaches above 50% and the overall performance of these devices is close to 5%, which is a good performance for this photoactive layer (PAL). The series resistance is close to 10 Ω , which is a decent result for devices with an area of 0.42 cm^2 , whereas the shunt resistance is clearly above 1 $\text{k}\Omega$, which is a good result for an organic solar cell.

While the device without any EEL showed a pronounced S-shape—corresponding to a blocking contact—at the open-circuit voltage (V_{OC}),^[17] a simple overcast with methanol *via* solvent dripping and spin casting resulted in an ohmic contact and an improved performance.^[18] The *I*-*V* curves of these devices are shown in Figure 2.

Devices with polyoxazoline polymers as ETL show an improving performance with increasing amine content with respect to

the amine groups in the side chain (with PMeOx₂₀ having 0% content, P(MeOx_{40} -stat-AmOx₁₀) having 20% amine content, and P(MeOx_{30} -stat-AmOx₂₀) having 40% amine content). The correlations between amine content and the photovoltaic parameters are shown in Figure 3. All photovoltaic parameters are roughly improved by about 10% for increased amine content, leading to a performance improvement by one-third. This is accompanied by a 40% drop in the series resistance and an increase by nearly 40% of the parallel resistance, demonstrating the effect coming from the CEL and its impact on selectivity and ease of charge extraction. Indeed, a further increase in the amine content does promise even higher performance parameters because no saturation was visible so far.

It was especially attractive that the amino acids performed so well, as they are low cost and show no issue with reproducibility, unlike polymers, which can vary from batch to batch. We investigated more in depth in how far the structural differences between the amino acids affected their performance. It is well established that the dipole moment of nitrogen containing organic molecules impacts performance in organic solar cells.^[4a]

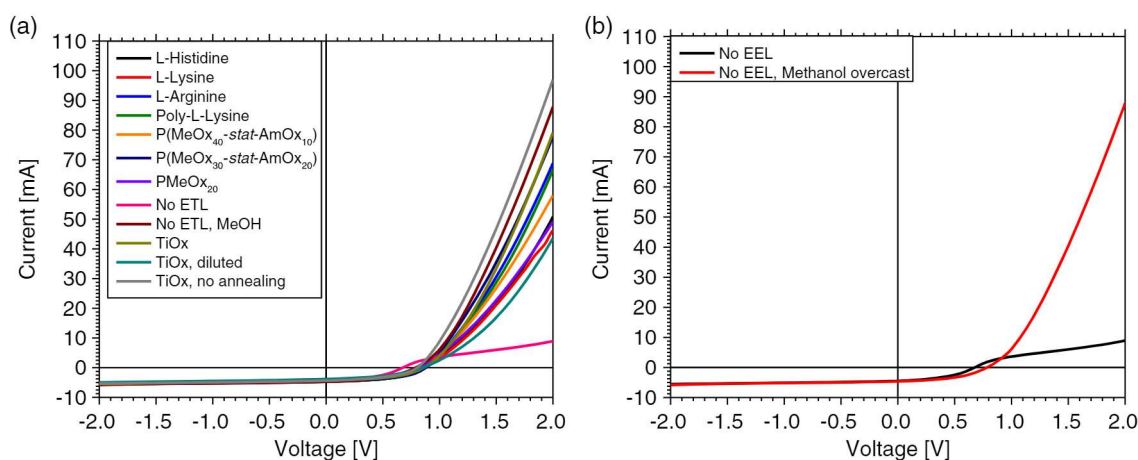


Figure 2. a) *I*-*V* curves for all solar cells before degradation and b) specifically again for the devices without EEL. The device without methanol overcast shows a severe S-shape around the open-circuit voltage, while that S-shape is entirely suppressed for the device with the methanol being overcast on the active layer before electrode deposition.

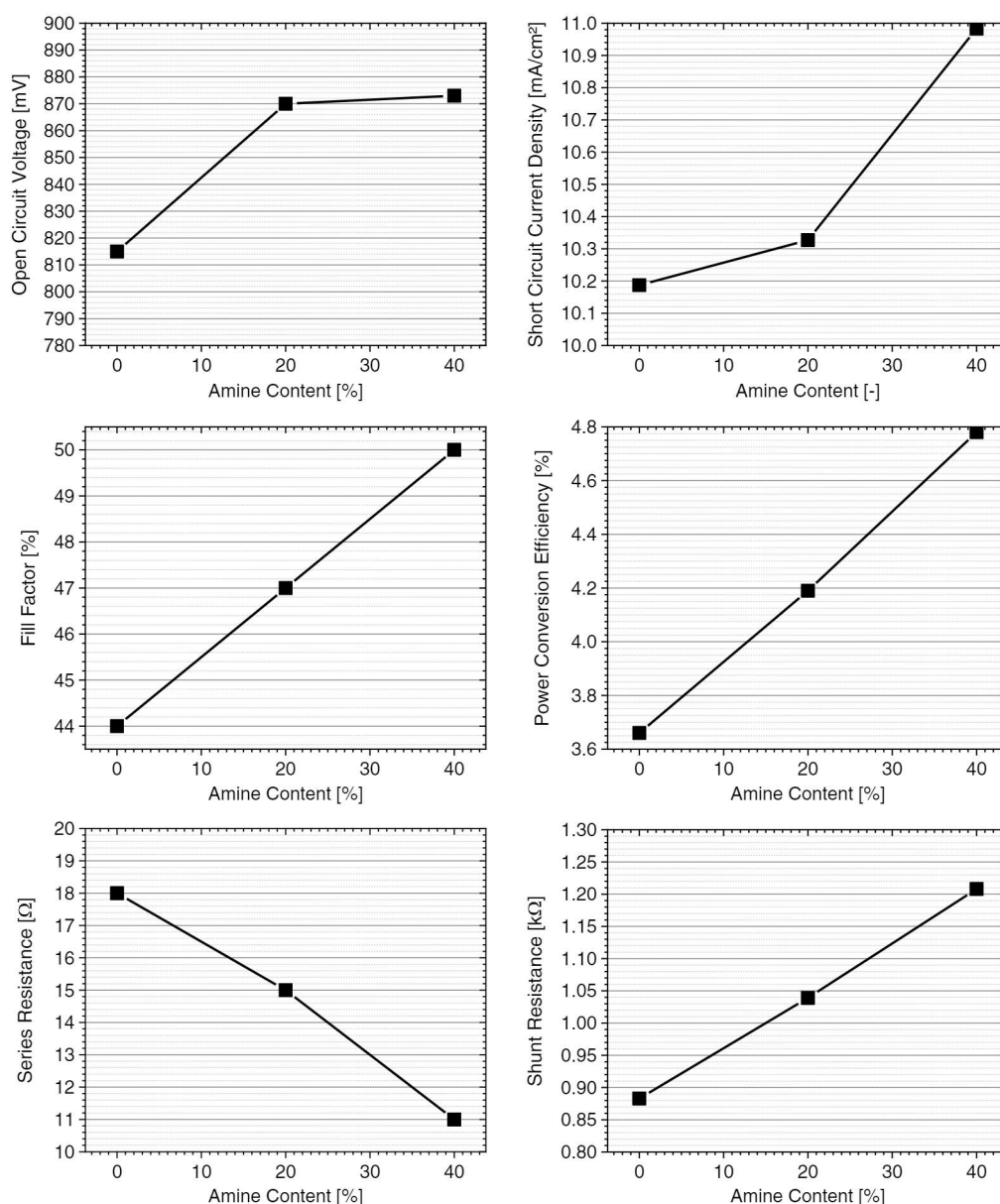


Figure 3. Correlations between amine content in the polyoxazoline polymer and statistical copolymers with the photovoltaic parameters of the solar cells containing the respective polymers as EEL.

All of the polar groups in these amino acids are proton donors or proton acceptors. Therefore, special attention was paid to the dissociation constants of the amine/imine and carboxylic groups within the amino acids.

In **Figure 4**, the correlation between dissociation constants of the different polar groups with respect to their position in the molecule and open-circuit voltage, fill factor, power conversion efficiency, and series resistance is shown. Figure 4a shows a clear direct proportionality between the dissociation constant of the amine/imine group in the side chain and the open-circuit voltage; the same is observed in Figure 4b,c for fill factor and power conversion efficiency. However, Figure 4d shows an inverse proportionality between dissociation constant and series resistance.

The dissociation constant of the different amine/imine groups is a direct proxy for the polarity of the respective groups, i.e., how willingly the nitrogen of the amine group will share its nonbinding electron pair and, therefore potentially, for their dipole moment. This correlation can be understood, if the amino acids are forming a mostly ordered layer on top of the active layer with the dipole moment of the amine/imine group in the side chain facing toward the active layer, which was reported in the past for PEI and PEIE by Zhou et al.^[4a]

To yield a better understanding for the effect of the EELs, Kelvin probe measurements were performed on samples consisting of layer stacks as sketched in the inset of **Figure 5b**. These measurements have been performed either in the dark or in under illumination, with a corresponding excitation density of

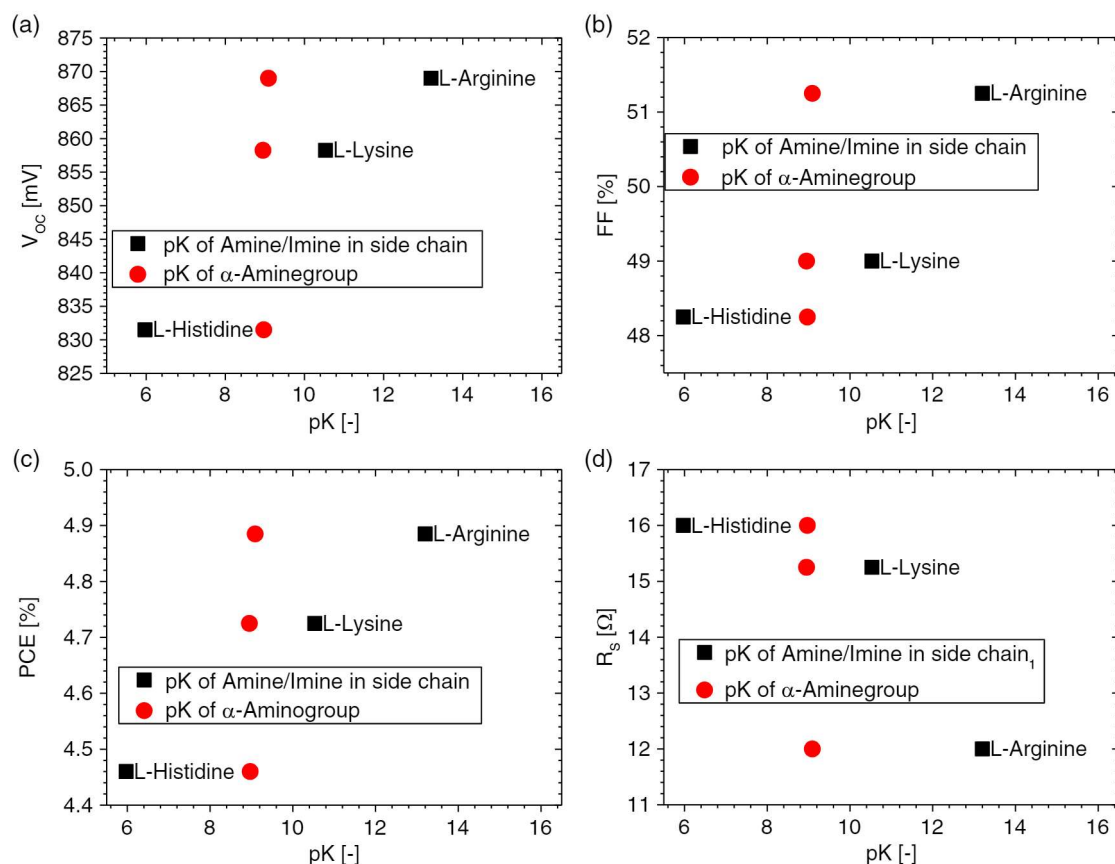


Figure 4. a) Dependence of the open-circuit voltage, b) fill factor, c) PCE, and d) R_s on the dissociation constant of the amine/imine group in side chain and α -amine group. There is a clear increase in V_{OC} with increasing pK of the side chain amine/imine group.

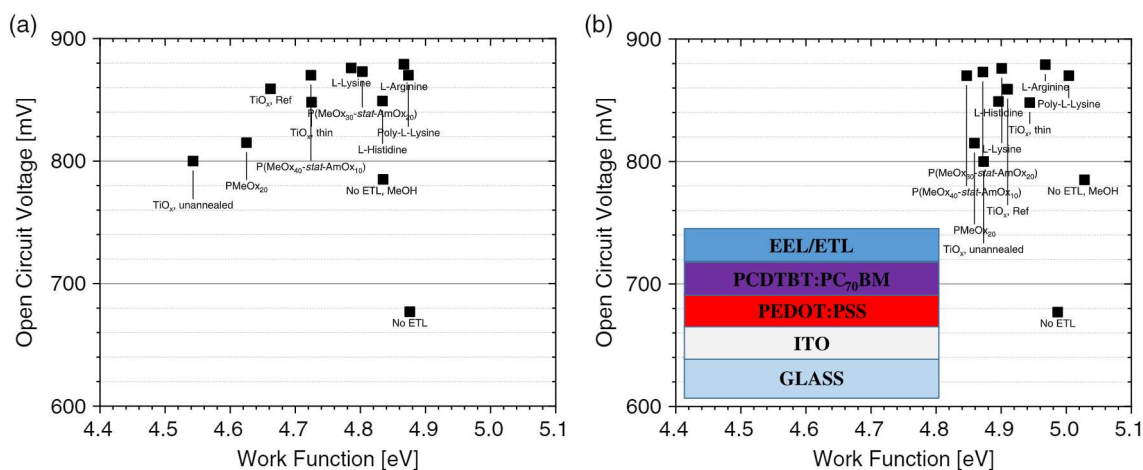


Figure 5. WF over open circuit voltage in a) dark and b) under illumination. Inset in (b) is the layer stack on which the WF was measured.

about 1 sun, yielding WF values that can be seen in the following schemes (Figure 5a,b). Intriguingly, the results displayed—if any at all—rather show an anticorrelation between the WF and the open-circuit voltage. In case of the nonilluminated layer stacks, increasing WFs do roughly correspond to increased photovoltages (Figure 5a); this seems at first glance contradictory; however, if we assume that WF changes are a result of interfacial

dipoles, which face with their positively charged part downward to the photoactive layer (and thus do attract electrons from within), the negatively charged part should face up to the outside or upper side of the layer stack. The latter situation is known for PEDOT:PSS to result in higher WFs too; however, the photoactive layer would then be processed on top of the PEDOT:PSS, enabling hole extraction, whereas in our case the photoactive

layer is buried below the CEL yielding an extraction for the opposite sign of charge—i.e., electrons. In addition, once the layer stack is illuminated, most of the applied EELs yield a WF at the upper end (compare with Figure 5b) of the values found for the dark case, thus confirming that rather high WFs measured on top of the layer stack are in correspondence of electron accumulation below the dipolar EEL. In addition, it should be considered here that the application of a metal electrode deposited from the gas phase (physical vapor deposition [PVD]) may result in a different electronic environment, and then the abrupt termination by the molecular dipoles of the EELs: the negative charge facing toward the metal may be well compensated for by the high electron density of the metal itself. Apart from these considerations of dipolar effects on charge extraction, there are several reports^[19] indicating the positive impact of CTLs

on reducing surface recombination at the electrode. The *pK*-value is also an indication for the readiness of the respective nitrogen of the different amine/imine groups to share one of its free electron pairs in a coordinative bond, or in other words, the *pK* indicates the strength of the Lewis basicity. As a consequence, an amine/imine group with a higher *pK* may more easily passivate defects at the interface between active layer and electrode, and therefore yield reduced surface recombination. This is also in good agreement with the trend seen for the polyoxazolines, as there is a direct proportionality between the open-circuit voltage and the amine content of these polymers, specifically.

Apart from the performance, the stability of organic solar cells is a decisive parameter for their applicability. Therefore, we studied the stability for accelerated aging under ISOS-L1 conditions using LED illumination without UV contents.^[20]

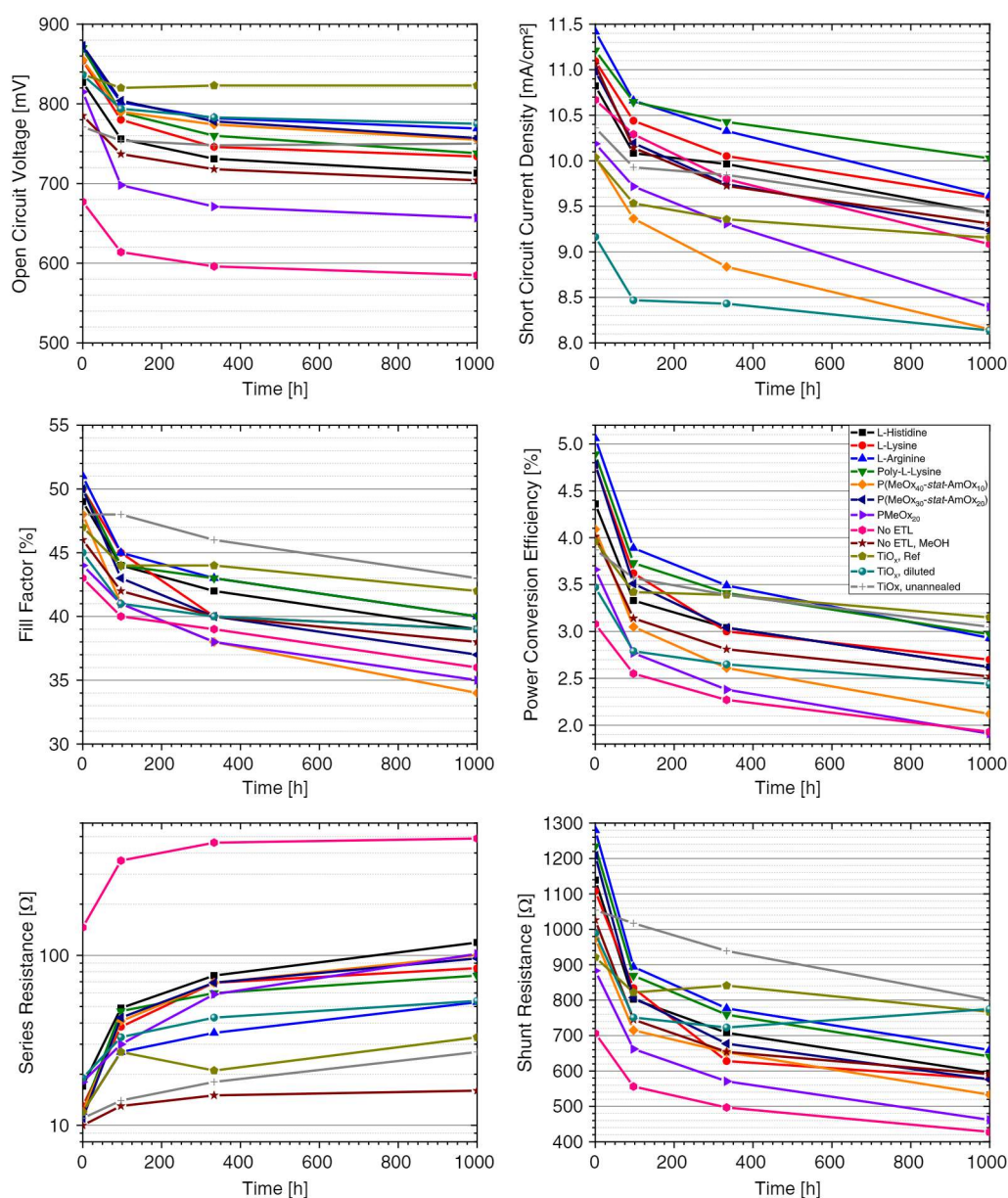


Figure 6. Aging curves for the best performing devices.

In **Figure 6**, the aging curves for the most stable devices for each EEL are shown. The decay curves generally follow a biexponential decay dynamic with a fast-initial decay, generally characterized as the burn-in and followed by a much slower decay. In **Figure 6**, the aging curves for all solar cell parameters for the longest living solar cells can be seen. For the open-circuit voltage, it can be seen that thicker TiO_x ETLs show no or a negligible burn-in, the thin TiO_x layer shows some burn-in, and all of the organic EELs reveal a clear burn-in. Interestingly, that burn-in was even stronger for L-lysine, poly-L-lysine, and PMeOx_{20} than for no interfacial layer. The simple overcast of the active layer with methanol considerably reduces the burn-in depth, whereas the long-term decay proceeds with a similar rate than the solar cell without overcast. The long-term decay rate of the thin TiO_x layer is similar to the solar cell without any interlayer, suggesting a similar interface and thereby only partial coverage or diffusion of Al toward the PAL through pinholes in the TiO_x layer.

The lifetime data of the devices are shown in **Table 2**. From the aging data shown in **Figure 6** and in **Figure 31–42**, Supporting Information, the burn-in time was estimated to be around 100 h; we then calculated the lifetime from the slope of between 333 and 1000 h. The lifetime energy yield (LEY)^[20b] for these devices was also determined, which is also shown in **Table 2**. For the amino acids EELs, there is some quite clear trend, which shows a reduction of lifetime with increasing pK_A . Poly-L-lysine has a similar lifetime and LEY to L-lysine, whereas for the polyoxazolines there is no clear trend with additional amine content. For the devices, without a transport layer the overcast with methanol alone results in an increase in the LEY by roughly 50%, which is quite a remarkable improvement. Solar cells with TiO_x as ETL show a reduction of lifetime and LEY upon thinning out the TiO_x layer

Table 2. Lifetime data of the solar cells aged under ISOS-L1 conditions. Some devices show a large standard deviation as there occurred ingress of oxygen and moisture, which accelerated degradation for individual cells.

ETL/EEL	Burn-in time [h]	Lifetime, $t_{5,80}$ [h]	Standard deviation [h]	LEY [kWh m^{-2}]	Standard deviation [kWh m^{-2}]
L-Histidine	≈100	1966	847	59.8	34.7
L-Lysine	≈100	1614	614	49.6	17.6
L-Arginine	≈100	1187	162	38.5	6.7
Poly-L-lysine	≈100	1434	188	45.8	4.9
P(MeOx_{40} -stat-AmOx ₁₀)	≈100	1084	184	25.7	5.9
P(MeOx_{30} -stat-AmOx ₂₀)	≈100	1546	270	45.3	6.5
PMeOx_{20}	≈100	1409	291	36.4	8.5
No EEL	≈100	1347	257	29.4	5.2
Methanol overcast on PAL (no EEL)	≈100	1542	284	42.8	8.4
TiO_x , reference	≈100	2703	1235	81.9	31.1
TiO_x , diluted	≈100	1812	434	44.6	9.8
TiO_x , unannealed	≈100	1226	398	39.4	12.6

as well as without annealing of the TiO_x layer. It can be expected that for a thinned out layer there should be more pinholes in that layer and a less complete interface between metal electrode and active layer, which seems to effect lifetime negatively. For the nonannealed device, condensation and densification are to be less sufficient than for the annealed TiO_x , resulting in a more permeable interface layer, with also a higher content of remaining organic residues.

3. Conclusion

In this work, we have presented a wide variety of organic interlayer materials that work sufficiently well as EEL. It was possible to obtain an improved understanding of their structure–property relationships. Following insights were gained based on this study: with increasing pK of the second amine group of amino acids, organic solar cell performance improved, which could be either due to dipolar effects at the interface between photoactive layer and metal electrode or tied to a reduction in surface recombination, originating from an interplay of their different functional proton donating/electron pair accepting and proton accepting/electron pair donating groups. For the subgroup of polyoxazolines, an increase in performance with an increasing content of amine groups was found. While exceptionally high stabilities remain an exclusive domain for optimally processed titanium oxides, the amino acid L-lysine resulted in a comparable stability to the metal oxide-based ETLs in this study and thereby presents an attractive, cheap, easy-processable, biocompatible, and biodegradable alternative to these.

4. Experimental Section

Polyoxazoline Preparation: 5-Aminovaleric (Alfa Aesar), acetic acid (Sigma-Aldrich), and triethylamine (Sigma-Aldrich) were used as purchased. Acetonitrile was obtained from a solvent purification system (SPS; Pure solv EN, InnovativeTechnology) and stored under argon. Methyloxazoline (Sigma-Aldrich) was dried over barium oxide (ACROS) overnight, distilled to dryness, and stored under argon (or “inert conditions”). Methyltosylate (Sigma-Aldrich) was stirred over calcium hydride (Sigma-Aldrich) overnight at 27 °C, distilled to dryness, and stored under argon. All other chemicals were obtained from commercial sources and used without further purification unless otherwise noticed. The synthesis of 2-(4-((*tert*-butoxycarbonyl)amino)butyl)-2-oxazoline (BocOx), the copolymerization of BocOx and MeOx as well as the deprotection of the polymer were done as reported in the literature with slight modification (endcapping with acetic acid and triethylamine instead of sodium azide).^[21]

Solution Preparation for EELs and ETLs: L-Histidine, L-lysine, L-arginine, PMeOx_{20} , P(MeOx_{40} -stat-AmOx₁₀), and P(MeOx_{30} -stat-AmOx₂₀) were dissolved in methanol at a concentration of 0.5 mg mL⁻¹ and 0.25 vol% of acetic acid was added.^[4c] Poly-L-lysine was used as a solution of 1 wt% in deionized water, which was diluted by the same volume of methanol to achieve a concentration of 0.5 wt% in a solvent ratio of water:methanol 1:1 to these solutions also 0.25 vol% of acetic acid was added. TiO_x was processed as previously reported;^[3d,22] only in the case of the diluted TiO_x , the precursor solution was diluted to 1/10 of the usual concentration by dilution with isopropanol.

Solution Preparation for Active Layer: PCDTBT (1 M) and PC₇₁BM (Solenne) were dissolved in a solvent mixture of CB:CF ratio 1:1. The concentration of PCDTBT was 5 mg mL⁻¹ and the ratio of PCDTBT to PCBM was 1:2. The solution was stirred for 2 weeks at 50 °C at 700 rpm.

Processing: Prestructured substrates of ITO on glass (Xinyan Technology Ltd., 10 Ohm sq⁻¹) were cleaned by ultrasonication for

15 min in toluene, followed by sonication for 15 min in isopropanol. Before coating, each substrate was individually dried with an air gun using dry N₂. Afterward PEDOT:PSS (Clevious PH) was spin-cast at 3000 rpm for 35 s and structured with a moist cotton tip; then they were transferred on a hot plate at 50 °C. All PEDOT:PSS samples were then annealed at 178 °C for 15 min and immediately after annealing transferred to a nitrogen glove box. PCDTBT-PC₇₁BM was spin-cast on the PEDOT:PSS at 1200 rpm for 45 s. Afterward the different EELs and ETLs were processed. For the organic EELs, multiple spin frequencies were used to vary the thickness. The chosen spin frequencies were 800, 1000, 1500, 2500, and 4000 rpm. The organic EEL solutions were spin-cast as prepared at the aforementioned spin frequencies. For the solar cells with the methanol, overcast 1 mL of methanol was dropped on the active layer, followed by spinning at 3000 rpm for 30 s to remove the Methanol. The TiO_x layers were processed according to the same procedure as earlier reported,^[3d] only in the cast of the nonannealed samples, no annealing was performed after deposition. Following the samples were placed into a mask and aluminum was evaporated at a pressure of below 5E-5 mbar. After deposition of the electrode, the size of the solar cells was determined by the overlap of patterned top and bottom electrode and resulted in 0.42 cm² devices; the solar cells were sealed with glass slides using a UV curable epoxy glue.

Characterization: Samples were characterized under a LED solar simulator (Wavelabs Sinus 70) calibrated to 1 sun intensity and with an AM1.5G spectrum. The solar cells were measured from -2 to 2 V with a NPLC of 1, a wait time of 10 ms, and a step size of 10 mV. External quantum efficiency (EQE) was characterized using a BENTHAM PVE300. The EQE was measured in a range from 300 to 900 nm in 10 nm steps; this measurement was performed without and with a light bias. To investigate the WF of different CELs, a single-point Kelvin probe system from Anfatec Instruments AG was used. All the measurements were performed in ambient air. Highly oriented pyrolytic graphite (HOPG-WF = 4.46 eV) which is chemically stable in the ambient atmosphere was used for the calibration of the Kelvin probe system. The measurements were carried out at 22 °C and 20–30% relative humidity conditions.

Degradation: Degradation experiments were performed on a self-built aging setup. The light source was white light LEDs and the temperature in the setup was set to 45 °C with the temperature sensor being shaded. The conditions were kept in accordance to ISOS-L1 protocol. Light intensity of the LED was set to an excitation density of 1 sun for these cells.

Supporting Information

Supporting Information is available from the Wiley Online Library or from the author.

Acknowledgments

Open access funding enabled and organized by Projekt DEAL.

Conflict of Interest

The authors declare no conflict of interest.

Keywords

organic charge extraction layers, organic solar cells, stability, structure-property-relationships

Received: January 31, 2020

Revised: July 8, 2020

Published online: August 12, 2020

- [1] a) Y. Cui, H. Yao, J. Zhang, T. Zhang, Y. Wang, L. Hong, K. Xian, B. Xu, S. Zhang, J. Peng, Z. Wei, F. Gao, J. Hou, *Nat. Commun.* **2019**, *10*, 2515; b) Y. Lin, B. Adilbekova, Y. Firdaus, E. Yengel, H. Faber, M. Sajjad, X. Zheng, E. Yarali, A. Seitkhan, O. M. Bakr, A. El-Labban, U. Schwingenschlöggl, V. Tung, I. McCulloch, F. Laquai, T. D. Anthopoulos, *Adv. Mater.* **2019**, *31*, 1902965; c) J. Yuan, Y. Zhang, L. Zhou, G. Zhang, H.-L. Yip, T.-K. Lau, X. Lu, C. Zhu, H. Peng, P. A. Johnson, M. Leclerc, Y. Cao, J. Ullanski, Y. Li, Y. Zou, *Joule* **2019**, *3*, 1140; d) Q. Liu, Y. Jiang, K. Jin, J. Qin, J. Xu, W. Li, J. Xiong, J. Liu, Z. Xiao, K. Sun, S. Yang, X. Zhang, L. Ding, *Sci. Bull.* **2020**, *65*, 272.
- [2] a) H. Hoppe, N. S. Sariciftci, *J. Mater. Res.* **2004**, *19*, 1924; b) T. Kirchartz, P. Kaienburg, D. Baran, *J. Phys. Chem. C* **2018**, *122*, 5829.
- [3] a) W. C. H. Choy, D. Zhang, *Small* **2016**, *12*, 416; b) G. Teran-Escobar, J. Pampel, J. M. Caicedo, M. Lira-Cantu, *Energy Environ. Sci.* **2013**, *6*, 3088; c) Z. Huai, L. Wang, Y. Sun, R. Fan, S. Huang, X. Zhao, X. Li, G. Fu, S. Yang, *ACS Appl. Mater. Interfaces* **2018**, *10*, 5682; d) R. Roesch, K.-R. Eberhardt, S. Engmann, G. Gobsch, H. Hoppe, *Sol. Energy Mater. Sol. Cells* **2013**, *117*, 59; e) Z. Yin, J. Wei, Q. Zheng, *Adv. Sci.* **2016**, *3*, 1500362; f) A. G. Suren, H. Ilona Maria, B. Eva, C. Michael, H. Markus, R. S. Roar, B. Gisele Alves dos Reis, J. Mikkel, C. K. Frederik, *J. Phys. D: Appl. Phys.* **2017**, *50*, 103001; g) R. Meitzner, T. Faber, S. Alam, A. Amand, R. Roesch, M. Büttner, F. Herrmann-Westendorf, M. Presselt, L. Ciammaruchi, I. Visoly-Fisher, S. Veenstra, A. Diaz de Zerio, X. Xu, E. Wang, C. Müller, P. Troshin, M. D. Hager, S. Köhn, M. Dusza, M. Krassas, S. Züfle, E. Kymakis, E. A. Katz, S. Berson, F. Granek, M. Manceau, F. Brunetti, G. Polino, U. S. Schubert, M. Lira-Cantu, et al. *Sol. Energy Mater. Sol. Cells* **2019**, *202*, 110151.
- [4] a) Y. Zhou, C. Fuentes-Hernandez, J. Shim, J. Meyer, A. J. Giordano, H. Li, P. Winget, T. Papadopoulos, H. Cheun, J. Kim, M. Fenoll, A. Dindar, W. Haske, E. Najafabadi, T. M. Khan, H. Sojoudi, S. Barlow, S. Graham, J.-L. Brédas, S. R. Marder, A. Kahn, B. Kippelen, *Science* **2012**, *336*, 327; b) F. A. Larrain, C. Fuentes-Hernandez, W.-F. Chou, V. A. Rodriguez-Toro, T.-Y. Huang, M. F. Toney, B. Kippelen, *Energy Environ. Sci.* **2018**, *11*, 2216; c) Z. Zheng, R. Wang, H. Yao, S. Xie, Y. Zhang, J. Hou, H. Zhou, Z. Tang, *Nano Energy* **2018**, *50*, 169; d) B. Yang, S. Zhang, S. Li, H. Yao, W. Li, J. Hou, *Adv. Mater.* **2017**, *31*, 1804657; e) D. Bilby, B. Frieberg, S. Kramadhati, P. Green, J. Kim, *ACS Appl. Mater. Interfaces* **2014**, *6*, 14964.
- [5] a) G. M. Kim, I. S. Oh, A. N. Lee, S. Y. Oh, *J. Mater. Chem. A* **2014**, *2*, 10131; b) L. Yan, Y. Song, Y. Zhou, B. Song, Y. Li, *Org. Electron.* **2015**, *17*, 94; c) X. Min, F. Jiang, F. Qin, Z. Li, J. Tong, S. Xiong, W. Meng, Y. Zhou, *ACS Appl. Mater. Interfaces* **2014**, *6*, 22628; d) B. A. E. Courtright, S. A. Jenekhe, *ACS Appl. Mater. Interfaces* **2015**, *7*, 26167.
- [6] A. Li, R. Nie, X. Deng, H. Wei, S. Zheng, Y. Li, J. Tang, K.-Y. Wong, *Appl. Phys. Lett.* **2014**, *104*, 123303.
- [7] X. Zhu, B. Guo, J. Fang, T. Zhai, Y. Wang, G. Li, J. Zhang, Z. Wei, S. Duhm, X. Guo, M. Zhang, Y. Li, *Org. Electron.* **2019**, *70*, 25.
- [8] a) Y. Hirose, C. I. Wu, V. Aristov, P. Soukiassian, A. Kahn, *Appl. Surface Sci.* **1997**, *113–114*, 291; b) M. A. Baldo, S. R. Forrest, *Phys. Rev. B* **2001**, *64*, 085201; c) B. N. Limketkai, M. A. Baldo, *Phys. Rev. B* **2005**, *71*, 085207.
- [9] U. Würfel, L. Perdígón-Toro, J. Kurpiers, C. M. Wolff, P. Caprioglio, J. J. Rech, J. Zhu, X. Zhan, W. You, S. Shoaee, D. Neher, M. Stollerfoht, *J. Phys. Chem. Lett.* **2019**, *10*, 3473.
- [10] T. Kirchartz, B. E. Pieters, K. Taretto, U. Rau, *Phys. Rev. B* **2009**, *80*, 035334.
- [11] Z. Hu, Z. Zhong, K. Zhang, Z. Hu, C. Song, F. Huang, J. Peng, J. Wang, Y. Cao, *NPG Asia Mater.* **2017**, *9*, e379.
- [12] J. Kim, A. Ho-Baillie, S. Huang, *Sol. RRL* **2019**, *3*, 1800302.

- [13] R. Roesch, M. Seeland, M. Baerenklau, G. Gobsch, H. Hoppe, *Sol. Energy Mater. Sol. Cells* **2013**, *111*, 212.
- [14] S. Beaupré, M. Leclerc, *J. Mater. Chem. A* **2013**, *1*, 11097.
- [15] a) C. H. Peters, I. T. Sachs-Quintana, J. P. Kastrop, S. Beaupré, M. Leclerc, M. D. McGehee, *Adv. Energy Mater.* **2011**, *1*, 491; b) W. R. Mateker, I. T. Sachs-Quintana, G. F. Burkhard, R. Cheacharoen, M. D. McGehee, *Chem. Mater.* **2015**, *27*, 404.
- [16] L. Ye, H. Hu, M. Ghasemi, T. Wang, B. A. Collins, J.-H. Kim, K. Jiang, J. H. Carpenter, H. Li, Z. Li, T. McAfee, J. Zhao, X. Chen, J. L. Y. Lai, T. Ma, J.-L. Bredas, H. Yan, H. Ade, *Nat. Mater.* **2018**, *17*, 253.
- [17] A. Wagenpfahl, D. Rauh, M. Binder, C. Deibel, V. Dyakonov, *Phys. Rev. B* **2010**, *82*, 115306.
- [18] a) L. Ye, Y. Jing, X. Guo, H. Sun, S. Zhang, M. Zhang, L. Huo, J. Hou, *J. Phys. Chem. C* **2013**, *117*, 14920; b) H. Zhou, Y. Zhang, J. Seifert, S. D. Collins, C. Luo, G. C. Bazan, T.-Q. Nguyen, A. J. Heeger, *Adv. Mater.* **2013**, *25*, 1646; c) S. Guo, B. Cao, W. Wang, J.-F. Moulin, P. Müller-Buschbaum, *ACS Appl. Mater. Interfaces* **2015**, *7*, 4641.
- [19] a) K. M. Knesting, H. Ju, C. W. Schlenker, A. J. Giordano, A. Garcia, O. N. L. Smith, D. C. Olson, S. R. Marder, D. S. Ginger, *J. Phys. Chem. Lett.* **2013**, *4*, 4038; b) J. Reinhardt, M. Grein, C. Bühler, M. Schubert, U. Würfel, *Adv. Energy Mater.* **2014**, *4*, 1400081; c) S. Wheeler, F. Deledalle, N. Tokmoldin, T. Kirchartz, J. Nelson, J. R. Durrant, *Phys. Rev. Appl.* **2015**, *4*, 024020.
- [20] a) M. O. Reese, S. A. Gevorgyan, M. Jorgensen, E. Bundgaard, S. R. Kurtz, D. S. Ginley, D. C. Olson, M. T. Lloyd, P. Moryllo, E. A. Katz, A. Elschner, O. Haillant, T. R. Currier, V. Shrotriya, M. Hermenau, M. Riede, K. R. Kirov, G. Trimmel, T. Rath, O. Inganas, F. L. Zhang, M. Andersson, K. Tvingstedt, M. Lira-Cantu, D. Laird, C. McGuinness, S. Gowrisanker, M. Pannone, M. Xiao, J. Hauch, et al., *Sol. Energy Mater. Sol. Cells* **2011**, *95*, 1253; b) R. Roesch, T. Faber, E. von Hauff, T. M. Brown, M. Lira-Cantu, H. Hoppe, *Adv. Energy Mater.* **2015**, *5*, 24; c) E. A. K. Mark, V. Khenkin, A. Abate, G. Bardizza, J. J. Berry, C. J. Brabec, F. Brunetti, V. Bulović, Q. Burlingame, A. Di Carlo, R. Cheacharoen, Y.-B. Cheng, A. Colmann, S. Cros, K. Domanski, M. Dusza, C. J. Fell, S. R. Forrest, Y. Galagan, D. Di Girolamo, M. Grätzel, A. Hagfeldt, E. von Hauff, H. Hoppe, J. Kettle, H. Köbler, M. S. Leite, S. Liu, Y.-L. Loo, J. M. Luther, et al., *Nat. Energy* **2020**, *5*, 35; d) M. V. Khenkin, E. A. Katz, A. Abate, G. Bardizza, J. J. Berry, C. Brabec, F. Brunetti, V. Bulović, Q. Burlingame, A. Di Carlo, R. Cheacharoen, Y.-B. Cheng, A. Colmann, S. Cros, K. Domanski, M. Dusza, C. J. Fell, S. R. Forrest, Y. Galagan, D. Di Girolamo, M. Grätzel, A. Hagfeldt, E. von Hauff, H. Hoppe, J. Kettle, H. Köbler, M. S. Leite, S. Liu, Y.-L. Loo, J. M. Luther, et al., *Nat. Energy* **2020**, *5*, 35.
- [21] a) M. Hartlieb, D. Pretzel, K. Kempe, C. Fritzsche, R. M. Paulus, M. Gottschaldt, U. S. Schubert, *Soft Matter* **2013**, *9*, 4693; b) T. Lühmann, M. Schmidt, M. N. Leiske, V. Spieler, T. C. Majdanski, M. Grube, M. Hartlieb, I. Nischang, S. Schubert, U. S. Schubert, L. Meinel, *ACS Biomater. Sci. Eng.* **2017**, *3*, 304.
- [22] J. Y. Kim, S. H. Kim, H.-H. Lee, K. Lee, W. Ma, X. Gong, A. J. Heeger, *Adv. Mater.* **2006**, *18*, 572.

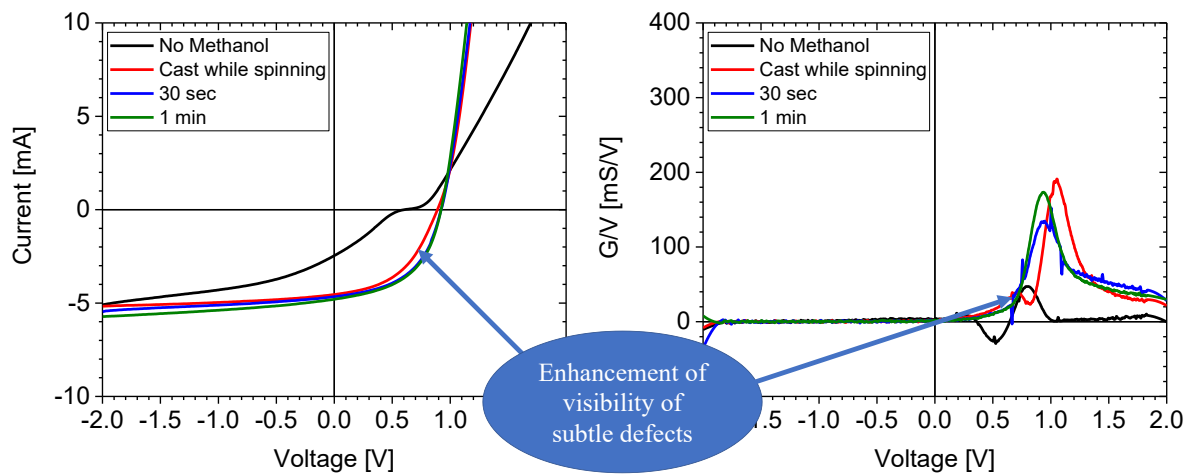
Publications P1 to P5

Publication P5

An effective method of reconnoitering current-voltage (IV) characteristics of organic solar cells

Rico Meitzner, Jose Prince Madalaimuthu, Shahidul Alam, Md Moidul Islam, Sebastian Peiler, Aman Anand, Johannes Ahner, Martin D. Hager, Ulrich S. Schubert, Yingping Zou, Frédéric Laquai, Harald Hoppe

Journal of Applied Physics D **2022**, 132, 015001



With the permission of AIP Publishing, Copyright © 2022.

An effective method of reconnoitering current-voltage (*IV*) characteristics of organic solar cells

Cite as: J. Appl. Phys. **132**, 015001 (2022); doi: [10.1063/5.0089706](https://doi.org/10.1063/5.0089706)

Submitted: 28 February 2022 · Accepted: 8 June 2022 ·

Published Online: 5 July 2022



Rico Meitzner,^{1,2,a)} Jose Prince Madalaimuthu,^{1,2} Shahidul Alam,^{1,2,3} Md Moidul Islam,^{1,2} Sebastian Peiler,^{1,2} Aman Anand,^{1,2} Johannes Ahner,² Martin D. Hager,^{1,2} Ulrich S. Schubert,^{1,2} Yingping Zou,⁴ Frédéric Laquai,³ and Harald Hoppe^{1,2}

AFFILIATIONS

¹Center for Energy and Environmental Chemistry Jena (CEEC Jena), Friedrich Schiller University Jena, 07743 Jena, Germany

²Laboratory of Organic and Macromolecular Chemistry (IOMC), Friedrich Schiller University Jena, 07743 Jena, Germany

³King Abdullah University of Science and Technology (KAUST), KAUST Solar Center (KSC), Physical Sciences and Engineering Division (PSE), Thuwal 23955-6900, Kingdom of Saudi Arabia

⁴College of Chemistry and Chemical Engineering, Central South University, Changsha 410083, China

^{a)}Author to whom correspondence should be addressed: rico.meitzner@uni-jena.de

ABSTRACT

Current-voltage (*IV*) characterization is the most fundamental measurement performed on solar cells. This measurement is commonly used to extract basic solar cell parameters, such as open circuit voltage, short circuit current density, fill factor, and power conversion efficiency. We were able to obtain a fast tool to find defective behavior using Simulation Program with Integrated Circuit Emphasis simulations and generate an understanding of which device property can create such defective behaviors by analyzing the second derivative of *IV* curves.

Published under an exclusive license by AIP Publishing. <https://doi.org/10.1063/5.0089706>

I. INTRODUCTION

Organic solar cells represent a highly promising technology for the future of sustainable energy.^{1–3} Due to their specific applicability for agrivoltaic applications, they can enable rapid electrification, particularly in more remote locations.^{4–6} Recently, they have achieved 18% Power Conversion Efficiency (PCE) on lab scale⁷ and around 14% on module scale.³ They can obtain a very low environmental footprint^{8,9} and have shown that they are able to achieve long lifetimes sufficient for market entry.^{10,11} Their development is, for the moment, still driven mainly by serendipity, as many metrics of their materials cannot easily be predicted just from their structure. Hence, many compounds have to be synthesized and the properties have to be experimentally determined.

The most basic measurement with which every solar cell is evaluated is a current-voltage (*IV*) characterization, where the solar cell is measured under an AM1.5G compatible light source, to determine its performance. The solar cell under these circumstances should behave like a diode under illumination and should, therefore, follow the Shockley equation¹² with an additional term for the series and shunt resistance that a real solar cell always has,

$$I = I_L - I_0 \left\{ \exp \left(\frac{q(V + IR_S)}{nk_B T} \right) - 1 \right\} - \frac{V + IR_S}{R_{Sh}}, \quad (1)$$

with *I* being the current, *I_L* the photocurrent, *I₀* the dark saturation current, *q* the elementary charge, *V* the applied voltage, *R_S* the series resistance, *n* the diode ideality factor, *k_B* the Boltzmann constant, *T* the temperature, and *R_{Sh}* the shunt resistance.

Any deviation from the behavior of an ideal diode is usually associated with performance losses. Hence, the shape of the *IV* curve is also the most fundamental indicator of a well-functioning or aberrant device. Obtaining a better understanding of aberrations in an *IV* curve can be the first step to understand which part of the device/layer stack is not working as expected. A usual way to do so can be simulations of the *IV* behavior. A well-established tool to do so is SPICE^{13–15} (Simulation Program with Integrated Circuit Emphasis), which allows to model equivalent circuits of solar cells.

It has already been widely used in the analysis of organic solar cells. For example, Zuo *et al.* used an equivalent circuit model to understand the occurrence of S-shapes in vacuum processed organic solar cells in dependence on the anode buffer layer that

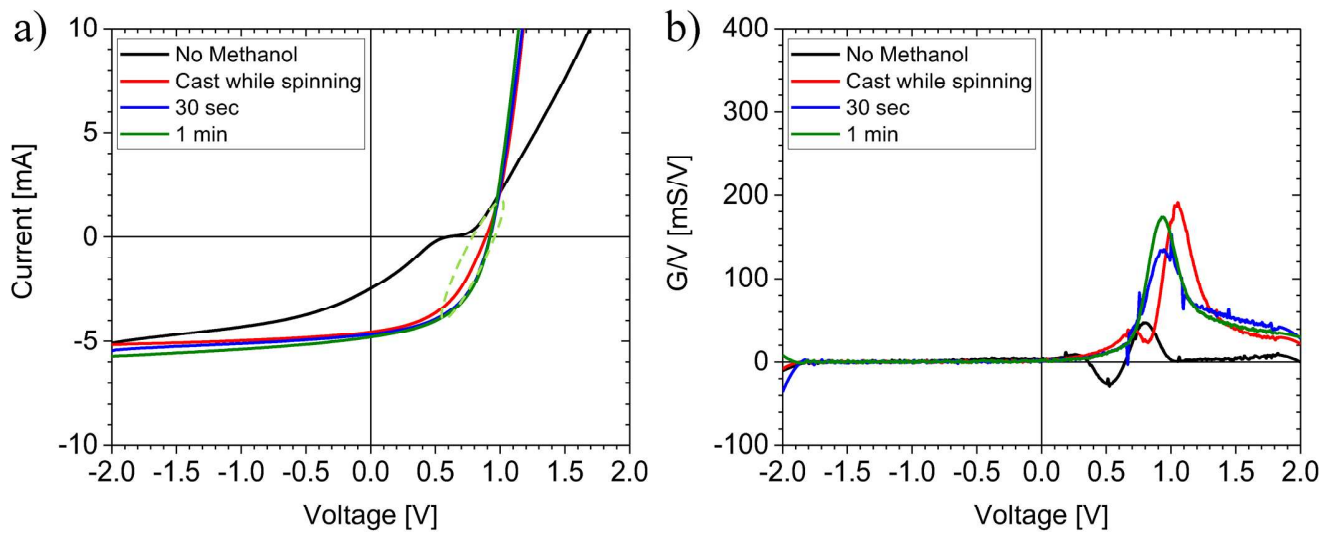


FIG. 1. *IV* curves (a) of PCDTBT:PC₇₁BM based organic solar cells without and with an overcast of methanol done on top of the active layer and their respective second derivatives (b).

was used.¹⁶ They, thereby, found that their results were best explained by assuming a Schottky contact at the interface to the anode buffer layer and the active layer. Yoo *et al.* studied light dependence of organic solar cell performance via the usage of equivalent circuit models.¹⁷ They found that it was not possible to sufficiently describe their experimental results with a circuit model containing only a single diode and a single shunt resistance, but instead, they had to add a second one of each of these components, showing light-dependent parameters. Though they also stated that from these fitting parameters alone, it is not sufficiently possible to draw conclusions about individual physical processes occurring in the solar cell and more sophisticated methods have to be applied to gain a deeper understanding of the processes.

Qi *et al.* studied the changes in fill factor (FF) in organic solar cells using equivalent circuit models. They modeled the impact of series and shunt resistances, as well as of dark saturation current density and diode ideality factor on the FF. Furthermore, they studied how the S-shapes can be explained with equivalent circuit models and concluded that the various physical processes that can result in an S-shape in the end still result in a common effect, which is a reduction in the internal electric field due to charge accumulation and, thereby, hinder charge carrier extraction and increase recombination. Ecker *et al.* also studied the impact of light soaking on inverted organic solar cells with a titanium oxide electron transport layer (ETL) via the usage of equivalent circuit models.¹⁸ They proposed a circuit with multiple capacitances, where one was associated with the TiO_x layer, while another one with the capacitance of the active layer. They found that upon light soaking, the capacitance of the active layer is reduced due to a reduction of resistance of the TiO_x layer, therefore increasing the internal electric field in the active layer and helping with charge extraction.

S-shapes in the *IV* curves of organic solar cells are a well-known deviation from ideality.^{12,13,19} They can be caused by blocking

contacts, reductions of charge carrier mobility of one charge carrier, space charge zones, for example, due to the accumulation of trapped charge carriers, and limited surface recombination at any of the charge extraction layers. Besides the S-shapes, there can also be more subtle abnormalities,^{20,21} which nonetheless reduce the overall

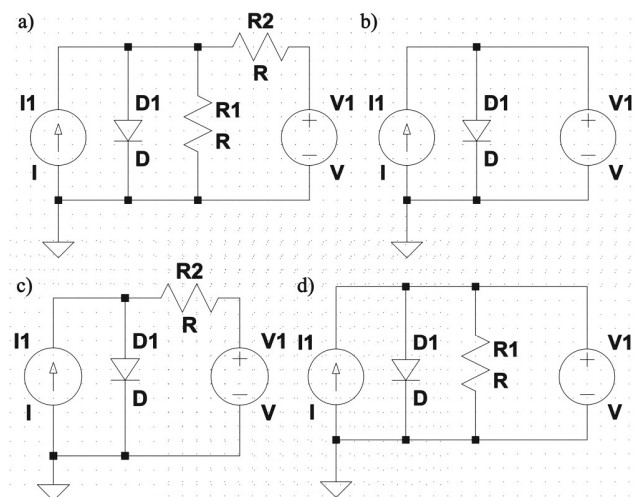


FIG. 2. Equivalent circuits of solar cells in LTSpice: (a) Standard equivalent circuit of a solar cell with photocurrent (I1), Diode (D1), Shunt Resistance (R1), Series Resistance (R2); (b) circuit used to evaluate the impact of dark saturation current and diode ideality factor on the second derivative of the *IV* curve; (c) circuit used to evaluate the impact of series resistance on the second derivative; (d) circuit used to evaluate the impact of shunt resistance on the second derivative.

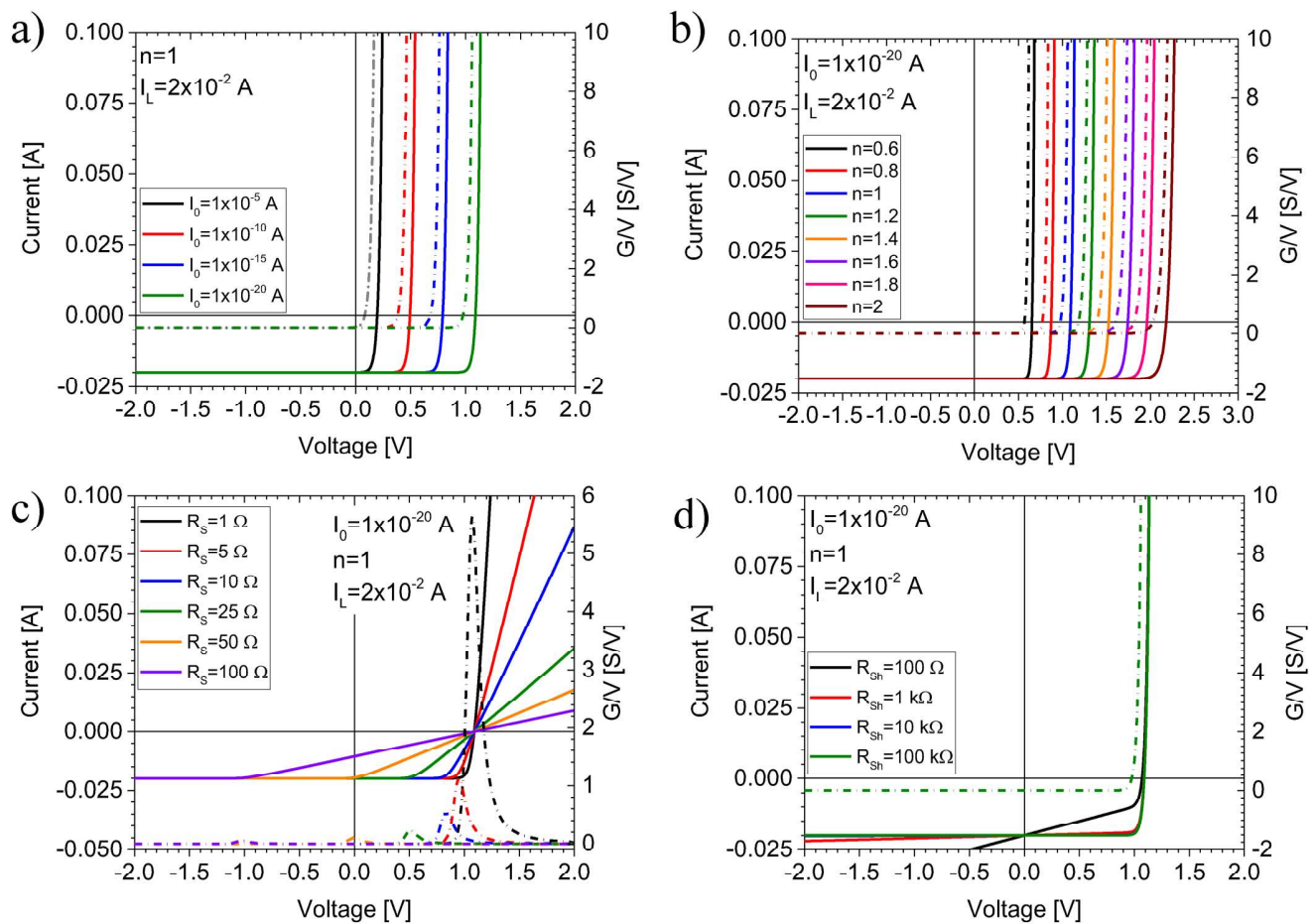


FIG. 3. *IV* curves simulated in LTSpice plus their respective second derivatives: (a) impact of dark saturation current variation; (b) impact of diode ideality factor variation; (c) impact of series resistance variation; (d) impact of shunt resistance variation.

performance of a device, and actually for an aged device, might be an early indicator of further degradation in the future.

The scope of this paper is to present an additional and new way on how to analyze data obtained from *IV* characterizations. On the one hand, we determined the second order derivatives of the *IV* curves in order to emphasize the characteristics of the measured curves. On the other hand, however, we used SPICE,¹⁵ in order to address electric circuits and their *IV* characteristics. This enables us to narrow down the type of particular appearing defects. Thus, we are able to apply only the really required sophisticated methods to study device defects in organic solar cells and analyze them faster.

II. EXPERIMENTAL

A. Materials

ITO glass was obtained from Xinyan Technology Ltd. and had a sheet resistance of $10 \Omega/\text{sq}$. The PEDOT:PSS

[poly(3,4-ethylenedioxythiophene) polystyrene sulfonate] used was Clevis PH from Heraeus for unaged devices; for the devices on which aging was performed, PVP AI 4083 was used. As donor polymer PCDTBT (poly[9-(1-octylonyl)-9H-carbazole-2,7-diyl]-2,5-thiophenediyl-2,1,3-benzothiadiazole-4,7-diyl-2,5-thiophenediyl], poly[N-9'-heptadecanyl-2,7-carbazole-alt-5,5-(4',7'-di-2-thienyl-2',1',3'-benzothiadiazole)]) obtained from I-material was used. The acceptor used was PC₇₁BM ([6,6]-phenyl-C71-butyric acid methyl ester) that was obtained from nano-C. A solution of PCDTBT:PC₇₁BM in CF:CB (1:1) was prepared two weeks before the processing of the devices. The PCDTBT concentration was 5 mg/ml and the ratio between PCDTBT and PC₇₁BM was 1:2; it was kept at 50 °C and stirred at 700 rpm. For the devices shown in Figs. 10 and S2 in the [supplementary material](#), solutions of TTFQx-T1:PC₇₁BM, TTFQx-T1:ITIC, HFAQx-T:PC₇₁BM, and HFAQx-T:ITIC were prepared in the glovebox with a ratio of 1:1.5 in chlorobenzene. The solutions were kept stirred overnight on a hot plate at 50 °C.

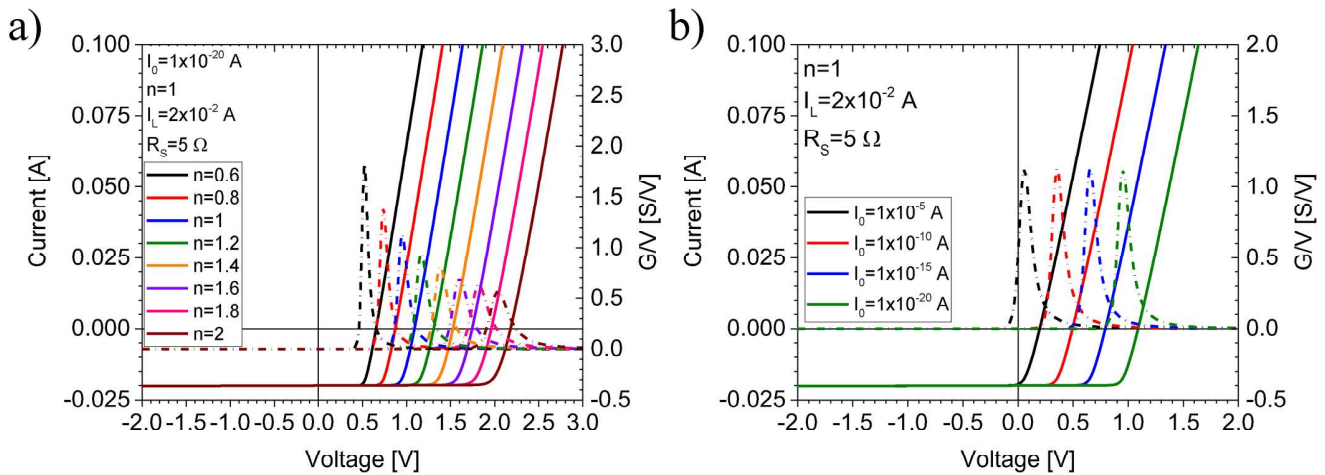


FIG. 4. Combined impact of series resistance and (a) diode ideality factor and (b) dark saturation current.

B. Processing

Substrates were cleaned by first sonification of the ITO glass substrates in toluene for 15 min, followed by sonification for another 15 min in isopropanol. Following this, the substrates were dried with dry nitrogen. PEDOT:PSS was coated via spin coating on the substrates at 3000 rpm for 35 s. Each sample was structured via the usage of a moist cotton tip and annealed at 178 °C for 15 min. After annealing, they were immediately transferred into a nitrogen glovebox. PCDTBT:PC₇₁BM solution was spin-cast on the PEDOT:PSS at 1200 rpm for 45 s. For different sample processing, methanol was either applied after active layer processing or not. For the samples with methanol treatment, they were either spun up again and methanol was dropped onto the spinning active layer or the samples were at rest. Methanol was dropped on the active layer and the sample was spun again for either 30 s or 1 min. After methanol was initially dropped onto the sample, for aged devices, the active layer was post-treated with methanol for 45 s. After the active layer processing and potential post-treatment, the samples were transferred to a shadow mask and placed into a vacuum

chamber to thermally evaporate an aluminum electrode. At a pressure below 5E-5 mbar, a 200 nm thick Al electrode was deposited onto the samples. Following, the samples were sealed with a glass slide and UV curable epoxy glue.

Processing for the devices in Figs. 10 and S2 in the supplementary material followed a similar procedure as with the PCDTBT:PC₇₁BM devices, with the following alterations; for TTFQx-T1:PC₇₁BM solutions, before spin casting, 0.5 vol. % DIO was added; TTFQx-T1:ITIC devices were thermally annealed at 150 °C for 10 min inside the glovebox; for HFAQx-T:PC₇₁BM solutions, before spin casting, 0.25 vol. % DIO was added; HFAQx-T:ITIC devices were thermally annealed at 130 °C for 10 min inside the glovebox. Additionally, in these devices, a Mg layer of 50 nm thickness was thermally evaporated before the deposition of the Al electrode.

C. Characterization

Samples were characterized using a solar simulator (Wavelabs Sinus 70) calibrated at an intensity of 1 sun and with an AM 1.5G spectrum. A SMU (Keithley 2400) was used to record the IV curves, the settings were NPLC of 1, a wait time of 10 ms, and a measurement range of -2 to 2 V split into 10 mV measurement intervals. Samples were aged in a custom setup at 45 °C ambient temperature and under a white light LED, compatible with ISOS-L1 protocols.^{23,24} Aged samples were measured and automated at 30 min intervals with a sweep range from -2 to 2 V in 10 mV intervals, with an NPLC of 1 and a wait time of 10 ms. A Keithley 2700 SMU was used in combination with a multiplexer from Keithley.

Anfatec Instruments AG (Germany) single-point Kelvin Probe (KP) system was used for work function measurements. All of the measurements were carried out in the open air. The KP system was calibrated using highly oriented pyrolytic graphite (HOPG) with a known work function of 4.46 (±) 0.04 eV. HOPG was freshly sliced

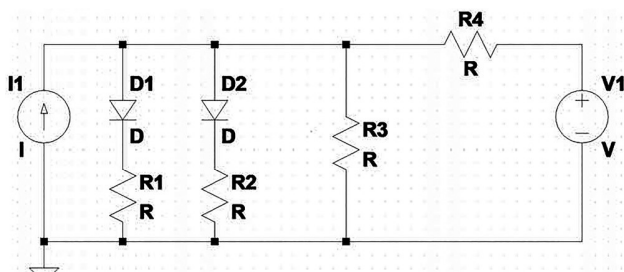


FIG. 5. Equivalent circuit in LTSpice to study the origin of abnormal behavior of the IV curve in the devices seen in Fig. 1.

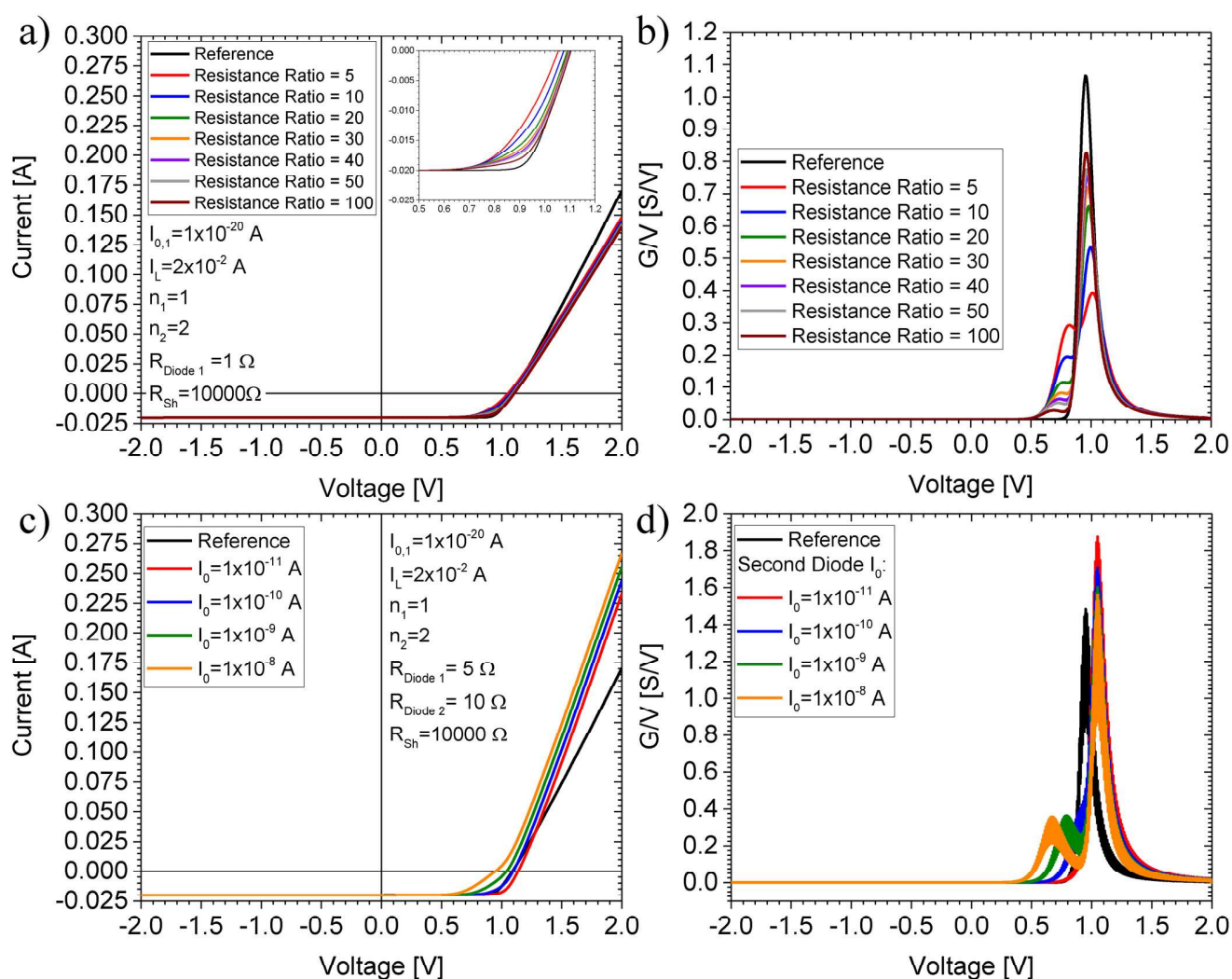


FIG. 6. Simulation results from LTSpice for the equivalent circuit shown in Fig. 5. There are clearly two distinct peaks visible, whose position and ratio can be neatly modified by the proper choice of parameters; (a) I/V curves for the variation of resistance ratio between R_1 and R_2 , the inset is showing a close up of the I/V curves around the maximum power point; (b) respective second derivative of the I/V curves in (a); (c) I/V curves for the variation of dark saturation current of the weak performing diode.

with the use of a sticky tape for each calibration of the KP system, exposing a pristine graphite surface.

D. Simulations

All equivalent circuits in this paper were simulated using the software LTSpice,²⁵ due to its free-of-cost availability and compatibility with various operating systems.

III. RESULTS AND DISCUSSION

In Fig. 1, the I/V curves of conventional organic solar cells based on an active layer of PCDTBT:PC₇₁BM are shown. The cells

were treated with methanol after spin casting the active layer. On the basis of an earlier work, we knew that treatment with methanol is able to reduce the S-shape character of the I/V curve of an organic solar cell.²² The first I/V curve in Fig. 1(a) shows a cell where no methanol was used as a post active layer processing step and one can see a clear S-shape in the I/V curves of all the cells on this device. In Fig. 1(a), the second I/V curve shows the cell where after the active layer deposition, 1 ml of methanol was dropped on the active layer while the substrate was spinning. One can clearly see an improvement in the device characteristics, but there is still only a weakly visible kink around the maximum power point (MPP) of the cells, which is marked with a light green oval. To get

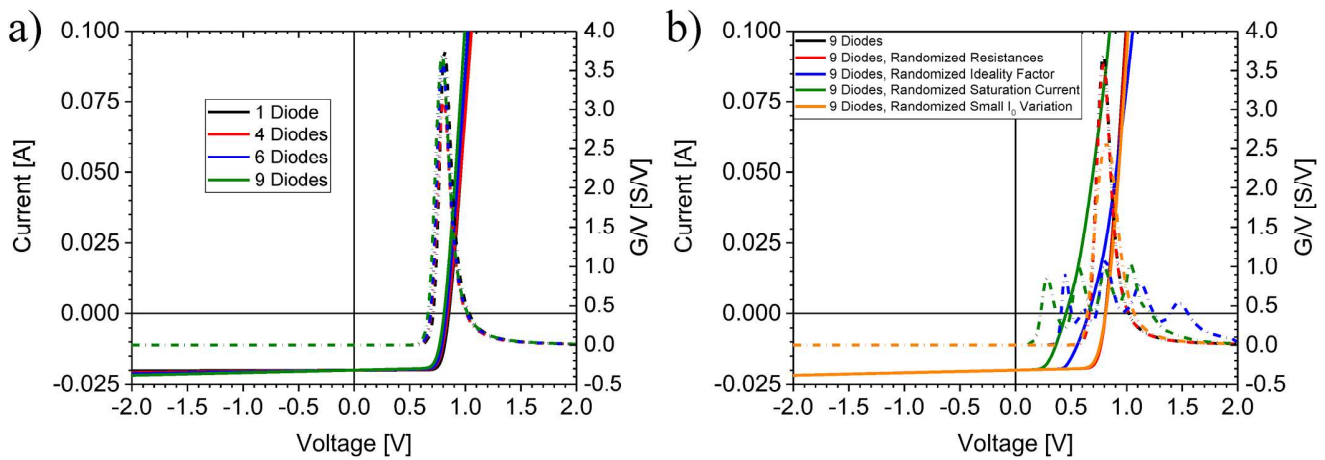


FIG. 7. *IV* curve simulations of circuits containing multiple sub-solar cells as shown in Fig. 2(a). For more details, see the supplementary material; (a) identical parameters for all sub-solar cells, overall device series resistance kept constant and (b) increased variation of sub-solar cell variation.

a better picture—if this kink might still be a very weak S-shape—we calculated the second derivative of the *IV* curve, as an S-shape should have an inflection point and should, therefore, show up as a crossing of the voltage axis in the second derivative. The second derivative for this cell is shown in (b), and it can be seen that there is no crossing of the voltage axis; instead, there is only a flat spot. From the second derivative of the first *IV* curve seen in Fig. 1(a), which is shown in (b), one can clearly see that an S-shape is also resulting in a crossing of the voltage axis. For the last two cells shown in Fig. 1(a), methanol was dropped on the active layer after its processing and the devices were kept coated with methanol for either 30 s or up to 1 min before it was spun off the films. For both of these devices, the flat spot in the *IV* curve visible as a valley in the second derivative disappeared, and only a single peak remained, which was above the value of the open-circuit voltage of the devices.

To gain a better understanding of what these different shapes of second derivatives mean for the processes happening in the solar cell, we performed simulations of the *IV* curves via the usage of SPICE. First, we wanted to understand the contributions of different circuit elements in the standard equivalent circuit used for solar cells on the second derivative. Figure 2 shows the different equivalent circuits we used in SPICE, (a) is the well-established equivalent circuit of a solar cell with a photocurrent source (I_1), a diode (D1), a shunt resistance (R1), and a series resistance (R2); (b) was the circuit used to gain an understanding of the parameters impacting the second derivative in terms of the diode parameters, with only a diode being present. Furthermore, (c) and (d) were the basis for studying the impact of either series or shunt resistance on the second derivative.

In Fig. 3, the simulated *IV* curves and their respective second derivatives are shown, (a) and (b) are based on simulation results done with the circuits shown in Fig. 2(b), while for Fig. 3(a), the diode ideality factor n was kept constant and the dark saturation current I_0 was varied for (b) I_0 was kept constant, while n was

varied. The variation of I_0 and n only results in a shift of where the second derivative is starting to increase, which is an expected result, as without series and shunt resistance, the diode equation is a simple exponential function and will keep its principle shape even after derivation only with a modified pre-factor. Figure 3(c) shows the simulation results for the circuit shown in Fig. 2(c) with R_S added; here, I_0 and n were kept constant, while R_S was varied. The second derivative in this case shows a clear peak around the open-circuit voltage of the simulated *IV* curve and it is qualitatively similar to the second derivative of the solar cells *IV* curves shown in Figs. 1(f) and 1(h). This peak can be understood when looking at what the second derivative represents, namely, a change in conductivity with the applied bias. The only element in the circuit showing a bias-dependent conductivity is the diode. Because for increasing voltage bias, the diode behavior dominates the *IV* characteristic, and thus, the increasing bias causes an increase in current density. For a greater voltage bias, however, the ohmic part of the series resistor will start to govern the *IV* characteristic. Because of the linear relation between current and voltage for an ohmic resistor, the second derivative of the current with respect to voltage bias is zero, which is why the whole *IV* characteristic of the solar cells becomes zero for sufficient great bias; thus, the increasing current for diode-governed bias and decreasing current until zero for ohmic-governed bias explain why in any real solar cell the second derivative of the *IV* curve is expected to show a peak. This

TABLE I. Possible impacts of methanol washing on the active layer.

Hypothesis	“Short-term”	“Long-term”	Probability
Removal of impurities	x	X	Possible
Formation of a SAM	x	X	Low
Stratification of active layer		X	Possible

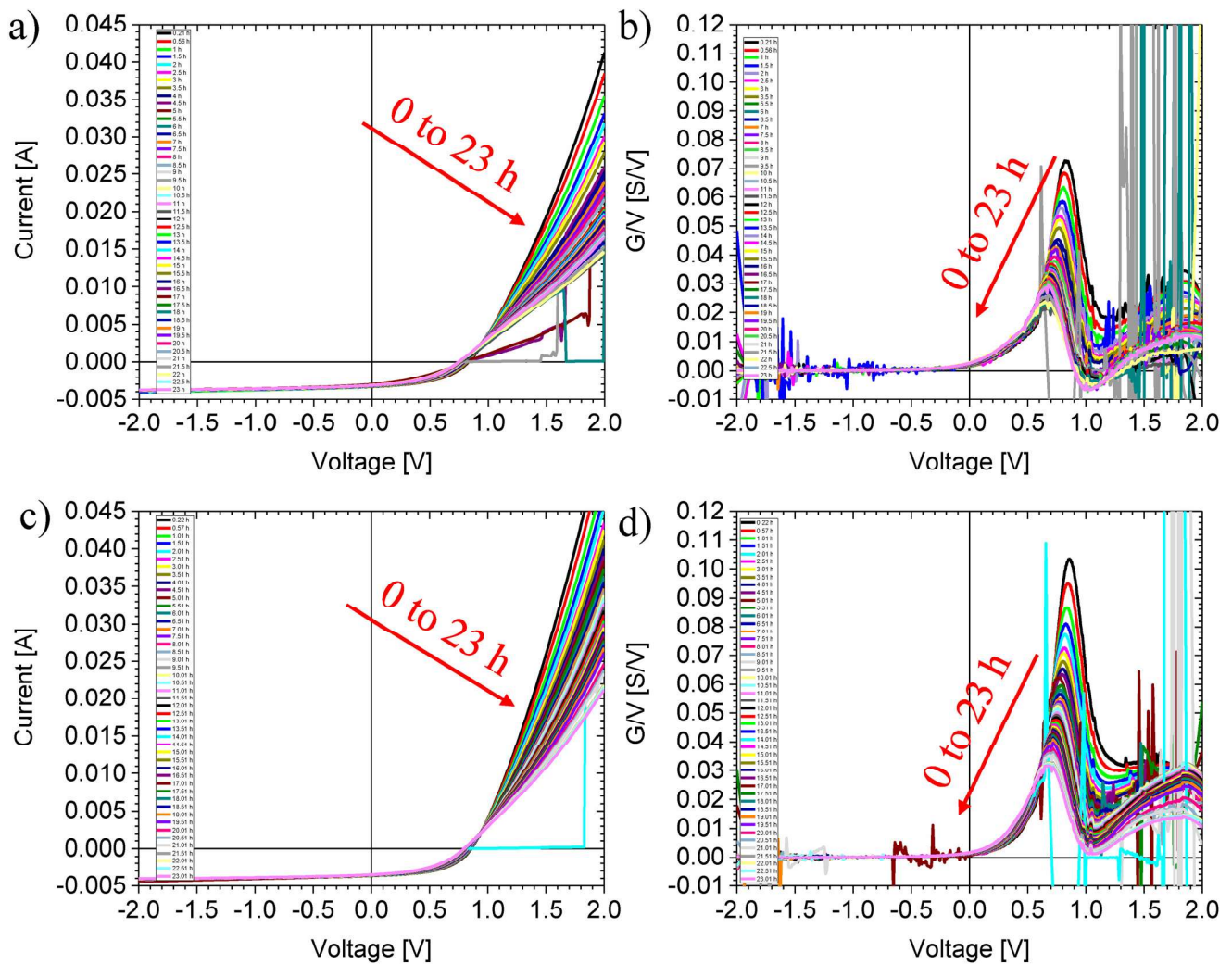


FIG. 8. *IV* curves and their respective second derivatives for organic solar cells (OSCs) of the first 24 h, aged under ISOS-L1 conditions. Each curve was measured automatically every 30 min. For the second derivative, some curves were plotted with 90% transparency for better visibility. (a) *IV* curve for the device developing a blocking contact within 24 h; (b) respective second derivative; (c) device is not developing a blocking contact within 24 h; (d) respective second derivative.

behavior can be witnessed for the second order derivatives. Figure 3(d) shows the *IV* curve of the simulation done with the equivalent circuit shown in Fig. 2(d). All the curves shown for the second derivative are on top of each other, i.e., they do not vary with shunt resistance, as all the other parameters were constant for these simulations. This result can be easily understood as the term for shunt resistance in the diode equation is a linear term, i.e., it disappears after twice differentiating the equation.

From Fig. 3(c), we saw some interesting interactions between the diode in the circuit and the series resistance on the second derivative of the *IV* curve, i.e., a peak started to form. For a better understanding of the shape and position of this peak, we further studied the interplay between series resistance, dark saturation

current, and diode ideality factor. The results of these simulations can be seen in Fig. 4; the equivalent circuit used was the same as for Fig. 3(c). In Fig. 4(a), the impact of the diode ideality factor can be seen on the height, position, and width of the peak in the second derivative—an increase in n results in a reduction in peak size, a shift in peak position toward higher voltages, and an increase in the overall width of the peak. Figure 4(b), on the other hand, shows the impact of dark saturation current on the peak, and the only impact this parameter has is a shift in peak position with a shift toward higher voltages with a reduction in dark saturation current.

From previous simulations, we saw that a combination of the series resistor and diode results in a peak in the second derivative.

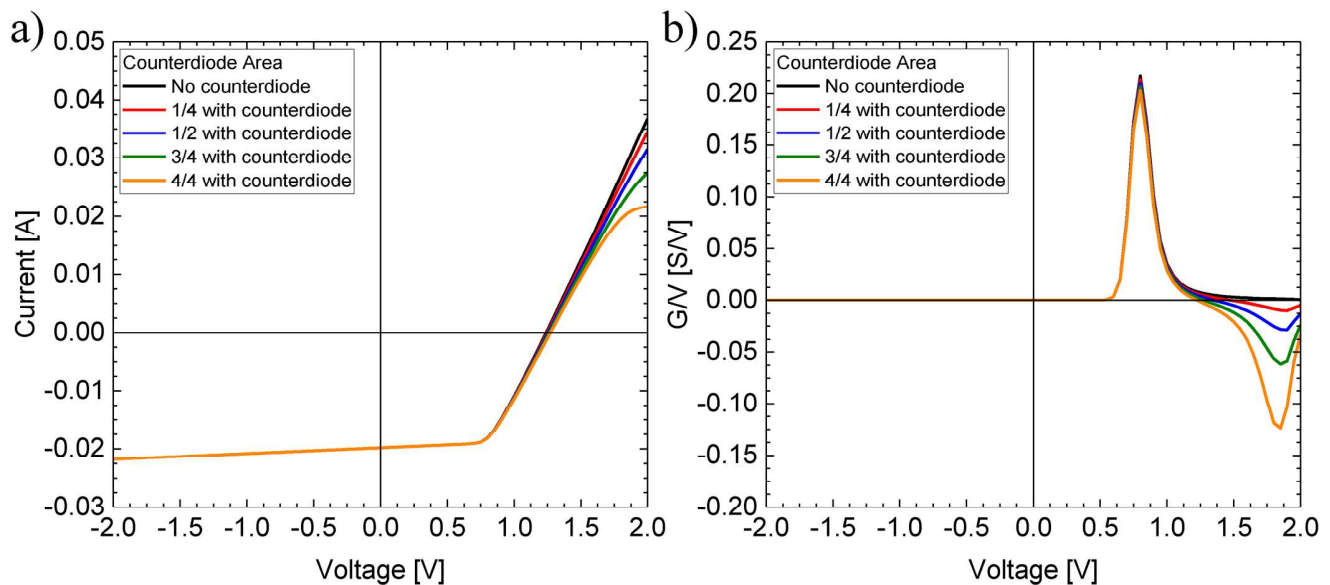


FIG. 9. Simulation of the formation of a blocking contact over time. (a) IV curves from SPICE simulation, (b) Respective second derivatives of the IV curves from (a).

This showed that for the shape of the second derivative found for the solar cell with a simple overcast of methanol while spinning, shown in Fig. 1(b), it is required to have two diodes in parallel, to see such a feature of the main peak with an associated side peak. For evaluation of such a phenomenon, we simulated the circuit seen in Fig. 5 in LTSpice.

The resulting IV curves of the aforementioned simulations are shown in Fig. 6. As we already saw from Figs. 3(c) and 4, there is a combined impact on the shape of the peak in the second derivative of the IV curves from the interaction of I_0 , n , and R_s , and we performed multiple simulations where we modified these parameters between two diodes. Thereby, we assumed the diodes to perform worse than the other; hence, we inherently set the dark saturation current of the second diode significantly lower than that of the well-functioning diode. The results of these simulations can be seen in Fig. 6. In (a) and (b), we varied the ratio of resistance associated with the respective diodes. We assumed that the regions with a well-functioning diode should generally show a low contact resistance and should, therefore, have an inherently lower resistance than the badly functioning diode, which shows a high dark saturation current and, therefore, much leakages. From (a), one can see that the parallel diode with a large dark saturation current results in a reduction in the fill factor. This reduced fill factor is more pronounced when the associated contact resistance of the diode is better, i.e., lower, as this results in a larger current flow across the defective diode. From the associated second derivative shown in Fig. 6(b), one can see that the second diode indeed results in a secondary peak, which shifts toward lower voltages with an increased contact resistance and additionally reduces in peak height, while the main peak increases with a reduction in the secondary peak height. In Figs. 6(c) and 6(d), the resistance ratio between the two

diodes is kept constant, but the dark saturation current of the secondary diode was increased. Again, this increase results in a clear reduction of the fill factor and also the open-circuit voltage, once the secondary diode's dark saturation current has increased sufficiently enough. With regard to the second derivative, see Fig. 6(d), a secondary peak can be seen and with an increase in the dark saturation current of the defective diode, that secondary peak shifts toward lower voltages, while the main peak is reduced in height.

The simulation results in Fig. 6 can successfully reproduce the shape of the second derivative seen for the device shown in Fig. 1 with only methanol overcast during spinning, though they are quantitatively not sufficient. In principle, as a real device consists of many diodes in parallel to each other, we created several increased equivalent circuit models based on multiple parallel-connected diodes with four, six, and up to nine diodes, and the equivalent circuits can be seen in the supplementary material. In Fig. 7, these simulation results are shown for (a) all the parameters that we kept the same between the diodes; also, the overall value of the series resistance, which would be globally measured equal, to get a comparable result in terms of the overall shape of the IV curve. What can be seen from the second derivative is that with an entirely homogenous device in terms of diode parameters, there is basically no difference between a single diode model and a model with multiple diodes. In (b), we additionally varied the different parameters of the diodes and their associated contact resistance, while a variation of contact resistances within the parameter space we chose does not seem to have an impact. In the variation space we used for the diode ideality factor and the dark saturation current, a multitude of peaks appears. As this did not represent the variation we saw in any of the devices studied, we chose a smaller variation for the dark saturation current, and instead of multiple peaks, we got a

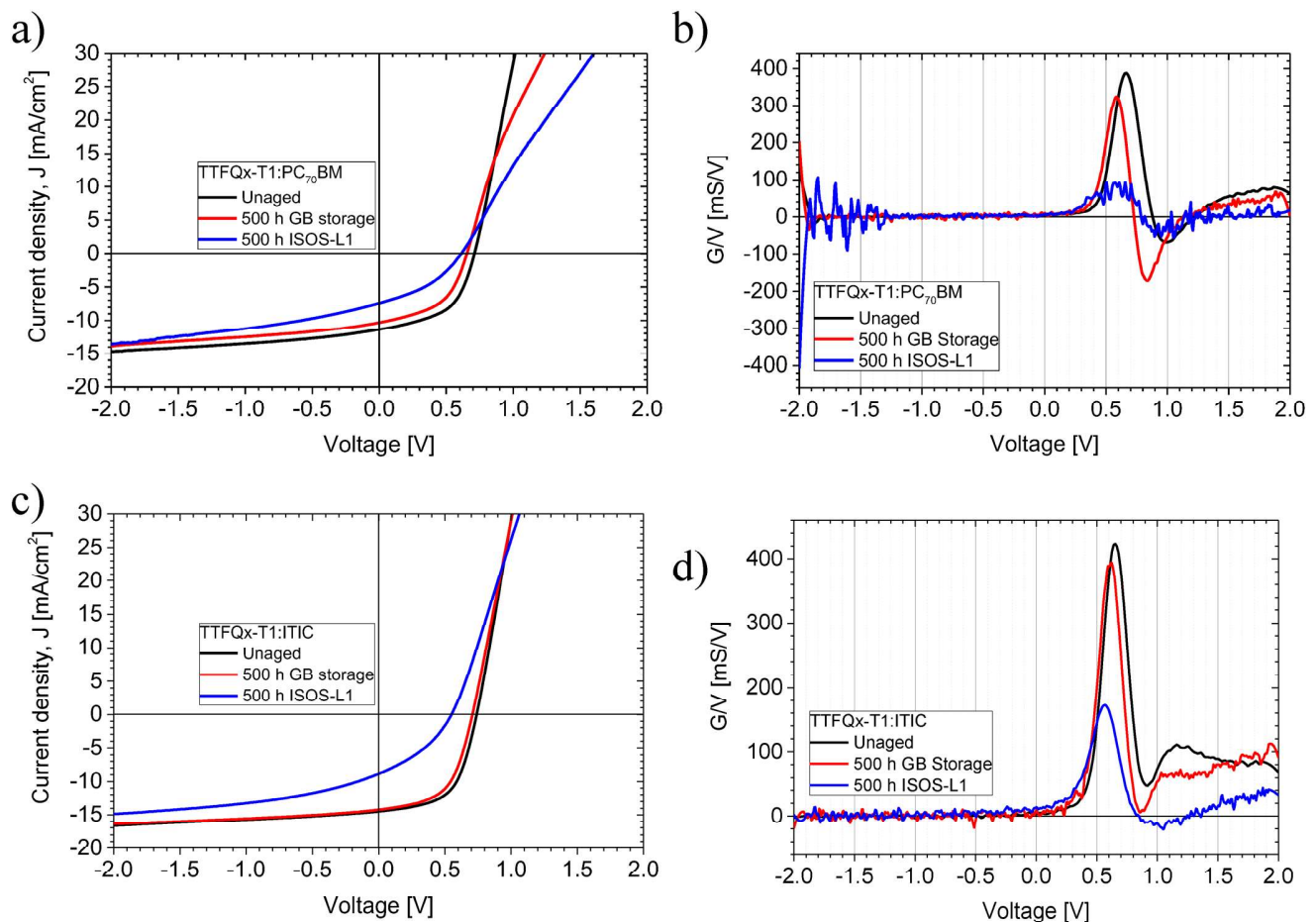


FIG. 10. Conventional organic solar cells with various active layers aged under ISOS-D1 and ISOS-L1 conditions. (a) IV curves of unaged and aged TTFQx-T1:PC₇₀BM devices, (b) respective second derivatives to [(a) and (c)] IV curves of unaged and aged TTFQx-T1:ITIC devices, (d) respective second derivatives to (c).

peak with a reduced height as well as an increased width. Though this also does not fully quantitatively describe the second derivatives we found for the devices in Fig. 1, we gained a thorough understanding of how different parameters influence the second derivative and how to interpret different shapes.

With the previous simulations and their results, we can now return to the IV curves obtained experimentally (compare with Fig. 1). As shown by the simulations, a dual peak is only possible with two parallel diodes, where one of the diodes performs significantly worse than the other. Such a worse performing diode would be especially characterized by a significantly larger dark saturation current. This increase in dark saturation current density could be the result of several factors, like a high doping level, which would lead to a Schottky-like contact at the interface between the organic semiconductor and metal electrode. This likely stems from an inhomogeneous vertical phase separation as one possible effect. The homogenization of performance for devices with a longer soaking

time of methanol on top of the active layer film suggests a process driven by diffusion of the material in the active layer as one of the causes for the improvement. However, it cannot be the sole reason; else, the short contact during spin coating would not already show an improvement. Therefore, on the one hand, we propose the formation of a passivating layer due to adsorbed methanol, combined with (at more extended times of methanol exposure) a more favorable vertical phase separation of the blend as the cause for improvement seen from the methanol treatment. We summarized our possible hypothesis why the methanol treatment results in an improvement in Table I, together with an assessment of their probability. Further investigations are ongoing.

Another topic to be mentioned not fully reflected by the simulations done in LTSpice is that all the IV curves of well-functioning solar cells do not immediately fall back to zero in the second derivative when the series resistance starts dominating the device behavior. Instead, they tend to stabilize toward a constant value larger

than zero. A short discussion on the possible origin of this effect is given in the [supplementary material](#), as further investigations are ongoing at the moment.

Finally, herein, we also want to show the newly presented method applied to aged organic solar cells. In [Fig. 8](#), the consecutive *IV* curves of devices aged under ISOS-L1^{23,24} conditions with a white light LED at 45 °C are shown. The devices consisted of a layerstack of ITO/PEDOT:PSS[PVP AI 4083]/PCDTBT:PC₇₁BM/Al. As can be seen in [Fig. 8\(a\)](#), a very subtle S-shape in the *IV* curve toward the end of the 24 h of aging has been developed, while the device shown in [Fig. 8\(c\)](#) does not show an S-shape at the end of the 24 h. The respective second derivatives of the *IV* curves, shown in [Figs. 8\(b\)](#) and [8\(d\)](#), show some interesting developments; for (b), one can see that there are clearly two inflection points from the second derivative for the devices showing an S-shape, this dual inflection point develops at around 15 h. There is also some difference in the fresh devices for (b) and (d); both show a rather constant second derivative between 1.5 and 2 V. It should be noted that a constant second derivative can, in principle, be associated with a space-charge-limited current (SCLC), whose development over time displays a possible degradation route. In the case of (b), from the beginning, there is already a very weakly “blocking” contact with a valley in the second derivative. This valley further grows in depth up until 15 h, where it crosses the abscissa, and thereupon, keeps further moving toward negative values. A similar trend is shown in (d), but the valley is not there from the start of the experiment and also does not reach negative values. Therefore, the *IV* curve also does not show an S-shape even for the longest times shown here, but from the development of (b), the formation of an S-shape is expected. Another interesting observation is that the peaks in (b) and (d) show broad extensions toward voltages of 0 V. From the simulations shown in [Figs. 4](#) and [7](#), that very broad extension of this peak can only be explained by a broad distribution of the values of I_0 and/or R_s of the devices. Upon aging, this distribution also shifts toward lower voltages, showing an inhomogeneous degradation of I_0 and/or R_s . In [Fig. 9](#), the development of a blocking contact that takes up more and more of the solar cell area is shown; besides the plateau toward larger biases, it is well able to reproduce the behavior seen in the devices shown in [Fig. 8](#). Note that the equivalent circuits for this simulation are shown in [Figs. S57–S61](#) in the [supplementary material](#). Though it can show the behavior we have seen in the aged devices sufficiently well, we are not ruling out other mechanisms.

In [Fig. 10](#), an additional sample of the aged organic solar cell devices is depicted, which exhibits a conventional layer architecture of glass/ITO/PEDOT:PSS/photoactive layer/Mg/Al. For the fullerene-based device, there is already a weak blocking contact visible in the second derivative for the fresh device, severe enough to result in an S-shape in the *IV* curve. This blocking contact becomes even more severe after 500 h of glovebox storage. As the storage in the glovebox precludes effects like oxidation of the low work function electrodes, the most likely culprit for the observed effect is an unfavorable vertical phase separation of the donor and acceptor, i.e., the polymer is preferentially segregating toward the Mg contact and vice versa. This effect becomes even more severe under ISOS-L1 conditions, as the increased temperature is driving forward the diffusion-driven process more quickly. In the ITIC based device, there is also some blocking character visible in the

second derivative, but it is not fully able to block the current in the forward direction. This suggests a reduced driving force for vertical phase separation of the donor and acceptor, in contrast to the combination of the fullerene acceptor. Upon glovebox storage, the blocking contact also got more pronounced without resulting in an S-shape in the *IV* curve. Already during 500 h of ISOS-L1 aging, an S-shape in the *IV* curve has been formed. Besides that, there is a pronounced reduction in peak height in the second derivative without a large shift in position. This suggests a combined increase in diode ideality factor and series resistance with an additional increase in dark saturation current. All mentioned effects would result in a peak reduction, while an increase in diode ideality factor and series resistance would move the peak toward lower voltages, while an increase in diode ideality factor results in the peak moving toward higher voltages compensating for the increase in the other two metrics.

IV. CONCLUSION

Concluding, we have presented a new method to analyze the defects in solar cells via the usage of already existing data from measurements routinely performed as the most basic procedure for any solar cell. This method allows for quick hypothesis generation and can, therefore, assist researchers to focus their efforts on more specific methods. Furthermore, it can be used in aging experiments of the solar cells as an early warning proxy for significant changes in the device to come, as it can detect subtle changes in the *IV* curve with ease. The latter itself is the one measure that is probed throughout the whole experiment—usually during aging experiments—and, therefore, readily available for analysis. Therefore, a steady analysis of the second derivative of *IV* characteristics allows researchers to retrieve samples from an aging experiment at times, where the most important knowledge can be gained on the changes responsible for degradation. We further have presented that the assumption of a simple Shockley equation with series and shunt resistance cannot be enough to adequately describe the behavior of organic solar cells as this is also the basis behind the operation of SPICE and none of the simulated second derivative curves were fully able to represent the measured curves, not even fully qualitatively.

SUPPLEMENTARY MATERIAL

See the [supplementary material](#) for additional *IV* curves, all equivalent circuits including the parameters used, and an additional calculation regarding the possible origin of the plateau seen at forward biases above 1 V, in all measured *IV* curves.

ACKNOWLEDGMENTS

R.M., H.H., and U.S.S. gratefully acknowledge the Deutsche Forschungsgemeinschaft (DFG) for financial support. U.S.S. is grateful to the Thüringer Ministerium für Wirtschaft, Wissenschaft und Digitale Gesellschaft (TMWWDG) for funding the CEEC Jena. The project underlying these results was funded by the Free State of Thuringia under No. 2016 IZN 0009 and co-financed by funds from the European Union within the framework of the European Regional Development Fund (ERDF). S.A. and F.L. are grateful for

the support from the King Abdullah University of Science and Technology (KAUST) Office of Sponsored Research (OSR) under Award No. OSR-2018-CARF/CCF-3079.

AUTHOR DECLARATIONS

Conflict of Interest

The authors have no conflicts to disclose.

Author Contributions

Rico Meitzner: Conceptualization (equal); Data curation (equal); Formal analysis (equal); Investigation (equal); Methodology (equal); Project administration (equal); Software (equal); Writing – original draft (equal); Writing – review and editing (equal). **Jose Prince Madalaimuthu:** Formal analysis (supporting); Investigation (supporting). **Shahidul Alam:** Data curation (supporting); Formal analysis (supporting); Investigation (supporting). **Md Moidul Islam:** Investigation (supporting). **Sebastian Peiler:** Investigation (supporting). **Aman Anand:** Investigation (supporting); Writing – original draft (supporting). **Johannes Ahner:** Investigation (supporting). **Martin D. Hager:** Funding acquisition (equal); Investigation (supporting). **Ulrich S. Schubert:** Funding acquisition (lead); Writing – original draft (supporting). **Yingping Zou:** Funding acquisition (equal); Investigation (supporting). **Frédéric Laquai:** Funding acquisition (equal); Investigation (equal); Writing – original draft (equal). **Harald Hoppe:** Funding acquisition (equal); Supervision (lead); Writing – original draft (equal).

DATA AVAILABILITY

The data that support the findings of this study are available from the corresponding author on reasonable request.

REFERENCES

- ¹N. Espinosa, M. Hosel, M. Jorgensen, and F. C. Krebs, *Energy Environ. Sci.* **7**(3), 855–866 (2014).
- ²A. Distler, C. J. Brabec, and H.-J. Egelhaaf, *Prog. Photovoltaics: Res. Appl.* **29**(1), 24–31 (2021).
- ³S. Dong, T. Jia, K. Zhang, J. Jing, and F. Huang, *Joule* **4**(9), 2004–2016 (2020).
- ⁴R. Meitzner, U. S. Schubert, and H. Hoppe, *Adv. Energy Mater.* **11**(1), 2002551 (2021).
- ⁵C. J. M. Emmott, J. A. Röhr, M. Campoy-Quiles, T. Kirchartz, A. Urbina, N. J. Ekins-Daukes, and J. Nelson, *Energy Environ. Sci.* **8**(4), 1317–1328 (2015).
- ⁶Y. Liu, P. Cheng, T. Li, R. Wang, Y. Li, S.-Y. Chang, Y. Zhu, H.-W. Cheng, K.-H. Wei, X. Zhan, B. Sun, and Y. Yang, *ACS Nano* **13**(2), 1071–1077 (2019).
- ⁷Q. Liu, Y. Jiang, K. Jin, J. Qin, J. Xu, W. Li, J. Xiong, J. Liu, Z. Xiao, K. Sun, S. Yang, X. Zhang, and L. Ding, *Sci. Bull.* **65**(4), 272–275 (2020).
- ⁸N. Espinosa, M. Hosel, D. Angmo, and F. C. Krebs, *Energy Environ. Sci.* **5**(1), 5117–5132 (2012).
- ⁹N. Espinosa, Y.-S. Zimmermann, G. A. Dos Reis Benatto, M. Lenz, and F. C. Krebs, *Energy Environ. Sci.* **9**(5), 1674–1680 (2016).
- ¹⁰R. Sun, W. Wang, H. Yu, Z. Chen, X. Xia, H. Shen, J. Guo, M. Shi, Y. Zheng, Y. Wu, W. Yang, T. Wang, Q. Wu, Y. Yang, X. Lu, J. Xia, C. J. Brabec, H. Yan, Y. Li, and J. Min, *Joule* **5**(6), 1548–1565 (2021).
- ¹¹Y. Li, X. Huang, K. Ding, H. K. M. Sheriff, L. Ye, H. Liu, C.-Z. Li, H. Ade, and S. R. Forrest, *Nat. Commun.* **12**(1), 5419 (2021).
- ¹²A. Kumar, S. Sista, and Y. Yang, *J. Appl. Phys.* **105**(9), 094512 (2009).
- ¹³G. del Pozo, B. Romero, and B. Arredondo, *Sol. Energy Mater. Sol. Cells* **104**, 81–86 (2012).
- ¹⁴A. Pozza, G. Bardizza, T. Sample, and E. Dunlop, “Analysis based on I-V curve changes of organic photovoltaic mini-modules subjected to degradation under different temperature and humidity conditions,” in *29th European Photovoltaic Solar Energy Conference and Exhibition*, Amsterdam, Netherlands, 22–26 September (2014).
- ¹⁵L. W. P. D. O. Nagel, *SPICE Simulation Program with Integrated Circuit Emphasis* (Electronics Research Laboratory, College of Engineering, University of California, Berkeley, 1973).
- ¹⁶L. Zuo, J. Yao, H. Li, and H. Chen, *Sol. Energy Mater. Sol. Cells* **122**, 88–93 (2014).
- ¹⁷S. Yoo, B. Domercq, and B. Kippelen, *J. Appl. Phys.* **97**(10), 103706 (2005).
- ¹⁸B. Ecker, H.-J. Egelhaaf, R. Steim, J. Parisi, and E. von Hauff, *J. Phys. Chem. C* **116**(31), 16333–16337 (2012).
- ¹⁹J. C. Wang, X. C. Ren, S. Q. Shi, C. W. Leung, and P. K. L. Chan, *Org. Electron.* **12**(6), 880–885 (2011).
- ²⁰S. R. Cowan, P. Schulz, A. J. Giordano, A. Garcia, B. A. MacLeod, S. R. Marder, A. Kahn, D. S. Ginley, E. L. Ratcliff, and D. C. Olson, *Adv. Funct. Mater.* **24**(29), 4671–4680 (2014).
- ²¹S. Trost, T. Becker, A. Polywka, P. Görrn, M. F. Oszajca, N. A. Luechinger, D. Rogalla, M. Weidner, P. Reckers, T. Mayer, and T. Riedl, *Adv. Energy Mater.* **6**(15), 1600347 (2016).
- ²²R. Meitzner, J. Essomba, S. Alam, A. Anand, N. Engel, K. Fulbert, K. Kuma, F. Ayuyasmin, M. M. Islam, C. Ugokwe, U. S. Schubert, and H. Hoppe, *Energy Technol.* **8**(12), 2000117 (2020).
- ²³M. O. Reese, S. A. Gevorgyan, M. Jørgensen, E. Bundgaard, S. R. Kurtz, D. S. Ginley, D. C. Olson, M. T. Lloyd, P. Morvillo, E. A. Katz, A. Elschner, O. Haillant, T. R. Currier, V. Shrotriya, M. Hermenau, M. Riede, K. R. Kirov, G. Trimmel, T. Rath, O. Inganäs, F. Zhang, M. Andersson, K. Tvingstedt, M. Lira-Cantu, D. Laird, C. McGuinness, S. Gowrisanker, M. Pannone, M. Xiao, J. Hauch, R. Steim, D. M. DeLongchamp, R. Rösch, H. Hoppe, N. Espinosa, A. Urbina, G. Yaman-Uzunoglu, J.-B. Bonekamp, A. J. J. M. van Breemen, C. Girotto, E. Voroshazi, and F. C. Krebs, *Sol. Energy Mater. Sol. Cells* **95**(5), 1253–1267 (2011).
- ²⁴M. V. Khenkin, E. A. Katz, A. Abate, G. Bardizza, J. J. Berry, C. Brabec, F. Brunetti, V. Bulović, Q. Burlingame, A. Di Carlo, R. Cheacharoen, Y.-B. Cheng, A. Colmann, S. Cros, K. Domanski, M. Dusza, C. J. Fell, S. R. Forrest, Y. Galagan, D. Di Girolamo, M. Grätzel, A. Hagfeldt, E. von Hauff, H. Hoppe, J. Kettle, H. Köbler, M. S. Leite, S. Liu, Y.-L. Loo, J. M. Luther, C.-Q. Ma, M. Madsen, M. Manceau, M. Matheron, M. McGehee, R. Meitzner, M. K. Nazeeruddin, A. F. Nogueira, Ç. Odabaşı, A. Osherov, N.-G. Park, M. O. Reese, F. De Rossi, M. Saliba, U. S. Schubert, H. J. Snaith, S. D. Stranks, W. Tress, P. A. Troshin, V. Turkovic, S. Veenstra, I. Visoly-Fisher, A. Walsh, T. Watson, H. Xie, R. Yıldırım, S. M. Zakeeruddin, K. Zhu, and M. Lira-Cantu, *Nat. Energy* **5**(1), 35–49 (2020).
- ²⁵See <https://www.analog.com/en/design-center/design-tools-and-calculators/ltspsice-simulator.html> for information regarding LTSpice: Analog Devices (Last viewed 16 May 2022)